



THE HONG KONG
POLYTECHNIC UNIVERSITY

香港理工大學

Pao Yue-kong Library

包玉剛圖書館

Copyright Undertaking

This thesis is protected by copyright, with all rights reserved.

By reading and using the thesis, the reader understands and agrees to the following terms:

1. The reader will abide by the rules and legal ordinances governing copyright regarding the use of the thesis.
2. The reader will use the thesis for the purpose of research or private study only and not for distribution or further reproduction or any other purpose.
3. The reader agrees to indemnify and hold the University harmless from and against any loss, damage, cost, liability or expenses arising from copyright infringement or unauthorized usage.

IMPORTANT

If you have reasons to believe that any materials in this thesis are deemed not suitable to be distributed in this form, or a copyright owner having difficulty with the material being included in our database, please contact lbsys@polyu.edu.hk providing details. The Library will look into your claim and consider taking remedial action upon receipt of the written requests.

**AIRFOIL TONAL NOISE REDUCTION BY
MEANS OF LOCALIZED FLOW-INDUCED
PANEL VIBRATION**

MUHAMMAD IRSALAN ARIF

PhD

The Hong Kong Polytechnic University

2022

THE HONG KONG POLYTECHNIC UNIVERSITY
DEPARTMENT OF MECHANICAL ENGINEERING

**Airfoil Tonal Noise Reduction by Means
of Localized Flow-Induced Panel
Vibration**

Muhammad Irsalan Arif

A thesis submitted in partial fulfillment of the requirements for
the degree of Doctor of Philosophy

September 2021

CERTIFICATE OF ORIGINALITY

I hereby declare that this thesis is my own work and that, to the best of my knowledge and belief, it reproduces no material previously published or written, nor material that has been accepted for the award of any other degree or diploma, except where due acknowledgment has been made in the text.

Muhammad Irsalan Arif

Abstract

In this research a novel passive control method for airfoil tonal noise using localized flow-induced vibration is proposed and numerically explored with a short elastic panel flush mounted on the suction surface of a NACA 0012 airfoil at a low Reynolds number of 5×10^4 and Mach number of 0.4. The numerical model is governed by two-dimensional compressible Navier-Stokes equations together with equation of state and solved by direct aeroacoustic simulation (DAS) solver based on the conservation element and solution element (CE/SE) method. The key idea is to absorb the energy of natural instabilities arising in the laminar boundary layer by locally self-sustained flow-induced vibration of the short panel which results in reduced flow instabilities for scattering at airfoil trailing edge and weakened aeroacoustic-feedback loop responsible for tonal noise radiation without any adverse effect on airfoil aerodynamics.

In the first part of research, a complete methodology of elastic panel design based on its material, structural properties, location etc is developed and the noise reduction potential of the designed airfoil configurations with panel is evaluated using a reduced order model, namely perturbation evolution method (PEM). The developed PEM technique allows much quicker panel design iterations with inputs of reasonable approximation and only requires 10% of the computing time required for a corresponding full DAS. The effects of panel resonance and non-resonance condition under the fluid loading are also evaluated by

PEM which reveal that a resonant panel located just ahead of the sharp growth of natural boundary layer instability within the airfoil separation bubble provides the maximum noise reduction.

Secondly, high-fidelity DAS calculations are carried out for the optimum elastic panel airfoil configuration to uncover the mechanism of tonal noise reduction using localized flow-induced vibration in a quantitative manner. The analysis of numerical results reveals that a resonating elastic panel just at the onset of sharp growth of boundary layer instability provides an overall tonal noise reduction up to 3 dB. Such significant noise reduction is achieved without any sacrifice in the original aerodynamic characteristics of the airfoil.

In the latter part of this research, the designed approach for airfoil tonal noise reduction is further enhanced by introducing structural coupling of elastic panels over the airfoil. The results of comprehensive aerodynamic and acoustic analyses, using high fidelity direct aeroacoustic simulation, of airfoil-panel configurations, show that an average and maximum noise reduction up to 7.6 dB and 7.9 dB can be achieved respectively, without any adverse effect on overall airfoil aerodynamics when strong coupled structural resonance between the panels prevails. This noise reduction is higher than twice of that from the configuration with a single panel which firmly illustrates the synergy of coupled flow-induced structural resonance of the panels prevailing in noise reduction.

Finally, an airfoil with multi-panel configuration is proposed which could provide tonal noise reduction for a range of angles of attack. A detailed design concept is presented based on the rigid airfoil characteristics at different angles of attack. Different extent of noise reduction by designed airfoil configuration is observed for the range of angle of attack making it a promising approach for modifying the acoustics of existing aerodynamic or wing profiles operating at variable loading conditions.

Research Output / Publications

To this date, following research has been produced or is under review

Book chapters

- I. Arif, G. C. Y. Lam, R. C. K. Leung and D. Wu (2021), “Leveraging Flow-Induced Vibration for Manipulation of Airfoil Tonal Noise,” *Flinovia—Flow Induced Noise and Vibration Issues and Aspects-III: A Focus on Measurement, Modeling, Simulation and Reproduction of the Flow Excitation and Flow Induced Response*, Springer.

Journal articles

- I. Arif, D. Wu, G. C. Y. Lam and R. C. K. Leung (2020), “Exploring Airfoil Tonal Noise Reduction with Elastic Panel Using Stability Analysis Technique,” *AIAA Journal*, Vol. 58, No. 11, pp. 4958-4968.
- I. Arif, G. C. Y. Lam, R. C. K. Leung and D. Wu (2020), “Passive Airfoil Tonal Noise Reduction by Localized Flow-Induced Vibration of an Elastic Panel,” *Aerospace Science and Technology*, Vol. 107, 106319.
- I. Arif, G. C. Y. Lam and R. C. K. Leung (2021), “Coupled Structural Resonance of Elastic Panels for Suppression of Airfoil Tonal Noise.,” *Journal of Fluids and*

Structures (under review).

- I. Arif, G. C. Y. Lam and R. C. K. Leung (2022), “Distributed Compliance System Airfoil for Tonal Noise Reduction at Various Loaded Conditions,” *Journal of Fluid Mechanics* (under preparation).

Conference proceedings

- I. Arif, G. C. Y. Lam, R. C. K. Leung and D. Wu (2019), “Leveraging Surface Aeroacoustic-Structural Interaction for Airfoil Tonal Noise Reduction—A Parametric Study,” *25th AIAA/CEAS Aeroacoustics Conference*, Delft, Netherlands, Paper No. AIAA 2019-2758.
- R. C. K. Leung, G. C. Y. Lam, I. Arif and D. Wu (2019), “Leveraging Flow-Induced Vibration for Manipulation of Airfoil Tonal Noise,” *FLINOVIA III-Flow Induced Noise and Vibration Issues and Aspects*, Lyon, France.
- I. Arif, G. C. Y. Lam and R. C. K. Leung (2020), “Assessing Airfoil Tonal Noise Reduction Potential Using Flow-Induced Vibration of an Elastic Panel at Various Angles of Attack,” *49th INTER-NOISE and NOISE-CON Congress and Conference Proceedings*, Institute of Noise Control Engineering, Seoul, Korea.
- I. Arif, G. C. Y. Lam and R. C. K. Leung (2021), “Numerical Study of Airfoil Tonal Noise Reduction using Dual-Segmented Elastic Panel Configuration,” *50th INTER-NOISE and NOISE-CON Congress and Conference Proceedings*, Institute of Noise Control Engineering, Washington, USA.

Acknowledgments

I am grateful to Almighty Allah for providing me the opportunity, capability and strength to accomplish this challenging task. Without the support and assistance from different individuals it was not possible to complete this journey.

Firstly and foremostly, I would like to acknowledge my chief research supervisor Dr. Randolph Chi Kin Leung for his continuous assistance, guidance and encouragement throughout this tough journey. His precious and inspirational advices which I received during our long discussions not only facilitated me to overcome the technical problems but also transpired great positivity in my approach. His inquisitive nature to understand the underlying physical mechanisms behind every outcome motivated me to become a critical thinker.

I would also like to thank my senior colleague Dr. Garret Chi Yan Lam for his support on every technical issue which I encountered during my tenure. I am also indebted to my other group fellows Dr. Harris Ka Heng Fan, Racer Ka Hei LAM, Rehan Naseer for their time and assistance whenever I approached them. I would also like to acknowledge The Hong Kong Polytechnic University for providing all the necessary resources and a research conducive environment to accomplish my PhD studies without any administrative hindrance.

Most importantly, I cannot thank enough my wife for her moral support and encouragement throughout my studies. Sharing my problems with her during my tough days only helped me in coming out stronger than before. Also, the continuous prayers and wishes of my parents and other family members worked wonders for me which are beyond my imagination.

Contents

Abstract	iv
Research Output / Publications	vi
Acknowledgments	ix
List of Figures	xv
List of Tables	xxvi
Abbreviations	xxix
Nomenclature	xxx
1 Introduction	1
1.1 Literature Review	3
1.1.1 Airfoil Tonal Noise Mechanism	3
1.1.2 Noise Control Methods	11
1.1.3 Aerodynamic Control by Fluid-Structure Interactions	15
1.2 Objectives of the Present Study	20
1.3 Overview of the Study	22
1.4 Organization of the Thesis	24
2 Numerical Methods	26

2.1	Introduction	26
2.2	Aeroacoustic Solver	27
2.2.1	Conservation Element and Solution Element Method (CE/SE)	29
2.3	Structural Solver	44
2.3.1	Boundary Conditions	46
2.4	Aeroacoustic-Structural Coupling	49
2.5	Perturbation Evolution Method (PEM)	54
2.5.1	Methodology	55
2.5.2	Mathematical Formulation	58
2.5.3	Coupling of PEM with CE/SE Method	60
2.5.4	Perturbations	61
2.6	Conclusions	63
3	Direct Aeroacoustic Simulation of Rigid Airfoil	67
3.1	Introduction	67
3.2	Problem Formulation and Numerical Method	68
3.2.1	Airfoil Selection	68
3.2.2	Computational Setup	69
3.2.3	Grid Generation	74
3.3	Direct Aeroacoustic Simulation of Rigid Airfoil	76
3.3.1	Time-Averaged Aerodynamics	77
3.3.2	Unsteady Airfoil Aerodynamics	85
3.3.3	Airfoil Acoustics	90
3.4	Conclusions	100
4	Assessment of Airfoil Tonal Noise Reduction Potential using Per-	
	turbation Evolution Method	102
4.1	Introduction	102

4.1.1	Design of Elastic Panel	103
4.2	PEM Analysis	109
4.2.1	Base Flow	109
4.2.2	Perturbation	111
4.3	Verification of Proposed Methodology	114
4.4	Assessment of Noise Reduction by Elastic Panels	120
4.5	Structural Response of Elastic Panel	123
4.6	Conclusions	127
5	Airfoil Tonal Noise Reduction by Localized Flow-Induced Panel	
	Vibration	129
5.1	Introduction	129
5.2	Aerodynamic Analysis	130
5.3	Time-Frequency Analysis	141
5.4	Airfoil Acoustics	147
5.5	Panel Dynamics	155
5.6	Comparison of DAS and PEM Prediction	158
5.7	Conclusions	161
6	Reduction of Airfoil Tonal Noise by Coupled Panel Resonance	164
6.1	Introduction	164
6.2	Airfoil-Panel Configurations	166
6.2.1	Panel Length	166
6.2.2	Panels Coupling Setup	167
6.2.3	Panel Structural Properties	173
6.3	Assessment of Noise reduction Potential by PEM	174
6.4	DAS Analysis of Airfoil-Panel Configurations	177
6.4.1	Airfoil Aerodynamics	180

6.4.2	Airfoil Acoustics	186
6.4.3	Panel-Structure Coupling	188
6.4.4	Relationship between Near Flow Field and Acoustics	209
6.5	Conclusions	217
7	Multi-Panel Configuration for Noise Reduction at Various Loaded Conditions	220
7.1	Introduction	220
7.2	Methodology	221
7.2.1	Choice of the Range of AoA	221
7.2.2	Design and Analysis Methodology	223
7.3	Rigid Airfoil Analyses	224
7.3.1	Time-Averaged Analysis	226
7.3.2	Unsteady Flow Analysis	229
7.4	Elastic Panel Design	233
7.5	Assessment of Noise Reduction by PEM	241
7.6	Multi-Panel Configuration	245
7.6.1	Panel Design Concept	245
7.6.2	Noise Reduction Potential of MPC	246
7.6.3	Structural Responses of Elastic Panels	252
7.7	Discussion on MPC Noise Reduction Potential	257
7.8	Conclusions	258
8	Conclusions	260
8.1	Summary and Research Achievements	260
8.2	Limitations and Future Works	264
	References	266

List of Figures

1.1	Frequency structure observed by Paterson et al. (1973).	4
1.2	Feedback loop mechanism proposed by Desquesnes et al. (2007).	8
1.3	Different airfoil noise reduction mechanisms. (a) Biomimetic airfoil (Wang et al. 2017a), (b) sawtooth trailing edge (Gruber et al. 2010), (c) trailing edge flaplets (Talboys and Brücker 2018), (d) trailing edge perforations (Geyer and Sarradj 2014).	19
2.1	Schematic of triangulate grids. A , C , E and G are the centroids of the grids; B , D and F are the nodes; G^* is the solution point; and - - - is the boundary of CE.	32
2.2	Schematic of conservation element $CE(G^*, n)$. - - - is the boundary of $SE(G^*, n)$	33
2.3	Schematic of solution element $SE(G^*, n)$	33
2.4	Schematic of conservation element of hexahedron. (a) $A_1B_1G_1F_1 - A_0B_0G_0F_0$, (b) $B_1C_1D_1G_1 - B_0C_0D_0G_0$, (c) $D_1E_1F_1G_1 - D_0E_0F_0G_0$ and (d) $A_1B_1C_1D_1E_1F_1$	35
2.5	Definition of P_i	40
2.6	Schematic of analytical domain of dependence and analytical domain of dependence.	41
2.7	Illustration of stability criterion.	41
2.8	Schematic of mesh at fluid-panel interface (Fan 2018).	47

2.9	Forces balance on control volume.	51
2.10	Newton's method iterative procedure.	53
2.11	Evolution of weak Gaussian perturbation over the airfoil from $t =$ $0 - 1.0$	64
2.12	Evolution of weak Gaussian perturbation over the airfoil from $t =$ $1.2 - 2.2$	65
3.1	NACA 0012 airfoil profile.	68
3.2	Schematic sketch of the computational domain.	71
3.3	A typical time history of pressure at $(x, y) = (0.5, 3)$ for rigid airfoil case at $M = 0.4$, $Re = 5 \times 10^4$ and $AoA = 5^\circ$	72
3.4	Distribution of virtual probes around the airfoil trailing edge. . .	73
3.5	Schematic sketch of the computational domain for G2.	75
3.6	Definition of mesh parameters.	75
3.7	Coefficient of lift and drag for different grids. - - -, G1; - - -, G2; and - - -, G3.	79
3.8	Distribution of (a) time-averaged C_p ; and (b) time-averaged C_f around rigid airfoil. —, suction surface; —, pressure surface. . . .	81
3.9	Time-averaged flow field. (a) u and (b) v	82
3.10	Time-averaged flow field. (a) p and (b) ρ	83
3.11	(a) Velocity streamlines over the airfoil surface; and (b) closeup view of airfoil suction surface indicating flow separation and reat- tachment points.	84
3.12	Flow field distribution of velocity fluctuations over rigid airfoil. (a) u'_{rms} and (b) v'_{rms}	86
3.13	Reynolds stress distribution over the rigid airfoil.	86

3.14	(a) Distribution of spectrum of transverse velocity fluctuations v' along the airfoil. (b) Spatial growth of flow instability over the airfoil suction surface at $(f_{bl})_0$ and $(f_{bl})_1$. The horizontal red dashed-dot lines in (a) indicate the $(f_{bl})_n$, $n = 1, 2, 3$ and the vertical blue dashed lines in (b) indicate the boundary layer separation and reattachment points.	88
3.15	FFT spectra of (a) C_L and (b) C_D	89
3.16	Instantaneous vorticity distribution on rigid airfoil.	91
3.17	Instantaneous acoustic fluctuation p'	93
3.18	Azimuth plot of time-averaged p/p_∞ at (a) $r = 2$ and (b) $r = 3$. —, rigid airfoil; —, Jones et al. (2008).	94
3.19	Time history of pressure fluctuations at different azimuth locations. (a) $\theta = 45^\circ$, (b) $\theta = 135^\circ$, (c) $\theta = 225^\circ$ and (d) $\theta = 315^\circ$. The horizontal red dashed lines indicate maximum and minimum values.	96
3.20	FFT spectra of p' at $r = 3$ for different azimuth locations. (a) $\theta = 45^\circ$, (b) $\theta = 135^\circ$, (c) $\theta = 225^\circ$ and (d) $\theta = 315^\circ$	97
3.21	(a) Azimuthal spectrum of acoustic fluctuations p' at $r = 3$; and (b) directivity of p' spectrum at $r = 3$	99
4.1	Spatial growth of flow instability with a snapshot of vorticity distribution. The two blue dashed lines show the extent of separation bubble. The small figure shows snapshot of the flow.	105
4.2	Schematic sketch of the flow problem and the locations of elastic panels.	106
4.3	Steady base flow of RS case. (a) Distribution of total velocity. (b) Distribution of pressure. (c) Relative error of pressure from initial flow solution at $(x, y) = (0.4, 0.07)$, $(0,0)$ and $(0,1)$	111

4.4	PEM analysis excited by a Gaussian perturbation. (a) Evolution of transverse velocity fluctuations v' over panel. (b) Snapshots of panel displacements at maximum v' during intervals A and B. A thin red line is drawn at $y=0$ for reference.	113
4.5	Evolution of aeroacoustic feedback loop illustrated with transverse velocity fluctuations v'	116
4.6	Relative percentage deviation ($= 0.25\%$) of total velocity between EP1 _R and RS base flow determined from DAS solutions.	118
4.7	Azimuth distributions of acoustic p'_{rms} for EP1 _R case. —, from PEM solution; —, from DAS solution.	119
4.8	Effect of elastic panel on flow instability evolution at 99% chord location. First row, EP1; second row, EP2; third row, EP3. —, with panel; —, without panel (i.e. RS).	122
4.9	Effect of elastic panel on noise generation. (a), (c) and (e) distribution of p'_{rms} ; (b), (d) and (f) $\Delta SPL_{reduction}$. —, with resonant panel; —, with non-resonant panel; - - -, RS cases.	124
4.10	Vibratory responses of elastic panels. —, resonant panel; —, non-resonant panel. Left column, snapshots of vibration modes at $t = 6$. Right column, time histories of displacements at panel center.	126
5.1	Distribution of C_f on airfoil. The highlighted portion indicates the coverage of elastic panel. - - -, RS; —, EP1 _{NR} ; —, EP1 _R	131
5.2	Streamlines over the airfoil surface. (a) RS, (b) EP1 _{NR} , (c) EP1 _R . Closeup view of airfoil suction surface indicating flow separation and reattachment points. (d) RS; (e) EP1 _{NR} ; (f) EP1 _R	132
5.3	Time-averaged streamwise velocity profile. (a) RS, (b) EP1 _{NR} and (c) EP1 _R	134

5.4	Boundary layer profiles at different chord locations. - - - -, RS; —, EP1 _{NR} ; —, EP1 _R	135
5.5	Coefficient of (a) lift C_L and (b) drag C_D . - - -, RS; —, EP1 _{NR} ; —, EP1 _R	137
5.6	Velocity fluctuations u'_{rms} and v'_{rms} . (a) and (d), RS; (b) and (e), EP1 _{NR} ; (c) and (f), EP1 _R	139
5.7	Reynolds stress distribution over the airfoil surface. (a) RS, (b) EP1 _{NR} , (c) EP1 _R	140
5.8	Velocity profiles in airfoil near wake region at $x = 1.05$. —, RS; —, EP1 _{NR} ; —, EP1 _R	141
5.9	Spatial growth of flow instability over airfoil suction surface. - - - -, RS; —, EP1 _{NR} ; —, EP1 _R	142
5.10	Deviation in magnitude of transverse velocity fluctuations $ v' $ at airfoil suction surface for EP1 _R and EP1 _{NR} with respect to RS. (a) (f_{bl}) ₀ =3.37, (b) (f_{bl}) ₁ =6.6. —, EP1 _{NR} ; —, EP1 _R	144
5.11	Time history of transverse velocity fluctuations v' . (a) $x = 0.3$, (b) $x = 0.5$, (c) $x = 0.7$, (d) $x = 0.8$, (e) $x = 0.9$ and (f) $x = 0.99$, - - - -, RS; —, EP1 _{NR} ; —, EP1 _R	146
5.12	Deviation in overall magnitude of transverse velocity fluctuations v' at airfoil suction surface for EP1 _R and EP1 _{NR} with respect to RS. —, EP1 _{NR} ; —, EP1 _R	147
5.13	Instantaneous acoustic fluctuation p' at the moment of C_L peak. (a) RS, (b) EP1 _{NR} and (c) EP1 _R	148
5.14	Azimuthal distributions of acoustic fluctuations p' spectra at $r = 3$. (a) RS, (b) EP1 _{NR} and (c) EP1 _R	150
5.15	Spectra of overall pressure fluctuations around the airfoil at $r = 3$. (a) —, RS; (b) —, EP1 _{NR} ; (c) —, EP1 _R	151

5.16	Azimuth distribution of (a) p'_{rms} at $r = 3$ and (b) SPL reduction at $r = 3$. - - - -, RS; —, EP1 _{NR} ; —, EP1 _R	153
5.17	(a) Azimuth plot of p'_{rms} at $r = 3$ and (b) SPL reduction plot at $r = 3$. - - - -, RS; —, EP1 _R ; —, EP2 _R ; —, EP3 _R . The blue shaded area indicates noise amplification.	154
5.18	Vibration response of EP1 _R . (a) $t = 1$, (b) $t = 2$, (c) $t = 3$, (d) $t = 4$, (e) $t = 5$, and (f) $t = 6$	156
5.19	(a) Temporal evolution of panel deflection and (b) phase plane plot at center of panel.	157
5.20	Time histories of panel displacements and their frequency spectra. (a) and (b) 20%, (c) and (d) 40%, (e) and (f) 60%, (g) and (h) 80% panel length.	159
5.21	Azimuth distribution of p'_{rms} at $r = 3$ for EP1 _R case with PEM and DAS.—, PEM solution; —, DAS solution.	160
6.1	(a) Distribution of spectrum of transverse velocity fluctuations along the airfoil, and (b) spatial growth of flow instability over the airfoil suction surface at $(f_{bl})_0$. The blue shaded area in (b) indicates the coverage of panel for SP1 as defined in Section 6.2.2.	168
6.2	Virtual probes location around the airfoil at $r = 3$	170
6.3	Phase difference between the acoustic signals at location $(r, \theta) = (-1.12, 135^\circ)$ and velocity signals along the airfoil chord. (a) wrapped phase plot, and (b) unwrapped phase plot.	171
6.4	Schematic sketch of airfoil-panel configuration designs. ①, first panel; ②, second panel.	173

6.5	(a) PEM prediction of spatial growth of boundary layer instabilities at $(f_{bl})_0$. (b) Deviation in magnitude of transverse velocity fluctuations v' along airfoil suction surface from RS. Note that the results for SCC3 and SP1 almost overlap.	178
6.6	Effect of elastic panel(s) on noise generation from PEM analysis. (a) Distribution of p'_{rms} at $r = 3$, and (b) $\Delta SPL_{reduction}$ at $r = 3$. The area shaded in gray indicates SPL amplification. Note that the data for SCC3 and SP1 almost overlaps.	179
6.7	Time-averaged streamlines over the airfoil surface; (a) RS, (b) SP1, (c) SP2, and (d) SCC1. Closeup views of airfoil suction surface indicating flow separation and reattachment points; (e) RS, (f) SP1, (g) SP2, and (h) SCC1. ①, first panel; ②, second panel.	181
6.8	Time history of transverse velocity fluctuations v' . (a) $x = 0.7$, (b) $x = 0.8$, (c) $x = 0.9$, and (d) $x = 0.99$. —, RS; —, SP1; —, SCC1.	183
6.9	Velocity profiles in airfoil near wake region at (a) $x = 1.05$, and (b) $x = 1.5$. —, RS; —, SP1; —, SP2; —, SCC1.	185
6.10	Instantaneous pressure fluctuations p' . (a) RS, (b) SP1, (c) SP2, and (d) SCC1.	187
6.11	Azimuth distributions of (a) p'_{rms} at $r = 3$, and (b) $\Delta SPL_{reduction}$ at $r = 3$. —, RS; —, SP1; —, SP2; —, SCC1.	189
6.12	Comparison of the amplitude of Fourier transform for first three modes at the selected frequencies $f = 1.1, 2.2$ and 3.3 extracted by FMD. (a) SP1, (b) SP2, (c) first panel of SCC1, and (d) second panel of SCC1. —, first mode; - - - -, second mode; - · - ·, third mode.	191

6.13	Panel dynamics. SP1 and the first panel of SCC1: (a) panel displacement spectra. SP2 and the second panel of SCC1: (b) panel displacement spectra. —, SP1; —, SP2; —, SCC1.	193
6.14	Panel dynamics. SP1 and the first panel of SCC1: (a) phase plots of centres of panel. SP2 and the second panel of SCC1: (b) phase plots of centres of panel. —, SP1; —, SP2; —, SCC1.	194
6.15	(a) Spectrum of cross wavelet coherence among the two panels for SCC1. (b) Spectrum of phase difference among the two panels for SCC1. The horizontal black dot-dashed line indicates the $(f_{bl})_0$	196
6.16	Coherence of vibration responses of the two panels for SCC1. (a) Magnitude-squared coherence γ^2 , (b) phase difference θ_{ab}	197
6.17	Snapshots of the p' over the panels and panel displacements in SCC1 within one period $T_d = 1/(f_{bl})_0$. ①, first panel; ②, second panel.	199
6.18	Wavenumber-frequency spectra for SCC1. (a) w and (c) p' for the first panel, (b) w and (d) p' for the second panel. Yellow dashed lines correspond to $\pm 0.65U_\infty$; red dashed line corresponds to acoustic velocity.	201
6.19	Space-time evolution of panel w' for the first panel of SCC1. (a) full w' . (b) Downstream propagating w' waves. (c) Upstream propagating w' waves.	203
6.20	Space-time evolution of flow p' for the first panel of SCC1. (a) full p' . (b) Downstream propagating p' waves. (c) Upstream propagating p' waves.	205
6.21	Space-time evolution of panel w' for the second panel of SCC1. (a) full w' . (b) Downstream propagating w' waves. (c) Upstream propagating w' waves.	206

6.22	Space-time evolution of flow p' for the second panel of SCC1. (a) full p' . (b) Downstream propagating p' waves. (c) Upstream propagating p' waves.	207
6.23	Spectra of cross-correlation for SCC1 between time signal of w at location of maximum displacement and (a) downstream propagating p' waves for first panel, (c) upstream propagating p' waves for first panel. Spectrum of cross-correlation for SCC1 between time signal of w at location of maximum displacement and (b) downstream propagating p' waves for second panel, (d) upstream propagating p' waves for second panel.	210
6.24	(a) Spatial growth of flow instability over the airfoil suction surface at frequency $(f_{bl})_0$. (b) Deviation of spectral amplitude $ v' $ at airfoil suction surface with respect to RS at $(f_{bl})_0 = 3.3$. —, RS; —, SP1; —, SP2; —, SCC1.	211
6.25	Spectra of magnitude-squared coherence γ_{12}^2 between the acoustic signal at $(r, \theta) = (-1.12, 135^\circ)$ and velocity signals along the airfoil chord. (a) RS, (b) SP1, (c) SP2, and (d) SCC1. The horizontal yellow dot-dashed lines indicate the frequencies $(f_{bl})_n$, $n = 0, 1, 2$. The vertical orange dotted lines indicate the panel edges.	213
6.26	Coherence plot at (a) $(f_{bl})_0=3.37$, (b) $(f_{bl})_1=6.6$ and (c) $(f_{bl})_2=10$. —, RS; —, SP1; —, SP2; —, SCC1. The vertical black dotted lines indicate the panel edges.	215
6.27	Spectra of phase difference θ_{12} between the acoustic signal at a location $(r, \theta) = (-1.12, 135^\circ)$ and velocity signals along the airfoil chord. (a) RS, (b) SP1, (c) SP2, and (d) SCC1. The horizontal yellow dot-dashed lines indicate the $(f_{bl})_n$, $n = 1, 2, 3$, and the vertical black dotted lines indicate the panel edges.	216

6.28 (a) Designed framework for panel pair configuration design, and (b) Identification of feasible locations for panel placement.	217
7.1 Variation of λ_{conv} with AoA	224
7.2 Schematic of the proposed methodology.	225
7.3 Time-averaged C_p distribution over the airfoil.	227
7.4 Time-averaged C_f distribution over the airfoil. (a) suction surface and (b) pressure surface.	228
7.5 Variation of time-averaged separation point, reattachment point and length of separation bubble.	229
7.6 Time dependent C_L variation. —, $AoA = 3^\circ$; —, $AoA = 5^\circ$; —, $AoA = 7^\circ$	231
7.7 FFT spectra of time dependent C_L variation. (a) $AoA = 3^\circ$, (b) $AoA = 5^\circ$ and (c) $AoA = 7^\circ$	232
7.8 Iso-contours of instantaneous vorticity for $AoA = 3^\circ$ at different time instances.	234
7.9 Iso-contours of instantaneous vorticity for $AoA = 5^\circ$ at different time instances.	235
7.10 Iso-contours of instantaneous vorticity for $AoA = 7^\circ$ at different time instances.	236
7.11 Frequency spectra of transverse velocity fluctuations. (a) $AoA =$ 3° , (b) $AoA = 5^\circ$ and (c) $AoA = 7^\circ$. The vertical black dashed lines indicate boundary layer separation and reattachment loca- tions. The horizontal red dot-dashed lines indicate the dominant frequencies of the boundary layer instabilities.	238
7.12 Spatial growth of flow instability over the airfoil suction surface.	239
7.13 Schematic sketch of the airfoil configurations with single elastic panels. (a) $AoA = 3^\circ$. (b) $AoA = 5^\circ$. (c) $AoA = 7^\circ$	240

7.14	Azimuth distribution of p'_{rms} at $r = 3$. (a) $AoA = 3^\circ$. (b) $AoA = 7^\circ$. —, RS; —, EP _{AoA=3°} ; —, EP _{AoA=7°}	243
7.15	Azimuth distribution of $\Delta SPL_{reduction}$ at $r = 3$. —, EP _{AoA=3°} ; —, EP _{AoA=5°} ; —, EP _{AoA=7°}	244
7.16	Schematic sketch of the MPC design concept.	246
7.17	Comparison of azimuth distributions of p'_{rms} at $r = 3$ between MPC and RS. (a) $AoA = 3^\circ$, (b) $AoA = 5^\circ$, and (c) $AoA = 7^\circ$. —, RS; —, MPC.	248
7.18	Comparison of azimuthal distribution of $\Delta SPL_{reduction}$ at $r = 3$ between MPC and respective RS. —, $AoA = 3^\circ$; —, $AoA = 5^\circ$; —, $AoA = 7^\circ$. The area shaded in red indicates SPL amplification.	249
7.19	FFT spectra at different $AoAs$. (Left column) $x = 0.9$ and (right column) $x = 0.99$. (a) and (b) $AoA = 3^\circ$, (c) and (d) $AoA = 5^\circ$, (e) and (f) $AoA = 7^\circ$. —, RS; —, MPC.	251
7.20	Vibratory responses of elastic panels for MPC at $t = 5$. (a) $AoA = 3^\circ$, (b) $AoA = 5^\circ$, and (c) $AoA = 7^\circ$. —, EP1; —, EP2; —, EP3; - - -, single resonant panel for corresponding AoA i.e. $x = 0.65 - 0.70$ for (a), $x = 0.40 - 0.45$ for (b) and $x = 0.20 - 0.25$ for (c).	254
7.21	Vibratory responses of elastic panels for MPC at $t = 6$. (a) $AoA = 3^\circ$, (b) $AoA = 5^\circ$, and (c) $AoA = 7^\circ$. —, EP1; —, EP2; —, EP3; - - -, single resonant panel for corresponding AoA i.e. $x = 0.65 - 0.70$ for (a), $x = 0.40 - 0.45$ for (b) and $x = 0.20 - 0.25$ for (c).	255

- 7.22 Vibratory responses of elastic panels for MPC at $t = 7$. (a) $AoA = 3^\circ$, (b) $AoA = 5^\circ$, and (c) $AoA = 7^\circ$. —, EP1; —, EP2; —, EP3; - - -, single resonant panel for corresponding AoA i.e. $x = 0.65 - 0.70$ for (a), $x = 0.40 - 0.45$ for (b) and $x = 0.20 - 0.25$ for (c). 256

List of Tables

3.1	Mesh size around airfoil for different grids	74
3.2	Mesh parameters for the complete domain for different grids (minimum mesh size/maximum mesh size)	76
3.3	Time-averaged aerodynamic parameters	80
4.1	Listing of normalized elastic panel parameters. Stainless steel is assumed for material properties.	109
4.2	A comparison of level of noise reduction of EP1 _R case from PEM and DAS solutions.	119
4.3	Effect of the presence of elastic panel on v'_{rms} in EP1, EP2 and EP3 cases.	121
5.1	Aerodynamic coefficients for RS, EP1 _{NR} and EP1 _R cases. Values in brackets show the relative changes from RS case.	137
5.2	A comparison of level of noise reduction of EP1 _R case from PEM and DAS solutions.	160
6.1	Details of airfoil-panel configurations design.	174
6.2	Normalized elastic panel parameters.	174
6.3	Effectiveness of airfoil configurations in tonal noise reduction (PEM prediction).	177
6.4	Comparison of $ v'^2 $ for different configurations.	184

6.5	Aerodynamic coefficients for RS, SP1, SP2 and SCC1 cases. Values in brackets show the percent deviation from RS case.	186
7.1	Comparison of time-averaged aerodynamic parameters.	230
7.2	Normalized elastic panel parameters	241
7.3	Panel effectiveness at different flow conditions	242
7.4	Effectiveness of multi-panel configuration at different flow conditions	250

Abbreviations

CE/SE	Conservation Element and Solution Element
CFL	Courant–Friedrichs–Lewy condition
DAS	Direct Aeroacoustic Simulation
EP	Elastic Panel
FFT	Fast Fourier Transform
FMD	Fourier Mode Decomposition
K-H	Kelvin-Helmholtz instabilities
LBL	Laminar Boundary Layer
LSB	Laminar Separation Bubble
MAV	Micro Air Vehicle
MPC	Multi-Panel Airfoil Configuration
N-S	Navier Stokes
NC	Non-Coupled Configuration
NRBC	Non-Reflecting Boundary Condition
PEM	Perturbation Evolution Method
RS	Rigid Airfoil
SCC	Strongly Coupled Airfoil Configuration
SP	Single Panel Airfoil Configuration
T-S	Tollmien–Schlichting wave
TBL	Turbulent Boundary Layer
WCC	Weakly Coupled Airfoil Configuration

Nomenclature

A	amplitude of perturbation
AoA	angle of attack
a	speed of sound
C	panel structural damping coefficient
C_D	coefficient of drag
C_f	coefficient of friction
C_L	coefficient of lift
C_p	coefficient of pressure
c	airfoil chord
c_p	specific heat at constant pressure
Δd_{le}	distance between leading edge of two panels
dt	time step size
E	energy
$\mathbf{F}, \mathbf{G}, \mathbf{U}$	flow flux conservation variables
f	frequency
$(f_{bl})_n$	n^{th} harmonic of natural boundary layer instability
$(f_{EP})_n$	n^{th} natural frequency of panel vibration mode
$f_{exc,n}$	frequency of acoustic excitation
h	panel thickness
K	stiffness of foundation supporting panel
k	wavenumber
k_{th}	thermal conductivity
L	panel length

l_p	location on panel
M	Mach number
N	panel internal tensile stress
n	mode number
P_r	Prandtl number
p, ρ	pressure and density
q_x, q_y	heat flux
R	specific gas constant for air
Re	Reynolds number based on airfoil chord
R_{pw}	normalized cross-correlation between pressure and displacement waves
S	panel bending stiffness
SPL	sound pressure level
T	temperature
T	panel external tension
T_d	time period
t	time
u, v	velocity components along streamwise and transverse directions
W_{ab}	cross wavelet coherence among the panels
w, \dot{w}	panel vibration displacement and velocity
$Y_{(k,f)}$	two-dimensional FFT in wavenumber-frequency domain
δ	offset from airfoil local radii of curvature
γ	specific heat ratio
γ_{12}^2	magnitude-squared coherence function between two signals
τ_{xx}, τ_{yy}	flow shear stresses
μ	viscosity
λ_{conv}	convective disturbance wavelength
θ_{12}	phase difference between two signals
ϕ_n	phase of acoustic excitation
σ	normal stress
∇	divergence operator

Subscripts

∞	freestream condition
b	boundary element
$base$	base flow
far	far field
g	ghost element
le	leading edge
NR	non-resonating panel
R	resonating panel
rms	root mean square value
$reatt$	boundary layer reattachment point
sep	boundary layer separation point
te	trailing edge

Superscript

'	perturbation
^	dimensional quantities
*	complex conjugate

Chapter 1

Introduction

Self-noise generation of an airfoil operating at low/moderate freestream Reynolds number (Re) is one of the most undesirable aspects associated with its operations. The mechanism of airfoil self-noise generation has been studied over the years by several researchers since the early stages of airfoil aeroacoustics studies and has been explored to date. Brooks et al. (1989) gave a classification of the different flow physical mechanisms that can lead to noise radiation from airfoil. They categorized different airfoil self-noise mechanisms at subsonic flow conditions. The first category is turbulent boundary layer (TBL) trailing edge noise which is associated with the flow turbulence passing over the trailing edge at high Re . Secondly, at low Re , the laminar boundary layer (LBL) develops over the airfoil and the noise generation is associated with the vortex shedding. Another form of airfoil self-noise is due to vortex shedding occurring at the aft region of blunt trailing edge. Also, at high angles of attack ($AoAs$), the separated flow may cause stall which results in low-frequency noise radiation. Lastly, noise can be radiated due to the formation of tip vortices occurring at the tips of wings or blades. Usually, when considering tonal noise of low Re airfoil flow (typically $Re < 10^5$), most studies focus upon trailing edge noise which arises from a complex interaction between laminar boundary-layer instabilities on the airfoil surfaces and the

acoustic pressure field generated by the flow. A resonant aeroacoustic feedback loop mechanism is usually in place for the production of discrete tones. The study of airfoil tonal noise is still of high importance as the tonal noise generation at low Re is associated with a large number of applications in the modern era including cooling fans, unmanned air vehicles (UAVs), and micro air vehicles (MAVs) etc. The impact of tonal noise is much more severe than broadband noise generated by the airfoil. Its interest has been rising in the aerodynamic research community in recent years due to the increasing frequency of operations of MAVs and UAVs in close proximity to people. These vehicles are commonly propelled with efficient electric motors now and the tonal noise from their wings starts to emerge as a major contributor to the overall noise radiation. The unwanted noise associated with operations of these devices certainly undermines their capabilities and effectiveness especially in the case of UAVs where minimal noise is desired for surveillance operations. Therefore, in a military context low or suppressed noise radiation from their wings is imperative in vehicle design which helps increase the survivability of vehicles during operation. On the other hand, for many civil goals these vehicles are popularly used for such purposes as aerial searching, film making, law enforcement, etc. The low noise performance would enlarge the possible range of missions and minimize acoustic nuisance to the environment. Similarly, the noise generated due to wind turbines has been reported to severely affect the population in its near vicinity (Abbasi et al. 2015, Botelho et al. 2017, van Kamp and van den Berg 2018). Hence, a significant effort has been invested by the aerospace/mechanical research community to understand the complete noise generation mechanism and design the control strategies for its reduction or complete elimination. The present study also focuses on the airfoil tonal noise generation at low Re flow and an attempt has been made to develop a passive airfoil tonal noise reduction method using localized flow-induced vibration of an

elastic panel mounted on the surface of the airfoil.

1.1 Literature Review

Over the years, researchers have studied and explored the phenomenon of airfoil self-noise generation and attempted to understand the underlying physics. The airfoil noise generation phenomenon involves the interaction among different physical mechanisms involving hydrodynamics, acoustics, and even structural dynamics in some cases. Hence, the study of airfoil tonal noise require in-depth understanding of all the physical processes involved and their inter-dynamics. In recent times, with advancements in computational and experimental facilities, numerous efforts have been made to propose/develop new methods to suppress the airfoil noise generation. The following section presents a brief review on the tonal noise generation mechanism and some of the existing airfoil noise control methods along with their strengths and limitations.

1.1.1 Airfoil Tonal Noise Mechanism

One of the earliest and fundamental studies on airfoil noise generation was carried out by Paterson et al. (1973) who carried out the experimental investigation of NACA 0012 and NACA 0018 airfoil in a low turbulence open jet wind tunnel. They observed that the spectrum of sound frequencies was proportional to the 0.85 power of the freestream velocity. The dominant tone obeyed the power relation over a finite range of Re until a jump to different frequency was observed. The structure of this spectrum with a dominant tone (also denoted as primary tone) and multiple secondary tones is called a ladder-type structure with rungs of ladder constituted by primary tones as shown in Figure 1.1. The phenomenon of ladder structure is related to the superposition of tones at frequencies

f_n and broadband content is the acoustic spectrum that is centered at a particular frequency (Arbey and Bataille 1983, Chong et al. 2013a). As a result of the superposition of multiple tones, a dominant/main tone can be clearly identified. Paterson et al. (1973) observed that the dominant tone follows a relationship of $f = V^{1.5}$. Based on airfoil chord c , viscosity ν , and a proportionality constant k , an expression was developed as:

$$f^* = \frac{f c}{u_\infty} = k \sqrt{\frac{c u_\infty}{\nu}} = k \sqrt{Re_c}. \quad (1.1)$$

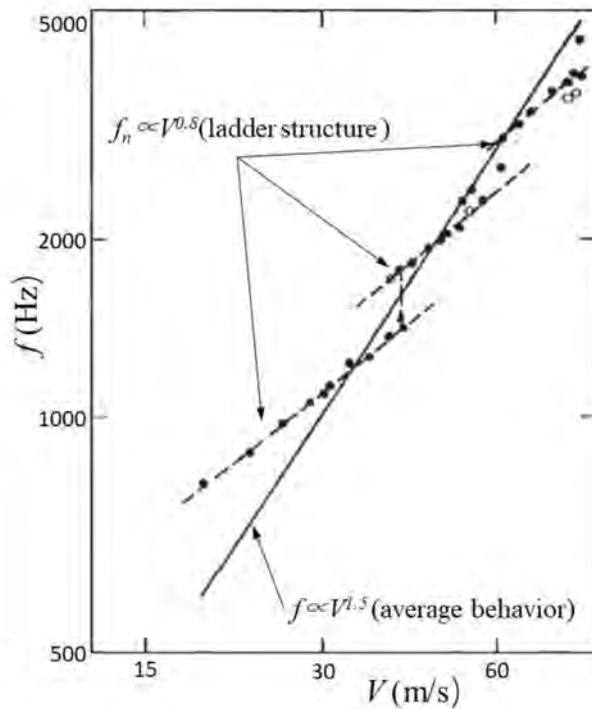


Figure 1.1: Frequency structure observed by Paterson et al. (1973).

Since the benchmark study of Paterson et al. (1973), the research of airfoil tonal noise has received significant attention. A number of studies have been conducted to further understand the phenomenon of multiple tones occurrence through a frequency selection mechanism based on the feedback loop (Plogmann et al. 2013, Fosas de Pando et al. 2014, Nguyen et al. 2015, Pröbsting et al. 2015).

The concept of feedback loop was first proposed by Tam (1974) who disagreed with the opinion that the discrete tone phenomenon is only caused by the vortex shedding. Tam (1974) observed a self-excited feedback loop between the airfoil trailing edge and in the wake region which was found to be responsible for the generation of discrete tones. He described the self-excited feedback loop as an interaction between the unstable laminar boundary layer and acoustic waves. A similar phenomenon of feedback loop was also observed by Wright (1976). Arbey and Bataille (1983) described the noise generation mechanism due to the scattering of surface pressure fluctuations within the boundary layer at the airfoil trailing edge. They also observed the feedback loop mechanism in their study as reported by Tam (1974). However, it was proposed that the pressure fluctuations propagate upstream at a point on airfoil where these instabilities are formed. The explanation of the feedback loop observed by Arbey and Bataille (1983) differed from Tam (1974) in terms of the location of feedback loop and presence of source relative to the trailing edge. The location of hydrodynamic instabilities was observed at the point of maximum velocity over the airfoil. At the in-phase condition of the acoustic and hydrodynamic fluctuations at this particular location, the fluctuations are observed to be amplified (Paterson et al. 1973, Tam 1974). The resulting fluctuation convects downstream and completes the feedback loop. Nash et al. (1999) carried out experimental investigations on NACA 0012 in low turbulence closed wind tunnel. They disagreed with the proposed feedback mechanisms presented by Tam (1974) and proposed that the vortex shedding process is responsible for tonal noise generation and feedback loop. In contrast to previous studies, only a single dominant tone in frequency scale was observed without any ladder structure unlike previous studies (Paterson et al. 1973, Fink 1975). They attributed this phenomenon to a carefully controlled experimental environment. They also identified that the previous studies have not

taken into account the influence of the separation bubble near the airfoil trailing edge and the resulting tonal noise generation. It was observed that the unstable Tollmien–Schlichting (T-S) waves due to instabilities within the laminar boundary layer convect downstream and grow until it reaches airfoil trailing edge and roll up into vortices. The generated vortices subsequently interact with the trailing edge and generate scattered oscillating field with a similar frequency to that of T-S waves. This oscillating field moves upstream to almost the half chord length which is also the point where the boundary layer instabilities appear. It was proposed that the fluctuating flow provides a feedback mechanism for the most amplified instability which results in tonal noise generation. Nash et al. (1999) agreed with Arbey and Bataille (1983) that the feedback loop mechanism occurs between the source at the trailing edge and an upstream point at the airfoil surface. However, in contrast to Arbey and Bataille (1983), this upstream location was observed at the point of maximum velocity on an airfoil whereas Nash et al. (1999) proposed this location at the half chord. In their comprehensive numerical study on airfoil tonal noise, Desquesnes et al. (2007) proposed the presence of secondary feedback loop as well. They observed that the instabilities within the laminar boundary layer appear as T-S waves when boundary layer separation occurs. These T-S waves subsequently interact with airfoil trailing edge and forms a dipolar acoustic source. Subsequently, the resulting acoustic waves travel upstream along the airfoil and creates a feedback loop. They further observed that at high flow speeds and high AoA , the boundary layer becomes turbulent and a similar dipole acoustic source is formed at trailing edge with cardioid directivity (Figure 1.2). However, the nature of noise generation is broadband in this case. The observed secondary feedback loop by Desquesnes et al. (2007) is similar to the study of Arbey and Bataille (1983). However, Arbey and Bataille (1983) only conducted their experiments at $AoA = 0^\circ$ whereas the non-zero AoA condi-

tions were investigated by Desquesnes et al. (2007). Chong et al. (2013a) studied both zero and non-zero *AoAs* for NACA 0012 airfoil. They also observed the phenomenon of acoustic feedback loop which occurs between airfoil trailing edge and at an upstream location of the airfoil. However, in contradiction to previous studies except for Nakano et al. (2007), they proposed that the upstream location of the feedback loop is the point on airfoil where the boundary layer instabilities originate. The concept of feedback loop was further modified by Chong et al. (2013a) who suggested that the inception point of the boundary layer is a better choice.

Arbey and Bataille (1983) proposed a feedback loop model where they suggested that the acoustic waves radiate at an upstream location on the point of maximum velocity on the airfoil surface. The mathematical formulation for the calculation of frequency of tones in the noise spectrum based on the proposed feedback loop model was presented as:

$$f_n^+ = \frac{c_r}{L} \left(n + \frac{1}{2} \right) \left(1 + \frac{c_r}{c_0 - u_\infty} \right). \quad (1.2)$$

where L is the length of feedback loop, c_r is the convective disturbance velocity and n is an arbitrary fitted positive integer. An empirical relation for Δf was also proposed by Arbey and Bataille (1983) for NACA 0012 which is given by:

$$\Delta f^+ = \frac{L_f \Delta f}{u_\infty} \approx K M a_0^{-0.15}. \quad (1.3)$$

where $K = 0.37(\pm 0.02)$. A number of recent studies have investigated the upstream effect of feedback loop (Takagi and Konishi 2010, Arcondoulis et al. 2013, Chong et al. 2013a). The effect on tonal noise emission due to vortex shedding from laminar separation bubble (LSB) was observed by employing a splitter plate by Takagi and Konishi (2010). An increase in unsteady pressure spectra was ob-

served due to the broadening of energy contents. The acoustic feedback loop for an airfoil with an embedded cavity was investigated by Schumacher et al. (2014). The instability waves at the dominant frequency were observed downstream of the cavity and the frequency spacing was found to be inversely proportional to the distance between trailing edge and cavity. Arcondoulis et al. (2019) in their comprehensive experimental study presented a dual acoustic feedback model, where feedback processes were found to act independently on the airfoil pressure and suction surfaces between the point of boundary layer separation and the trailing edge.

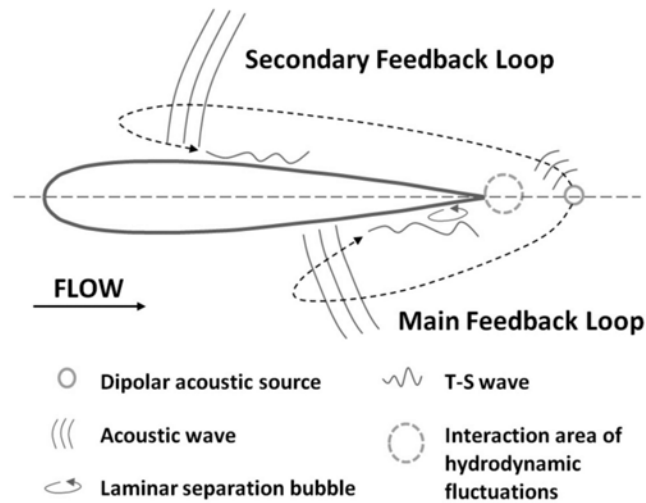


Figure 1.2: Feedback loop mechanism proposed by Desquesnes et al. (2007).

One of the most interesting discussions on the airfoil tonal noise generation is to identify whether the events occurring on the pressure side of the airfoil or the suction side are responsible for eventual tonal noise generation. Earlier studies mostly focused on pressure side flow separation and the resulting tonal noise generation; however, some of the later studies even noticed the role of the suction surface of the airfoil in tonal noise generation at some flow conditions. Paterson et al. (1973) observed no change in tonal noise behaviour when the airfoil

suction surface was tripped, whereas the tonal noise was almost eliminated on tripping the pressure side of the airfoil. Hence, the tonal noise generation was mostly associated with the events occurring on the pressure surface of airfoil. However, Jones et al. (2010) observed that the events on the suction surface are responsible for tonal noise generation. In their experimental study, Inasawa et al. (2010) observed that the suction surface of airfoil is responsible for feedback loop at low Re up to 2.1×10^5 . The involvement of both suction and pressure side of airfoil in tonal noise generation indicates their dependence based on a number of flow conditions such as freestream Re , freestream Mach number (M), airfoil profile, and incidence of flow. A comprehensive study on tonal noise regime for a NACA 0012 airfoil at low to moderate Re (3×10^4 - 2.3×10^5) and effective AoA from 0° to 6.3° was carried out by Pröbsting et al. (2015). Their study presents a very valuable overview of the tonal noise regime and their dependence on either suction side or pressure side or interaction of both sides of airfoil based on Re and AoA . Chong et al. (2013a) and Plogmann et al. (2013) observed multiple tones and ladder-like structure in their experimental studies. Plogmann et al. (2013) showed that the boundary layer becomes turbulent when the pressure side boundary layer was tripped and subsequently separation bubble and tonal noise was suppressed. Tam and Ju (2012) performed numerical simulations of NACA 0012 at low Re and M at zero incidence. They observed a single tone for each case similar to the observations of Nash et al. (1999). Desquesnes et al. (2007) in their numerical investigation observed the involvement of both the pressure and suction surfaces in tonal noise generation. Jones and Sandberg (2011) carried out numerical investigations for NACA 0012 airfoil at low Re and different flow conditions where the suction surface of the airfoil was found to be responsible for tonal noise generation. Their results supported Desquesnes et al. (2007) and Nash et al. (1999) observations that the tonal noise generation is related to

rolling over of vortices at airfoil trailing edge. They further suggested that the feedback mechanism plays a vital role in vortex formation. Fosas de Pando et al. (2014) utilized direct numerical simulations and global stability analysis in their research to study the feedback loop mechanism and found the involvement of instability processes on the suction and pressure surface boundary layers together with their cross-interaction by acoustic radiation at the trailing edge. Later, an experimental study using particle image velocimetry (PIV) was carried out by Pröbsting et al. (2014) to investigate the tonal noise generation mechanism. They observed an amplitude modulation of velocity fluctuations near the trailing edge. A subsequent study by Pröbsting et al. (2015) revealed that the tonal noise generation is based on the feedback mechanism on the airfoil suction surface at low Re . However, with an increase in Re the phenomenon gradually shifts to the pressure side. A recent study by Sanjose et al. (2019) shows a significant connection between tonal noise and T-S waves. The authors used modal analysis to observe tonal noise mechanism and found a significant role of flow dynamics on the airfoil suction surface in noise generation. Ricciardi et al. (2020) carried out a numerical study on primary and secondary tones generation on NACA 0012 at different flow conditions. A non-symmetric flow even at zero incidence with a separation bubble only at one side of airfoil was observed. Their results suggested that the noise generation is dependent on multiple frequencies of T-S wave instabilities which are related to both the main tone and secondary tones. The secondary tones are generated by the coupling between separation bubble motion and T-S instabilities. This phenomenon results in modulation of flow behavior as well as acoustic radiation.

1.1.2 Noise Control Methods

Previous discussions show a large amount of research has been carried out to enhance the understanding of tonal noise generation mechanism over the past few decades; however, the study on its control and reduction is still being explored. A brief description on some of the existing noise control methods and their effectiveness is discussed.

1.1.2.1 Bio-inspired Features and Trailing Edge Modifications

One of the most common approaches for airfoil self-noise reduction is to mimic bio-inspired features of owl due to their silent flight characteristics (Figure 1.3(a)). Herr and Dobrzynski (2005) and Finez et al. (2010) utilized the bio-inspired approach by utilizing trailing edge brushes similar to the feathers of owls. A broadband noise reduction up to 8 dB was observed by Herr and Dobrzynski (2005) at a wide frequency range whereas Finez et al. (2010) further proposed brush design for better performance where the application of trailing edge brushes have found to reduce the noise level up to 10 dB. However, this method suffered from the aerodynamic performance degradation. Wang et al. (2017a) proposed a biomimetic NACA 0012 airfoil based on the combination of wavy leading edge, serrated trailing edge, and surface ridges. A noise reduction up to 13 dB was observed around the airfoil due to the transformation of laminar vortex shedding into regular horse shoe vortices in the wake and reduction in spanwise correlation of large scale vortices. Fan et al. (2018b) carried out the numerical investigation on a NACA 65-(12)10 airfoil with wavy leading edges subjected to incoming anisotropic turbulence at high Re. A noise reduction up to 9.5 dB was achieved around the airfoil; however, a significant rise in aerodynamic drag of 300% was also observed due to modifications in the airfoil profile.

A number of studies have been carried out to investigate the noise reduc-

tion potential of airfoil with different trailing edge modifications (Howe 1991, Herr and Dobrzynski 2005, Herr 2007, Finez et al. 2010, van der Velden et al. 2016, Arce Leon et al. 2016, León et al. 2016, Avallone et al. 2017, van der Velden and Oerlemans 2017, Avallone et al. 2018). One of the benchmark studies on trailing edge modification was carried out by Howe (1991) who used serrated trailing edge at high Re for noise reduction. A significant amount of research has been carried out since Howe (1991) proposed approach (Parchen et al. 1999, Oerlemans et al. 2009, Gruber et al. 2011, Chong et al. 2013a). Gruber et al. (2010) conducted a detailed parametric study of different sawtooth serrated trailing edges to analyze the effect of serration height, width, and amplitude on noise reduction (Figure 1.3(b)). However, aerodynamic effects due to modifications were not reported. Hansen et al. (2012) applied serration treatment on the airfoil leading edge and claimed a significant reduction in tonal noise. Unfortunately, there is a serious collateral effect with such modification as the aerodynamic performance of the airfoil was found seriously penalized. Moreau and Doolan (2016) performed an experimental study on the acoustics of a flat plate with different sawtooth trailing edge serrations at low Re . An overall sound pressure level (SPL) reduction of 11 dB was observed for a trailing edge with wide serrations due to reduction in the turbulent velocity fluctuations at lower frequencies; whereas, the narrow serrations resulted in an increase in noise levels at low Re . The utilization of slits and perforated serrations have also found to be effective in noise reduction where a noise reduction of 5 dB for slits and 1 dB for perforated serrations is observed (Gruber et al. 2013). León et al. (2018) employed trailing edge serrations with different degrees of permeability on a NACA 0018 airfoil and examined their acoustic characteristics. Their experimental investigations revealed that the mixed solid-slitted configurations can achieve a higher noise reduction up to 8 dB whereas the noise reduction potential significantly decreases for fully slitted configuration.

Chong et al. (2013b) utilized three-dimensional serrations of different amplitudes and wavelengths on a NACA 0012 airfoil. A broadband noise reduction up to 6 dB was observed for smaller serration angles and large amplitude. However, high-amplitude noise was also observed due to serration bluntness. Later, this limitation was resolved by using a porous material between the cut-in serrations to suppress the narrow-band noise and an additional noise reduction of 1.5 dB was achieved (Vathylakis et al. 2015, Chong and Dubois 2016). Clark et al. (2017) investigated the noise reduction of an airfoil by employing the surface treatments to replicate the effect of owl's downy canopy. Different variants of design were experimentally tested where a maximum of 10 dB reduction in broad band noise was achieved. However, a slight increase in aerodynamic drag was also observed.

Generally speaking, the aforementioned modifications in airfoil geometry resulted in considerable noise reduction; however, there exist certain limitations associated with their applicability such as aerodynamic performance degradation, manufacturing complexities, and noise amplification at certain conditions.

1.1.2.2 Porous Trailing Edge

In recent years, airfoils equipped with porous trailing edges have also gained significant attention in the aeroacoustics community (Figure 1.3(d)). A detailed investigation on the effect of porosity and resistivity on the acoustic characteristics of a porous airfoil was carried out by Sarradj and Geyer (2007) where the noise generation by porous airfoils was found to be much lower than the rigid airfoil. However, the relationship between the material properties and noise reduction could not be established. Later, Geyer and Sarradj (2014) investigated the airfoil acoustic characteristics with different lengths of porous material with different porous materials and resistivity. It was observed that the airfoil with a larger porous region achieved a high noise reduction but also resulted in air-

foil aerodynamic degradation. Also, the airfoil equipped with a low resistivity porous material was also found to be responsible in adversely affecting the airfoil aerodynamics. Similarly, Herr et al. (2014) carried out a parametric study to investigate the effect of porous material on noise reduction. They utilized different materials including aluminum foam, perforated plate, and sintered bronze powder and observed a higher noise reduction for material with low resistivity. The mechanism of noise reduction was associated with the pressure release across the porous material. Recently, Alejandro et al. (2017) investigated the acoustic characteristics of a NACA 0018 airfoil equipped with an open-cell metal foam porous trailing edge. The effect of different pore sizes and permeability was also examined where a positive effect in noise attenuation by porous material with larger pores was observed which is in agreement with the previous observations (Geyer and Sarradj 2014, Herr et al. 2014). Subsequently, Rubio Carpio et al. (2018) and Rubio Carpio et al. (2019) investigated the effect of permeable and non-permeable porous trailing edges. It was observed that noise reduction is achieved when both sides of the airfoil are connected through the porous trailing edge. However, an increase in noise level was observed at high frequencies which limits its applicability. Teruna et al. (2020) performed a numerical investigation on a similar configuration of Rubio Carpio et al. (2018) for the airfoil equipped with open-cell metal foam porous trailing edge to further examine the flow characteristics for the porous trailing edge. It was observed that the impedance of the airfoil with a fully porous trailing edge decrease along the chord which redistributes the noise scattering. In a numerical investigation by Koh et al. (2018), the effect of porosity and permeability on the porous impedance and noise reduction in the turbulent boundary layer is analyzed. A noise reduction of 12 dB was observed by the porous trailing edge configuration. Bernicke et al. (2019) performed the numerical investigation by a hybrid zonal tool to analyze the noise reduction by

porous trailing edge for NACA 0012. Wang (2018) applied perforations at the trailing edge for noise reduction but the aerodynamic performance of the airfoil was severely degraded.

Application of porous trailing edge has been shown able to reduce the *SPL* at low frequencies; however, the noise is adversely amplified at high frequencies (Geyer et al. 2010). These additional high frequency components may be prominent in audible range and create unpleasant psycho-acoustical impact to community (Waye and Öhrström 2002, Pedersen and Persson Waye 2004).

1.1.3 Aerodynamic Control by Fluid-Structure Interactions

Airfoil operating at low Re are associated with wide variety of applications including UAVs, cooling fans and High Altitude Long Endurance (HALE) aircraft (Roberts 1980, Lissaman 1983, Patil et al. 2001, Shyy et al. 2008, Dong et al. 2019). However, there exist two inherent major issues associated with its operations in these conditions. Firstly, the flow is usually laminar and is highly sensitive to even mild adverse pressure gradient which subsequently results in formation of LSB or boundary layer transitioning to turbulent. As a result, the aerodynamic performance is severely affected even at low $AoAs$ (Arena and Mueller 1980, Alam and Sandham 2000). Secondly, airfoil operations at low Re flow is usually responsible for tonal noise generation due to flow scattering at the sharp trailing edge forming a continuous feedback loop between the source and an upstream location on the airfoil (Desquesnes et al. 2007, Jones et al. 2008, Arcondoulis et al. 2018) which affects the operations of some devices in this flow regime.

Motivated by the flexibility of the bat wings and its adaptability features, flexible wings/airfoils have received significant attention in past few decades due

to their favorable characteristics at low Re flow and improved airfoil aerodynamics at certain flow conditions (Smith and Shyy 1995, Lian and Shyy 2007, Hu et al. 2008, Tamai et al. 2008, Gordnier 2009, He and Wang 2020). The membrane wings/airfoils are found to have better static stability (Albertani et al. 2007, Stanford et al. 2007) as well as high lift to drag ratio as compared to rigid wing/airfoil (Shyy et al. 1999, Stanford et al. 2008). Furthermore, these flexible airfoils have shown to be effective in delaying stall characteristics at high AoA (Lian et al. 2003).

The study of flexible structures subjected to incoming flow involves complex fluid-structure interactions which evolve the boundary layer characteristics due to strong coupling between membrane dynamics and flow unsteadiness. Hence it requires in-depth understanding of the panel dynamics and flow responsiveness due to fluid-structure interactions. In an experimental study by Galvao et al. (2006), the membrane wing was found to produce higher lift than rigid airfoil at moderate to high AoA . However, this phenomenon was associated with higher drag due to high camber and membrane fluctuations. Song et al. (2008) carried out an in-depth experimental study on a membrane wing with low aspect ratio. The compliance of membrane wing was examined for low Re flows where a high lift slope and a delay in stall were observed as compared to the rigid airfoil. A series of experiments were conducted by Rojratsirikul et al. (2010a, 2011) to study the aeroelasticity of membrane wings for low to moderate Re flows for a wide range of $AoAs$. It was observed that the membrane fluctuations at low Re flow excite the shear layer which results in rolling up of vortices. As a result, the detached shear layer moves closer to membrane surface and produces lesser drag, and enhance stall characteristics of the wing.

With an increase in computational power and complexity in handling complex fluid-structure problems, a number of computational studies on flexible mem-

brane airfoil have also been conducted. Gordnier (2009) carried out a comprehensive numerical investigation of membrane wing airfoil at low Re of 2500 and different $AoAs$. The effect of membrane dynamics and different flow conditions were studied which revealed a rise in lift coefficient at higher $AoAs$ and a delay in stall as well. The observed phenomenon of rolling up of vortices and their convection closer to airfoil surface were in agreement with the Rojratsirikul et al. (2010b). However, a decrease in lift to drag ratio for the low aspect ratio membrane wing was observed at lower AoA (Gordnier and Attar 2014). Recently, Serrano-Galiano et al. (2018) carried out a detailed numerical investigation of membrane airfoil at low AoA to study its fluid-structure interaction where the introduction of upstream propagating pressure waves driven by membrane vibrations was found to be responsible for loss in aerodynamic efficiency.

The literature on flexible wings/airfoils suggests that an improvement in airfoil aerodynamic characteristics at moderate to high AoA can be achieved, however at low AoA the aerodynamic efficiency is considerably degraded. Hence, there exist two major concerns regarding their applicability; firstly, since most of the low Re devices are required to operate at low to moderate $AoAs$, the aerodynamic performance degradation at low $AoA \leq 5^\circ$ (Gordnier and Attar 2014, Serrano-Galiano et al. 2018) poses serious concerns in their real world applications. Secondly, the aeroacoustics aspect of these flexible airfoil/membrane has not been investigated in any of the previous studies. Although, the flexible membrane devices designed to operate at low Re flows can enhance the airfoil aerodynamics but can also adversely increase the airfoil noise radiation due to membrane fluctuations which alter the flow dynamics in its vicinity. The membrane airfoils utilized in earlier research (Rojratsirikul et al. 2010b, Gordnier 2009, Serrano-Galiano et al. 2018) have a much higher structural wavelength than acoustic wavelength which would usually create disturbances in the far-field

and radiate energy into the fluid (Fahy and Gardonio 2007).

In recent years, flow control methods based on the fluid-structure interactions have also been attempted and employed on the airfoil; however, most of them are aimed to enhance the aerodynamic characteristics such as airfoil stall (Dong et al. 2015, Di et al. 2017, Açıkel and Genc 2018, Genç et al. 2020, Lei et al. 2020). Hence, the rationale behind the design of flexible panel(s)/membrane in these studies is entirely incompatible/unsuitable for airfoil noise control. The utilization of flexible structures for airfoil noise control has received very little attention in the literature. Only a few studies can be found in literature owing to the complexity of using flexible structures in the experimental or computational analysis. Schlanderer and Sandberg (2013) numerically investigated a flat plate with a flexible trailing edge and achieved some noise reduction as compared to a flat plate with rigid trailing edge at low and moderate frequencies; however, an increase in noise level was observed at the eigen-frequencies of flexible trailing edge. Kamps et al. (2017) used silicone flaplets on a NACA 0010 airfoil and achieved some tonal noise reduction but no change in broadband reduction was observed. Talboys and Brücker (2018) in their study on NACA 0012 with flexible trailing edge extensions, named as flaplets (Figure 1.3(c)), showed that the flaplets can stabilize the shear layer at low Re and low AoA which could ultimately lead to a reduction in the boundary layer thickness on airfoil suction surface and results in lower aerodynamic drag. Later, Talboys et al. (2019) in their experimental study investigated the possibility of noise reduction using an array of flaplets on the trailing edge of NACA 0012 airfoil at low to moderate Re with a wide range of angles. It was hypothesized that the flaplets installed on the pressure side of the airfoil can modify the laminar separation bubble and result in tonal noise reduction. Noise reduction was achieved at low frequencies but an increase in noise was observed at high frequencies ($\geq 2\text{Hz}$). Recently, Zhou et al. (2020) in-

investigated the effect of different shapes and flexibility of serrated trailing edge. It is observed that the flexible serration can provide an additional noise reduction up to 2-3 dB at high frequencies as compared to rigid serrations at the airfoil trailing edge.

Although the employment of flexible trailing edge in different studies has shown noise reduction potential, but these configurations inadvertently degraded airfoil aerodynamics. Hence the utilization of flexible structures in improving/maintaining the aerodynamic performance of the airfoil as well as reducing its noise radiation remains a dilemma as the design method on improving one aspect can adversely affect the other.

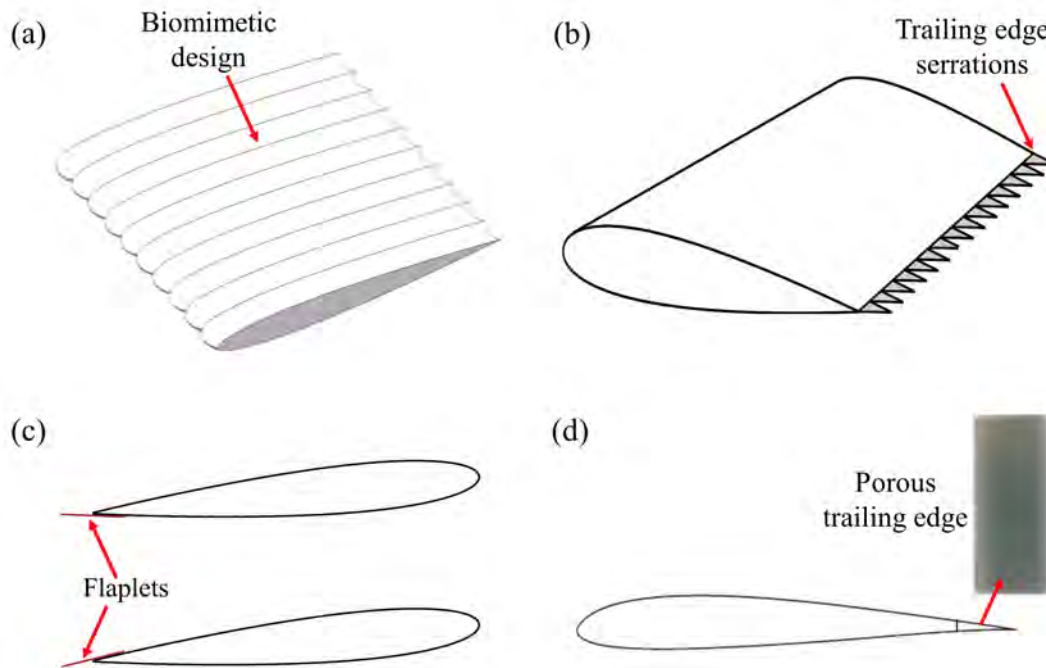


Figure 1.3: Different airfoil noise reduction mechanisms. (a) Biomimetic airfoil (Wang et al. 2017a), (b) sawtooth trailing edge (Gruber et al. 2010), (c) trailing edge flaplets (Talboys and Brücker 2018), (d) trailing edge perforations (Geyer and Sarradj 2014).

1.2 Objectives of the Present Study

Numerous studies have been carried out in the past with an attempt to reduce the tonal noise generated by airfoil at low Re . A number of passive methods have been proposed in this research area over the past few decades. All these studies mentioned above require complex geometrical modifications that are difficult to implement in practical situations due to complexity in manufacturing. Furthermore, utilization of fluid-structure interactions in airfoil noise control has not been truly explored. The existing noise control strategies discussed in preceding sections have few major limitations which restrict their applicability in a real-world environment. Some of these include aerodynamic performance degradation, complex geometrical modifications which are difficult to manufacture and install, transition of laminar boundary layer to turbulent, and applicability in a narrow range of operations (low-frequency range).

Motivated by this challenging problem, the present study proposes a novel methodology of airfoil tonal noise reduction which can alleviate all the aforementioned shortcomings to some extent. Therefore, a passive method involving localized flow-induced vibration of elastic panel is utilized in the present study with an aim to reduce the airfoil tonal noise with minimal or no loss in its aerodynamic performance. In contrast to existing noise control methods which usually apply modification on airfoil trailing edge or leading edge, the proposed methodology explores other possible locations on airfoil surface to weaken, or even eliminate, the unsteady flow fluctuations within the airfoil boundary layer before they reach airfoil trailing edge and eventually scatter as noise radiation. The proposed approach in the present study utilizes small elastic panel(s) flush-mounted on the airfoil surface which is/are excited by the oncoming flow fluctuations conveyed with airfoil boundary layer flow. A similar flow-structure interaction phenomenon was investigated in a previous experimental and numerical study of aerodynamic

and structural resonance of an elastic airfoil exposed to excitation by oncoming periodic discrete vortices which were produced by two upstream cylindrical vortex generators (Luk et al. 2004). The results of their study clearly illustrate that when the elastic airfoil is subjected to an oncoming excitation, the airfoil absorbs the kinetic energy carried by the oncoming vortical flow to sustain its flow-induced vibration. However, there is a potential drawback with their approach. Leung and So (2001) carried out a detailed numerical study of flow-induced vibration of the vortex-airfoil system and their results showed that an elastic airfoil in aerodynamic or structural resonance may radiate loud loading noise. There is a possibility that whilst the elastic panel in structural resonance is absorbing energy from boundary layer flow fluctuations, its own flow-induced vibration might radiate overwhelming loading noise with a level comparable to, or even higher than, that of original airfoil tonal noise so that an overall noise amplification rather than reduction is achieved. Recently, Wu et al. (2018) attempted to utilize flexible panel on airfoil surface, however, the panel structural resonance under the fluid loading could not be achieved. Also, the structural parameters were selected without any clear rationale. Hence, the dependence of panel parameters such as material, thickness, and tension, etc on aeroacoustics performance is uncertain.

The present study aims to achieve an in-depth understanding of the panel design/implementation strategy and also study the possible limitations associated with this approach which could inadvertently result in noise amplification. Some of the major objectives of the present study are:

1. To explore the possibility of tonal noise reduction using localized flow-induced vibration of an elastic panel mounted on the airfoil surface.
2. To develop a complete panel design methodology including its location, length, material, and structural properties to identify the role of panel parameters and to analyze the effect of structural resonance/non-resonance condition

on noise reduction performance.

3. To formulate and implement a reduced-order linearized model for quick preliminary assessment of noise reduction potential of designed panel configurations.
4. To analyze the aeroacoustic characteristics of designed optimal configurations and investigate the physical mechanism of tonal noise reduction.
5. To enhance the noise reduction potential of developed approach by using multiple elastic panels for tonal noise reduction.
6. To design a multi-panel airfoil configuration capable of providing tonal noise reduction at variable loading conditions.

1.3 Overview of the Study

With the advancement in computational resources, numerical analysis can provide an opportunity to explore the dynamics of flow, acoustic and structural with high accuracy. A number of benchmark studies have been conducted using high fidelity numerical simulations in the field of aeroacoustics which have provided in-depth details regarding the underlying physical mechanism of noise generation (Desquesnes et al. 2007, Jones et al. 2008, Tam and Ju 2012, Lam and Leung 2018, Fan 2018). Hence, the present research also utilizes high-fidelity direct aeroacoustic simulation (DAS) for its capability to resolve the coupling between the unsteady airfoil aerodynamic and acoustic solutions with high accuracy. To solve the unsteady compressible Navier-Stokes (N-S) equations, conservation element and solution element (CE/SE) method is adopted. It is a robust and highly accurate method which enforces strict physical conservation laws in N-S equations in both space and time domains (Lam et al. 2014a, Chang 1995). Unlike other

conventional numerical schemes that are based on finite volume and finite element methods, it unifies the treatment of both space and time domain. The control volume is considered as conservation element (CE) in the space-time domain and the flux conservation is enforced in CE. The evaluation of the space-time flux utilizes the solution element (SE) which relies on the Taylor expansion of solutions about the solution point. Since its inception, it has been successfully applied to simulate various aeroacoustics problems (Yu and Chang 1997, Guo et al. 2004, Loh and Hultgren 2006, Lam and Leung 2018). The nonlinear coupling between flow fluctuation and panel structural dynamics in this study is resolved with a monolithic scheme developed by Fan et al. (2018a).

The present proposed methodology aims to leverage similar flow energy absorption phenomenon with an elastic panel(s) so as to greatly suppress the boundary layer flow unsteadiness before their eventual scattering as noise. The aeroacoustic feedback loop is weakened and the airfoil tonal noise is thus reduced. In principle the feasibility of an elastic panel design for noise reduction can be explored in detail with high-fidelity DAS (e.g. Lam et al. (2014a)) or such sophisticated experimental techniques as in Arcondoulis et al. (2019). However, it is too prohibitive in extensive deployment of resources and time to search for optimal design with these approaches within the vast design space of multiple panel physical parameters. Therefore, to develop the panel design methodology in a much quicker way, a reduced-order linearized model, namely perturbation evolution method (PEM), is developed and successfully implemented. PEM only requires 10% of the computational time required for high-fidelity simulations and can provide a reasonable qualitative assessment of panel effectiveness in tonal noise reduction. The designed airfoil configurations would be further evaluated by DAS analysis to investigate the tonal noise reduction mechanism by an elastic panel(s) under actual flow conditions.

1.4 Organization of the Thesis

The remainder of the thesis is organized as the following.

Chapter 2 presents the comprehensive details of the numerical methods. The implementation of CE/SE method to solve unsteady N-S is discussed along with the details of boundary conditions. Also, a brief detail on the aeroacoustic-structural coupling is also presented in this chapter. Subsequently, mathematical formulation of PEM and its coupling with CE/SE is also presented in this chapter.

In **Chapter 3**, details on the numerical setup are presented including airfoil profile, computational domain, grid generation, and grid independence study. Subsequently, a comprehensive aerodynamic and acoustic analysis of rigid airfoil is analyzed in this chapter which helps in establishing the base flow for PEM analysis and also helps in the development of panel design methodology.

Chapter 4 presents the PEM analysis for rigid airfoil and airfoil configurations with elastic panel. The noise reduction potential of design configurations is assessed using PEM and a comparative analysis is carried out.

Chapter 5 presents the DAS of airfoil configuration with designed elastic panel. A comprehensive aerodynamic and acoustic analysis is carried out in detail to study the effects of elastic panel in tonal noise reduction.

In **Chapter 6**, a comprehensive analysis on the airfoil equipped with coupled panel configuration is presented. A complete design rationale is developed and different coupled and non-coupled configurations are assessed by PEM. Subse-

quently, DAS is carried out for coupled configuration and a comparative analysis is also carried out with single panel configurations.

In **Chapter 7**, aeroacoustic analysis of airfoil at different loading conditions is presented and a multi-panel configuration is designed to provide tonal noise reduction at different flow incidence.

Chapter 8 presents the summary of research achievements and conclusions drawn from the research along with the suggestions for further research in this area.

Chapter 2

Numerical Methods

2.1 Introduction

In this chapter, details of the numerical methods employed in the present study and their implementation strategies are presented. The present study of airfoil tonal noise reduction involves complex interactions between unsteady flow, panel structural vibration, and acoustics. A numerical approach capable of resolving all these physical phenomena covering both aerodynamic and acoustic scales is required. Therefore, direct aeroacoustic simulation (DAS) approach is adopted for its capability to resolve the coupling between the unsteady airfoil aerodynamic and the acoustic solutions with high accuracy. To solve the unsteady compressible N-S equations in DAS, conservation element and solution element (CE/SE) method is adopted. The nonlinear coupling between flow fluctuation and panel structural dynamics is resolved with a monolithic scheme developed by Fan et al. (2018a). One of the goals of the present study is aimed to utilize the fluid-structure interactions of an elastic panel on the surface of an airfoil for tonal noise reduction. The panel design depends on a number of engineering parameters such as its material, length, and structural properties. Hence, it is too prohibitive in extensive deployment of resources and time to search for optimal

panel design with DAS. Therefore, an alternate approach, namely perturbation evolution method (PEM), is developed in the present study to explore the potential of elastic panel configurations in tonal noise reduction requiring much shorter computational time and resources. Details of the numerical methods, their mathematical modeling, and implementation are presented in subsequent sections.

2.2 Aeroacoustic Solver

The problem of interest for the present study involves key aerodynamic and acoustic features due to unsteady flow over the airfoil. Since the acoustic features are simply the unsteady flow motions in compressible flow (Crighton 1981), it is essential to adopt a numerical method that can simultaneously solve both the unsteady flow and acoustics. Although there exist some hybrid approaches where the flow features and acoustics are solved in separate steps (Singer et al. 2000), these methods are unable to capture the nonlinear interactions between the hydrodynamic flow and the generated acoustics. Hence, the numerical model based on DAS is employed in the present study due to its capability to accurately capture flow and acoustic features. DAS solves unsteady compressible N-S equations and equation of state simultaneously. Its applicability in aeroacoustic research has been validated by a number of researches including airfoil acoustics, jet flows, cavity, and duct flow (Jones et al. 2008, Desquesnes et al. 2007, Lam et al. 2014a, Gloerfelt et al. 2003). The unsteady flow problem is governed by two-dimensional compressible N-S equations along with ideal gas law for calorically perfect gas. Unless otherwise specified, all the variables are considered in their non-dimensional form. Taking the fluid properties of freestream with dimensional velocity \hat{U}_∞ and airfoil chord \hat{c} as reference, the two-dimensional N-S

equations in strong conservative form can be written as:

$$\frac{\partial \mathbf{U}}{\partial t} + \frac{\partial (\mathbf{F} - \mathbf{F}_v)}{\partial x} + \frac{\partial (\mathbf{G} - \mathbf{G}_v)}{\partial y} = 0, \quad (2.1)$$

The above equation is normalized by reference density, velocity, viscosity, temperature, specific heat at constant pressure \hat{c}_p in free stream flow, and reference chord length. The speed of sound is defined by $\hat{a}_\infty = (\gamma \hat{R} \hat{T}_\infty)^{1/2}$ where $\gamma = 1.4$ and the specific gas constant for air $\hat{R} = 287.058 J/(kgK)$. The dimensionless numbers of the flow Re , M and Pr can be calculated by:

$$Re = \hat{\rho}_\infty \hat{U}_\infty \hat{c}_\infty / \hat{\mu}_\infty, \quad M = \hat{U}_\infty / \hat{a}_\infty, \quad Pr = \hat{c}_{p,0} \hat{\mu}_\infty / \hat{k}_{th\infty} = 0.71, \quad (2.2)$$

where \hat{k}_{th} is reference thermal conductivity. In Eq 2.1, \mathbf{U} , \mathbf{F} and \mathbf{G} are given by:

$$\mathbf{U} = [\rho \quad \rho u \quad \rho v \quad \rho E]^T, \quad (2.3)$$

$$\mathbf{F} = [\rho u \quad \rho u^2 + p \quad \rho uv \quad (\rho E + p)u]^T, \quad (2.4)$$

$$\mathbf{G} = [\rho v \quad \rho uv \quad \rho v^2 + p \quad (\rho E + p)v]^T. \quad (2.5)$$

The flux vectors \mathbf{F}_v and \mathbf{G}_v are defined by:

$$\mathbf{F}_v = (1/Re)[0 \quad \tau_{xx} \quad \tau_{xy} \quad \tau_{xx}u + \tau_{xy}v - q_x]^T, \quad (2.6)$$

$$\mathbf{G}_v = (1/Re)[0 \quad \tau_{xy} \quad \tau_{yy} \quad \tau_{xy}u + \tau_{yy}v - q_y]^T, \quad (2.7)$$

where τ_{xx} , τ_{xy} and τ_{yy} are defined by:

$$\tau_{xx} = \left(\frac{4}{3} \frac{\partial u}{\partial x} - \frac{2}{3} \frac{\partial v}{\partial y} \right) \mu, \quad \tau_{yy} = \left(\frac{4}{3} \frac{\partial v}{\partial y} - \frac{2}{3} \frac{\partial u}{\partial x} \right) \mu, \quad \tau_{xy} = \left(\frac{\partial u}{\partial x} - \frac{\partial v}{\partial y} \right) \mu.$$

The total energy E and pressure p are defined as:

$$E = p/\rho(\gamma - 1) + (u^2 + v^2)/2, \quad p = \rho T/(\gamma M^2), \quad (2.8)$$

and the thermal fluxes are calculated by:

$$q_x = [\mu/(\gamma - 1)PrM^2] (\partial T/\partial x), \quad q_y = [\mu/(\gamma - 1)PrM^2] (\partial T/\partial y). \quad (2.9)$$

2.2.1 Conservation Element and Solution Element Method (CE/SE)

2.2.1.1 Overview

DAS requires a high accuracy and low dissipation numerical method due to inherent wide disparity among the energy and length scales between flow dynamics and acoustics (Lam et al. 2014a). A high numerical dissipation may introduce nonphysical behaviors and must be carefully controlled as they may affect the propagation of weak acoustic fluctuations within the flow and may therefore result in severe inaccuracies in the present study. One of the methods to overcome this limitation is to utilize high-order schemes (Visbal and Gordnier 2004); however, these high-order schemes are inevitably computationally expensive. The traditional method of using finite-difference scheme of higher spatial orders for studying the aeroacoustic problems (Desquesnes et al. 2007, Jones et al. 2010) requires additional numerical treatments to ensure high accuracy which are difficult to implement in complex flow problems such as shock wave interactions. Furthermore, the finite-difference method greatly depends on uniform/regular mesh and is not recommended for complex geometries (Anderson and Wendt 1995). Finite element method is a better choice for complex geometries; however, it also requires high computational resources due to large matrix calculations. The finite volume method is also a popular approach which is utilized to solve unsteady N-S equations where the flux from each mesh surface is evaluated. However, this method requires flux reconstruction on the mesh surface which requires extensive numerical calculations. Furthermore, the inclusion of artificial viscosity further increases the computational time and limits its applications in complex geometries.

An alternative yet efficient approach to overcome these limitations is to

utilize the space-time conservation element and solution element (CE/SE) method developed by Chang (1995). It is a robust and highly accurate method which enforces strict physical conservation laws in N-S equations in both space and time domains (Lam et al. 2014a). Unlike other conventional numerical schemes that are based on finite volume and finite element methods, it unifies the treatment of both space and time domain. Since its inception, it has been successfully applied to simulate various aeroacoustics, shock interaction, and jet noise problems (Lam and Leung 2018, Venkatachari et al. 2008, Loh et al. 2001). Lam et al. (2014b) successfully implemented the CE/SE method to analyze the complex aeroacoustic interactions at both subsonic and supersonic flow speeds within the duct. Recently, Arif et al. (2020) have also utilized the CE/SE method to accurately capture the aeroacoustic phenomenon of airfoil flow and the acoustic feedback mechanism responsible for the airfoil tonal noise generation. Their studies exhibit the robust capability of this scheme in resolving flow dynamics and acoustic solutions with high accuracy.

2.2.1.2 Mathematical Formulation of CE/SE

To calculate the flow flux through the surface of finite control volume in Euclidean space, two important numerical constructs, namely the conservation element (CE) and solution element (SE), are defined. The CE is a finite control volume in the space-time domain while the SE is used to store the flow solutions. With a properly defined CE and SE, the flow flux can be calculated by the flow quantities at the centroid of CE surface. Therefore, there is no need for the complex flux reconstruction as in finite volume method.

For the evaluation of flow flux through the surface in Euclidean space, the conservation element (CE) and solution element (SE) are defined. The control volume is considered as conservation element (CE) in the space-time domain and

the flux conservation is enforced in CE. The evaluation of the space-time flux utilizes the solution element (SE) which relies on the Taylor expansion of solutions about the solution point. The flow flux is calculated by determination of flow quantities at the centroid of CE. Hence, it omits the complex requirement of any flux reconstruction. CE/SE does not require any approximation method such as characteristics method, constraints etc, and only depends on Taylor's series expansion which greatly simplifies its applicability. It is a non-dissipative scheme which is neutrally stable and is compatible for both uniform and unstructured meshes as well. The accuracy of the method is up to second order although the method is built to first order in nature (Lam et al. 2014a). Based on the above mentioned advantages, CE/SE becomes a great choice to solve airfoil aeroacoustics for the present study with optimal computational resources. A detailed description of the implementation of CE/SE method can be found in Lam (2012). Only a brief discussion on the mathematical formulation is presented in this thesis.

Consider a Euclidean space with its spatial coordinates as x and y , and the time t . The N-S equation in strong conservation form can be written as:

$$\nabla \cdot \mathbf{K} = 0, \quad (2.10)$$

where $\nabla \cdot$ is the divergence operator in Euclidean space and $\mathbf{K} = [\mathbf{F} - \mathbf{F}_v, \mathbf{G} - \mathbf{G}_v, \mathbf{U}]$. Using Gauss's divergence theorem, Equation 2.10 can be written as:

$$\oint_{S(V)} \mathbf{K} \cdot ds = 0, \quad (2.11)$$

where $ds = [\Delta x, \Delta y, \Delta t]$ and $S(V)$ is the surface of an arbitrary space-time region V in Euclidean space. The computational domain is decomposed into the triangulate grids as shown in Figure 2.1. A grid BDF with its centroid G is shown in Figure 2.1, whereas A , C and E are the centroids of the adjacent grids. The conservation element (CE) is constructed by the connecting the nodes of a

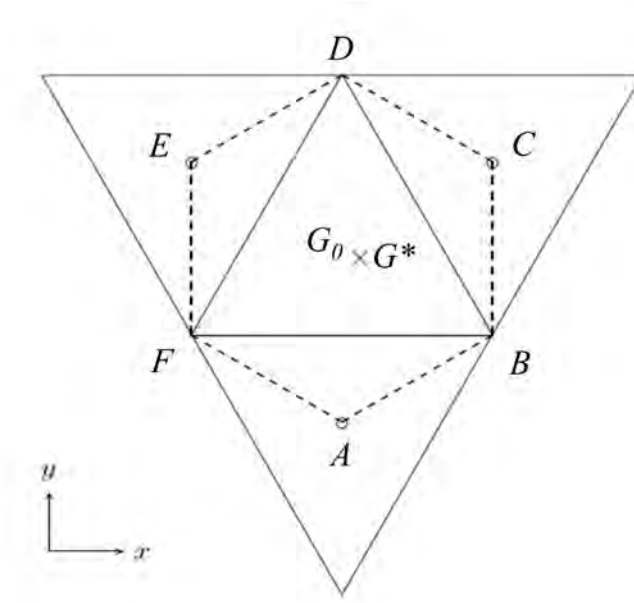


Figure 2.1: Schematic of triangulate grids. A , C , E and G are the centroids of the grids; B , D and F are the nodes; G^* is the solution point; and - - - is the boundary of CE.

grid to the adjacent centroids to form a boundary ($ABCDEF$). The centroid of the hexagon $ABCDEF$ is designated as G^* , which also forms the solution point of the hexagon. It is important to note that G^* and G may be located at different positions due to non-uniformity in the grids. The obtained hexagon is then extended in the time axis to form a hexagonal prism which also defines a CE. The conservation of flux is then enforced on this CE. Figure 2.2 shows the CE which is denoted by $CE(G^*, n)$, where G^* is the spatial location and n is the $n - th$ time level.

A solution element (SE) can be formed by all the planes adjacent to the corresponding solution point as shown in Figure 2.3. The flow variables $\phi(\mathbf{X}) = \mathbf{U}(\mathbf{X}), \mathbf{F}(\mathbf{X}), \mathbf{F}_v(\mathbf{X}), \mathbf{G}(\mathbf{X})$ or $\mathbf{G}_v(\mathbf{X})$ at a location $\mathbf{X}(x, y, t)$ within the solution element $SE(G^*, n)$ can be evaluated by the first-order expansion of the Taylor series from the solution point G^* :

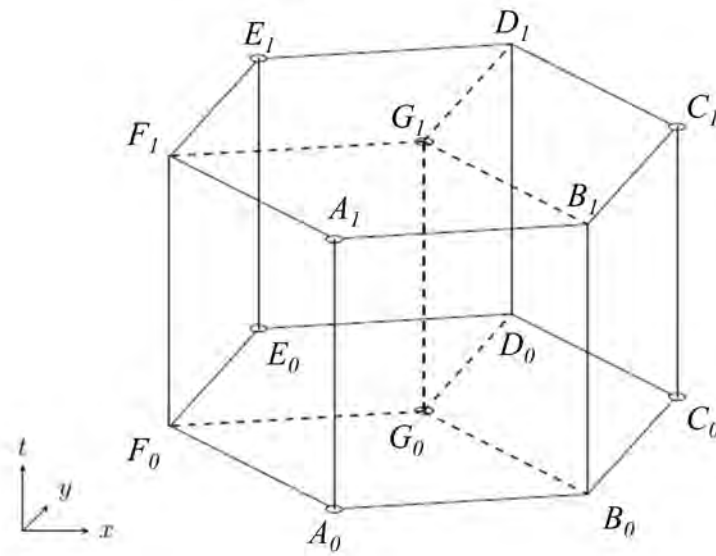


Figure 2.2: Schematic of conservation element $CE(G^*, n)$. - - - is the boundary of $SE(G^*, n)$.

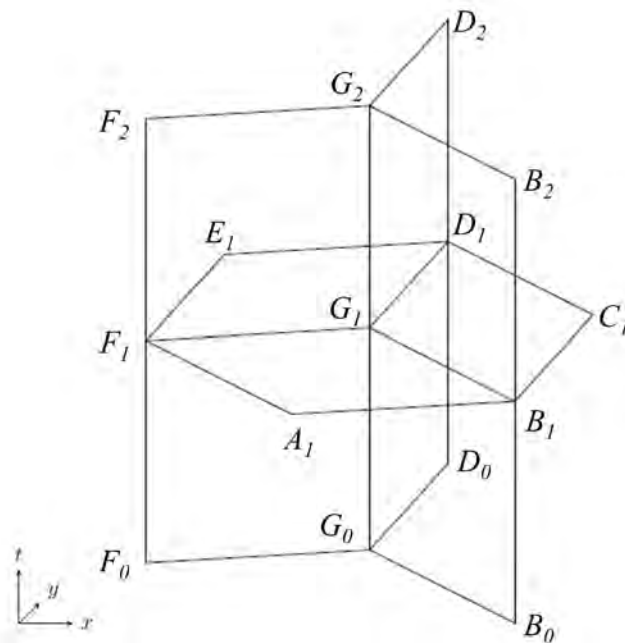


Figure 2.3: Schematic of solution element $SE(G^*, n)$.

$$\phi(\mathbf{X}) = \phi_{G^*} + (x - x_{G^*})(\phi_x)_{G^*} + (y - y_{G^*})(\phi_y)_{G^*} + (t - t_{G^*})(\phi_t)_{G^*}, \quad (2.12)$$

where the subscripts x , y and t are the derivatives with respect to x , y and t respectively. The viscous terms $\mathbf{F}_v(\mathbf{X})$ and $\mathbf{G}_v(\mathbf{X})$ are ascertained by a constant value at the solution point of G^* . Hence, the N-S can be written as:

$$(\mathbf{U}_t)_{G^*} = -(\mathbf{F}_x)_{G^*} - (\mathbf{G}_x)_{G^*}, \quad (2.13)$$

The flow quantities $\mathbf{K}(\mathbf{X})$ can be approximated by:

$$\mathbf{K}(\mathbf{X})_{G^*} \equiv [\mathbf{F}(\mathbf{X})_{G^*} - \mathbf{F}_v(\mathbf{X})_{G^*}, \mathbf{G}(\mathbf{X})_{G^*} - \mathbf{G}_v(\mathbf{X})_{G^*}, \mathbf{U}(\mathbf{X})_{G^*}]. \quad (2.14)$$

Similarly, all the fluxes through the planes in SE and flow variables can be approximated by the solution point G^* .

2.2.1.3 Time Marching of the Solution

In CE/SE method all the flow quantities are expressed by the conservation variables and their spatial derivatives, therefore updating the solution of \mathbf{U} , $\frac{\partial \mathbf{U}}{\partial x}$ and $\frac{\partial \mathbf{U}}{\partial y}$ becomes the most important part of this method. Details of the calculation of \mathbf{U} within a conservation element $CE(G^*, n)$ along with the updating process of $\frac{\partial \mathbf{U}}{\partial x}$ and $\frac{\partial \mathbf{U}}{\partial y}$ are presented in this section.

Consider a conservation element of hexahedron $A_1B_1G_1F_1 - A_0B_0G_0F_0$ as shown in Figure 2.4(a). The flux leaving the conservation element $CE(G^*, n)$ through surface $A_1B_1B_0A_0$, $A_1F_1F_0A_0$ and $A_0B_0G_0F_0$ may be calculated as:

$$\Upsilon_1^{n-1/2} = \Upsilon_{A_1B_1B_0A_0} + \Upsilon_{A_1F_1F_0A_0} + \Upsilon_{A_0B_0G_0F_0}, \quad (2.15)$$

where the flux through each CE is calculated by multiplying the value of flow

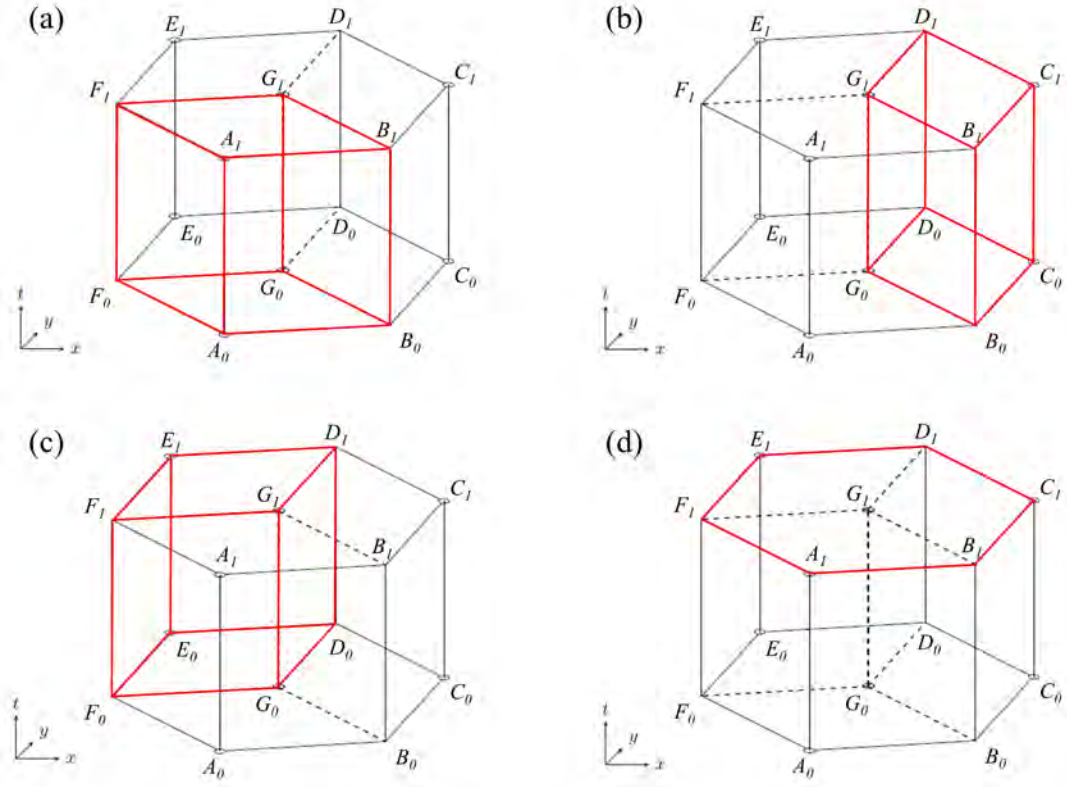


Figure 2.4: Schematic of conservation element of hexahedron. (a) $A_1B_1G_1F_1 - A_0B_0G_0F_0$, (b) $B_1C_1D_1G_1 - B_0C_0D_0G_0$, (c) $D_1E_1F_1G_1 - D_0E_0F_0G_0$ and (d) $A_1B_1C_1D_1E_1F_1$.

variables at the centroid of the surface to the area vector, such that:

$$\Upsilon_{A_1B_1B_0A_0} = \mathbf{K}(\chi_{A_1B_1B_0A_0})_{A^*} \cdot \mathbf{S}_{A_1B_1B_0A_0},$$

$$\Upsilon_{A_1F_1F_0A_0} = \mathbf{K}(\chi_{A_1F_1F_0A_0})_{A^*} \cdot \mathbf{S}_{A_1F_1F_0A_0},$$

$$\Upsilon_{A_0B_0G_0F_0} = \mathbf{K}(\chi_{A_0B_0G_0F_0})_{A^*} \cdot \mathbf{S}_{A_0B_0G_0F_0}.$$

where χ represents the centroid of the respective surfaces, which can be calculated by:

$$\begin{aligned} \chi_{A_1B_1B_0A_0} &= \left(t^{n-1/4}, \frac{1}{2}(x_{A_1} + x_{B_1}), \frac{1}{2}(y_{A_1} + y_{B_1}) \right), \\ \chi_{A_1F_1F_0A_0} &= \left(t^{n-1/4}, \frac{1}{2}(x_{A_1} + x_{F_1}), \frac{1}{2}(y_{A_1} + y_{F_1}) \right), \\ \chi_{A_0B_0G_0F_0} &= \left(t^{n-1/2}, \frac{1}{4}(x_{A_0} + x_{B_0} + x_{G_0} + x_{F_0}), \frac{1}{4}(y_{A_0} + y_{B_0} + y_{G_0} + y_{F_0}) \right). \end{aligned}$$

and \mathbf{S} represents the outward normal vector for the respective planes, which can be calculated by:

$$\begin{aligned} \mathbf{S}_{A_1B_1B_0A_0} &= \frac{dt}{2}(y_{B_1} - y_{A_1}, x_{A_1} - x_{B_1}, 0), \\ \mathbf{S}_{A_1F_1F_0A_0} &= \frac{dt}{2}(y_{F_1} - y_{A_1}, x_{A_1} - x_{F_1}, 0), \\ \mathbf{S}_{A_0B_0G_0F_0} &= \frac{dt}{2}(0, 0, -S_{A_0B_0G_0F_0}). \end{aligned}$$

where $S_{A_0B_0G_0F_0}$ is the area of the plane $A_0B_0G_0F_0$. The flow quantities \mathbf{K} at

point A^* can be estimated by:

$$\mathbf{K}(\chi_{A_1 B_1 B_0 A_0})_{A^*} = \begin{bmatrix} \mathbf{U}(\chi_{A_1 B_1 B_0 A_0})_{A^*} \\ \mathbf{F}(\chi_{A_1 B_1 B_0 A_0})_{A^*} - \mathbf{F}_v(\chi_{A_1 B_1 B_0 A_0})_{A^*} \\ \mathbf{G}(\chi_{A_1 B_1 B_0 A_0})_{A^*} - \mathbf{G}_v(\chi_{A_1 B_1 B_0 A_0})_{A^*} \end{bmatrix}^T, \quad (2.16)$$

$$\mathbf{K}(\chi_{A_1 F_1 F_0 A_0})_{A^*} = \begin{bmatrix} \mathbf{U}(\chi_{A_1 F_1 F_0 A_0})_{A^*} \\ \mathbf{F}(\chi_{A_1 F_1 F_0 A_0})_{A^*} - \mathbf{F}_v(\chi_{A_1 F_1 F_0 A_0})_{A^*} \\ \mathbf{G}(\chi_{A_1 F_1 F_0 A_0})_{A^*} - \mathbf{G}_v(\chi_{A_1 F_1 F_0 A_0})_{A^*} \end{bmatrix}^T, \quad (2.17)$$

$$\mathbf{K}(\chi_{A_0 B_0 G_0 F_0})_{A^*} = \begin{bmatrix} \mathbf{U}(\chi_{A_0 B_0 G_0 F_0})_{A^*} \\ \mathbf{F}(\chi_{A_0 B_0 G_0 F_0})_{A^*} - \mathbf{F}_v(\chi_{A_0 B_0 G_0 F_0})_{A^*} \\ \mathbf{G}(\chi_{A_0 B_0 G_0 F_0})_{A^*} - \mathbf{G}_v(\chi_{A_0 B_0 G_0 F_0})_{A^*} \end{bmatrix}^T. \quad (2.18)$$

It is important to note that all the viscous terms are assumed to be constant at solution point A^* , such that:

$$\mathbf{F}_v(\chi_{A_1 B_1 B_0 A_0})_{A^*} = \mathbf{F}_v(\chi_{A_1 F_1 F_0 A_0})_{A^*} = \mathbf{F}_v(\chi_{A_0 B_0 G_0 F_0})_{A^*}, \quad (2.19)$$

$$\mathbf{G}_v(\chi_{A_1 B_1 B_0 A_0})_{A^*} = \mathbf{G}_v(\chi_{A_1 F_1 F_0 A_0})_{A^*} = \mathbf{G}_v(\chi_{A_0 B_0 G_0 F_0})_{A^*}. \quad (2.20)$$

Similarly, the fluxes leaving the conservation element of hexahedron $B_1 C_1 D_1 G_1 - B_0 C_0 D_0 G_0$ as shown in Figure 2.4(b) can be calculated by:

$$\Upsilon_1^{n-1/2} = \Upsilon_{B_1 C_1 C_0 B_0} + \Upsilon_{C_1 D_1 D_0 C_0} + \Upsilon_{C_0 D_0 G_0 B_0}, \quad (2.21)$$

where

$$\Upsilon_{B_1 C_1 C_0 B_0} = \mathbf{K}(\chi_{B_1 C_1 C_0 B_0})_{C^*} \cdot \mathbf{S}_{B_1 C_1 C_0 B_0},$$

$$\Upsilon_{C_1 D_1 D_0 C_0} = \mathbf{K}(\chi_{C_1 D_1 D_0 C_0})_{C^*} \cdot \mathbf{S}_{C_1 D_1 D_0 C_0},$$

$$\Upsilon_{C_0 D_0 G_0 B_0} = \mathbf{K}(\chi_{C_0 D_0 G_0 B_0})_{C^*} \cdot \mathbf{S}_{C_0 D_0 G_0 B_0}.$$

where $\chi_{B_1 C_1 C_0 B_0}$, $\chi_{C_1 D_1 D_0 C_0}$ and $\chi_{C_0 D_0 G_0 B_0}$ are the centroids of the surfaces $B_1 C_1 C_0 B_0$,

$A_1F_1F_0A_0$ and $C_0D_0G_0B_0$ respectively, which are calculated by:

$$\begin{aligned}\chi_{B_1C_1C_0B_0} &= \left(t^{n-1/4}, \frac{1}{2}(x_{B_1} + x_{C_1}), \frac{1}{2}(y_{B_1} + y_{C_1}) \right), \\ \chi_{C_1D_1D_0C_0} &= \left(t^{n-1/4}, \frac{1}{2}(x_{C_1} + x_{D_1}), \frac{1}{2}(y_{C_1} + y_{D_1}) \right), \\ \chi_{C_0D_0G_0B_0} &= \left(t^{n-1/2}, \frac{1}{4}(x_{C_0} + x_{D_0} + x_{G_0} + x_{B_0}), \frac{1}{4}(y_{C_0} + y_{D_0} + y_{G_0} + y_{B_0}) \right).\end{aligned}$$

and the outward normal vectors for planes $B_1C_1C_0B_0$, $C_1D_1D_0C_0$ and $C_0D_0G_0B_0$ are calculated by:

$$\begin{aligned}\mathbf{S}_{B_1C_1C_0B_0} &= \frac{dt}{2}(y_{C_1} - y_{B_1}, x_{C_1} - x_{B_1}, 0), \\ \mathbf{S}_{C_1D_1D_0C_0} &= \frac{dt}{2}(y_{D_1} - y_{C_1}, x_{D_1} - x_{C_1}, 0), \\ \mathbf{S}_{C_0D_0G_0B_0} &= \frac{dt}{2}(0, 0, -S_{C_0D_0G_0B_0}).\end{aligned}$$

where $S_{C_0D_0G_0B_0}$ is the area of the plane $C_0D_0G_0B_0$. The flow quantities \mathbf{K} at point C^* can be calculated by:

$$\mathbf{K}(\chi_{B_1C_1C_0B_0})_{C^*} = \begin{bmatrix} \mathbf{U}(\chi_{B_1C_1C_0B_0})_{C^*} \\ \mathbf{F}(\chi_{B_1C_1C_0B_0})_{C^*} - \mathbf{F}_v(\chi_{B_1C_1C_0B_0})_{C^*} \\ \mathbf{G}(\chi_{B_1C_1C_0B_0})_{C^*} - \mathbf{G}_v(\chi_{B_1C_1C_0B_0})_{C^*} \end{bmatrix}^T, \quad (2.22)$$

$$\mathbf{K}(\chi_{C_1D_1D_0C_0})_{C^*} = \begin{bmatrix} \mathbf{U}(\chi_{C_1D_1D_0C_0})_{C^*} \\ \mathbf{F}(\chi_{C_1D_1D_0C_0})_{C^*} - \mathbf{F}_v(\chi_{C_1D_1D_0C_0})_{C^*} \\ \mathbf{G}(\chi_{C_1D_1D_0C_0})_{C^*} - \mathbf{G}_v(\chi_{C_1D_1D_0C_0})_{C^*} \end{bmatrix}^T, \quad (2.23)$$

$$\mathbf{K}(\chi_{C_0D_0G_0B_0})_{C^*} = \begin{bmatrix} \mathbf{U}(\chi_{C_0D_0G_0B_0})_{C^*} \\ \mathbf{F}(\chi_{C_0D_0G_0B_0})_{C^*} - \mathbf{F}_v(\chi_{C_0D_0G_0B_0})_{C^*} \\ \mathbf{G}(\chi_{C_0D_0G_0B_0})_{C^*} - \mathbf{G}_v(\chi_{C_0D_0G_0B_0})_{C^*} \end{bmatrix}^T. \quad (2.24)$$

All the viscous terms are assumed to be constant at solution point C^* , such that:

$$\mathbf{F}_v(\chi_{B_1C_1C_0B_0})_{C^*} = \mathbf{F}_v(\chi_{C_1D_1D_0C_0})_{C^*} = \mathbf{F}_v(\chi_{C_0D_0G_0B_0})_{C^*}, \quad (2.25)$$

$$\mathbf{G}_v(\chi_{B_1C_1C_0B_0})_{C^*} = \mathbf{G}_v(\chi_{C_1D_1D_0C_0})_{C^*} = \mathbf{G}_v(\chi_{C_0D_0G_0B_0})_{C^*}. \quad (2.26)$$

A similar procedure can be adopted for the third conservation element of hexahedron $D_1E_1F_1G_1 - D_0E_0F_0G_0$ as shown in Figure 2.4(c).

Finally, the area of the top surface of $CE(G^*, n)$ as shown in Figure 2.4(d) can be expressed as:

$$S_{top} = S_{A_1B_1C_1D_1E_1F_1} = S_{A_0B_0G_0F_0} + S_{C_0D_0G_0B_0} + S_{D_0E_0F_0G_0}, \quad (2.27)$$

The flux leaving through the top surface can be expressed as:

$$\Upsilon_{top}^n = S_{top} \cdot \mathbf{U}_G^n. \quad (2.28)$$

The flux conservation in $CE(G^*, n)$ is enforced by:

$$\Upsilon_{top}^n + \Upsilon_1^{n-1/2} + \Upsilon_2^{n-1/2} + \Upsilon_3^{n-1/2} = 0. \quad (2.29)$$

Hence, the conservation variables at the n -th time step can be evaluated by:

$$\Upsilon_{G^*}^n = -\frac{\Upsilon_1^{n-1/2} + \Upsilon_2^{n-1/2} + \Upsilon_3^{n-1/2}}{S_{top}}. \quad (2.30)$$

The calculation of \mathbf{U} is followed by the calculation of spatial derivatives $\frac{\partial \mathbf{U}}{\partial x}$ and $\frac{\partial \mathbf{U}}{\partial y}$. Chang et al. (1999) developed a dissipation scheme which calculates the gradient through a central finite difference method using the values at the solution points of the neighboring elements. However, the scheme suffered from numerical errors due to its reliance on simple mathematical operations without any physical aspects. Furthermore, the scheme is observed to be highly dissipative due to variation in CFL number at different locations such as boundary layer. To overcome these limitations, a Courant number insensitive scheme (CNIS) was developed by Chang and Wang (2002). In this scheme, the local CFL number is applied as a dissipation controlling parameter so that the small perturbations such as acoustic waves can be accurately resolved. However, CNIS is much more computationally expensive due to the involvement of six neighboring elements in its calculations to build up the numerical domain of dependence. To optimize the

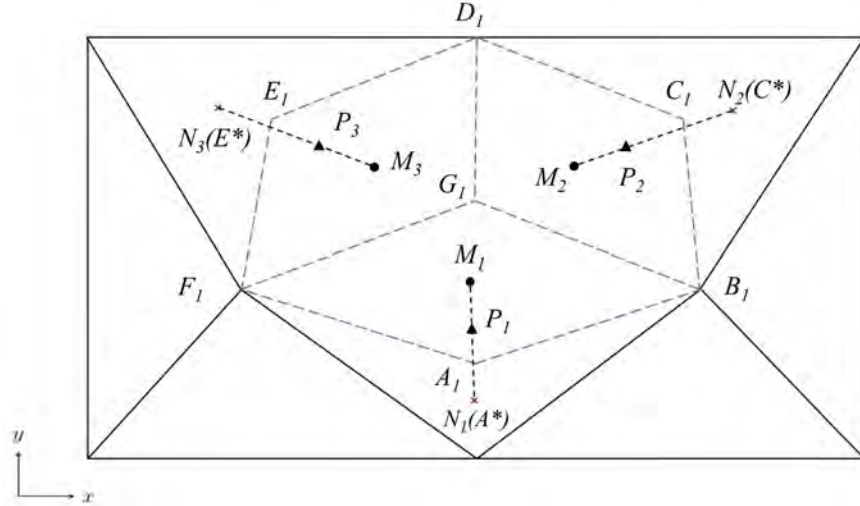


Figure 2.5: Definition of P_i .

computational resources, a simplified Courant number insensitive scheme (SC-NIS) developed by Yen and Wagner (2005) is utilized in this study. Details of its implementation are as follows.

Consider an element with planes $A_1B_1G_1F_1$, $B_1C_1D_1G_1$ and $D_1E_1F_1G_1$ with their centroids represented by M_1 , M_2 , and M_3 respectively as shown in Figure 2.5. The points P_i , $i = 1, 2, 3$, are located between the M_i and the corresponding solution point N_i . The physical location of P_i can be expressed as:

$$P_i = M_i + \text{CFL}(N_i - M_i) \quad (2.31)$$

The numerical domain of dependence of the solution element $SE(G^*, n)$ is shown in Figure 2.6. The analytical domain of dependence is represented by a circle at $(x, y) = 1/2(-udt, -vdt)$ from origin G^* with the radius $r = cdt$. The numerical calculations would be stable if the entire analytical domain of dependence is fully inside the numerical domain of dependence. For a side A^*C^* (Figure 2.7), the stability criterion would be valid if:

$$\text{CFL}_1 = \frac{|G^*S| + |G^*T|}{|G^*Q|} = dt \frac{\sqrt{u^2 + v^2} \cos(\varphi - \alpha) + c}{|G^*Q|} \leq 1. \quad (2.32)$$

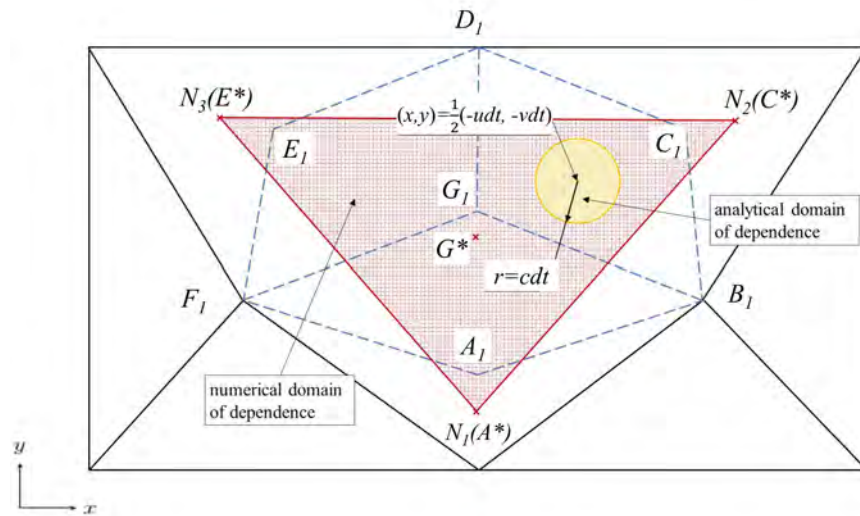


Figure 2.6: Schematic of analytical domain of dependence and analytical domain of dependence.

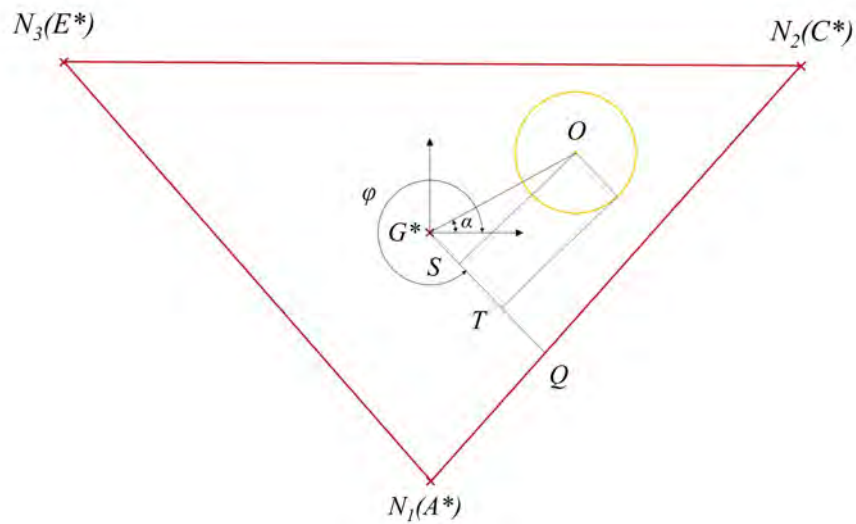


Figure 2.7: Illustration of stability criterion.

The CFL₂ and CFL₃ can be calculated in a similar manner for sides C^*E^* and E^*A^* respectively. The local CFL number is then selected by:

$$\text{CFL} = \max(\text{CFL}_1, \text{CFL}_2, \text{CFL}_3) \quad (2.33)$$

The location of P_i can therefore be determined. It is important to note that the centroid of $\Delta P_1 P_2 P_3$ does not coincide with the solution point G^* and therefore requires a translation such that the centroid of $\Delta P_1 P_2 P_3$ coincides with G^* :

$$\underline{P}_i = P_i + \left(G^* - \frac{\sum_{i=1}^3 P_i}{3} \right) \quad (2.34)$$

The conservation variables at point \underline{P}_i at n -th time step can be calculated by:

$$\underline{U}_{P_i}^n = \underline{U}_{N_i^*}^{n-1/2} + \delta x_{\underline{P}_i} \left(\frac{\partial \underline{U}}{\partial x} \right)_{N_i^*}^{n-1/2} + \delta y_{\underline{P}_i} \left(\frac{\partial \underline{U}}{\partial y} \right)_{N_i^*}^{n-1/2} + \frac{dt}{2} \left(\frac{\partial \underline{U}}{\partial t} \right)_{N_i^*}^{n-1/2}, \quad (2.35)$$

where $\delta x_{\underline{P}_i} = x_{\underline{P}_i} - x_{N_i^*}$ and $\delta y_{\underline{P}_i} = y_{\underline{P}_i} - y_{N_i^*}$. A central difference scheme is applied to calculate the spatial derivatives between the solution point G^* and corresponding P_i :

$$\left(\frac{\partial \underline{U}^i}{\partial x} \right)_{G^*}^{n-1/2} = \Delta_x^i / \Delta^i, \quad \left(\frac{\partial \underline{U}^i}{\partial y} \right)_{G^*}^{n-1/2} = \Delta_y^i / \Delta^i \quad (2.36)$$

where

$$\Delta^1 = \begin{vmatrix} \delta x^1 & \delta y^1 \\ \delta x^2 & \delta y^2 \end{vmatrix}, \quad \Delta^2 = \begin{vmatrix} \delta x^2 & \delta y^2 \\ \delta x^3 & \delta y^3 \end{vmatrix}, \quad \Delta^3 = \begin{vmatrix} \delta x^3 & \delta y^3 \\ \delta x^1 & \delta y^1 \end{vmatrix}, \quad (2.37)$$

and

$$\begin{aligned} \Delta_x^1 &= \begin{vmatrix} \delta \underline{U}^1 & \delta y^1 \\ \delta \underline{U}^2 & \delta y^2 \end{vmatrix}, \Delta_x^2 = \begin{vmatrix} \delta \underline{U}^2 & \delta y^2 \\ \delta \underline{U}^3 & \delta y^3 \end{vmatrix}, \Delta_x^3 = \begin{vmatrix} \delta \underline{U}^3 & \delta y^3 \\ \delta \underline{U}^1 & \delta y^1 \end{vmatrix}, \\ \Delta_y^1 &= \begin{vmatrix} \delta \underline{U}^1 & \delta x^1 \\ \delta \underline{U}^2 & \delta x^2 \end{vmatrix}, \Delta_y^2 = \begin{vmatrix} \delta \underline{U}^2 & \delta x^2 \\ \delta \underline{U}^3 & \delta x^3 \end{vmatrix}, \Delta_y^3 = \begin{vmatrix} \delta \underline{U}^3 & \delta x^3 \\ \delta \underline{U}^1 & \delta x^1 \end{vmatrix}, \\ \delta x^i &= x_{\underline{P}_i} - x_{G^*}, \delta y^i = y_{\underline{P}_i} - y_{G^*}, \delta \underline{U}^i = \underline{U}_{\underline{P}_i} - \underline{U}_{G^*}, i = 1, 2, 3. \end{aligned}$$

The spatial derivatives of the conservation variables are then calculated by:

$$\begin{aligned} \left(\frac{\partial \mathbf{U}}{\partial x}\right)_{G^*}^n &= \frac{\sum_{i=1}^3 (W^i)^\beta \left(\frac{\partial \mathbf{U}^i}{\partial x}\right)_{G^*}^n}{\sum_{i=1}^3 (W^i)^\beta}, \\ \left(\frac{\partial \mathbf{U}}{\partial y}\right)_{G^*}^n &= \frac{\sum_{i=1}^3 (W^i)^\beta \left(\frac{\partial \mathbf{U}^i}{\partial y}\right)_{G^*}^n}{\sum_{i=1}^3 (W^i)^\beta}. \end{aligned} \quad (2.38)$$

where $\beta > 0$, $W^1 = \xi_2 \xi_3$, $W^2 = \xi_1 \xi_3$ and $W^3 = \xi_1 \xi_2$ with

$$\xi_i = \sqrt{\left(\left(\frac{\partial \mathbf{U}^i}{\partial x}\right)_{G^*}^n\right)^2 + \left(\left(\frac{\partial \mathbf{U}^i}{\partial y}\right)_{G^*}^n\right)^2}, \quad i = 1, 2, 3$$

2.2.1.4 Boundary Conditions

Boundary conditions play a vital role in DAS analysis due to the physical size of computational domain. An incorrect domain size or inconsistent boundary condition may result in erroneous errors in the numerical simulation, hence, the selection of boundary conditions require careful deliberation and understanding of physical mechanisms involved. The implementation of boundary condition in CE/SE is based on ghost cell approach. Ghost elements are created by mirroring of boundary elements along the boundaries. Subsequently, the solutions are specified on these ghost elements based on the choice of the boundary condition. The boundary element of CE and SE can be built with the geometric data of the ghost cell. Based on the different types of boundary conditions, the corresponding solution values are assigned to the solution point of the ghost cell to evaluate the flux at each time step.

The non-reflecting boundary condition (NRBC) in DAS is particularly important as it aims to minimize the influence of boundary on the domain. Any numerical reflections from the boundary may contaminate the flow and especially the airfoil acoustics. In CE/SE method, the NRBC is designed to allow the flux from the interior domain to exit smoothly (Loh 2003). There exist two common types of NRBC in CE/SE. In Type I NRBC, the solution and spatial gradients

in ghost cell are given by:

$$\mathbf{U}_G = \mathbf{U}_B, \left(\frac{\partial \mathbf{U}}{\partial x}\right)_G = \left(\frac{\partial \mathbf{U}}{\partial x}\right)_B, \left(\frac{\partial \mathbf{U}}{\partial y}\right)_G = \left(\frac{\partial \mathbf{U}}{\partial y}\right)_B. \quad (2.39)$$

where the subscripts G and B represent the ghost and boundary cells respectively. Type 1 NRBC is mostly applied in supersonic flow problems (Loh and Hultgren 2006) as the flow speed is much higher than the speed of sound and the assignment of flow quantities of ghost cell by the boundary cell does not create any reflections. In Type II NRBC, the solution and spatial gradients in ghost cell are given by:

$$\rho_G = \rho_\infty, u_G = u_B, v_G = v_B, p_G = p_\infty, \quad (2.40)$$

$$\left(\frac{\partial \mathbf{U}}{\partial x}\right)_G = \left(\frac{\partial \mathbf{U}}{\partial x}\right)_B, \left(\frac{\partial \mathbf{U}}{\partial y}\right)_G = \left(\frac{\partial \mathbf{U}}{\partial y}\right)_B. \quad (2.41)$$

In CE/SE method, the no-slip boundary condition for an isothermal wall is specified as:

$$\rho_G = \rho_B, u_G = 0, v_G = 0, p_G = p_B. \quad (2.42)$$

2.3 Structural Solver

The nonlinear dynamic response of the elastic panel is modeled by solving the one-dimensional plate equation to the simplest approximation (Dowell 1975). The normalized governing equation for panel displacement w can be written as:

$$S_{\text{EP}} \frac{\partial^4 w}{\partial x^4} - (T_{\text{EP}} + N_{\text{EP}}) \frac{\partial^2 w}{\partial x^2} + \rho_{\text{EP}} h_{\text{EP}} \frac{\partial^2 w}{\partial t^2} + C_{\text{EP}} \frac{\partial w}{\partial t} + K_{\text{EP}} w = p_{ex} \quad (2.43)$$

where w is the panel displacement, $S_{\text{EP}} = \hat{S}_{\text{EP}} / \hat{\rho}_\infty \hat{U}_\infty^2 \hat{c}^3$ is the panel bending stiffness, $E_{\text{EP}} = \hat{E}_{\text{EP}} \hat{U}_\infty^2 / \hat{\rho}_\infty \hat{c}^4$ is the Young's Modulus of panel, ν is the Poisson's ratio, $T_{\text{EP}} = \hat{T}_{\text{EP}} / \hat{\rho}_\infty \hat{U}_\infty^2 \hat{c}$ is the external tensile stress in tangential direction, $N_{\text{EP}} = (E_{\text{EP}} h_{\text{EP}} / 2 L_{\text{EP}}) \int_0^{L_{\text{EP}}} (\partial w / \partial x)^2 dx$ is the internal tensile stress

in the tangential direction, $C_{EP} = \hat{C}_{EP}/\hat{\rho}_\infty\hat{U}_\infty$ is the structural damping coefficient of panel, $K_{EP} = \hat{K}_{EP}\hat{c}/\hat{\rho}_\infty\hat{U}_\infty$ is the stiffness of the foundation supporting the panel and $p_{ex} = \hat{p}_{ex}/\hat{\rho}_\infty\hat{U}_\infty^2$ is the net pressure exerted on the panel surface. For the present study, a very thin elastic panel is designed which is similar to membrane; therefore, C_{EP} , K_{EP} and S_{EP} are taken as effectively zero (Fan et al. 2018a, Dowell 1975).

The panel dynamic equation is solved by standard finite difference scheme where the panel is discretized into grids of constant size Δx . The spatial derivatives of the panel displacement w are evaluated using second-order central difference method (Hayek 2000) by:

$$\frac{\partial w^{n,j}}{\partial x} = w_x^{n,j} = \frac{1}{2\Delta x}(w^{n+1,j} - w^{n-1,j}), \quad (2.44)$$

$$\frac{\partial^2 w^{n,j}}{\partial x^2} = w_{xx}^{n,j} = \frac{1}{\Delta x^2}(w^{n+1,j} - 2w^{n,j} + w^{n-1,j}), \quad (2.45)$$

$$\frac{\partial^4 w^{n,j}}{\partial x^4} = w_{xxxx}^{n,j} = \frac{1}{\Delta x^4}(w^{n+2,j} - 4w^{n+1,j} + 6w^{n,j} - 4w^{n-1,j} + w^{n-2,j}), \quad (2.46)$$

where the subscripts j represents j -th time step and n represents n -th mesh point.

The time derivatives are calculated by:

$$\frac{\partial w^{n,j}}{\partial t} = \dot{w}^{n,j} = \frac{1}{2\Delta t}(w^{n,j+1} - w^{n,j-1}), \quad (2.47)$$

$$\frac{\partial^2 w^{n,j}}{\partial t^2} = \ddot{w}^{n,j} = \frac{1}{\Delta t^2}(w^{n,j+1} - 2w^{n,j} + w^{n,j-1}), \quad (2.48)$$

Using all these approximations in Equation 2.43, w can be evaluated by:

$$w^{n,j+1} = \frac{4\rho_p h_p w^{n,j} + (-2\rho_p h_p + C\Delta t)w^{n,j-1} + 2\Delta t^2 B}{2\rho_p h_p + C\Delta t}. \quad (2.49)$$

where $B = p_{ex} + (T_x + N_x)w_{xx}^{n,j} - D w_{xxxx}^{n,j} - K_p w^{n,j}$. Hence, after every time step the dynamics of all panel elements $\mathbf{W} = [w, \dot{w}, \ddot{w}]^T$ can be evaluated.

2.3.1 Boundary Conditions

For the fluid boundary in contact with the vibrating panel, the tangency condition in the y -axis is satisfied by:

$$v = \dot{w} + uw_x, \quad (2.50)$$

The normal pressure gradient condition is satisfied by:

$$\frac{\partial p}{\partial y} = \rho \frac{\partial v}{\partial t} + \rho u \frac{\partial v}{\partial x}, \quad (2.51)$$

such that the continuity of velocity and momentum is maintained at the fluid-structure interface. The present study only focuses on the fluid inertia effects and therefore the convective terms are ignored. Hence, the tangency and normal pressure gradient conditions become:

$$v - \dot{w} = 0, \quad (2.52)$$

$$\frac{\partial p}{\partial y} = \rho \ddot{w}. \quad (2.53)$$

The net pressure exerted on the vibrating panel can be calculated by:

$$p_{ex} = p_{panel,b} - p_{panel,a}, \quad (2.54)$$

where $p_{panel,a} = p_a + \rho_a \ddot{w}^n (\delta_a - w^n)$ and $p_{panel,b} = p_b - \rho_b \ddot{w}^n (\delta_b + w^n)$, and δ represents the offset of solution point from the panel surface without any deflection as shown in Figure 2.8. At each time step, the deformation of the fluid domain is evaluated by the panel displacement. Generally, grid remeshing is carried out at the deformed fluid domain to eliminate any strained mesh element where the solution can remain underresolved (So et al. 2003). However, remeshing procedure requires high computational resources as all the mesh points in the domain are required to be updated. Based on the characteristic feature of CE/SE method where the flow solution is calculated at the solution points (Lam 2012) and the

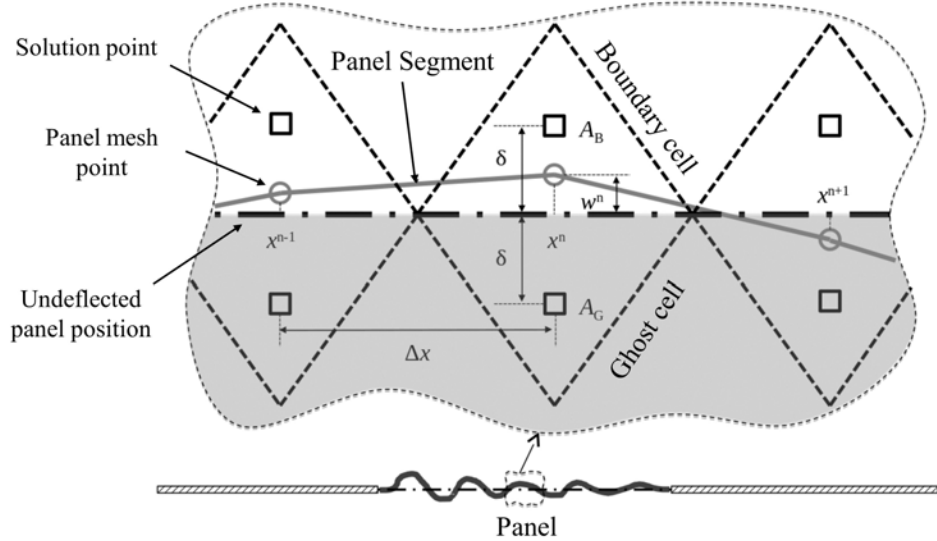


Figure 2.8: Schematic of mesh at fluid-panel interface (Fan 2018).

consideration of small panel displacements, the effect of fluid domain deformation is evaluated by a much simpler technique which is derived in the spirit of immersed element boundary method (Vitturi et al. 2007).

In CE/SE method, the solution points are not laid directly on the physical fluid domain boundary, rather the flow conditions at the boundary are manifested by placing a mirror ghost cell behind the boundary, i.e. A_G as shown in Figure 2.8. The flow variables are then specified at the ghost cell such that the desired flow conditions at the actual panel positions are implicitly applied by the interpolation of boundary and ghost cells. For rigid boundaries, the ghost point is specified with normal velocity $v_G = -v_B$ and its normal gradient as $v_{x,G} = -v_{x,B}$ to enforce the zero normal velocity condition. The tangential velocity is specified as $u_G = U_B$ and its gradient as $u_{y,G} = -u_{y,B}$. The displacement of the vibrating panel is assumed to be smaller than the offset δ of the solution point A_B , and hence its normal velocity v_G can be approximated by:

$$\frac{v_G - \dot{w}^n}{\delta + w^n} = \frac{\dot{w}^n - v_B}{\delta - w^n}. \quad (2.55)$$

The derivatives of v_G and p_G in the normal direction are similar to the derivatives

at the fluid-panel interface and can be written as:

$$p_{y,G} = -\rho_B \ddot{w}^n, \quad (2.56)$$

By first order finite difference approximation, it can be written as:

$$\begin{aligned} p_G &= P_B - 2\delta p_{y,G}, \\ v_{y,G} &= \frac{v_B - v_G}{2\delta} \end{aligned} \quad (2.57)$$

All the flow variables in the ghost cell for isothermal panel are evaluated by:

$$\begin{aligned} u_G &= u_B, \quad u_{x,G} = u_{x,B}, \quad u_{y,G} = -u_{y,B}, \\ v_G &= \dot{w}^n + \frac{\delta + w^n}{\delta - w^n} (\dot{w}^n - v_B), \quad v_{x,G} = v_{x,B}, \quad v_{y,G} = \frac{v_B - v_G}{2\delta}, \\ p_G &= p_B - 2\delta \rho_B \ddot{w}^n, \quad p_{x,G} = p_{x,B}, \quad p_{y,G} = \rho_B \ddot{w}^2. \end{aligned} \quad (2.58)$$

The fluid domain and panel share the same mesh and all the panel solution points are located adjacent to solution points of fluid domain as shown in Figure. 2.8. To approximate the fourth-order spatial derivative by second-order central difference scheme there should be four adjacent points for each solution point. However, the solution points are not enough at the boundaries $n = 1$ and n' , where n' is the total number of solution points of the panel. Therefore, additional ghost points are included at each panel end as $n = -1$ and $n = n' + 2$; and two boundary nodes as $n = 0$ and $n = n' + 1$. Boundary conditions such as pinned or clamped are applied at the edges. For the pinned-pinned condition, the displacement and bending moment are set as zero at the boundary nodes, such that:

$$w^{0,j} = w^{n'+1,j} = w_{xx}^{0,j} = w_{xx}^{n'+1,j} = 0. \quad (2.59)$$

Hence,

$$w^{-1,j} = -w^{1,j}, \quad w^{n'+2,j} = -w^{n',j}. \quad (2.60)$$

For clamped-clamped condition, the boundary conditions are defined as:

$$w^{0,j} = w^{n'+1,j} = w_x^{0,j} = w_x^{n'+1,j} = 0. \quad (2.61)$$

Hence,

$$w^{-1,j} = w^{1,j}, w^{n'+2,j} = w^{n',j}. \quad (2.62)$$

By applying the Taylor series expansion, the second-order spatial derivatives are written as:

$$w_{xx}^{1,j} = \frac{1}{\Delta x^2} \left(-4w^{1,j} + \frac{4}{3}w^{2,j} \right), w_{xx}^{n',j} = \frac{1}{\Delta x^2} \left(-4w^{n',j} + \frac{4}{3}w^{n'-1,j} \right), \quad (2.63)$$

and the fourth-order spatial derivatives are written as:

$$\begin{aligned} w_{xxxx}^{1,j} &= \frac{1}{\Delta x^4} \left(C'w^{1,j} - 8w^{2,j} + \frac{8}{5}w^{3,j} \right), \\ w_{xxxx}^{2,j} &= \frac{1}{\Delta x^4} \left(-8w^{1,j} + 8w^{2,j} + \frac{24}{5}w^{3,j} + \frac{8}{7}w^{4,j} \right), \\ w_{xxxx}^{n',j} &= \frac{1}{\Delta x^4} \left(C'w^{n',j} - 8w^{n'-1,j} + \frac{8}{5}w^{n'-2,j} \right), \\ w_{xxxx}^{n'-1,j} &= \frac{1}{\Delta x^4} \left(-8w^{n',j} + 8w^{n'-1,j} - \frac{24}{5}w^{n'-2,j} + \frac{8}{7}w^{n'-3,j} \right). \end{aligned} \quad (2.64)$$

where $C' = 16$ for pinned-pinned condition and $C' = 32$ for clamped-clamped condition.

2.4 Aeroacoustic-Structural Coupling

The nonlinear coupling between flow fluctuation and panel structural dynamics is resolved with a monolithic scheme developed by Fan et al. (2018a). In monolithic approach, all the physical domains are included in the governing equations by their reformulation and then discretized to solve all domains simultaneously. Hence, the scheme treats the fluid/panel system as a single entity and includes the effects of panel dynamics in an extra source term in the CE/SE numerical model which is then solved with a Newton iteration method with much faster convergence than the conventional partitioned approach. The approach provides unconditional stability due to inherent coupling which ensures the time accurate solutions (Greenshields and Weller 2005). The monolithic coupling scheme has

been successfully implemented to analyze the fluid-structural interactions in a Newtonian incompressible fluid where the flow and structure are discretized by finite element method and a matrix is formed based on the linearized coupled equations (Rugonyi and Bathe 2001). Also, the coupling scheme is fully validated with a series of benchmark aeroacoustic-structural interaction problems and is proven to accurately resolve aeroacoustic-structural coupling of various complexity (Fan et al. 2018a, 2015). Only a brief detail of its mathematical formulation is presented in this section.

Consider the stresses experienced by two small control volumes of fluid above and below the elastic panel segment as shown in Figure 2.9. The undeflected initial height of each control volume is defined by δ and $l(t)$ is the height of the control volume due to panel vibration with time. The subscripts a and b denote the variables above and below the panel respectively. The stress σ generated from the fluid-panel interface affects the fluid momentum in the normal direction. Hence, these effects are included as a source term \mathbf{Q} on the right hand side of Equation 2.1 as:

$$\frac{\partial \mathbf{U}}{\partial t} + \frac{\partial (\mathbf{F} - \mathbf{F}_v)}{\partial x} + \frac{\partial (\mathbf{G} - \mathbf{G}_v)}{\partial y} = \mathbf{Q}, \quad (2.65)$$

where

$$\begin{cases} [Q_1, Q_2, Q_3, Q_4]^T = -\frac{\partial p}{\partial y}[0, 0, 1, v]^T, & \text{along fluid/panel interface,} \\ 0, & \text{elsewhere.} \end{cases}$$

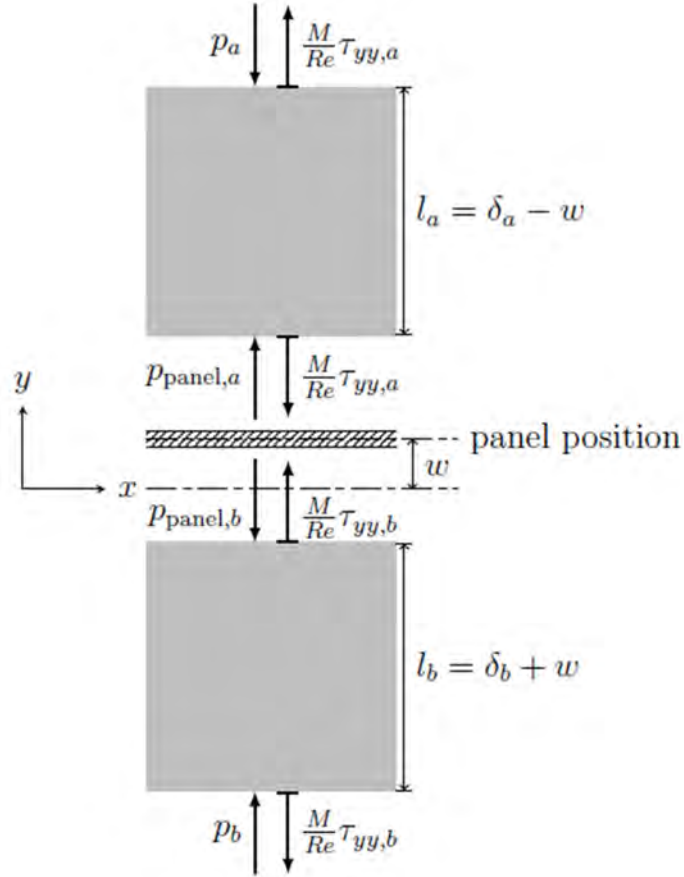


Figure 2.9: Forces balance on control volume.

All the elements of \mathbf{Q} are directly dependent on panel dynamics. The net external force applied to the panel is:

$$p_{ex} = \sigma_{panel,b} - \sigma_{panel,a} = \left(p_{panel,b} - \frac{M}{Re} \tau_{yy,b} \right) - \left(p_{panel,a} - \frac{M}{Re} \tau_{yy,a} \right), \quad (2.66)$$

Therefore, the panel dynamics equation (Equation 2.43) can be rewritten as:

$$S_{EP} \frac{\partial^4 w}{\partial x^4} - (T_{EP} + N_{EP}) \frac{\partial^2 w}{\partial x^2} + \rho_{EP} h_{EP} \frac{\partial^2 w}{\partial t^2} + C_{EP} \frac{\partial w}{\partial t} + K_{EP} w = \left(p_{panel,b} - \frac{M}{Re} \tau_{yy,b} \right) - \left(p_{panel,a} - \frac{M}{Re} \tau_{yy,a} \right). \quad (2.67)$$

The source term \mathbf{Q} in Equation 2.65 is a function of the solution vector \mathbf{U} and therefore it cannot be solved directly. Hence, Newton's method with an iterative procedure is used to solve \mathbf{U} (Loh 2005). The term $\partial\mathbf{U}/\partial t$ in Equation 2.65 can be defined as:

$$\frac{\partial\mathbf{U}}{\partial t} = \mathbf{Q} - \mathbf{H}', \quad (2.68)$$

where

$$\mathbf{H}' = \frac{\partial(\mathbf{F} - \mathbf{F}_v)}{\partial x} + \frac{\partial(\mathbf{G} - \mathbf{G}_v)}{\partial y}.$$

For the solution time marching at the j -th time step, the solution vector can be evaluated by approximating $\partial\mathbf{U}/\partial t = \Delta\mathbf{U}/\Delta t$:

$$\frac{\partial\mathbf{U}}{\partial t} = \mathbf{Q} - \mathbf{H}', \quad (2.69)$$

The local homogeneous solution \mathbf{U}_H when $\mathbf{Q} = 0$ is used to eliminate \mathbf{H}' . The Equation 2.69 can be written as:

$$\mathbf{U}_j - \Delta t\mathbf{Q}(\mathbf{U}_j) - \mathbf{U}_{j,H} = \Phi(\mathbf{U}_j) = 0 \quad (2.70)$$

The solution \mathbf{U}_j of this implicit equation is solved using Newton's method as shown in Figure 2.10 by iterating the equation:

$$\mathbf{U}_{j,k+1} = \mathbf{U}_{j,k} - \left(\frac{\partial\Phi}{\partial\mathbf{U}}\right)^{-1} \Phi(\mathbf{U}_{j,k}) \quad (2.71)$$

where k is the iteration index and $\partial\Phi/\partial\mathbf{U}$ is the Jacobian matrix which is defined as:

$$\frac{\partial\Phi}{\partial\mathbf{U}} = \mathbf{I} - \left[\Delta t \left(\mathbf{Q} + \frac{\partial\mathbf{Q}}{\partial\mathbf{U}}\right) + \mathbf{U}_{j,H} - \mathbf{U}_{j-1}\right] \quad (2.72)$$

At the j -th time step, the homogeneous solution $\mathbf{U}_{j,H}$ is evaluated by aeroacoustic model and then substituted in Equation 2.71 to start the iteration. The iteration

is progressed until the relative error between the two successive iterations satisfies the convergence criteria of 10^{-10} .

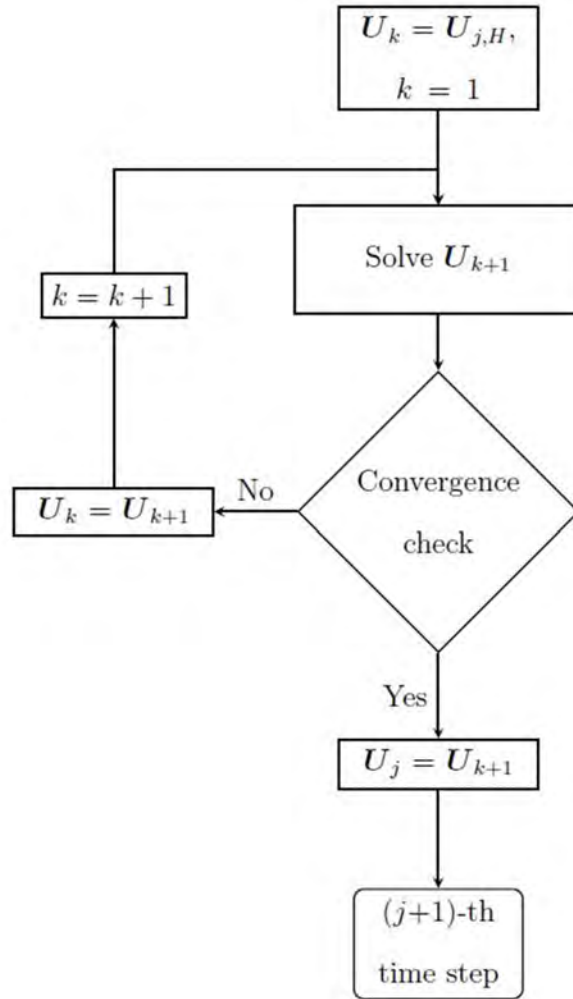


Figure 2.10: Newton's method iterative procedure.

In order to evaluate \mathbf{Q} and $\frac{\partial \mathbf{Q}}{\partial \mathbf{U}}$ in Equation 2.72, the pressure above and underneath the panel and the pressure gradients are determined from the panel dynamics and expressed in terms of \mathbf{U} as presented in detail by Fan (2018).

2.5 Perturbation Evolution Method (PEM)

The present study is aimed at utilizing fluid-structure interactions of an elastic panel mounted on the surface of airfoil for tonal noise reduction. The proposed approach aims to leverage flow energy absorption phenomenon with an elastic panel so as to greatly suppress the boundary layer flow unsteadiness before their eventual scattering as noise. Subsequently, the aeroacoustic feedback loop is weakened and the airfoil tonal noise is thus reduced. Essentially there are two advantages with the proposed approach. Firstly, although the panel is set to vibrate under the fluid loading, its vibration displacement should be small as compared to the airfoil chord given the comparatively weak flow fluctuation amplitudes than those reported in Luk et al. (2004). This would lead to a weak distortion of streamlines locally around the elastic panel which results in a very weak modification of pressure distribution around the airfoil. Secondly, the panel acts to absorb flow fluctuation energy using a reactive mechanism rather than a dissipative one so the airfoil skin friction drag is effectively not affected. As such the proposed approach would be able to reduce airfoil tonal noise yet it does not penalize airfoil aerodynamic performance. However, there is a potential drawback with their approach. Leung and So (2001) carried out a detailed numerical study of flow-induced vibration of vortex-airfoil system and their results showed that an elastic airfoil in aerodynamic or structural resonance may radiate loud loading noise. There is a possibility that whilst the elastic panel in structural resonance is absorbing energy from boundary layer flow fluctuations, its own flow-induced vibration might radiate overwhelming loading noise with a level comparable to, or even higher than, that of original airfoil tonal noise, so that an overall noise amplification rather than reduction is achieved. This suggests the necessity of careful panel design in adopting the proposed ideas for airfoil tonal noise mitigation.

In principle, the feasibility of an elastic panel design for noise reduction can

be explored in detail with high-fidelity DAS (e.g. Lam et al. 2014a, Desquesnes et al. 2007) or such sophisticated experimental techniques as in Arcondoulis et al. (2019). However, it is too prohibitive in extensive deployment of resources and time to search for an optimal design with these approaches within the vast design space of multiple panel physical parameters. Therefore, it is deemed essential to develop an alternate approach which allows much quicker panel design iterations with inputs of reasonable approximation of key noise production physics. Hence, a reduced-order linearized model, namely perturbation evolution method (PEM), is developed to explore the potential of elastic panel configurations in tonal noise reduction requiring much shorter computational time and resources. For PEM, an infinitesimal perturbation in the flow field is introduced near the point of interest (for e.g. leading edge of the airfoil in the present study). The introduced perturbation excites a range of frequencies at low amplitude and the response of this perturbation on the boundary layer is monitored. For a convectively stable flow the disturbance dies down while convecting downstream; whereas for a convectively unstable flow, the disturbance would lead to growing instabilities while convecting downstream (Huerre and Monkewitz 1990). Hence, PEM can be effectively utilized to analyze the convective boundary layer instabilities in the present study which eventually leads to tonal noise generation due to its scattering at the airfoil trailing edge. Furthermore, the method may also be employed in other aeroacoustic studies such as cavity flows etc. Details of the methodology and its implementation are given in the forthcoming sections.

2.5.1 **Methodology**

The proposed methodology is entirely based on the analysis of evolution of introduced weak perturbation but it is initiated with information available from DAS solution of rigid airfoil. The required information includes the base flow obtained

from time-averaging the DAS time-stationary solution and the flow characteristics of rigid airfoil. The former is taken as the base flow input for perturbation evolution method whereas the latter helps set the physical and material parameters for the design of elastic panel as well as its location. Numerical results show that a typical calculation with PEM for an airfoil with elastic panel takes only 10% of the computational time required for its corresponding full DAS calculation. The time saving allows design iteration within the multiple panel parameters space for optimal noise reduction in a much quicker manner. Once determined, the optimal panel design can then be incorporated into DAS calculation, or experimental study, for ascertaining the actual effectiveness of noise reduction.

The method originates from the basis of linear stability analysis which is widely used to study boundary layer transition phenomenon and provides an effective way to describe hydrodynamic stability responses over base shear flows qualitatively and quantitatively (Mack 1975, Huerre and Monkewitz 1990, Reed et al. 1996). Understanding the characteristics of a disturbance evolution is vital in analyzing the physical phenomenon in fluid mechanics. The stability analysis methods also rely on the same aspects where the evolution of disturbance and its interaction with different flow features is studied to uncover key physical mechanisms. Since the present study involves the analysis of boundary layer instabilities over the airfoil and its scattering at the trailing edge and related noise generation, the study of disturbances within the boundary layer and their evolution becomes critical. If the boundary layer is convectively stable, the disturbance would decay and there would be no further interaction of the disturbance with the trailing edge. On the other hand, if the boundary layer is convectively unstable, the disturbance would grow while convecting downstream and interact with the trailing edge. Although the classical linear stability analysis approach shows success in many studies of boundary layer transition and/or separation (Drazin

and Reid 2004, Theofilis 2003, Huerre and Monkewitz 1990), its requirement of a quasi-parallel incompressible steady base flow makes its application to the present study of airfoil tonal noise generation problem largely impractical. Jones et al. (2010) attempted to circumvent this limitation with an alternative numerical approach. This approach embraces essentially the same sense of classical linear stability analysis but it is applicable for compressible flow problems with non-parallel base flow. On similar lines, the flow stability characteristics by solving the compressible N-S equations directly with additional forcing terms are studied. The forcing terms are carefully prescribed so that in absence of any introduced perturbation, the time steadiness of the initial condition (i.e. the base flow) can be guaranteed over a long time marching of the numerical solution. The analysis is started after introducing a weak flow perturbation into the steady non-parallel compressible base flow and the subsequent flow perturbation responses and interactions are evolved with time marching of the forced equation. The calculated flow characteristics are able to delineate the role of separation bubble dynamics in airfoil tonal noise generation and subsequent acoustic feedback (Jones et al. 2010, Fosas de Pando et al. 2014). Recently, Unnikrishnan and Gaitonde (2016) developed a method which is capable of analyzing the effect of small perturbation propagation through complex unsteady turbulent flows. Their proposed method is based on two simultaneous large-eddy simulations denoted by ‘baseline’ and ‘twin’. At each time step, a small perturbation is introduced into the twin and the difference between the baseline and twin simulations is evaluated to study the effect of perturbation on the turbulent flow characteristics.

It must be borne in mind that a proper choice of the base flow is of critical importance to the successful application of the approach (Jones and Sandberg 2011). Some of the earlier researchers utilized velocity profile and Hartree profile as the initial base flow for the stability analysis (Fink 1978, Tam 1974, Archibald

1975). However, the selection of these base flows suffer from inaccuracies in the solution due to presence of adverse pressure gradients or flow separation. Another choice of base flow is to utilize the origin of flow from where the unsteadiness develops. This type of base flow can yield accurate growth rates but it suffers from significant deviation from the developed flow (Barkley 2006). One of the most common choices of base flow is to utilize the time-averaged flow once the solution is statistically periodic/stable. This approach has been successfully implemented by a number of researchers and has proven to yield much accurate results whilst capturing correct flow physics (Jones and Sandberg 2011, Fosas de Pando et al. 2014). Hence, the time-averaged flow solution of the rigid airfoil obtained from DAS is utilized as the base flow for PEM. Further details on the selection, setting, and validation of base flow are presented in Chapter 4.

2.5.2 Mathematical Formulation

Choosing the airfoil chord, free-stream density, and free-stream velocity as reference parameters, the normalized compressible N-S equations in two dimensions with a constant forcing term \mathbf{S} may be written in strong conservative form as:

$$\frac{\partial \mathbf{U}}{\partial t} + \frac{\partial(\mathbf{F} - \mathbf{F}_v)}{\partial x} + \frac{\partial(\mathbf{G} - \mathbf{G}_v)}{\partial y} = \mathbf{S} \quad (2.73)$$

Given a base flow for Equation 2.73, an infinitesimal perturbation is introduced to start the PEM calculation. Every flux variable in the equation can be expressed as a combination of a steady part and a fluctuating part, e.g:

$$\mathbf{U}(x, y, t) = \mathbf{U}_{base}(x, y) + \mathbf{U}'(x, y, t) \quad (2.74)$$

Taking the forcing term derived as spatial gradients of the base flow, Equation

2.73 becomes:

$$\begin{aligned} \frac{\partial(\mathbf{U}_{base} + \mathbf{U}')}{\partial t} + \left(\frac{\partial(\mathbf{F} - \mathbf{F}_v)}{\partial x} + \frac{\partial(\mathbf{G} - \mathbf{G}_v)}{\partial y} \right)_{base} + \left(\frac{\partial(\mathbf{F} - \mathbf{F}_v)}{\partial x} + \frac{\partial(\mathbf{G} - \mathbf{G}_v)}{\partial y} \right)' \\ = \mathbf{S} = \left(\frac{\partial(\mathbf{F} - \mathbf{F}_v)}{\partial x} + \frac{\partial(\mathbf{G} - \mathbf{G}_v)}{\partial y} \right)_{base}. \end{aligned} \quad (2.75)$$

Assuming no modification to the flow field to maintain the initial condition as a reference state, the behavior of small perturbations introduced to the solution of Equation 2.75 can be traced to illustrate stability behaviors. The final form of equation with small perturbations can be written as:

$$\frac{\partial(\mathbf{U}_{base} + \mathbf{U}')}{\partial t} + \left(\frac{\partial(\mathbf{F} - \mathbf{F}_v)}{\partial x} + \frac{\partial(\mathbf{G} - \mathbf{G}_v)}{\partial y} \right)' = 0. \quad (2.76)$$

If the base flow is applied as an initial condition, then the right hand side of Equation 2.75 becomes the source term. Hence, the base flow can be considered as steady:

$$\partial \mathbf{U}_{base} / \partial t = 0. \quad (2.77)$$

Substituting Equation 2.77 in Equation 2.76, the mathematical formulation can be written as:

$$\frac{\partial \mathbf{U}'}{\partial t} + \left(\frac{\partial(\mathbf{F} - \mathbf{F}_v)}{\partial x} + \frac{\partial(\mathbf{G} - \mathbf{G}_v)}{\partial y} \right)' = 0. \quad (2.78)$$

Note that the homogeneous Equation 2.78 has the same mathematical structure of the full nonlinear N-S equations for ordinary DAS calculation (Lam et al. 2014b) but all the primitive variables are replaced by their perturbations in the flux variables. Similar to DAS calculation, its solution should properly capture the nonlinear evolution and interactions of all flow perturbation, including acoustic disturbances, over a prescribed base flow. Therefore, the same numerical framework is adopted for solving Equation 2.78 due to its proven capability of resolving correctly the coupling between the scale disparate unsteady aerodynamics and acoustics of complex airfoil (Lam and Leung 2018). This capability

is particularly important in the PEM employed in the present study. As seen in Chapter 4, it allows to capture the nonlinear interaction associated with airfoil aeroacoustic feedback loop even though the analysis is initiated with an imposed perturbation with amplitude orders of magnitude weaker.

2.5.3 Coupling of PEM with CE/SE Method

Once the mathematical formulation of PEM is developed, it is important to couple the PEM with CE/SE method. By rearranging Equation 2.73, it can be written as:

$$\frac{\partial \mathbf{U}}{\partial t} + \left(\frac{\partial(\mathbf{F} - \mathbf{F}_v)}{\partial x} - \left(\frac{\partial \mathbf{F} - \mathbf{F}_v}{\partial x} \right)_{base} \right) + \left(\frac{\partial(\mathbf{G} - \mathbf{G}_v)}{\partial y} - \left(\frac{\partial \mathbf{G} - \mathbf{G}_v}{\partial y} \right)_{base} \right) = 0 \quad (2.79)$$

By integrating the CE, the equation can be written as:

$$\int \int \frac{\partial \mathbf{U}}{\partial t} dV + \int \int \left(\frac{\partial(\mathbf{F} - \mathbf{F}_v)}{\partial x} - \left(\frac{\partial \mathbf{F} - \mathbf{F}_v}{\partial x} \right)_{base} \right) dV + \left(\frac{\partial(\mathbf{G} - \mathbf{G}_v)}{\partial y} - \left(\frac{\partial \mathbf{G} - \mathbf{G}_v}{\partial y} \right)_{base} \right) dV = 0 \quad (2.80)$$

Applying the Gauss Law to Equation 2.80, it becomes:

$$\int_{CE} \mathbf{U} d\vec{s}_t + \int_{CE} ((\mathbf{F} - \mathbf{F}_v) - (\mathbf{F} - \mathbf{F}_v)_{base}) d\vec{s}_x + \int_{CE} ((\mathbf{G} - \mathbf{G}_v) - (\mathbf{G} - \mathbf{G}_v)_{base}) d\vec{s}_y = 0 \quad (2.81)$$

where $d\vec{s}_t$, $d\vec{s}_x$ and $d\vec{s}_y$ are the unit vectors along the t , x and y axes respectively.

Equation 2.81 can be further simplified by applying the definition of perturbation as $X' = X(t) - X_{base}$. Hence, Equation 2.81 can be written as:

$$\int_{CE} \mathbf{U} d\vec{s}_t + \int_{CE} ((\mathbf{F} - \mathbf{F}_v)') + \int_{CE} ((\mathbf{G} - \mathbf{G}_v)') = 0 \quad (2.82)$$

which fully restores the original form of CE/SE method (Lam et al. 2014a, Chang et al. 1999).

2.5.4 Perturbations

In principle, a PEM calculation is started with an introduction of a weak perturbation into the steady flow and the evolution of the perturbation is analyzed for determining the flow stability characteristics. For the designed approach in the present study, two types of weak perturbations are utilized. The first type is the weak Gaussian perturbation which is a divergence-free localized perturbation (Fosas de Pando et al. 2014) and is defined by:

$$\begin{aligned} u(x, y) &= -\frac{A}{\rho_{base}(x, y)} \frac{(y - y_0)}{r} \exp\left(-\frac{(x - x_0)^2 + (y - y_0)^2}{r^2}\right), \\ v(x, y) &= \frac{A}{\rho_{base}(x, y)} \frac{(x - x_0)}{r} \exp\left(-\frac{(x - x_0)^2 + (y - y_0)^2}{r^2}\right), \end{aligned} \quad (2.83)$$

where A and r are the amplitude and radius of perturbation respectively. It is important to identify the appropriate perturbation amplitude and its location at the initial phase. A high amplitude perturbation may completely distort the flow and may also invalidate the linearized flow theory. Also, the location of perturbation should be carefully selected such that it interacts with the evolving boundary layer to study its stability characteristics. Hence, for the present study, a weak perturbation with a small amplitude of 10^{-5} is introduced just above the airfoil surface which can generate a weak disturbance over the airfoil surface and convects towards the trailing edge.

The second type of perturbation utilized in the present study is the broadband acoustic excitation which can effectively produce weak perturbations within the flow continuously. Such excitation also mimics the continuous excitation ex-

perienced in actual flow past airfoil (Jones et al. 2010). The broadband acoustic excitation function may be defined as,

$$p'_{inc} = p_A \sum_{n=1}^{100} \sin(2\pi t f_{exc,n} + \phi_n), \quad (2.84)$$

where p_A is pressure amplitude which is constant to a wide range of frequencies $f_{exc,n}$ ranging from 0.1 to 10 with a uniform spacing of $\Delta f_{exc,n} = 0.1$, and uniformly random phase ϕ_n .

A test case is performed to analyze the evolution of perturbation and analyze the flow characteristics over the rigid airfoil. A Gaussian perturbation of very small amplitude of 10^{-5} is chosen which does not alter the overall flow characteristics. The perturbation is introduced close to the airfoil suction surface at a location $(x, y) = (0.35, 0.07)$. The snapshots of transverse velocity fluctuations v' flow field with a time interval of $dt = 0.2$ are shown in Figures 2.11 and 2.12. At $t = 0$, the perturbation strikes the suction surface of the airfoil and a weak wavepacket is generated. At $t = 0.2$, the wavepacket grows in strength and convects in downstream direction with the flow. From $t = 0.4 - 0.6$ the wavepacket further travels downstream with growing amplitude with a similar phenomenon as observed by Fosas de Pando et al. (2014) and Jones et al. (2010). At $t = 0.8$ the wavepacket reaches the trailing edge and the flow scattering takes place. As a result, the upstream travelling waves are generated. The upstream waves interact with the suction surface and a new wavepacket is generated again at $t = 1.0$. It is important to note that the generation of this new wavepacket is due to the self-sustained feedback loop forming between the trailing edge and the point of growth of instabilities within the boundary layer on the suction surface. From $t = 1.2 - 1.8$ (Figure 2.12), the new wavepacket again convects from the airfoil suction surface towards the trailing edge with a much higher amplitude than the preceding wavepacket. Subsequently, a new wavepacket is formed at $t = 2.0$ with higher amplitude and starts to travel towards the airfoil trailing edge at $t = 2.2$.

The process continues with time marching where the wavepackets with regular intervals are generated and convected towards the trailing edge of the airfoil with increasing amplitude. The PEM with a Gaussian perturbation shows that the process can effectively capture the hydrodynamic instabilities within the boundary layer and subsequent acoustic propagation and boundary layer receptivity to acoustic disturbances.

Although the application of Gaussian perturbation is able to clearly depict the hydrodynamic insatiabilities within the boundary layer and the acoustic propagation from airfoil trailing edge, it is subjected to some limitations with respect to the application of elastic panel. As the wavepackets are generated with regular intervals, the panel is not able to vibrate continuously to sustain its dynamics and absorb the flow energy, hence, broadband acoustic perturbation is utilized for the panel design in this research. Further details on the application of PEM are discussed in Chapter 4.

2.6 Conclusions

A detailed description on the numerical methods along with their mathematical formulation has been presented in this chapter. The problem of interest involves complex interactions between unsteady flow, panel structural vibration, and acoustics. Hence, a numerical approach capable of resolving all these physical phenomena covering both aerodynamic and acoustic scales is required. Therefore, DAS approach is utilized for its capability to resolve the coupling between the unsteady airfoil aerodynamic and acoustic solutions with high accuracy. To solve the unsteady compressible N-S equations, CE/SE method is adopted. The nonlinear coupling between flow fluctuation and panel structural dynamics is resolved with a monolithic scheme. Lastly, details on the methodology and implementation strategy of PEM is discussed along with a test case. All these numerical meth-

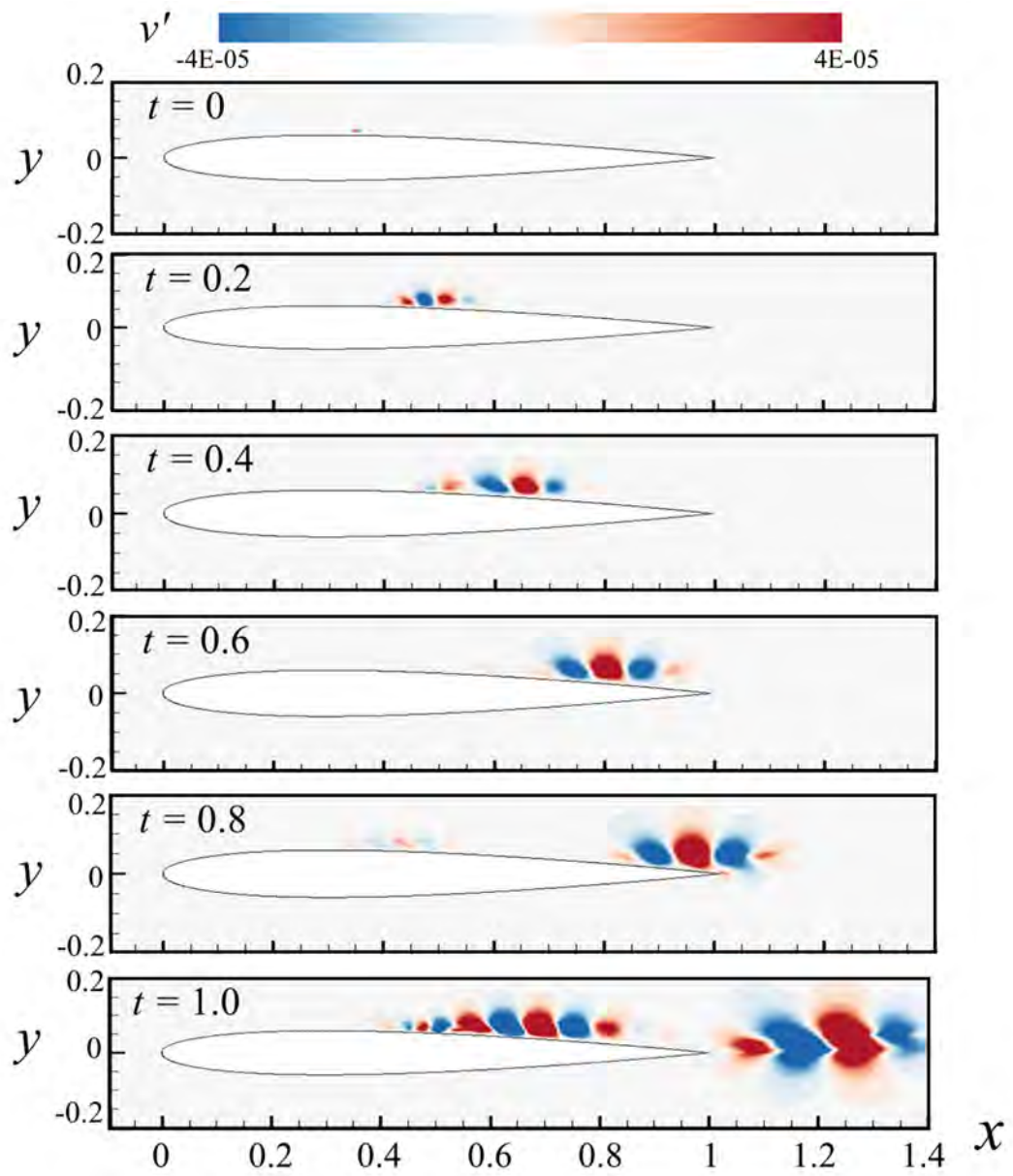


Figure 2.11: Evolution of weak Gaussian perturbation over the airfoil from $t = 0 - 1.0$.

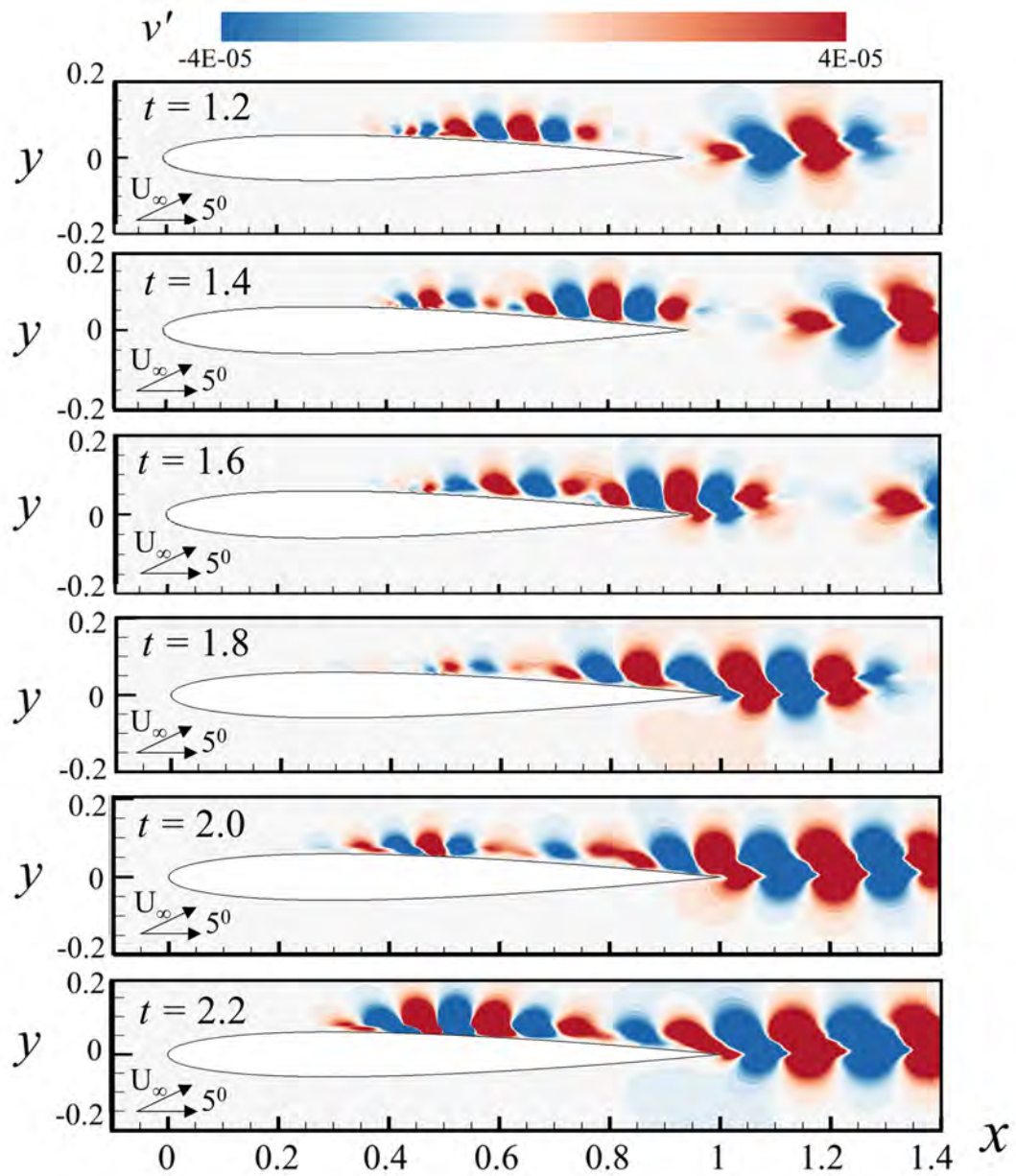


Figure 2.12: Evolution of weak Gaussian perturbation over the airfoil from $t = 1.2 - 2.2$.

ods would be applied in subsequent chapters to achieve the research objective of airfoil tonal noise reduction.

Chapter 3

Direct Aeroacoustic Simulation of Rigid Airfoil

3.1 Introduction

This chapter forms an important part of the present study as it would establish the framework of the study and help in building up the rationale for the proposed approach. The chapter is divided into two major parts. In the first part, details of the numerical setup including airfoil selection, preparation of computational domain, generation of grid, and grid independence study are presented. The results are compared with the literature to validate the methodology. In the second part of this chapter, DAS analysis of rigid airfoil is carried out and a comprehensive aerodynamic and acoustic analysis is presented. DAS analysis would also help in setting up the base flow for PEM analysis. Hence, the analysis of rigid airfoil would build a solid foundation of this research which is utilized throughout the research.

3.2 Problem Formulation and Numerical Method

3.2.1 Airfoil Selection

The present study is primarily based on the low Re flows where a laminar boundary layer is formed over a two-dimensional airfoil (i.e. $Re < 10^5$). Hence, the airfoil selection is quite important as it could directly affect the aerodynamic nature of the flow even in low Re flows. Therefore a NACA 0012 airfoil is chosen due to its wide adoption in many practical applications and vast amount of available literature (Desquesnes et al. 2007, Jones et al. 2010, Kim et al. 2011, Pröbsting et al. 2015, Di Ilio et al. 2018). NACA 0012 is one of the most commonly used symmetric airfoil for low Re flows; hence, the proposed approach of employing elastic panel on the airfoil could easily be implemented in practical situations. Furthermore, due to easy availability of aerodynamic and acoustics data for NACA 0012 in literature, the results of rigid airfoil could be easily validated as it would serve as a base flow for PEM. The NACA 0012 airfoil profile is generated by using the airfoil coordinates database of the University of Illinois at Urbana-Champaign (UICC) (Selig 2016) and shown in Figure 3.1. A total of 4000 points are used to generate the smooth airfoil profile with unity chord length.

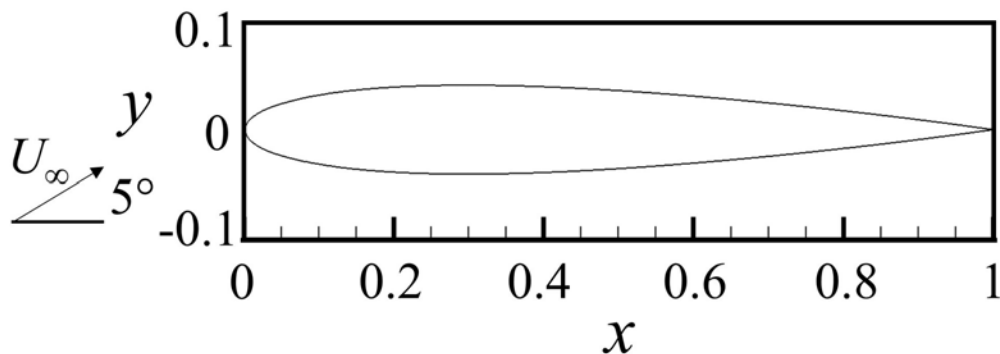


Figure 3.1: NACA 0012 airfoil profile.

3.2.2 Computational Setup

The present study aims to propose a method for airfoil tonal noise reduction, it is preferable to select the laminar flow condition which is responsible for tonal noise generation (Desquesnes et al. 2007, Arcondoulis et al. 2018, Jones 2008). Hence, a low freestream Re of 5×10^4 is chosen where the boundary layer tends to be laminar for the NACA 0012 airfoil (Jones et al. 2010). The selection of flow incidence angle also plays a critical role as a very low AoA can result in complex flow interaction among the pressure and suction sides of the airfoil (Fosas de Pando et al. 2014, Arcondoulis et al. 2019). On the other hand, a high AoA may result in strong flow separation on both surfaces of the airfoil and may even lead to stall. Hence, a nominal AoA of 5° is chosen for the initial part of the study. In the later part of the study (Chapter 7), numerical investigations at different flow $AoAs$ are also carried out and presented. The choice of freestream Mach number M requires careful deliberations as it is directly related to the control of CFL number for solution convergence. A lower M will lead to higher speed of sound and would require a much smaller interval of time step size for the control of CFL number which ultimately leads to higher computational time. On the other hand, a choice of too high M may not be experimentally replicated and may cause the flow to become locally transonic. Keeping in view the aforementioned considerations, a freestream Mach number of 0.4 is selected as a balance to minimize compressibility effects while maintaining $CFL \leq 1$. The choice of flow conditions follows the work of Jones et al. (2010) which would also provide a baseline for comparison of rigid airfoil aerodynamics and acoustics for validation of the present numerical scheme. For the cases with elastic panel, the panel is flush-mounted on the suction surface of the airfoil where both the ends of the panel are simply supported.

The selection of computational domain plays a vital role in numerical anal-

ysis. A relatively small computational domain could constrain the flow around the airfoil and even distort the acoustic characteristics due to numerical reflections with the boundaries whereas a large computational domain would certainly require much higher computational resources. The domain size for the present study is carefully chosen based on the knowledge of the NACA 0012 airfoil characteristics at low Re number (Desquesnes et al. 2007, Jones et al. 2008, Pröbsting et al. 2015). The convective wavelengths of the hydrodynamic disturbances λ_{conv} at the frequencies of interest for the selected flow conditions are ascertained based on the available literature (Arcondoulis et al. 2019, Pröbsting and Yarusevych 2015, Jones 2008). In order to ensure that the length of the domain is large enough for the wake structures to grow, saturate and dissipate, the domain length is chosen in a manner that it allows at least 20 wave cycles of lowest frequency of interest to pass through the domain. Furthermore, the upstream and downstream lengths around the airfoil are set comparable to the works of Jones (2008). Hence, a two-dimensional rectangular computational domain with a total length of 9.5 times airfoil chord and height of 9 chord lengths is generated for the present study. A buffer zone of width 1.5 surrounding the physical domain is set to eliminate any possible erroneous numerical reflection. The airfoil is located with its leading edge at $(x, y) = (0, 0)$ which is located at two chord lengths downstream of physical domain and its trailing edge is located at $(x, y) = (1, 0)$. A length of 5 chord is maintained at the downstream of trailing edge so that the airfoil wake is fully developed (Desquesnes et al. 2007, Jones et al. 2010). An upstream length of 3.5 chord is maintained to allow the propagation of upstream acoustic waves smoothly without any erroneous reflections. A schematic of the computational domain is shown in Figure 3.2. The dimensions shown are all made dimensionless with airfoil chord chosen as the reference length (i.e. $\hat{L}_0 = \hat{c}$). For the case of airfoil with elastic panel, the panel is flush-mounted on the surface of the

airfoil as shown in the small inset in Figure 3.2. All domain boundaries adopt non-reflecting boundary condition (Lam et al. 2014a) except the left and bottom boundaries which are defined by inlet boundary condition. All solid surfaces including the elastic panel are prescribed with no-slip boundary condition using near-wall approach described in Lam et al. (2014a). The boundary conditions in CE/SE method are based on a ghost-element approach. Ghost elements are created by mirroring of boundary elements along the boundaries as defined in Chapter 2.

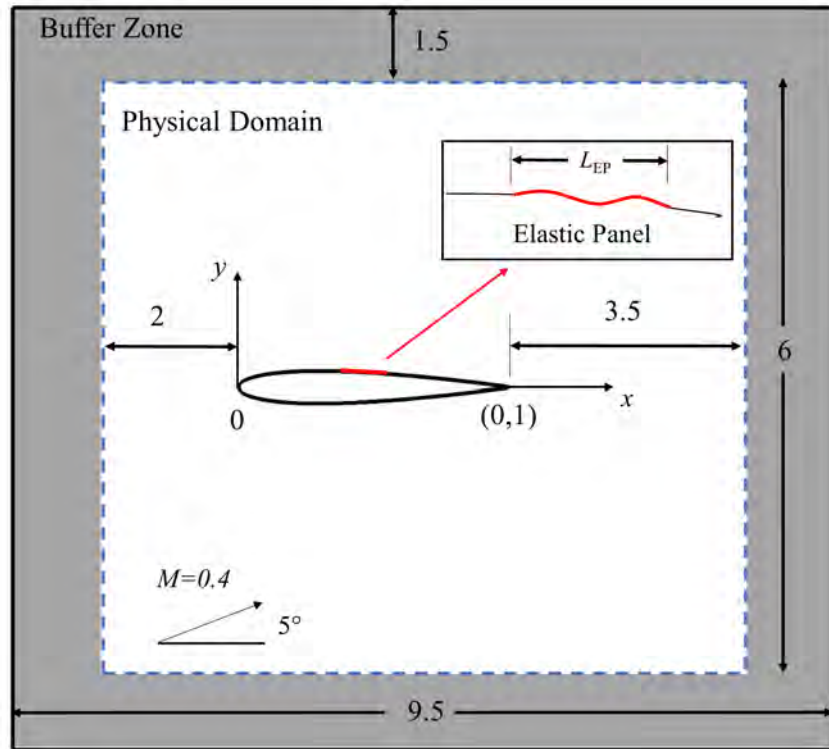


Figure 3.2: Schematic sketch of the computational domain.

For every calculation reported, the solution is initially progressed with a time step size Δt of 1×10^{-5} up till a non-dimensional time $t \sim 180$ so as to guarantee a time stationary state is achieved. The solution is then further time marched for a non-dimensional time episode of $t = 20$ for aerodynamic and acoustic analyses. A typical time history of pressure variation at a location (x, y)

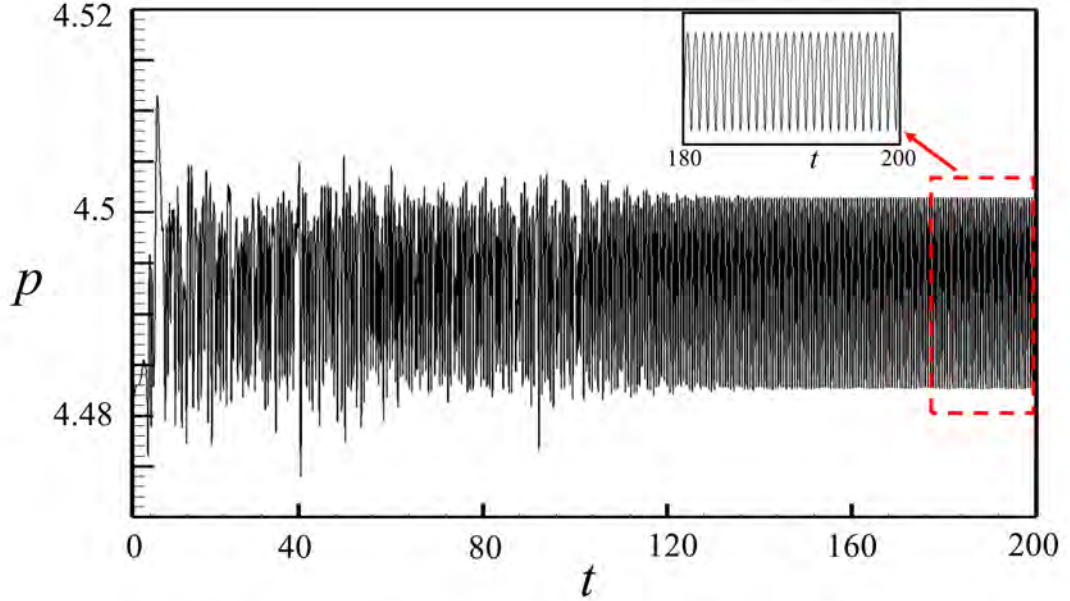


Figure 3.3: A typical time history of pressure at $(x, y) = (0.5, 3)$ for rigid airfoil case at $M = 0.4$, $Re = 5 \times 10^4$ and $AoA = 5^\circ$.

$(0.5, 3)$ for the rigid airfoil case at $M = 0.4$, $Re = 5 \times 10^4$ and $AoA = 5^\circ$ is shown in Figure 3.3. The small inset in the figure shows the time episode $t = 20$ of data collection for analysis. The calculations are carried out in University Research Facility in Big Data Analytics (UBDA) of The Hong Kong Polytechnic University which facilitates parallel processing with 494 CPU cores for a total of approximately 80,000 CPU hours for each case. To analyze the acoustical characteristics required in the present study, 180 virtual probes are placed all around the airfoil with azimuthal increment $d\theta = 2^\circ$ at radius $r = 2$ and 3 respectively (Figure 3.4). Furthermore, 4000 virtual probes have been placed over the airfoil within the boundary layer along suction and pressure surfaces respectively to analyze the airfoil hydrodynamic behavior.

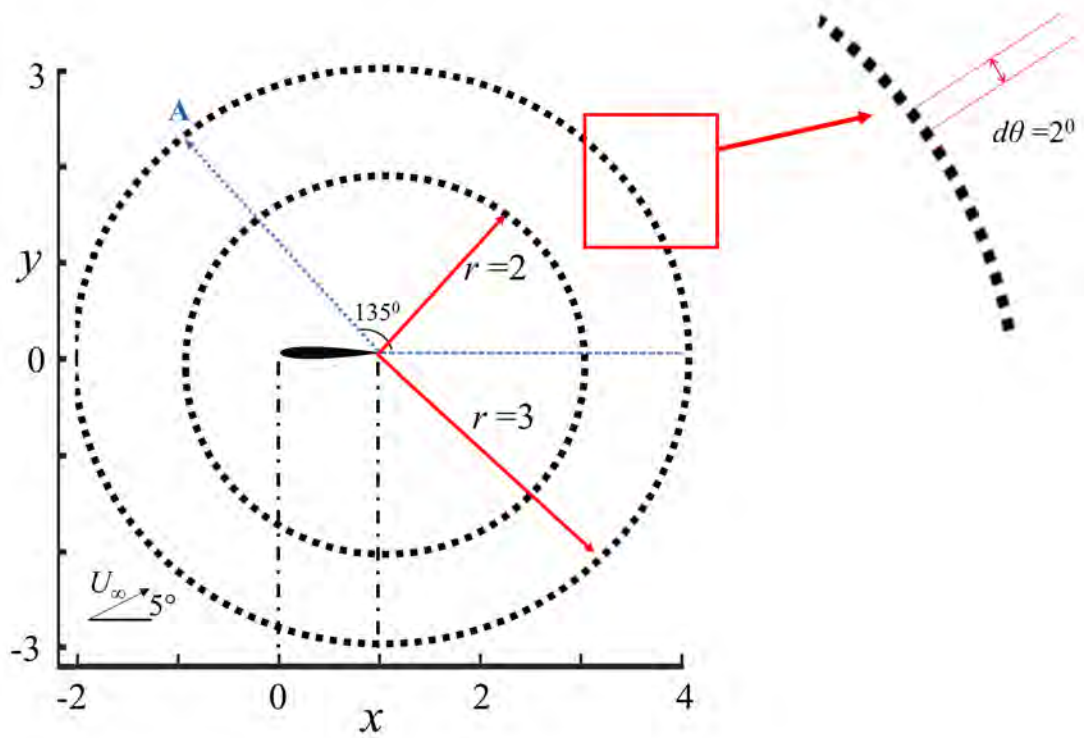


Figure 3.4: Distribution of virtual probes around the airfoil trailing edge.

Table 3.1: Mesh size around airfoil for different grids

Grid	Mesh Size					Mesh Parameters			
	w_{le}	h_{le}	w_{te}	h_{te}	w_{far}/h_{far}	$N_{suction}$	N_{offset}	N_{wake}	Total Mesh
G1	5.5×10^{-4}	5.5×10^{-4}	40×10^{-4}	5.5×10^{-4}	1×10^{-2}	800	51	1020	4.84×10^6
G2	5.0×10^{-4}	5.5×10^{-4}	9.0×10^{-4}	5.0×10^{-4}	1×10^{-2}	2000	63	1400	6.52×10^6
G3	4.5×10^{-4}	5.0×10^{-4}	7.5×10^{-4}	4.7×10^{-4}	1×10^{-2}	2300	74	1500	7.20×10^6

3.2.3 Grid Generation

For the present study, three different computational meshes, namely G1, G2 and G3, have been generated and evaluated to study the mesh dependence and numerical convergence. The mesh size around airfoil leading edge, trailing edge, and near wake (Figures 3.6(a)-(c)) are given special considerations for guaranteeing sufficient resolution for resolving the boundary layer evolution and subsequent acoustic propagation. Grid G2 is generated by refinement of G1 whereas G3 is generated by further refinement of G2. The resolution from G1 to G3 is refined by almost four times near the airfoil surface. The number of mesh elements along the airfoil surface, airfoil wake, and amount of layers within an offset of 0.05 from airfoil surface denoted by $N_{suction}$, $N_{offset_{0.05}}$ and N_{wake} respectively and other key locations are listed in Table 3.1 (Figure 3.6(d)). Also, the details of selected parameters for the complete domain for each grid are listed in Table 3.2. In the application of CE/SE method, a quadrangle mesh element is split into four triangles using diagonal cross-division (Lam et al. 2014a). Hence the total size of the mesh is four times the original quadrangle mesh size. A schematic sketch of the generated mesh for G2 is shown in Figure 3.5.

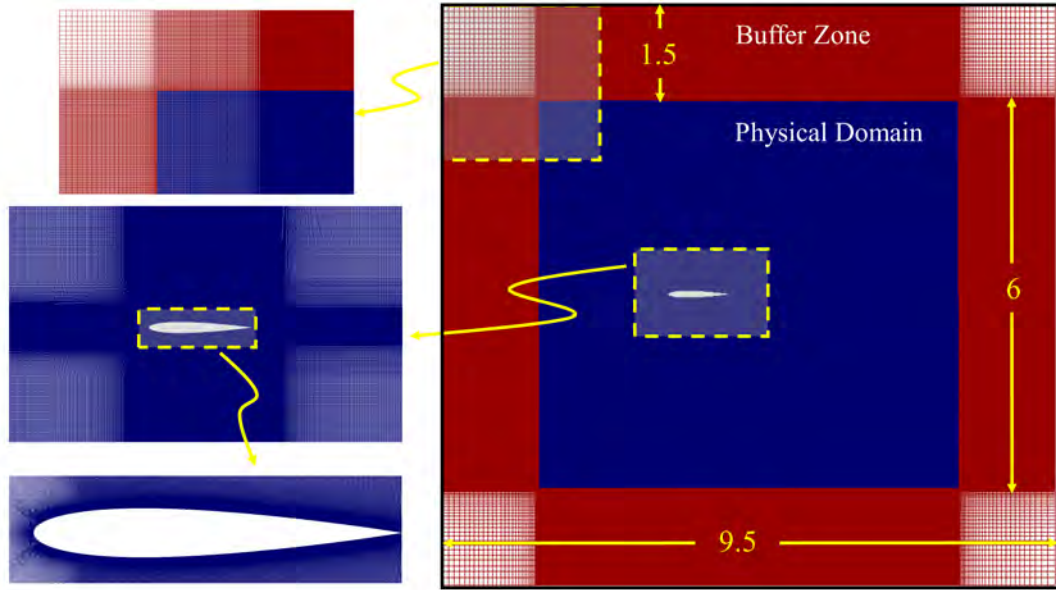


Figure 3.5: Schematic sketch of the computational domain for G2.

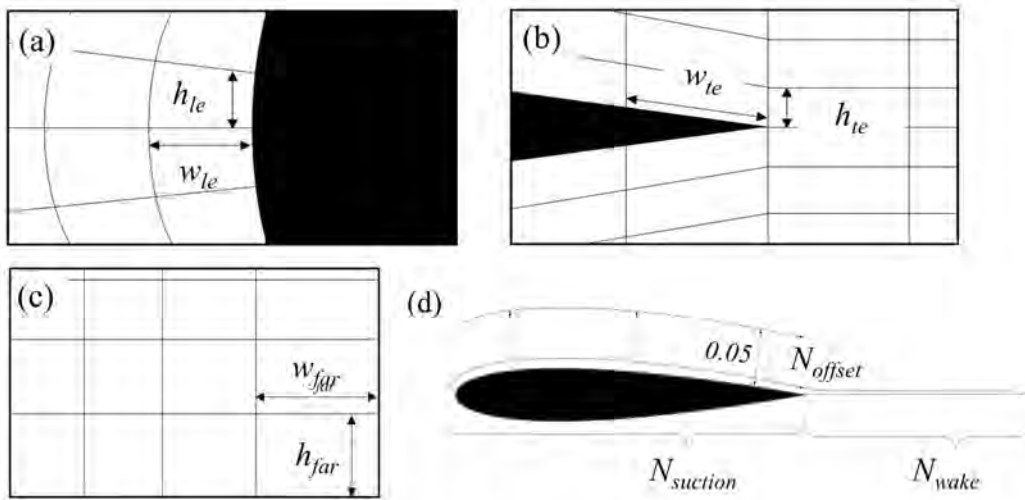


Figure 3.6: Definition of mesh parameters.

Table 3.2: Mesh parameters for the complete domain for different grids (minimum mesh size/maximum mesh size)

Grid	Physical domain					Buffer
	$x < -1$	$-1 \leq x \leq 2$	$x > 2$	$ y > 0.3$	$-0.3 \leq y \leq 0.3$	x, y
G1	0.01 / 0.02	0.001 / 0.008	0.008 / 0.01	0.005 / 0.02	0.0007 / 0.008	0.02 / 0.1
G2	0.008 / 0.009	0.0005 / 0.005	0.005 / 0.008	0.005 / 0.01	0.0005 / 0.005	0.01 / 0.1
G3	0.007 / 0.008	0.0004 / 0.005	0.004 / 0.007	0.004 / 0.01	0.0004 / 0.005	0.008 / 0.1

3.3 Direct Aeroacoustic Simulation of Rigid Airfoil

DAS for rigid airfoil (RS) is initially carried out for the selected flow conditions of $M = 0.4$, $Re = 5 \times 10^4$ and $AoA = 5^\circ$. A grid independence study is also performed for the selection of optimum mesh size and the results of numerical scheme are validated with the available literature. The important flow field and acoustic features such as boundary layer separation/reattachment, near wake characteristics, tonal noise spectra, and acoustic feedback loop are also evaluated for the RS case. Essentially there are three major objectives of carrying out the rigid airfoil analysis at the initial stage. Firstly, it would help in validation of the CE/SE method in resolving the interaction between flow field dynamics and acoustics effectively. Secondly, it would help in ascertaining important flow field and acoustic features such as boundary layer separation/reattachment, near wake characteristics, tonal noise spectra, and acoustic feedback loop. These characteristics would help in the subsequent design of elastic panel. Lastly, the time-averaged solution of RS would be later used in setting up the base flow for PEM.

3.3.1 Time-Averaged Aerodynamics

Aerodynamic characteristics of RS, based on time-averaged solution extracted over a period of thirty cycles of airfoil lift and drag fluctuations from time stationary solution, is evaluated to analyze flow characteristics over the airfoil surface including LSB. The coefficients of lift C_L and drag C_D are calculated by integrating the pressure and shear forces acting over the airfoil surface in their respective directions. For the said purpose, the results are evaluated over 4000 different points on the airfoil and are subsequently integrated to evaluate the normal c_n and axial c_a forces by using the following formulation (Anderson Jr 2011):

$$c_n = \frac{1}{c} \left[\int_0^c (C_{p,l} - C_{p,u}) dx + \int_0^c \left(C_{f,u} \frac{dy_u}{dx} + C_{f,l} \frac{dy_l}{dx} \right) dx \right] \quad (3.1)$$

$$c_a = \frac{1}{c} \left[\int_0^c \left(C_{p,u} \frac{dy_u}{dx} - C_{p,l} \frac{dy_l}{dx} \right) dx + \int_0^c (C_{f,u} + C_{f,l}) dx \right] \quad (3.2)$$

where C_p is the pressure coefficient, C_f is the skin friction coefficient, subscripts u and l denote upper and lower surfaces of the airfoil respectively. Subsequently, the C_L and C_D are evaluated by:

$$C_L = c_n \cos(AoA) - c_a \sin(AoA) \quad (3.3)$$

$$C_D = c_n \sin(AoA) - c_a \cos(AoA) \quad (3.4)$$

Figure 3.7 shows the calculated coefficient of lift C_L and drag C_D respectively for all three grids. For brevity, only a time episode of $0 < t < 3$ is shown. It is observed that the numerical solutions from G2 and G3 are almost identical and the results appear independent of grid size for these two grid configurations. However, a significant deviation in the numerical results is observed for G1. For G2 and G3, the magnitude of C_L and C_D periodically fluctuate with ranges of

0.46-0.51 and 0.015-0.020 respectively, whereas for G1, the magnitude of C_L and C_D fluctuates within 0.465-0.515 and 0.0145-0.021 respectively. Table 3.3 presents a summary of the calculated time-averaged aerodynamic parameters for all three grids along with its comparison with the available numerical and experimental studies (Jones 2008, Arcondoulis et al. 2013). It is important to note that the flow conditions of the experimental study carried out by Arcondoulis et al. (2013) slightly varies from the current study where a very low M of only 0.03 was considered in the experimental work as compared to M of 0.4. The aerodynamic results clearly indicate that the solutions from G2 and G3 yield almost identical values and are in excellent agreement with literature; whereas a slight deviation is observed for G1. Therefore, a refined grid G2 with a total quadrangular mesh size of 6.52×10^6 is selected for the present study for its best compromise between accuracy and optimum requirement of computational resources. Hence, further analysis in this thesis would be presented for G2 only.

Figure 3.8(a) shows the time-averaged pressure coefficient C_p over the suction and pressure surfaces of airfoil. On the suction surface, a sudden increase in C_p near the leading edge $0.04 < x < 0.2$ due to strong adverse pressure gradient can be observed. This is followed by a pressure plateau from $0.2 < x < 0.45$ and a rapid transition from $0.45 < x < 0.6$. From $0.6 < x < 0.79$, another pressure plateau is observed which is followed by an increase in C_p up till trailing edge. C_p on the pressure surface decreases smoothly from the airfoil leading edge up to $x \sim 0.3$ and increases slowly up till the airfoil trailing edge. The coefficient of friction C_f distribution over the airfoil suction surface is shown in Figure 3.8(b). The separation and reattachment point can be identified where C_f crosses zero. The boundary layer separation occurs at $x \sim 0.18$ and reattaches at $x \sim 0.585$ which shows strong agreement with Jones et al. (2008) as shown in Table 3.3. A laminar separation bubble of a length 0.4 is observed at the selected

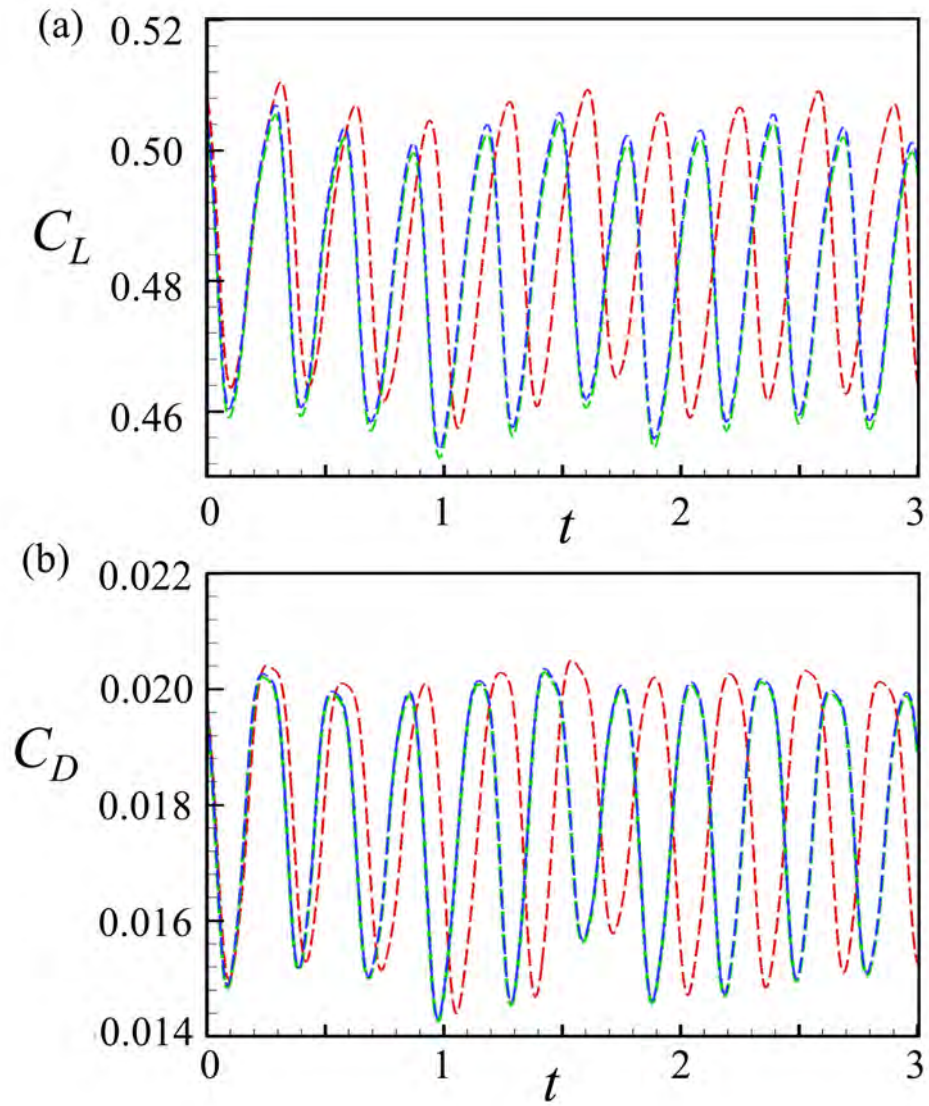


Figure 3.7: Coefficient of lift and drag for different grids. - - - , G1; - · - · , G2; and - - - , G3.

Table 3.3: Time-averaged aerodynamic parameters

Case	$C_{L,mean}$	$C_{D,mean}$	$f_{dominant}$	x_{sep}	x_{reatt}
Grid G1	0.4857	0.0183	3.31	0.21	0.601
Grid G2	0.4855	0.0185	3.37	0.18	0.585
Grid G3	0.4855	0.0185	3.37	0.18	0.585
Jones et al. (2008)	0.490	0.0201	3.37	0.151	0.582
Arcondoulis et al. (2013)	-	-	3.62	0.190	-

flow conditions whereas no boundary layer separation on the pressure surface is observed.

Figures 3.9 and 3.10 show the time-averaged flow field variables for the rigid airfoil. The small inset shows the close-up view around the airfoil. The flow field plots obtained from high-fidelity DAS help in identifying the key aerodynamic features around the airfoil such as flow separation/reattachment points, stagnation point at the airfoil leading edge, laminar separation bubble and airfoil wake. The high pressure region indicating the stagnation point can be identified around the airfoil leading edge in Figures 3.10(a) and (b) which is followed by a low pressure region over the suction surface of the airfoil. The flow velocity accelerates in this region and the flow separation occurs due to adverse pressure gradient as observed in Figures 3.9(a) and (b). The flow again reattaches at a downstream location on the airfoil surface and the vortex shedding over the airfoil surface produces a prominent wake region which is asymmetric due to the flow incidence of $AoA = 5^\circ$.

The characteristics of the boundary layer separation/reattachment and

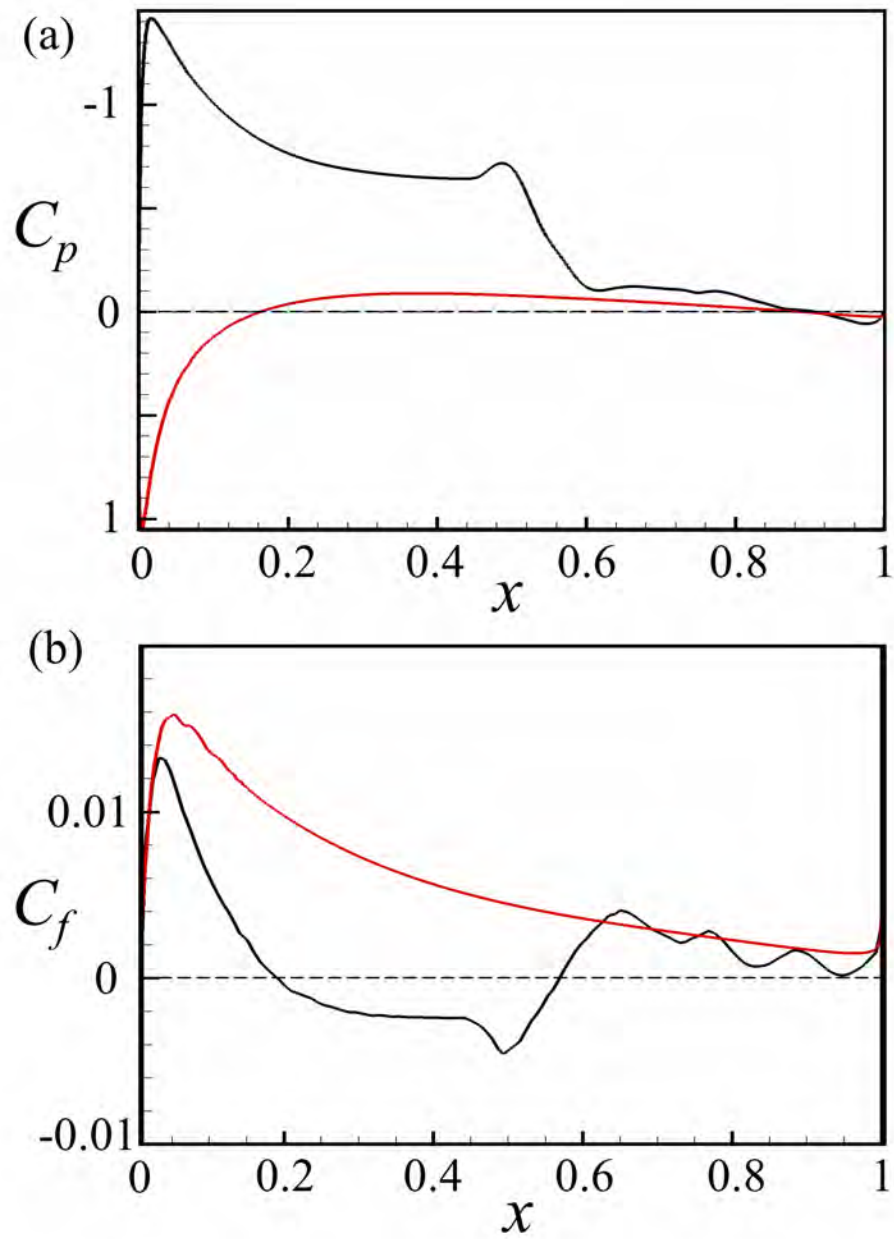


Figure 3.8: Distribution of (a) time-averaged C_p ; and (b) time-averaged C_f around rigid airfoil. —, suction surface; —, pressure surface.

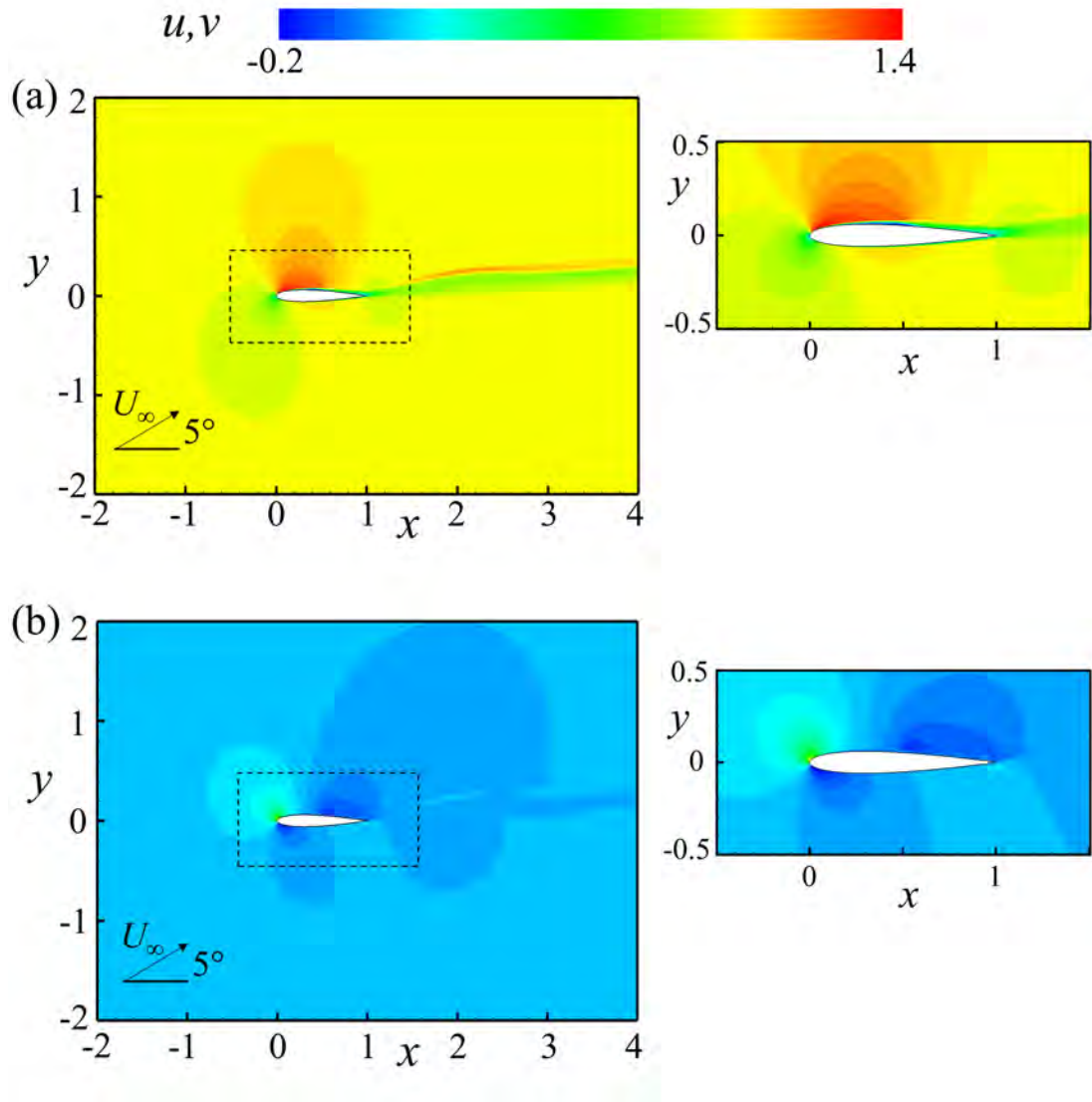


Figure 3.9: Time-averaged flow field. (a) u and (b) v .

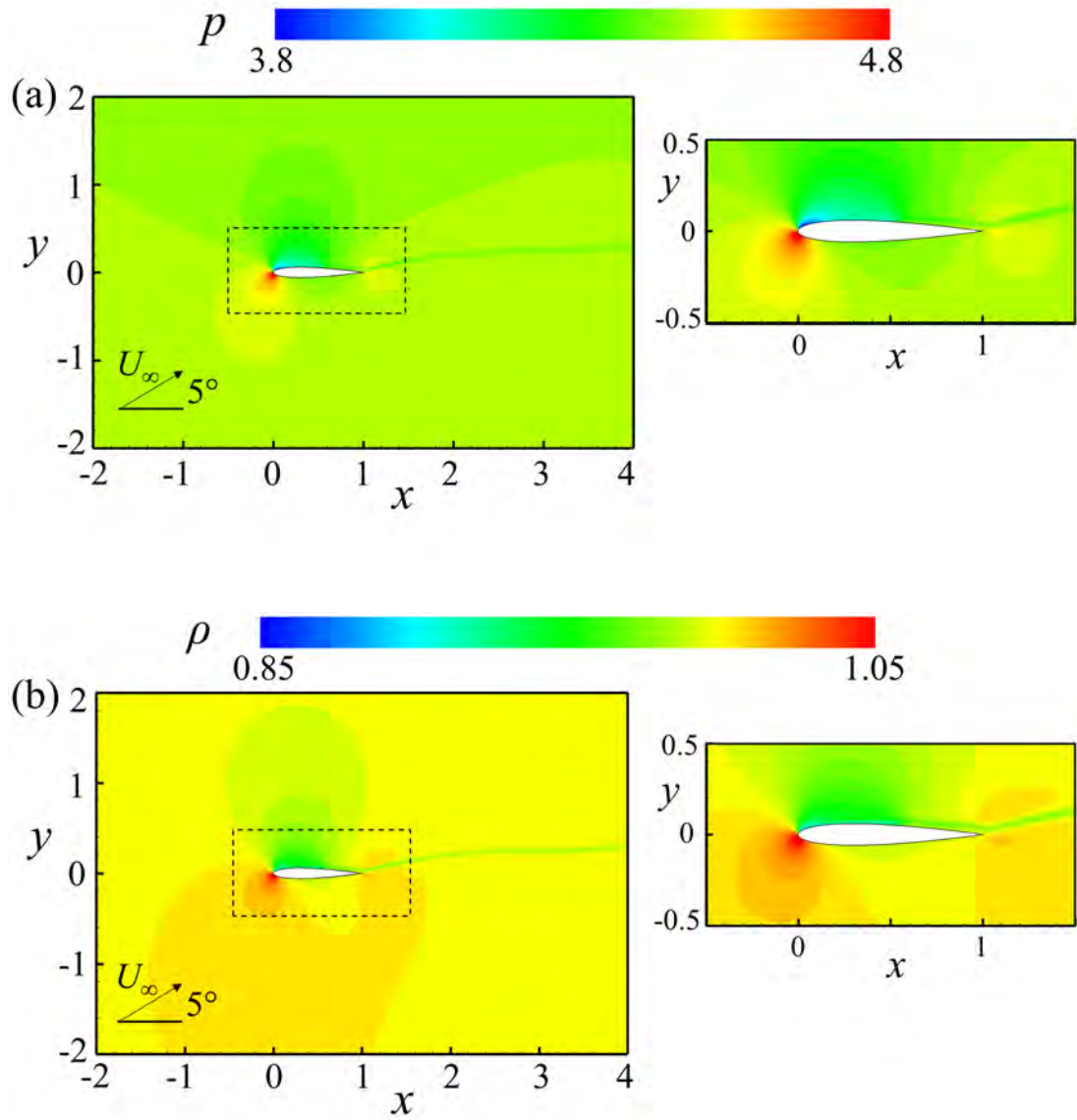


Figure 3.10: Time-averaged flow field. (a) p and (b) ρ .

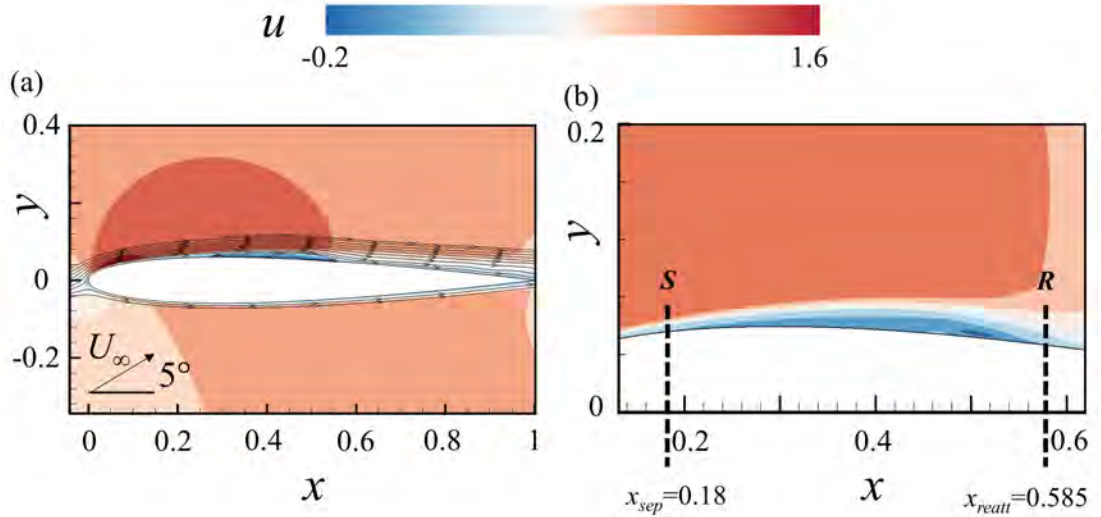


Figure 3.11: (a) Velocity streamlines over the airfoil surface; and (b) closeup view of airfoil suction surface indicating flow separation and reattachment points.

the separation bubble are further investigated in detail. Figure 3.11(a) shows the time-averaged velocity field along with streamlines around the rigid airfoil. The flow separation, reattachment, and separation bubble over the airfoil suction surface can be clearly observed along with the recirculation region prior to flow reattachment point. The flow behavior is further investigated by closeup view of the airfoil in Figure 3.11(b) to identify the flow separation and reattachment locations indicated by ‘S’ and ‘R’ respectively. The laminar boundary layer separation point occurs at $x \sim 0.18$ and a separation bubble is formed. The boundary layer instabilities start to grow within the separation bubble and the flow reattachment occurs at $x \sim 0.58$ as also observed in Figure 3.8(b). The nature of growth of boundary layer instabilities within the separation bubble and its evolution is further explored in subsequent sections.

Figures 3.12 (a) and (b) show the flow field distributions of u'_{rms} and v'_{rms} respectively for the rigid airfoil. It is observed that the prominent velocity

fluctuations start to emerge over the airfoil suction surface within the separation bubble which indicates the presence of strong flow instabilities in this region. These instabilities further grow in amplitude in the form of vortices and convect downstream towards the airfoil trailing edge and wake region. The presence of these instabilities within the airfoil boundary layer and the resulting vortex shedding over the airfoil trailing edge have found to be responsible for airfoil noise generation in a number of studies (Desquesnes et al. 2007, Jones et al. 2008, Arcondoulis et al. 2018). To further investigate the contribution of flow fluctuations and their subsequent effect on additional momentum fluxes in the flow, Reynolds stress ($|u'v'|/U_\infty^2$) is evaluated for the rigid airfoil case as shown in Figure 3.13. It is observed that the magnitude of fluctuations over the airfoil suction surface starts to increase at the rear end of separation bubble. The presence of high magnitude of Reynolds stress is attributed to the vortex shedding induced by the flow instabilities within the separation bubble (Genç et al. 2020). The magnitude of fluctuation further increases continuously towards the airfoil trailing edge and subsequently in the airfoil wake.

3.3.2 Unsteady Airfoil Aerodynamics

The frequency spectrum of transverse velocity fluctuations over the airfoil suction surface within the boundary layer is shown in Figure 3.14. In essence, the time traces of flow fluctuation at every location is captured along a contour well close parallel to airfoil suction surface. Every time trace is then processed through Fast Fourier Transform (FFT) to obtain its spectrum from which the characteristic frequencies and amplitudes of flow fluctuation are identified and determined. Spectrum is obtained by performing FFT based on the time history of non-dimensional time $t = 10$ with a sampling frequency of 1×10^5 for fine resolution. A Hamming window with no data overlapping is applied in the transform.

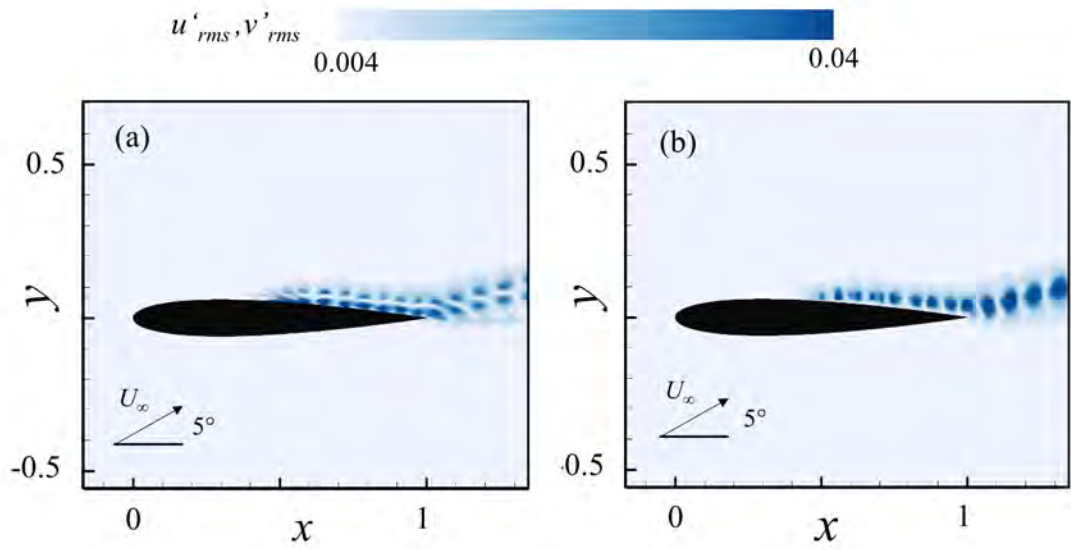


Figure 3.12: Flow field distribution of velocity fluctuations over rigid airfoil.

(a) u'_{rms} and (b) v'_{rms} .

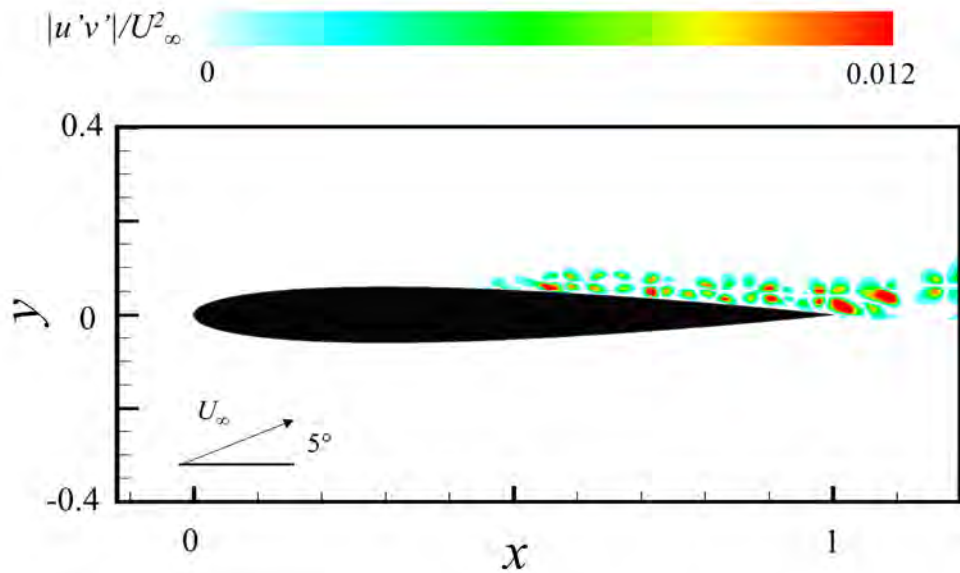


Figure 3.13: Reynolds stress distribution over the rigid airfoil.

In Figure 3.14(a), the FFT spectrum reveals that the natural airfoil boundary layer growth is dominated by the fundamental frequency $(f_{bl})_0 = 3.37$ along with its first and second harmonics observed at $(f_{bl})_1 = 6.67$ and $(f_{bl})_2 = 10.0$ respectively. It is interesting to note that the magnitude of velocity fluctuations becomes observable from $x \sim 0.4$ up to the airfoil trailing edge which indicates the presence of significant boundary layer instabilities. The magnitude of fluctuations observed at $(f_{bl})_0$ is much higher than its $(f_{bl})_1$ and $(f_{bl})_2$ except at $x = 0.7$ where the fluctuation magnitudes at all dominant frequencies are comparable. The observed fundamental frequency $(f_{bl})_0$ of the airfoil boundary layer growth over the suction surface is also similar to the study of Jones et al. (2008) and Arcondoulis et al. (2013) (Table 3.3).

To further investigate the flow behavior within the boundary layer over the suction surface, its natural stability characteristics are analyzed at $(f_{bl})_0$ and $(f_{bl})_1$ by extracting the amplitudes of v' from the FFT spectrum (Figure 3.14(a)) at the particular frequencies. Figure 3.14(b) shows the amplitudes of velocity fluctuations v' at both frequencies which start to increase at $x \geq 0.27$ and grow within $0.4 \leq x \leq 0.45$. The amplitude of $(f_{bl})_0$ grows remarkably to reach its plateau of 0.043 at $x \sim 0.5$, stays there up till $x \sim 0.57$, then drops rapidly to a dip at $x \sim 0.65$, and eventually grows mildly again. The amplitude of $(f_{bl})_1$ appears to grow in a more gradual fashion and fluctuates mildly around a value of 0.0125 beyond $x \sim 0.57$. It is interesting to see that the region for drastic stability amplification, i.e. $0.27 \leq x \leq 0.57$, is coincident with the emergence of the separation bubble on the airfoil suction surface. Such observation is consistent with the previous instability wave analysis by solving Orr-Sommerfeld equation (Jones et al. 2008).

Figures 3.15(a) and (b) show the FFT spectra of C_L and C_D , obtained for a time episode of $t = 20$ with a sampling frequency of 1×10^5 . The FFT

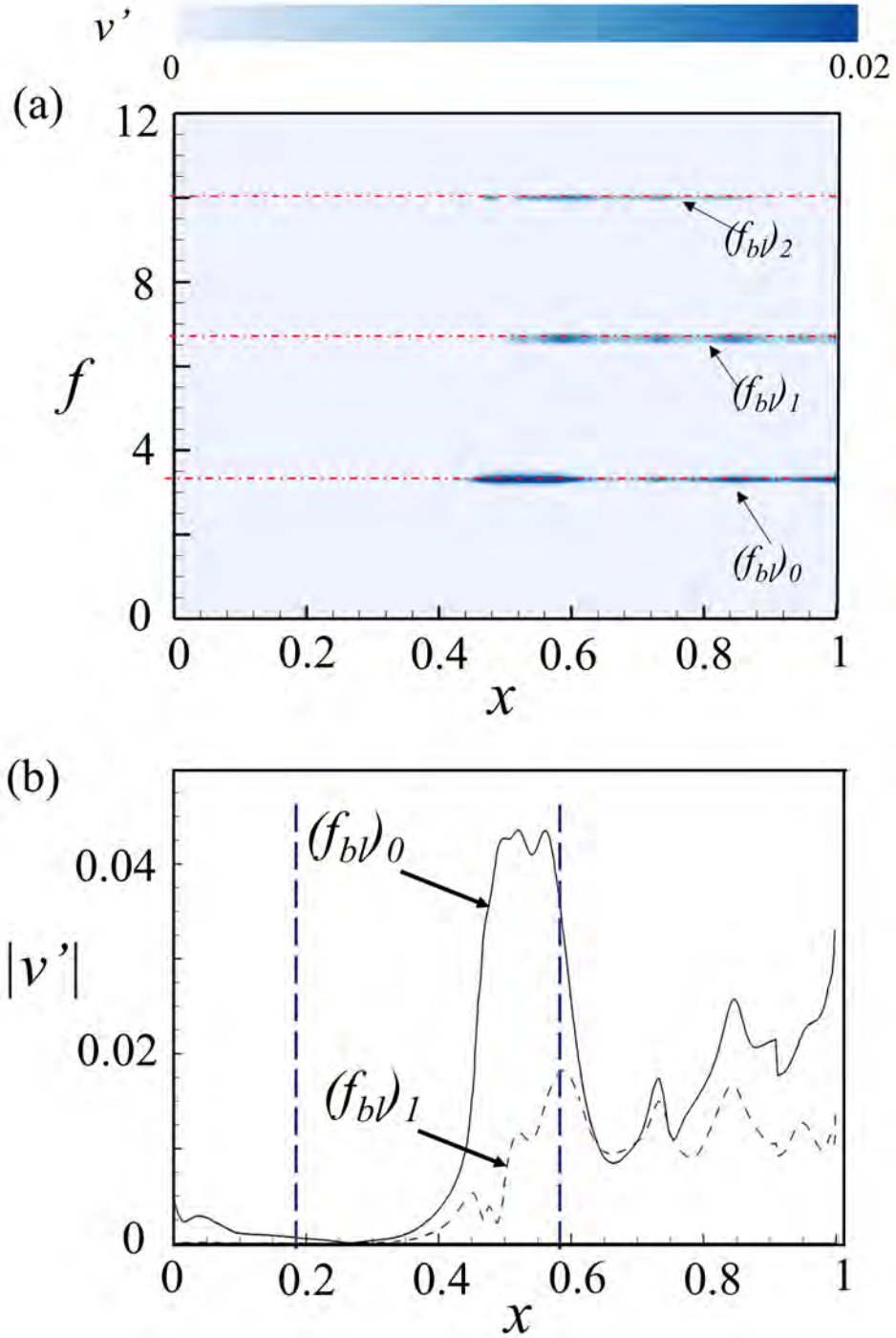


Figure 3.14: (a) Distribution of spectrum of transverse velocity fluctuations v' along the airfoil. (b) Spatial growth of flow instability over the airfoil suction surface at $(f_{bl})_0$ and $(f_{bl})_1$. The horizontal red dashed-dotted lines in (a) indicate the $(f_{bl})_n$, $n = 1, 2, 3$ and the vertical blue dashed lines in (b) indicate the boundary layer separation and reattachment points.⁸⁸

plots clearly indicate a dominant frequency of 3.37 and its higher harmonics as observed in Figure 3.14(a).

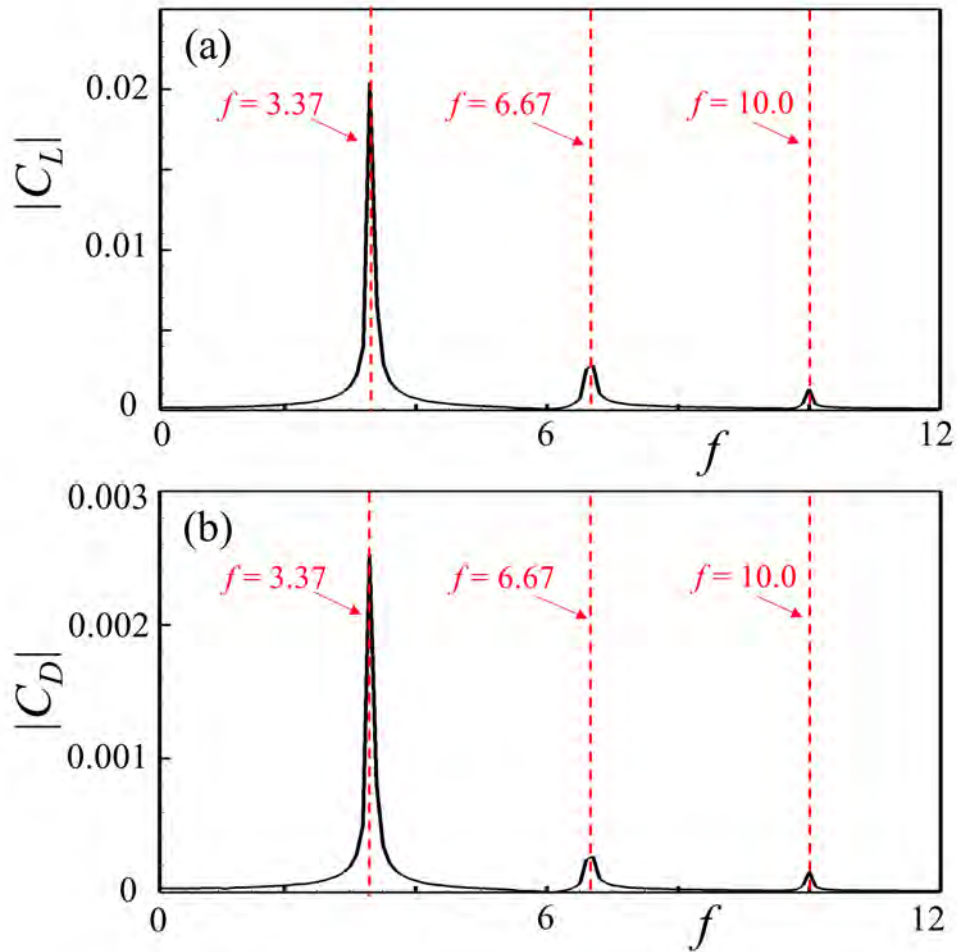


Figure 3.15: FFT spectra of (a) C_L and (b) C_D .

According to Lighthill's acoustic analogy (Lighthill 1954), the unsteady motions of vortices convecting over the airfoil generate noise which is similar to the scattering of an incident wave at a sharp edge. The passage of the vortical structures over the airfoil trailing edge into the wake generally creates discrete tones (Ffowcs Williams and Hall 1970, Crighton and Leppington 1971). Hence, it is essential to visualize the flow field sequence of vortex shedding over the airfoil to investigate the noise generation mechanism. Figure 3.16 show snapshots of the flow evolution within one lift cycle (peak to peak) for a non-dimensional time

$t/T_d = 0 - 1.08$, where the period $T_d = 1/(f_{bl})_0$. The unsteady flow exhibits the emergence of vortices from the separated shear layer on airfoil suction surface and its subsequent passage over the trailing edge of airfoil into the wake. The evolution of three vortices on the suction surface can be clearly observed. At the peak of the lift cycle ($t/T_d = 0$), the formation of vortex starts at $x \sim 0.58$ just at the onset of boundary layer reattachment point whereas the second and third vortices are already present at $x \sim 0.8$ and $x \sim 0.98$ on the suction surface. The vortices convect downstream with each time increment towards the airfoil trailing edge and subsequently detaches from airfoil surface to pair up with vortices from the pressure surface which induces counter-rotating vortex pair with strong transverse flow fluctuations ($t/T_d = 0.54$). The process of vortex formation at $x \sim 0.58$ begins again and a cycle is completed by $t/T_d = 1.08$ which corresponds to the peak of lift cycle.

3.3.3 Airfoil Acoustics

To analyze the noise generation mechanism, instantaneous fluctuating pressure field defined by $p'(x, t) = p(x, t) - p_{mean}(x)$ is plotted within one lift cycle (peak to peak) for a non-dimensional time $t/T_{dominant} = 0 - 1.08$ with equal intervals as shown in Figure 3.17. Mean pressure p_{mean} is evaluated by averaging the pressure over the non-dimensional time $t = 10$. Positive p' (red color) shows compression whereas negative p' (blue color) shows refractions of acoustic disturbances. The pressure fluctuations induced by the flow scattering at the trailing edge propagates in the radial direction and a discrete tone is observed. The scattering mechanism is mathematically explained by Crighton and Leppington (1971) where the sharp airfoil trailing provides singularity in a low-frequency limit of wave equations. Since the noise sources are mainly localized in the trailing edge and near-wake region, the acoustic plot can be utilized to track the propagation of waves from

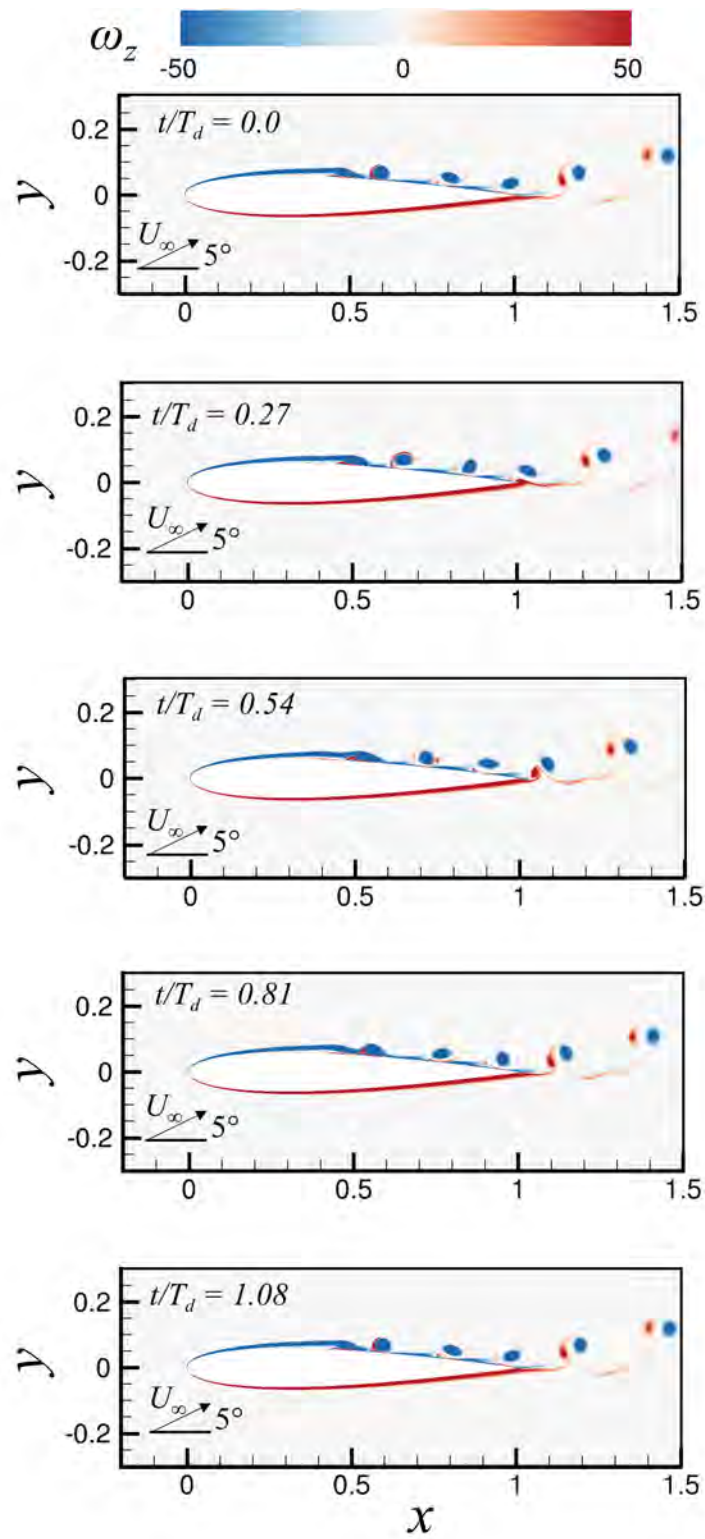


Figure 3.16: Instantaneous vorticity distribution on rigid airfoil.

airfoil wake to far field and upstream location of flow (Tam and Ju 2012). The plots reveal that the instabilities start to grow within the separation bubble on the suction surface and become highly unstable near the trailing edge and near wake region. These instabilities interact with the trailing edge and result in the scattering of acoustic waves. The airfoil wake is characterized by a row of vortices in a staggered fashion. It is also observed that the near wake vortices motion is asymmetric due to the current flow condition of $AoA = 5^\circ$. Hence, the distribution of the acoustic waves is not uniform in all directions as most of the waves are spread towards the forward half plane. A phase difference of 180° can be observed between the suction and pressure surface over the airfoil. At the peak of the lift cycle ($t/T_d = 0$), the instantaneous acoustic field has a completely opposite phase to the lowest point in lift fluctuation at $t/T_d = 0.54$ and the cycle repeats with equal intervals. The formation and spreading of the wavefronts at an upstream location on airfoil indicate the presence of feedback loop as well.

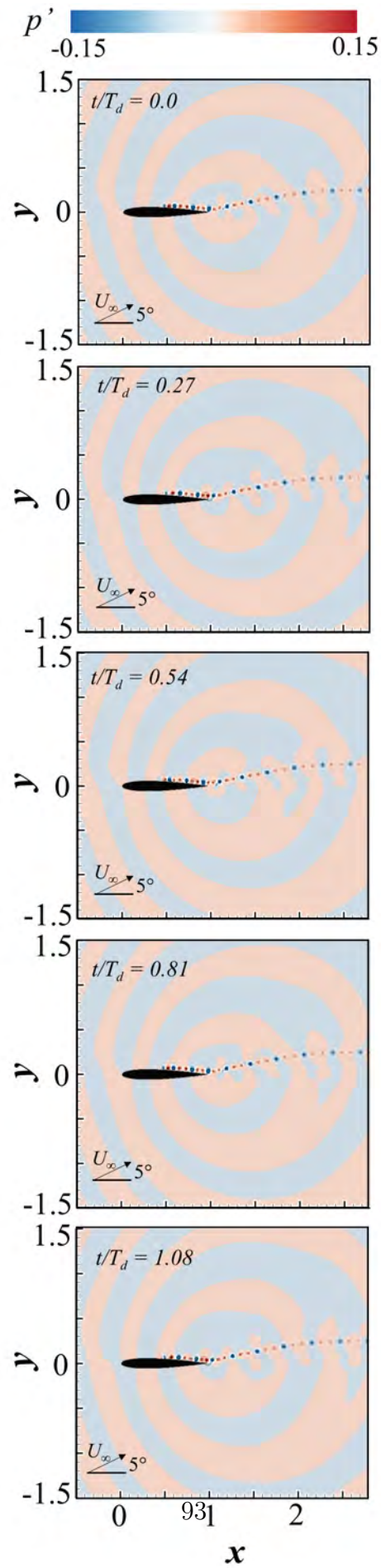


Figure 3.17: Instantaneous acoustic fluctuation p' .

To further analyze the acoustic propagation, azimuth plots of time-averaged pressure distributions for rigid airfoil at a radius of two and three airfoil chord lengths are plotted in Figure 3.18 and compared with the solution by Jones et al. (2008). The strong aerodynamic fluctuations inside the airfoil wake (i.e. $\theta = \pm 30^\circ$) dominate to mask out the acoustic fluctuations (Figure 3.17); thus, the data in this sector is not shown. A good agreement can be observed between the directivity pattern obtained from the present study and Jones et al. (2008) which further validates the numerical methodology. Only a slight deviation of 0.4% is observed at an azimuth location of $\theta \sim 120^\circ$ for both radii.

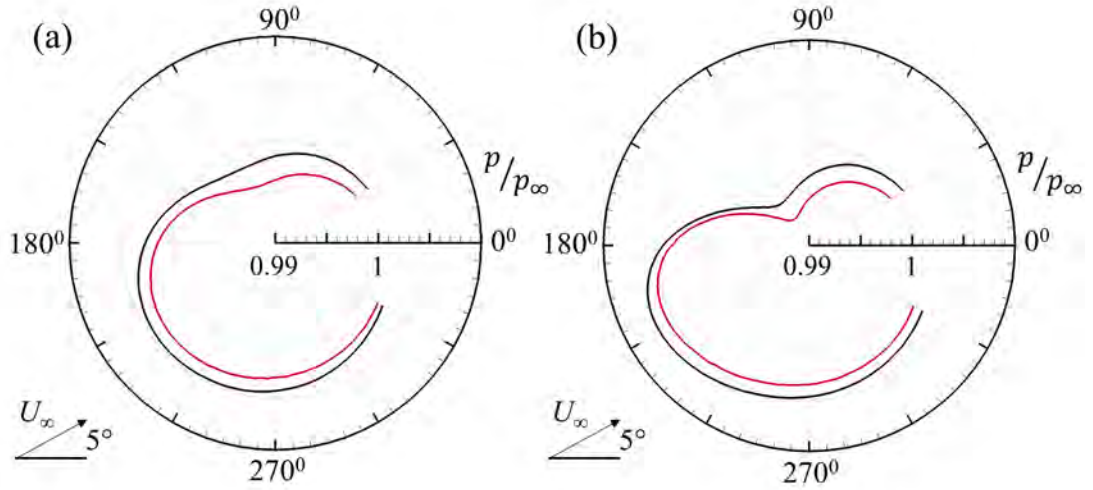


Figure 3.18: Azimuth plot of time-averaged p/p_∞ at (a) $r = 2$ and (b) $r = 3$.
—, rigid airfoil; —, Jones et al. (2008).

Figure 3.19 shows the time history of pressure fluctuations p' at $r = 3$ for different azimuth locations for a time episode of $t = 180 - 190$. The p' plot at all locations shows a uniform periodic behavior with different magnitudes. Interestingly, a difference in the magnitudes of p' at similar downstream locations above and below the airfoil, i.e. $\theta = 45^\circ$ and 315° is observed which indicates different extent of acoustic radiation by the airfoil at these locations. On the other hand, the magnitudes of p' at a similar upstream location above and below the

airfoil ($\theta = 135^\circ$ and 225°) is found to be similar. The noise radiation pattern of the rigid airfoil is further explored in Figure 3.21(b) in the subsequent paragraph.

Figure 3.20 shows the FFT spectrum of p' at $r = 3$ for the same azimuth locations of Figure 3.19. The FFT plots indicate a dominant frequency peak at 3.37 along with its higher harmonics at 6.67 and 10 at all these locations. The frequency content observed at these azimuth locations coincide with the frequency content of the boundary layer instabilities over the airfoil surface which indicates a direct effect of the flow instabilities on the acoustic radiation for the current flow condition.

Frequency spectrum of pressure fluctuations p' all around the airfoil at $r = 3$ is carried out to obtain the acoustic spectral directivity as shown in Figure 3.21(a). A full-length time history of 20 calculation time and a sampling frequency of 1×10^5 is selected for fine resolution. A Hamming window with no data overlapping is applied to p' . Strong contribution in acoustic waves generation can be observed at the fundamental frequency of 3.37 which corresponds to the fundamental frequency within the boundary layer $(f_{bl})_0$ (Figure 3.21(a)). The magnitude of fluctuations decreases as the frequency further increases up till 6.67 where a mild contribution to acoustics can be observed. The spectral content varies with azimuth location as well. The second and third quadrant contains the strongest and richest spectral content for both fundamental frequency and its first harmonics. The first and fourth quadrant are comparatively quiet with most of the contribution coming from the dominant frequency of 3.37 only. The observed spectral map indicates that the fundamental frequency of naturally growing flow instabilities within the boundary layer and vortex shedding which scatters at the trailing edge is the dominant acoustic source for the current configuration.

Figures 3.21(b) shows the azimuthal directivity of acoustic p'_{rms} evaluated at $r = 3$ from trailing edge. The acoustic solution within the sector $\theta = \pm 30^\circ$ is

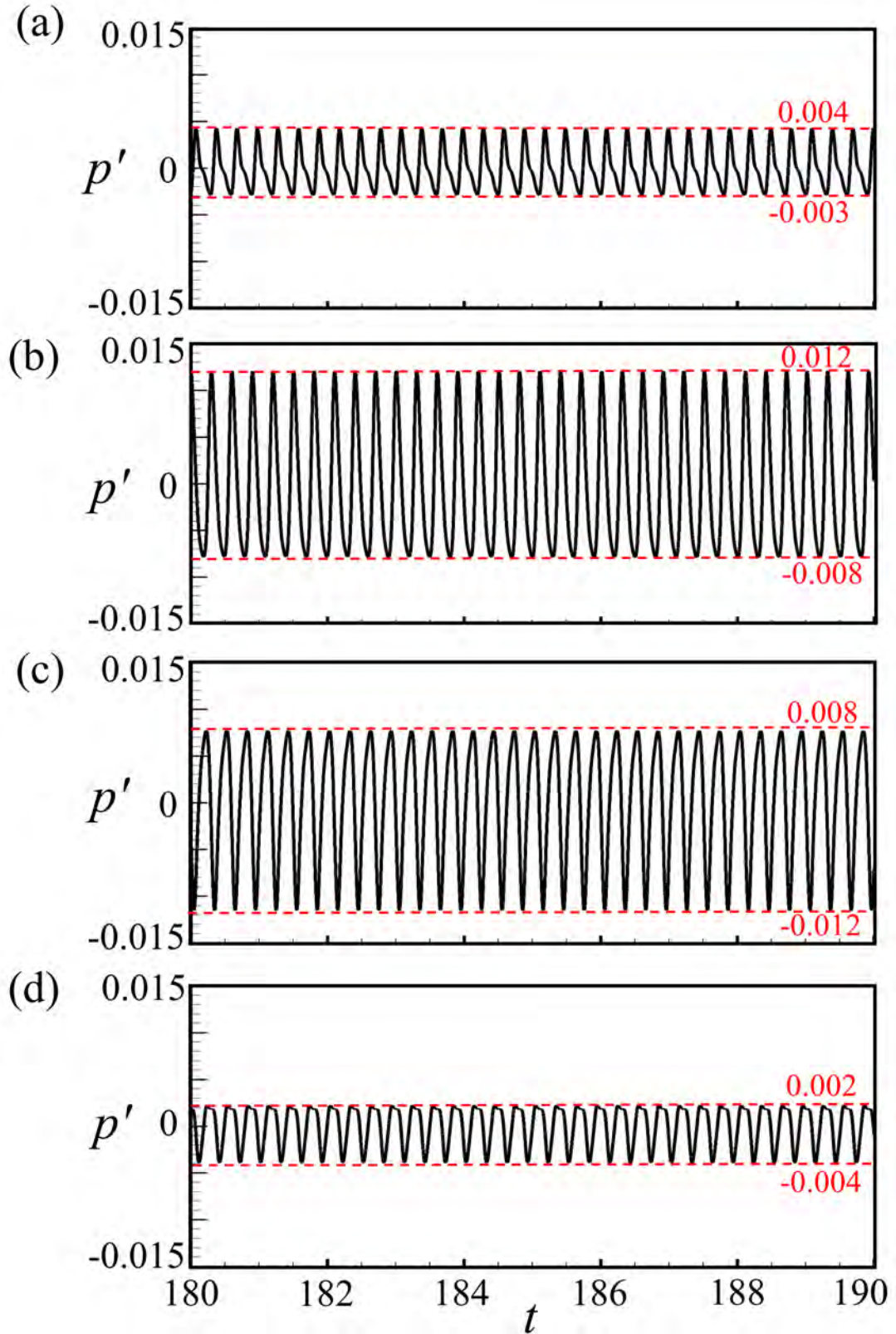


Figure 3.19: Time history of pressure fluctuations at different azimuth locations. (a) $\theta = 45^\circ$, (b) $\theta = 135^\circ$, (c) $\theta = 225^\circ$ and (d) $\theta = 315^\circ$. The horizontal red dashed lines indicate maximum and minimum values.

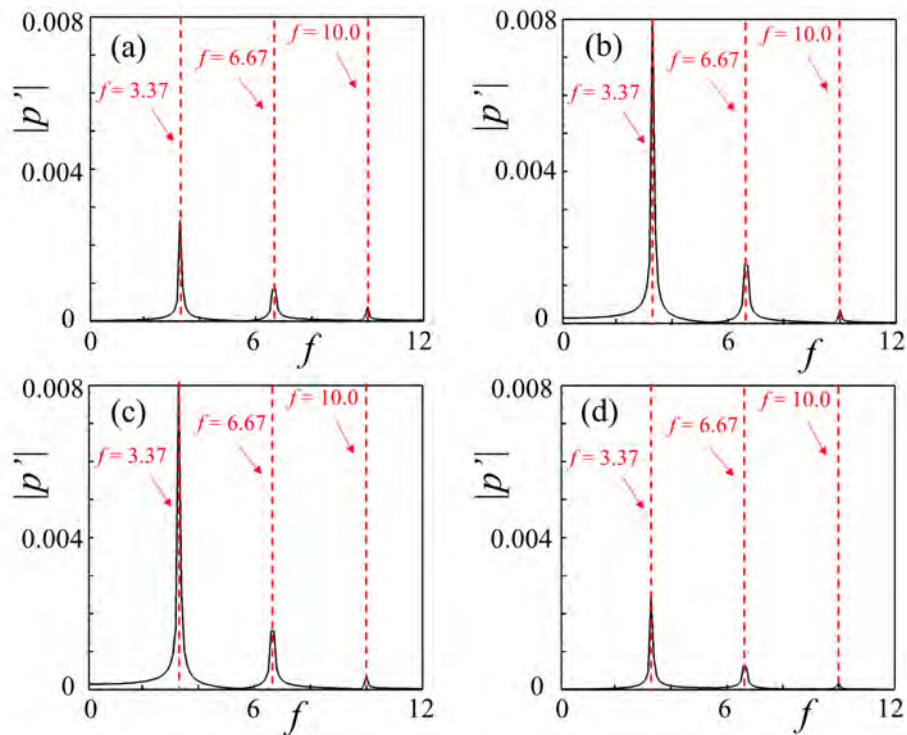


Figure 3.20: FFT spectra of p' at $r = 3$ for different azimuth locations. (a) $\theta = 45^\circ$, (b) $\theta = 135^\circ$, (c) $\theta = 225^\circ$ and (d) $\theta = 315^\circ$.

ignored as the contamination of aerodynamic pressure fluctuations right downstream of airfoil trailing edge makes the determination of acoustics there inaccurate. Due to the Doppler effect, the magnitude of sound waves increases in the upstream direction, whereas the magnitude reduces in the downstream direction (Crighton 1975). As a result, the directivity pattern of sound waves is affected and the propagation angle of sound pressure waves is shifted towards upstream. Hence, the noise radiation patterns in the figures look like dipoles skewed towards upstream with stronger radiation from the airfoil suction surface than pressure surface where the strongest radiation goes along $\theta \sim 130^\circ$ and 220° respectively.

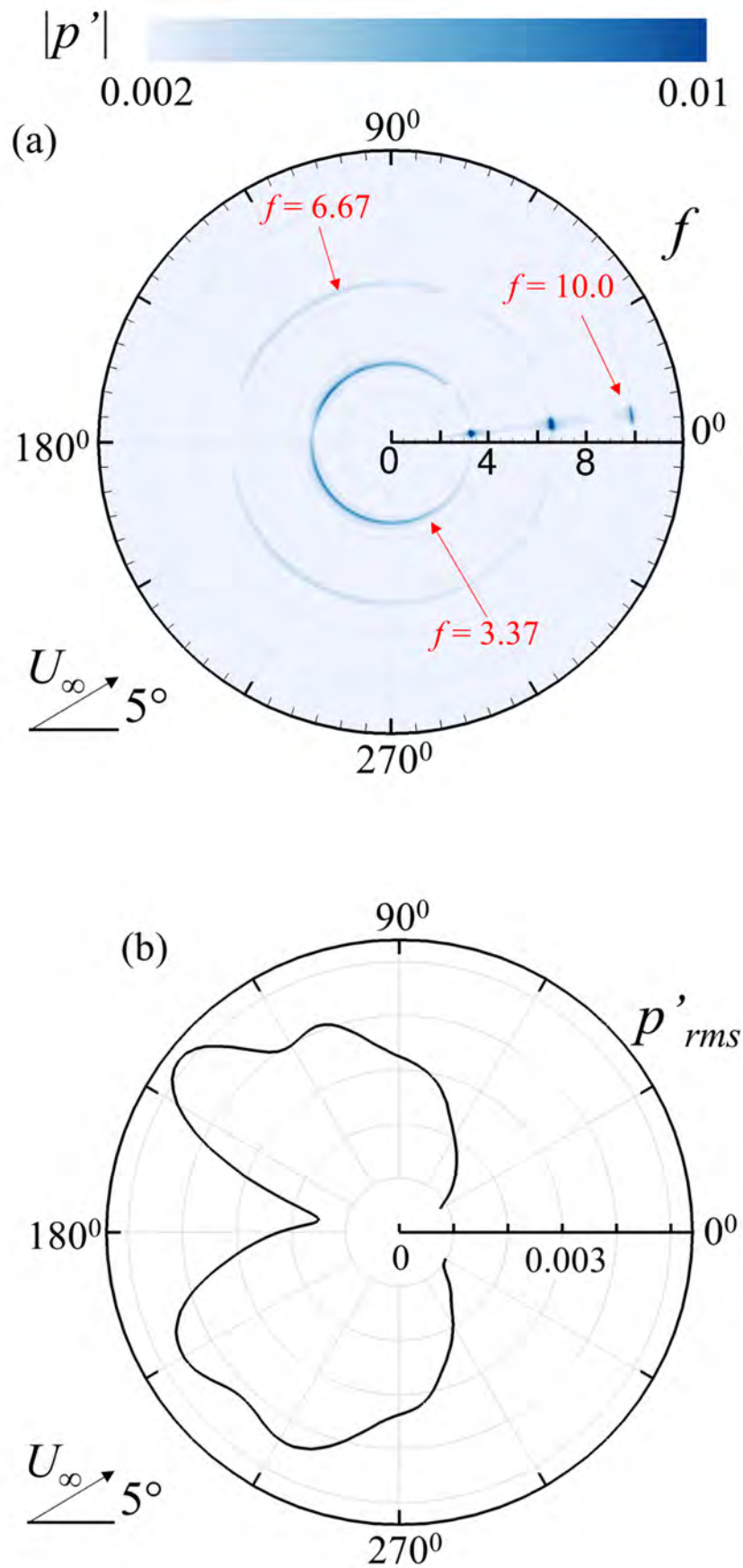


Figure 3.21: (a) Azimuthal spectrum of acoustic fluctuations p' at $r = 3$; and (b) directivity of p' spectrum at $r = 3$.

3.4 Conclusions

In this chapter, a comprehensive detail on the numerical setup including airfoil profile, domain setup, and grid generation is presented. Grid independence study is also carried out and the results are compared with the literature for validation of our numerical scheme (Jones 2008). It is observed that the numerical solutions from G2 and G3 are almost identical and the results appear independent of grid size for these two grid configurations. Also, the results obtained from G2 and G3 show excellent agreement with literature (Jones et al. 2008). However, a significant deviation in the numerical results was observed for G1. Hence, a refined grid G2 with a total quadrangular mesh size of 6.52×10^6 is selected due to its best compromise between accuracy and optimum requirement of computational resources.

In the latter half of this chapter, DAS analysis for rigid airfoil is presented for NACA 0012 airfoil at flow condition of $M = 0.4$, $AoA = 5^\circ$ and a low $Re = 5 \times 10^4$. The FFT spectrum reveals that the natural airfoil boundary layer growth is dominated by the fundamental frequency $(f_{bl})_0 = 3.37$ along with its first and second harmonics observed $(f_{bl})_1 = 6.67$ and $(f_{bl})_2 = 10.0$ respectively with much lower magnitudes. The flow behavior within the boundary layer over the suction surface at the fundamental frequency of natural instabilities $(f_{bl})_0$ shows interesting characteristics which would help in design of elastic panel for tonal noise reduction in the following chapters. Furthermore, the noise generation mechanism is analyzed in detail where the unsteady hydrodynamic flow over the airfoil exhibits the emergence of vortices from the separated shear layer on the suction surface and its subsequent passage over the trailing edge of airfoil into the wake which results in generation of discrete tones. The polar FFT spectrum indicates that the fundamental frequency of naturally growing flow instabilities within the boundary layer which scatters at the trailing edge is the dominant

acoustic source for the current configuration.

Chapter 4

Assessment of Airfoil Tonal Noise Reduction Potential using Perturbation Evolution Method

4.1 Introduction

In this chapter, a complete methodology of elastic panel design for airfoil configurations is developed and the noise reduction potential with panel is evaluated using PEM. In principle, the feasibility of an elastic panel design for airfoil tonal noise reduction can be explored in detail with DAS (e.g. Lam et al. (2014a)) or such sophisticated experimental techniques as in Arcondoulis et al. (2019). However, it is too prohibitive in extensive deployment of resources and time to search for an optimal design with these approaches within the vast design space of multiple panel physical parameters. Therefore, the PEM discussed in Chapter 2 is employed here as it allows much quicker panel design iterations with inputs of reasonable approximation of key noise production physics. It is worth noting that the proposed PEM technique takes barely 10% of the computing time of

DAS. It is a quicker way for studying the variation of the aeroacoustic feedback loop with various panel designs.

4.1.1 Design of Elastic Panel

As the primary goal of the present study is to design and employ an elastic panel flush-mounted on airfoil surface for reduction of tonal noise through fluid-structure interactions, it is imperative to develop a complete panel design methodology for the proposed approach that can be applied to any flow condition. The design of an elastic panel is based on different parameters such as its material, length, and structural properties; hence, these parameters must be carefully selected to achieve the optimum panel performance in tonal noise reduction. In the present study, a complete panel design methodology is formulated such that the proposed approach of utilizing the elastic panel can be applied at any flow condition.

For the design of an elastic panel, three major characteristics are required to be ascertained, namely, panel length, its location, and structural properties. Each of these parameters requires certain flow field knowledge from rigid airfoil flow characteristics for its selection and are discussed in this section.

4.1.1.1 Panel Location

One of the most important requirements for the implementation of the proposed approach is to ascertain the panel location over the airfoil suction surface as the panel is designed to be excited by the growing boundary layer instability convecting over it in such a way that the flow perturbation energy is effectively converted to sustain panel vibration. In this manner, the flow fluctuation energy can be expended to sustain panel vibrations which would help in reduction of kinetic energy of hydrodynamic fluctuations left for ultimate scattering at airfoil trailing

edge. Hence, the panel location must be set at a location where flow fluctuation energy is high and helps in panel vibration in the desired modal behavior. The choice of panel location is aided by the knowledge of flow characteristics of the natural boundary layer of the rigid airfoil flow which is already evaluated by the DAS analysis in Chapter 3. The FFT spectrum along a contour well close parallel to airfoil suction surface determined in Figure 4.1 reveals that the natural airfoil boundary layer growth is dominated by two frequencies, namely the fundamental $(f_{bl})_0 = 3.37$ and the first harmonic $(f_{bl})_1 = 6.67$. The distribution of the amplitudes of velocity fluctuation v' at $(f_{bl})_0$ and $(f_{bl})_1$ along airfoil chord is shown in Figure 4.1. Both amplitudes start to increase at $x \geq 0.27$ and grow within $0.4 \leq x \leq 0.45$. The amplitude of $(f_{bl})_0$ grows remarkably to reach its plateau of 0.0425 at $x \sim 0.5$, stays there up till $x \sim 0.57$, then drops rapidly to a dip at $x \sim 0.65$, and eventually grows mildly again. The amplitude of $(f_{bl})_1$ appears to grow in a more gradual fashion and fluctuates mildly around a value of 0.0125 beyond $x \sim 0.57$.

Based on the spatial growth characteristics of the flow instabilities within the boundary layer over the suction surface of airfoil, three different panel locations are selected. The first configuration EP1 is designed with an elastic panel located at 40% chord on airfoil suction surface corresponding to the rapid growth of instability within boundary layer. In the second configuration EP2, the elastic panel is placed at 45% chord location corresponding to fully established/maximum flow instability, and the last configuration EP3 is designed with an elastic panel placed at 90% chord near the airfoil trailing edge to study the feasibility of reducing flow fluctuation energy just before its scattering as airfoil noise.

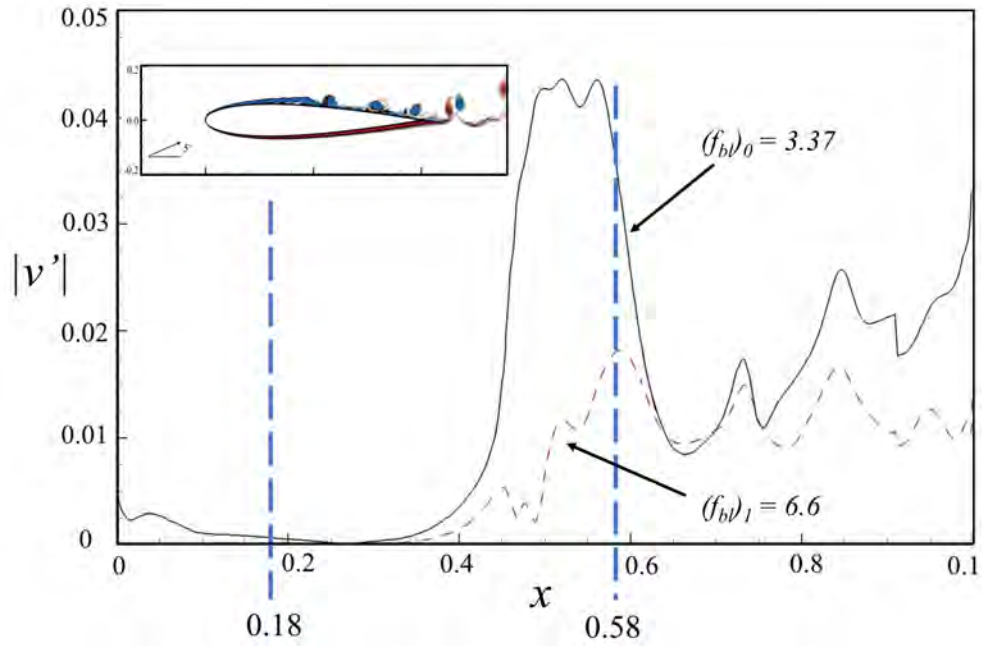


Figure 4.1: Spatial growth of flow instability with a snapshot of vorticity distribution. The two blue dashed lines show the extent of separation bubble. The small figure shows snapshot of the flow.

4.1.1.2 Panel Length

Most of the existing airfoil tonal noise reduction methods are based on geometric modifications of the airfoil (Geyer et al. 2010, Hansen et al. 2012, Wang et al. 2017b, Wang 2018). As a result, the overall airfoil aerodynamics is also affected due to these modifications which certainly limit their applicability in real-world environment. To overcome this limitation, the proposed approach of utilizing an elastic panel for airfoil tonal noise reduction is aimed to locally absorb the energy from boundary layer insatiabilities to sustain its vibration without affecting the overall flow dynamics, such that the airfoil aerodynamic characteristics remain unaffected. Hence, the length of panel is required to be minimal so that the radius of curvature over the airfoil suction surface is not affected. Also, Luk et al. (2004) and Leung and So (2001) observed that the maximum vibration of an

elastic airfoil can be achieved when the length of chord is set comparable to the wavelength of oncoming flow excitation. Based on these factors, the length of panel is set to 5% of chord which is comparable to the length of $(f_{bl})_0$ amplitude plateau as observed in Figure 4.1. Furthermore, it is important to make sure that the mounting of each panel does not distort the airfoil profile locally. Hence, the offset of each panel from local radii of curvature δ_{EP} can be calculated by:

$$r(x) = \frac{\sqrt[3]{(1 + (dy/dx)^2)}}{|d^2y/dx^2|} \quad (4.1)$$

where $y = y(x)$ is the NACA 0012 profile. The values of δ_{EP} for various panel designs are evaluated and listed in Table 4.1. It can be observed that the panel offset is negligible as compared to airfoil chord so that the streamlines of base flow in proximity of panels can be considered effectively unaltered. A schematic sketch of the flow problem and locations of elastic panels in various designs are shown in Figure 4.2.

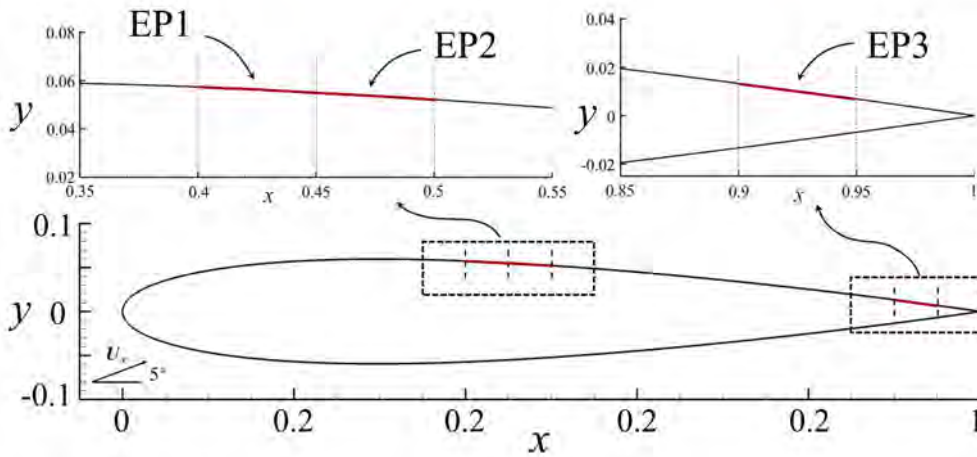


Figure 4.2: Schematic sketch of the flow problem and the locations of elastic panels.

4.1.1.3 Structural Properties

The nonlinear dynamic response of the elastic panel is modeled by solving the one-dimensional plate equation to the simplest approximation (Dowell 1975). The normalized governing equation for panel displacement is already presented in Chapter 2 and can be written as:

$$S_{\text{EP}} \frac{\partial^4 w}{\partial x^4} - (T_{\text{EP}} + N_{\text{EP}}) \frac{\partial^2 w}{\partial x^2} + \rho_{\text{EP}} h_{\text{EP}} \frac{\partial^2 w}{\partial t^2} + C_{\text{EP}} \frac{\partial w}{\partial t} + K_{\text{EP}} w = p_{ex} \quad (4.2)$$

The panel dynamic equation (Equation (4.2)) is solved by the standard finite difference method. The nonlinear coupling between flow fluctuation and panel structural dynamics is resolved with a monolithic scheme developed by Fan et al. (2018a). In essence, the scheme treats the fluid/panel system as a single entity and includes the effects of panel dynamics in an extra source term in the CE/SE numerical model which is then solved with a Newton iteration method.

The natural frequencies of a strongly coupled structure–fluid system are dependent on the bounded/unbounded fluid loading. For the type of short elastic panel considered in this study, the structural wavenumber is higher than acoustic wavenumber, so the fluid would exert an inertial loading on the structure. As a result, the natural frequency of the panel would be slightly lower than its in-vacuo value (Fahy and Gardonio 2007). The panel natural frequency f_{EP} for normal mode should include the effect of added mass (Dugundji et al. 1963). The in-vacuo natural frequency f of a rectangular elastic panel fixed from both ends can be calculated by:

$$f_{(n,m)} = \frac{a_{\text{EP}}}{2} \sqrt{\left(\frac{n}{L1}\right)^2 + \left(\frac{m}{L2}\right)^2}, \quad (4.3)$$

where $L1$ and $L2$ are the panel length and width respectively, whereas n and m are their respective modes. The speed of transverse waves on the panel a_{EP} can be defined as:

$$a_{EP} = \sqrt{\frac{T_{EP}}{\rho_{EP}h_{EP}}}, \quad (4.4)$$

where T_{EP} is the external tensile stress per unit length. In a two-dimensional flow problem, the panel with no structural damping and bending stiffness behaves like a one-dimensional membrane, so Equation 4.4 can be further simplified as:

$$f_n = \left(\frac{n}{2L_{EP}}\right) \sqrt{\frac{T_{EP}}{\rho_{EP}h_{EP}}} \quad (4.5)$$

The frequency of panel calculated by the above formulation does not cater the effect of fluid loading on the panel. Therefore, for the calculation of natural frequency of panel in the presence of flow field $(f_{EP})_n$, an added mass term is introduced (Fahy and Gardonio 2007, Dugundji et al. 1963):

$$(f_{EP})_n = \frac{f_n}{\sqrt{\left(1 + \frac{A_m}{\rho_{EP}h_{EP}}\right)}} \quad (4.6)$$

where, $A_m = (\rho_{\infty}L_{EP}/\pi n)$ is the added mass per unit length. Equation 4.6 can be further written in the desired form as:

$$(f_{EP})_n = \frac{n}{2L_{EP}} \sqrt{\frac{T_{EP}}{\rho_{EP}h_{EP}}} / \sqrt{1 + \frac{L_{EP}}{\pi n \rho_{EP}h_{EP}}} \quad (4.7)$$

Two types of panel structural properties are set. One type is set to make one of its natural modal frequencies almost the same as the dominant $(f_{bl})_0$ so that flow-induced panel resonance is likely to occur (designated with a subscript 'R'). The resonant panels in this study are designed to resonate at their third natural mode with the dominant frequency of the natural boundary layer instabilities. Basically, the panel modal shape does not effect the noise reduction performance; provided that the resonance condition is achieved. The choice of third mode in this study is based upon the practical considerations of the panel thickness,

Table 4.1: Listing of normalized elastic panel parameters. Stainless steel is assumed for material properties.

Case	Geometrical parameters				Material properties		Panel natural frequency			
	x_{EP}	δ_{EP}	L_{EP}	h_{EP}	T_{EP}	ρ_{EP}	$(f_{EP})_1$	$(f_{EP})_2$	$(f_{EP})_3$	
Non-resonant panel	EP1 _{NR}	0.40	9.2×10^{-5}							
	EP2 _{NR}	0.45	7.96×10^{-5}	0.05	0.009	4.023	6367.35	2.6453	5.2909	7.9366
								(79%)	(157%)	(236%)
EP3 _{NR}	0.90	4.51×10^{-5}								
Resonant panel	EP1 _R	0.40	9.2×10^{-5}							
	EP2 _R	0.45	7.96×10^{-5}	0.05	0.009	0.725	6367.35	1.123	2.246	3.369
								(33%)	(67%)	(100%)
EP3 _R	0.90	4.51×10^{-5}								

density and tension. The second type of panel is set with any of its natural modal frequencies distant from any f_{bl} so that panel resonance is avoided (designated with a subscript 'NR'). The details of all panel parameters set for the present study are given in Table 4.1.

4.2 PEM Analysis

4.2.1 Base Flow

In the absence of any introduced perturbation \mathbf{U}_{base} has to remain unchanged when it is marched with Equation (2.73) over a long time; otherwise, the solution will be driven by the evolution of base flow itself due to rapid solution divergence rather than by the intended evolution of flow instability characteristics. Jones et al. (2010) attempted different ways of producing base flow solutions for their stability analysis. They found that the time average of flow solution produced

by direct simulation of the original problem is a promising choice. The unsteady solution is fully validated and shown able to accurately reproduce all the key tonal noise generation features reported in previous numerical studies by means of compact finite difference calculation (Jones et al. 2008, 2010). For the base flow in the present study, thirty cycles of the DAS time stationary solution are taken and averaged in time to produce the base flow solution \mathbf{U}_{base} (Figure 4.3(a) and 4.3(b)). The quality of \mathbf{U}_{base} is checked by solving it as initial condition with Equation (2.78) in the absence of any flow perturbation. The deviation of flow solution from initial \mathbf{U}_{base} at different key locations is shown in Figure 4.3(c). Very little deviation prevails in the beginning of the calculation which promptly becomes saturated with a relative numerical error level well below 10^{-10} . This error level is five orders of magnitude weaker than the introduced excitation amplitude and, as shown clearly in subsequent discussions, is around six orders of magnitude weaker than the PEM solution. Therefore, the \mathbf{U}_{base} adopted is considered to satisfy the requirement $\partial\mathbf{U}_{base}/\partial t \sim 0$ effectively.

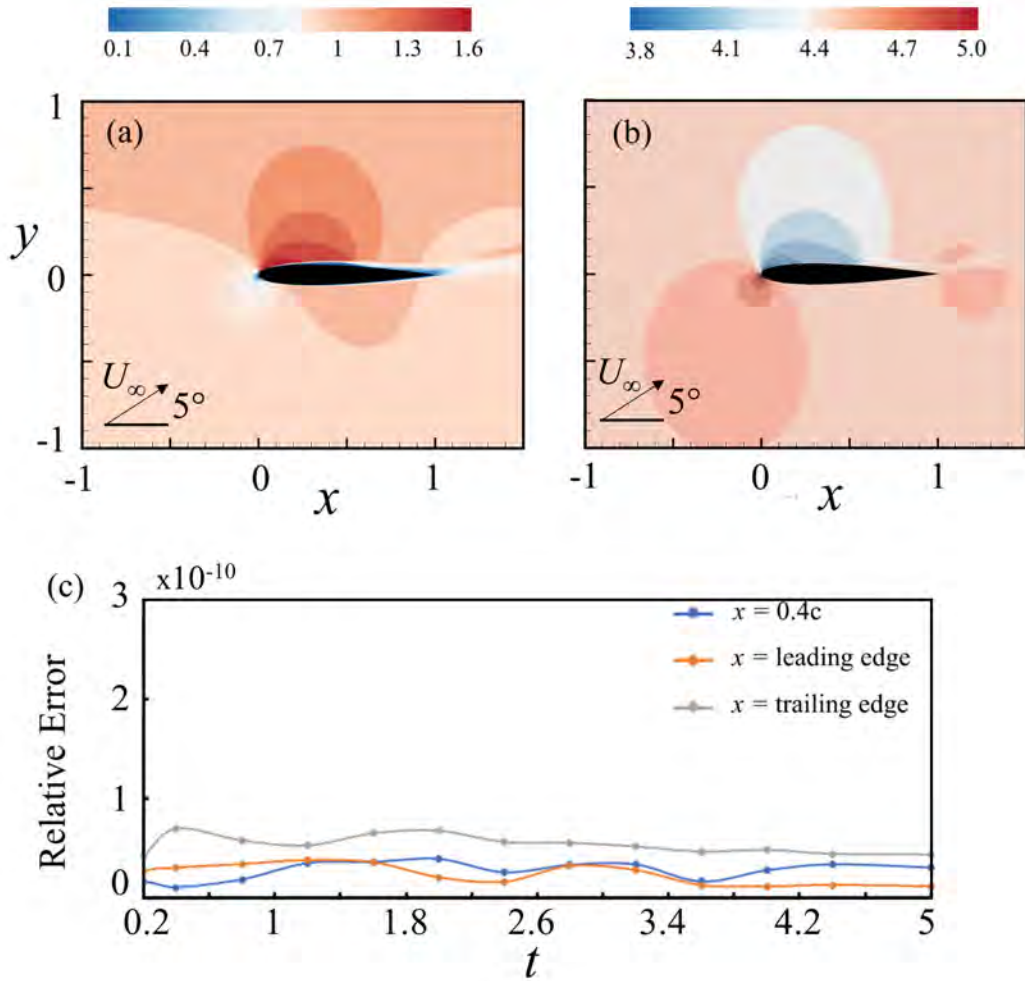


Figure 4.3: Steady base flow of RS case. (a) Distribution of total velocity. (b) Distribution of pressure. (c) Relative error of pressure from initial flow solution at $(x, y) = (0.4, 0.07)$, $(0,0)$ and $(0,1)$.

4.2.2 Perturbation

As discussed in Chapter 2, the prescription of weak perturbation for initiating the evolution of flow instability requires careful consideration in PEM. Jones et al. (2010) applied local periodic volume forcing within the airfoil boundary layer. Alternatively, Fosas de Pando et al. (2014) made use of an artificial weak divergence-free Gaussian perturbation released at an upstream location very close

to the airfoil as the external excitation. Both ways allowed the artificial perturbation to convect freely with the evolution of numerical solution to hit the airfoil leading edge and produce the actual flow perturbations required for subsequent analysis.

A similar method is adopted by introducing a weak Gaussian perturbation near the airfoil leading edge for PEM analysis as described in Chapter 2. The evolution of flow instability in terms of velocity fluctuation v' over the panel within the airfoil suction surface boundary layer is shown in Figure 4.4(a). The perturbation initiates a wavepacket due to flow instabilities and is convected downstream until it reaches the trailing edge of airfoil where it scatters as acoustic waves. The acoustic wave propagates upstream, hits the separation point and produces a stronger second wavepacket with an interval (Figure 4.4(a)). It is important to realize that this wavepacket is triggered by the receptivity of boundary layer to free-stream disturbances originated downstream. It is stronger than the first one produced by the perturbation and subsequently scatters a stronger acoustic wave back to separation point to close the aeroacoustic feedback loop. The feedback loop continues and generates subsequent wavepackets with regular interval as shown in Figure 4.4(a) which is similar to the phenomenon observed by Jones et al. (2010). However, the panel must vibrate continuously to effectively absorb flow fluctuation energy. Therefore, it is imperative that the panel vibration follows the designed criteria and sustains the vibration in designated mode. It is observed that the panel vibration is favourable and effective for the time interval (A) when the wavepacket convects over the airfoil. However, the panel motion almost vanishes during the time interval (B) between the generation of next wavepacket due to feedback loop (Figure 4.4(b)). Whilst the perturbation is able to induce the occurrence of the aeroacoustic feedback loop as reported in previous studies, it is only able to induce the panel to give a vibration in every

cycle of feedback rather than sustaining a continuous vibration throughout the entire feedback loop process. Hence, excitation by a Gaussian perturbation could not be utilized in the present situation.

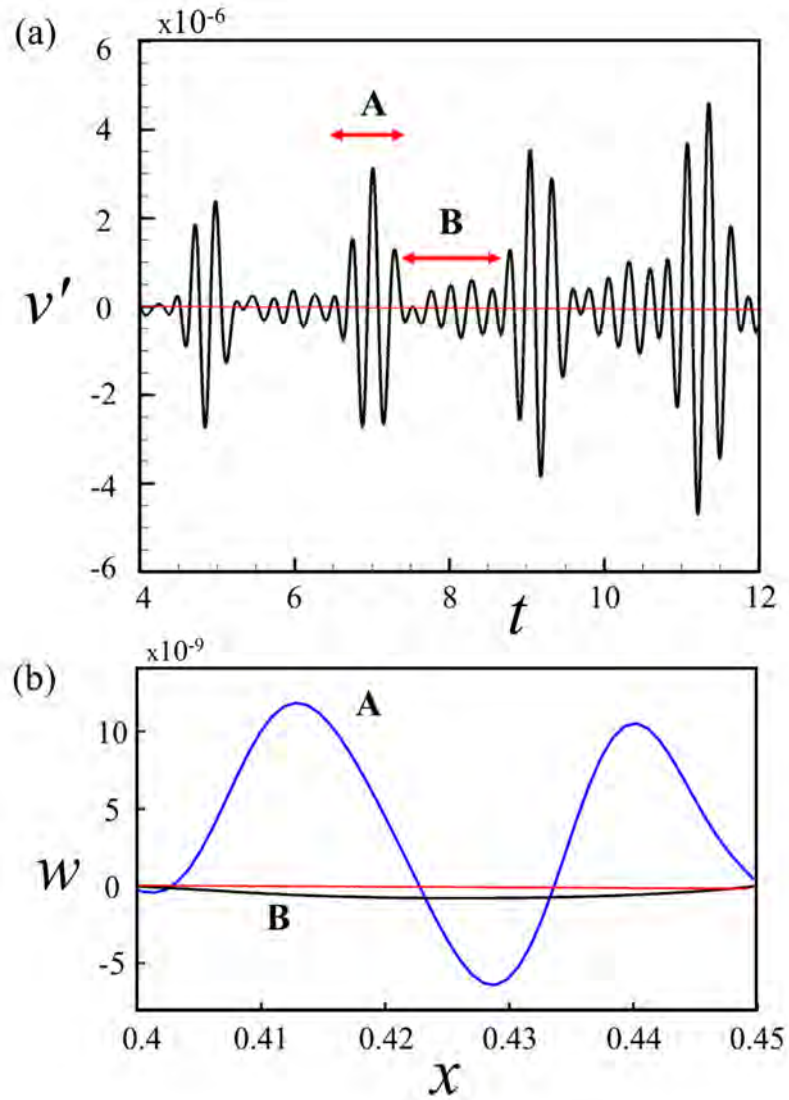


Figure 4.4: PEM analysis excited by a Gaussian perturbation. (a) Evolution of transverse velocity fluctuations v' over panel. (b) Snapshots of panel displacements at maximum v' during intervals A and B. A thin red line is drawn at $y=0$ for reference.

The method is changed to utilize broadband acoustic excitation in the PEM analysis which can effectively produce weak perturbations within the flow continuously. Such excitation also mimics the continuous excitation experienced in actual flow past airfoil (Jones et al. 2010). The broadband acoustic excitation function is defined as:

$$p'_{inc} = p_A \sum_{n=1}^{100} \sin(2\pi t f_{exc,n} + \phi_n), \quad (4.8)$$

where p_A is pressure amplitude which is constant to wide range of frequencies $f_{exc,n}$ ranging from 0.1 to 10 with a uniform spacing of $\Delta f_{exc,n} = 0.1$, and random phase ϕ_n . A weak excitation of $p_A = 10^{-5}$ is introduced near the leading edge of airfoil at a location $(x, y) = (-0.015, -0.01)$ to generate weak artificial perturbations. When the acoustic excitation interacts with leading edge of airfoil, a downstream travelling wavepacket over the airfoil suction surface is generated. As a result of broadband nature of excitation, it would excite a number of panel natural modal frequencies. However, at the dominant frequency of naturally evolving boundary layer disturbance on airfoil suction surface the flow-induced structural resonance may occur and the panel would respond accordingly. The numerical results show that the selected artificial disturbance is able to maintain its localized flow perturbation properties well during solution time marching. The feasibility of the use of broadband excitation for PEM analysis in the present study is discussed in next section.

4.3 Verification of Proposed Methodology

The effect of elastic panel in each EP case is explored from a comparison of its numerical results with those obtained from its reference calculation with the panel replaced by the original rigid airfoil profile. The latter is labeled as RS. Before

starting the comparison it is important to check if the PEM for RS case is able to reproduce the key physical processes responsible for tonal noise generation. The evolution of flow instability is analyzed in terms of the instantaneous snapshots of distribution of velocity fluctuation v' with a time interval $dt = 0.2$ as shown in Figure 4.5. At $t = 0$, the perturbation strikes the suction surface of the airfoil and a weak wavepacket is generated. The introduced excitation perturbation is convected following a streamline of base flow and initiates a wavepacket triggered by the local inflectional velocity profiles of the base flow. The wavepacket is found to possess similar characteristics of T-S waves as observed in laminar boundary layers over a flat plate (Ruban 1984). The wavepackets further convect towards airfoil trailing edge with increasing magnitude and ultimately scatters to acoustic wave radiating away from surface and pressure sides of the airfoil. The acoustic wave propagates upstream, hits the separation point again and produces another wavepacket. It is important to realize that this wavepacket is triggered by the receptivity of boundary layer to free-stream disturbances originated downstream. The flow instabilities and acoustic wave appear continuously with the repetition of aeroacoustic feedback loops. These observations are consistent with those reported in previous studies calculated with different numerical approaches (Jones et al. 2010, Fosas de Pando et al. 2014). Unlike the case of PEM with weak Gaussian excitation, the broadband excitation is able to produce weak perturbations within the flow continuously which allows the panel to sustain its vibration. The evolution of flow instability clearly indicates that the PEM analysis with broadband excitation is able to capture the aeroacoustic feedback loop responsible for airfoil tonal noise generation correctly and provide a quality reference solution for illustrating the effects of elastic panel. In fact same aeroacoustic feedback loops are also observed in the full DAS calculation of the airfoil in the previous chapter.

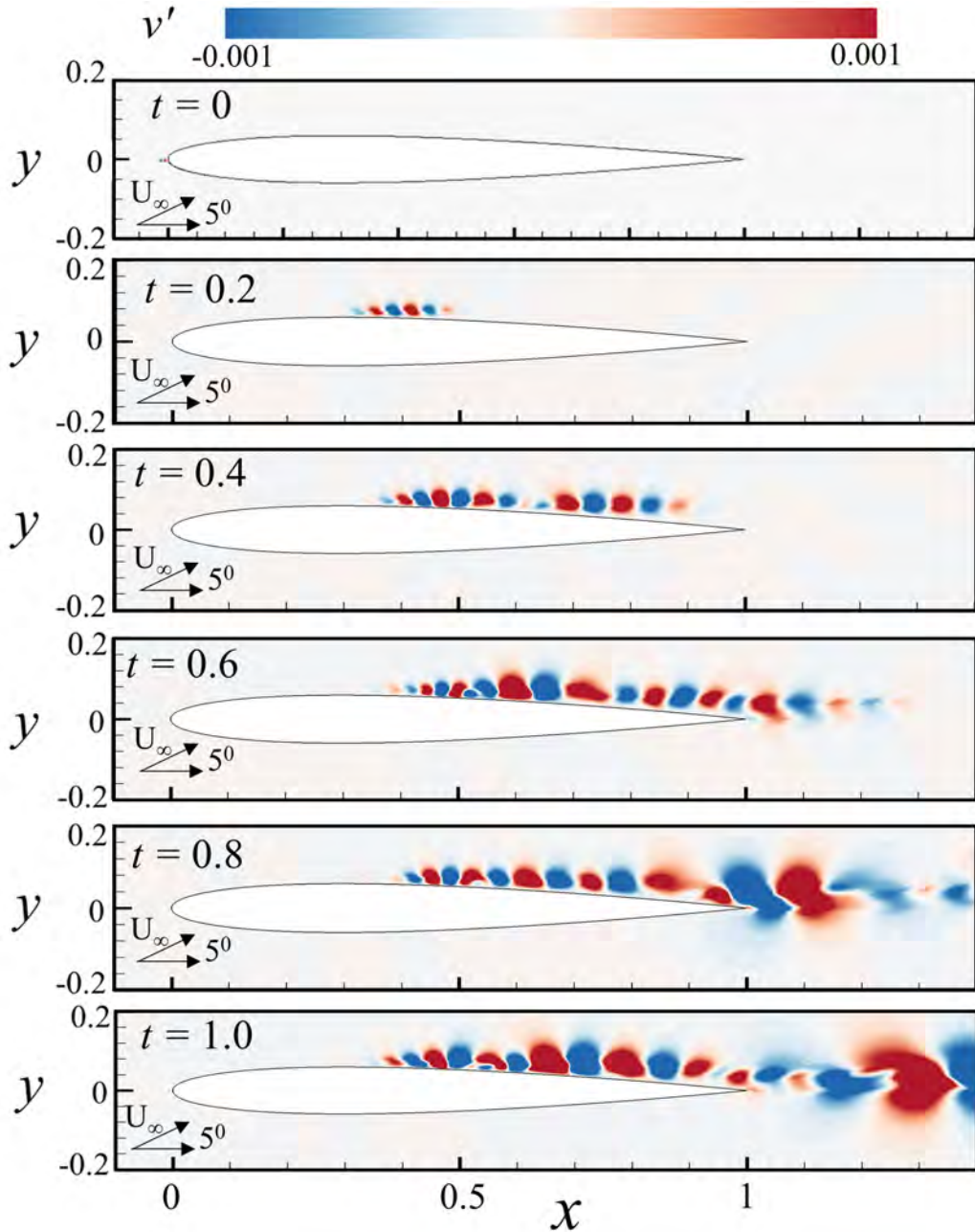


Figure 4.5: Evolution of aeroacoustic feedback loop illustrated with transverse velocity fluctuations v' .

Now an elastic panel is readily installed onto airfoil suction surface for studying its potential for airfoil tonal noise reduction. However, in view of the rationale of proposed design methodology, a base flow with elastic panel installed is generally not known *a priori* as its DAS calculation has not yet been car-

ried out. To circumvent this difficulty it is proposed to adopt the base flow of RS case in PEM calculations of airfoil with elastic panel cases. This choice is based on two assumptions. The first arises from the benefit of the chosen short panel length. The second arises from the fact that the setting of PEM allows the elastic panel to be primarily responsive only to the convecting flow instability and scattered acoustic disturbances whose velocity fluctuation magnitudes are at least two orders of magnitude weaker than the steady base flow. The panel vibration response is expected to follow the same order of magnitude so it should not modify the base flow significantly. It is essential to verify these assumptions before proceeding to an extensive study of noise reduction with various elastic panel designs. For this purpose, an additional DAS calculation is carried out with an arbitrary choice of panel design, (EP1_R). Its base flow solution is obtained from averaging the time stationary solution in time for comparison with RS base flow. Figure 4.6(a) shows the distribution of percentage deviation (i.e. $(EP1_R)_{base} - (RS)_{base} / (RS)_{base}$) between the total velocity fields of two base flow solutions. It shows that there is a modification in the proximity of elastic panel but its deviation is almost two orders of magnitude weaker than the velocity fluctuations obtained from PEM analysis results. No significant difference between mean flows of RS and EP1_R cases is observed. Furthermore, the azimuthal distributions of acoustic p'_{rms} captured at a radius of three chord lengths (i.e. $r = 3$) from trailing edge obtained from PEM and DAS solutions are compared in Figure 4.7 which shows a good qualitative agreement. The levels of noise reduction $\Delta SPL_{reduction} = 20 \times \log_{10} (p'_{rms,EP}/p'_{rms,RS})$ derived from two types of calculations are found in excellent agreement too (Table 4.2). Therefore, all these evidences lend strong concrete support to the adoption of RS base flow as a reasonably good approximation for base flow for PEM calculation of EP cases. The results also reflect that the proposed methodology is able to correctly predict

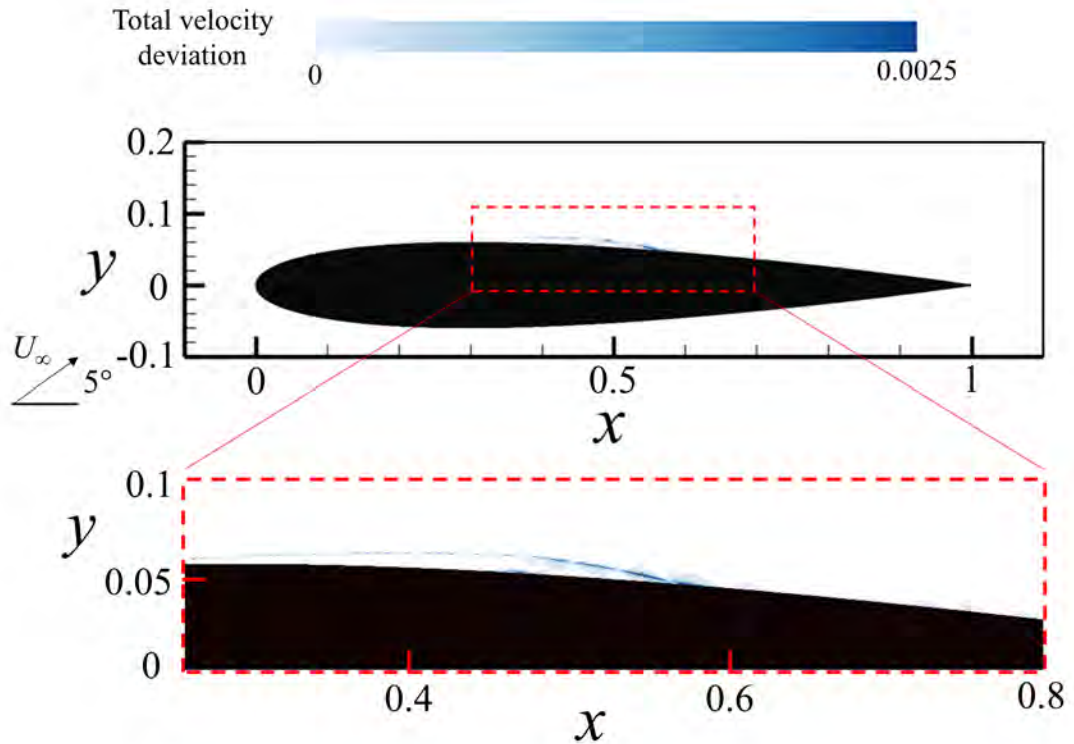


Figure 4.6: Relative percentage deviation (= 0.25%) of total velocity between EP1_R and RS base flow determined from DAS solutions.

the trend of noise reduction by the elastic panel in actual flow by virtue of its capability of capturing the fundamental airfoil tonal noise generation processes as indicated in early discussions. It is worth noting that for the perturbation evolution method a simulation requires a time marching within 10 non-dimensional time units with a time step size of 10^{-5} to reach saturated regime. However, a typical DAS calculation has to march in time over 160-200 non-dimensional time units to reach time stationarity. Hence, a significant saving of more than 90% of actual calculation time is achieved using the PEM.

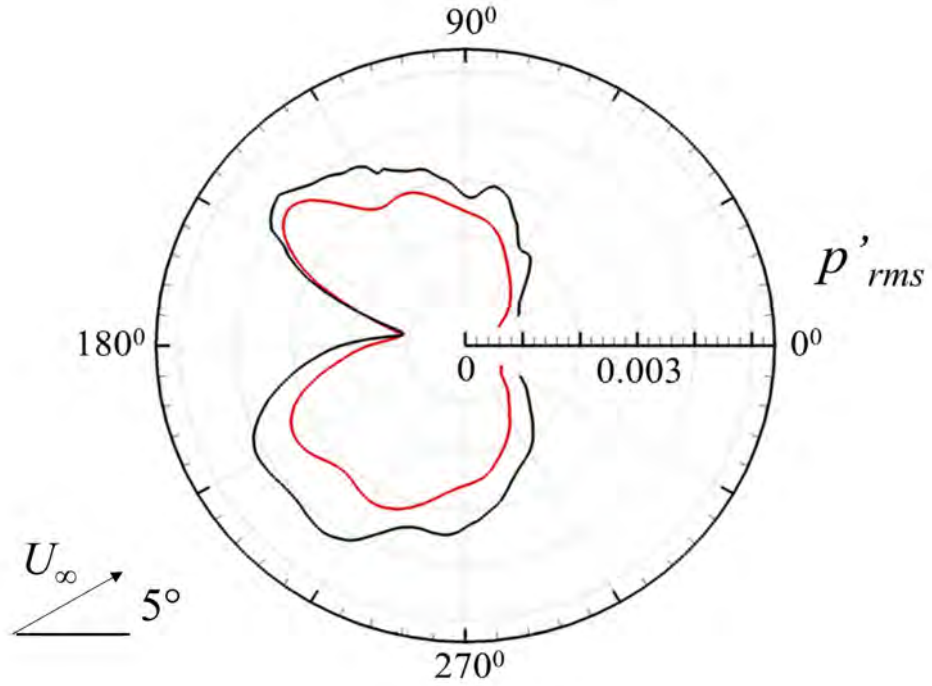


Figure 4.7: Azimuth distributions of acoustic p'_{rms} for EP1_R case. —, from PEM solution; —, from DAS solution.

Table 4.2: A comparison of level of noise reduction of EP1_R case from PEM and DAS solutions.

	PEM result	DAS result
Average $\Delta SPL_{reduction}$	2.10 dB	2.50 dB
Maximum $\Delta SPL_{reduction} / \theta_{max}$	2.40 dB / 130°	3.0 dB / 120°

4.4 Assessment of Noise Reduction by Elastic Panels

The focus of the forthcoming discussions is put in the region around the airfoil trailing edge where the oncoming flow instability scatters into airfoil tonal noise. Figure 4.8 (first row) shows a comparison of transverse velocity fluctuation v' of flow instability captured at $x = 0.99$ from the solutions of non-resonant EP1_{NR} and resonant EP1_R cases during $t = 4-8$ where the feedback loop has been established already. The flow-induced vibration of elastic panel appears to provide continuous suppression of flow instability growth. The extent of instability suppression appears strongly dependent on panel structural properties. It is stronger in case EP1_R than that in case EP1_{NR}. This observation provides good support to the fact that a resonant panel absorbs the flow energy more effectively and leaves less flow distortion for the scattering at airfoil trailing edge. To further illustrate this view, a consistent time window of a single wavepacket in each case is taken and the v'_{rms} values are calculated within this time window of the particular wavepacket. The calculated v'_{rms} values are listed in Table 4.3. The percentage loss of energy from the respective RS case is also given together in the brackets. It is evident that the reduction of flow energy is fairly uniform with a non-resonant panel but it appears to differ in intensity when a resonant panel is mounted. The suppressed flow instability should produce less effective scattering at trailing edge and subsequently lower noise radiation. This inference receives concrete support from the acoustic solutions shown in Figures 4.9(a) and 4.9(b). The acoustic solution within the sector $|\theta| \leq 30^\circ$ is ignored as the contamination of aerodynamic pressure fluctuations downstream of airfoil trailing edge makes the determination of acoustics inaccurate at these locations. These figures show that the noise radiation pattern looks like a dipole skewed towards upstream with

Table 4.3: Effect of the presence of elastic panel on v'_{rms} in EP1, EP2 and EP3 cases.

Location	RS	EP1 _{NR}	EP1 _R	EP2 _{NR}	EP2 _R	EP3 _{NR}	EP3 _R
$x = 0.8$	2.0096×10^{-3}	1.6482×10^{-3}	1.5077×10^{-3}	1.8330×10^{-3}	1.7987×10^{-3}	2.0017×10^{-3}	1.9705×10^{-3}
		(-17.98%)	(-24.97%)	(-8.78%)	(-10.49%)	(-0.39%)	(-1.94%)
$x = 0.9$	2.3637×10^{-3}	1.9091×10^{-3}	1.6910×10^{-3}	2.1919×10^{-3}	2.0173×10^{-3}	2.3259×10^{-3}	2.3160×10^{-3}
		(-19.23%)	(-28.46%)	(-10.23%)	(-14.65%)	(-1.60%)	(-2.02%)
$x = 0.99$	4.6241×10^{-3}	3.4304×10^{-3}	2.9992×10^{-3}	3.9466×10^{-3}	3.7207×10^{-3}	4.4486×10^{-3}	4.4466×10^{-3}
		(-25.81%)	(-35.13%)	(-14.65%)	(-19.53%)	(-3.79%)	(-3.83%)

stronger radiation from airfoil suction surface than from pressure surface. The strongest radiation goes along $\theta \sim 130^\circ$ and 220° respectively. More noise reduction toward upstream is observed than downstream. A resonant panel achieves an average $\Delta SPL_{reduction} \sim 2.1$ dB around most azimuth locations with a maximum reduction of ~ 2.4 dB along $\theta \sim 130^\circ$. However, a non-resonant panel achieves an average of ~ 1.2 dB reduction and its maximum of ~ 1.5 dB only.

The transverse velocity fluctuations v' of flow instability for EP2 cases are shown in Figure 4.8 (second row). Generally similar effects of elastic panel to EP1 cases can still be observed, but the suppression of flow instability is less pronounced even though the elastic panel location coincides with the occurrence of strongest natural boundary layer instability (Figure 4.1). All the flow instability evolution patterns are very similar to EP1 cases (Figure 4.8). The v'_{rms} values are evaluated in the same way as for EP1 cases and the results are shown in Table 4.3. They show transfer of flow energy to vibrating panel but their effectiveness are reduced by half for both non-resonant and resonant panels. The directivity of noise radiation is similar to EP1 cases (Figure 4.9(c)). Fortunately, there is

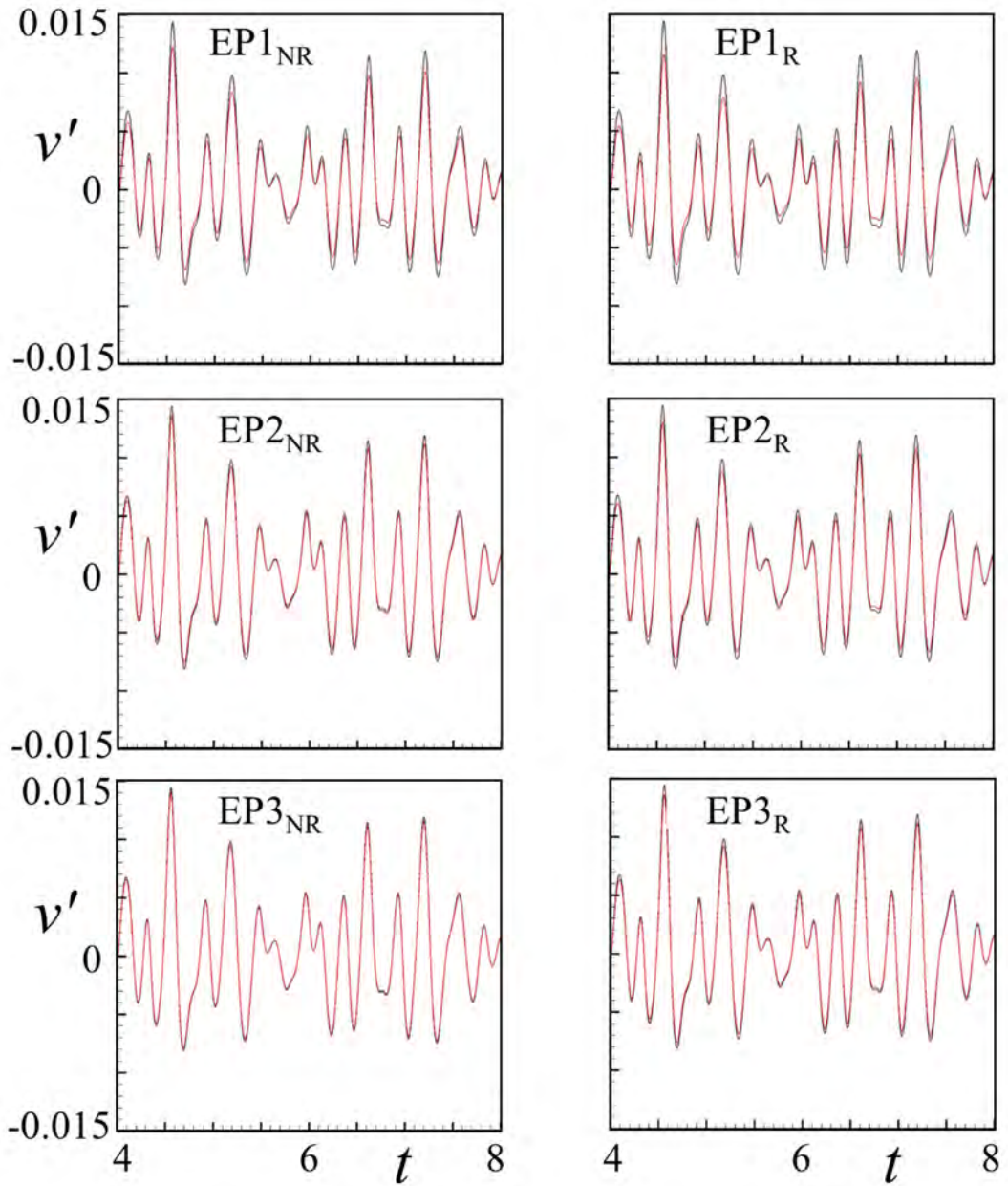


Figure 4.8: Effect of elastic panel on flow instability evolution at 99% chord location. First row, EP1; second row, EP2; third row, EP3. —, with panel; —, without panel (i.e. RS).

still noise reduction as observed in Figure 4.9(d). A non-resonant panel achieves a fairly uniform noise reduction with an average $\Delta SPL_{reduction} \sim 0.45$ dB around the airfoil with a maximum reduction of ~ 0.6 dB but a resonant panel enhances the noise reduction to $\Delta SPL_{reduction} \sim 0.7$ dB with a maximum reduction of ~ 0.84 dB.

Figure 4.8 (third row) shows the transverse velocity fluctuations v' of flow instability for EP3 cases. In contrast with EP1 and EP2 cases, the EP3 panel is at a distance of only 0.05 from airfoil trailing edge and the abrupt change of pressure behind the airfoil trailing edge imposes an irregular growth on the flow instability. The calculated v'_{rms} values for both resonant and non-resonant cases are shown in Table 4.3. The directivity of noise radiation and noise reduction are shown in Figure 4.9(e) and (f). This time the noise radiation gives a different pattern from EP1 and EP2 cases where the reduction as well as amplification in pressure fluctuations can be observed. Both resonant and non-resonant panels provide more or less the same noise reduction pattern with strongest reduction of around 0.5 dB at $\theta \sim 170^\circ$. However, regions around $\theta \sim 50 - 60^\circ$, $\theta \sim 120 - 150^\circ$ and $\theta \sim 180 - 240^\circ$ shows some noise amplification as well. Hence, it implies that the location of panel near the trailing edge of airfoil is not effective in suppressing flow instabilities and can result in noise amplification as well.

4.5 Structural Response of Elastic Panel

The response of elastic panel due to boundary layer instabilities and subsequent fluid-structure interactions for EP1, EP2 and EP3 are shown in Figure 4.10. A snapshot at $t = 6$ is chosen as a reference for all panel configurations based on the moderate fluctuations at this instance observed in v'_{rms} plots. The design parameters for resonant panel are set in a manner that flow-induced structural resonance occurs at the third natural mode as already shown in Table 4.1.

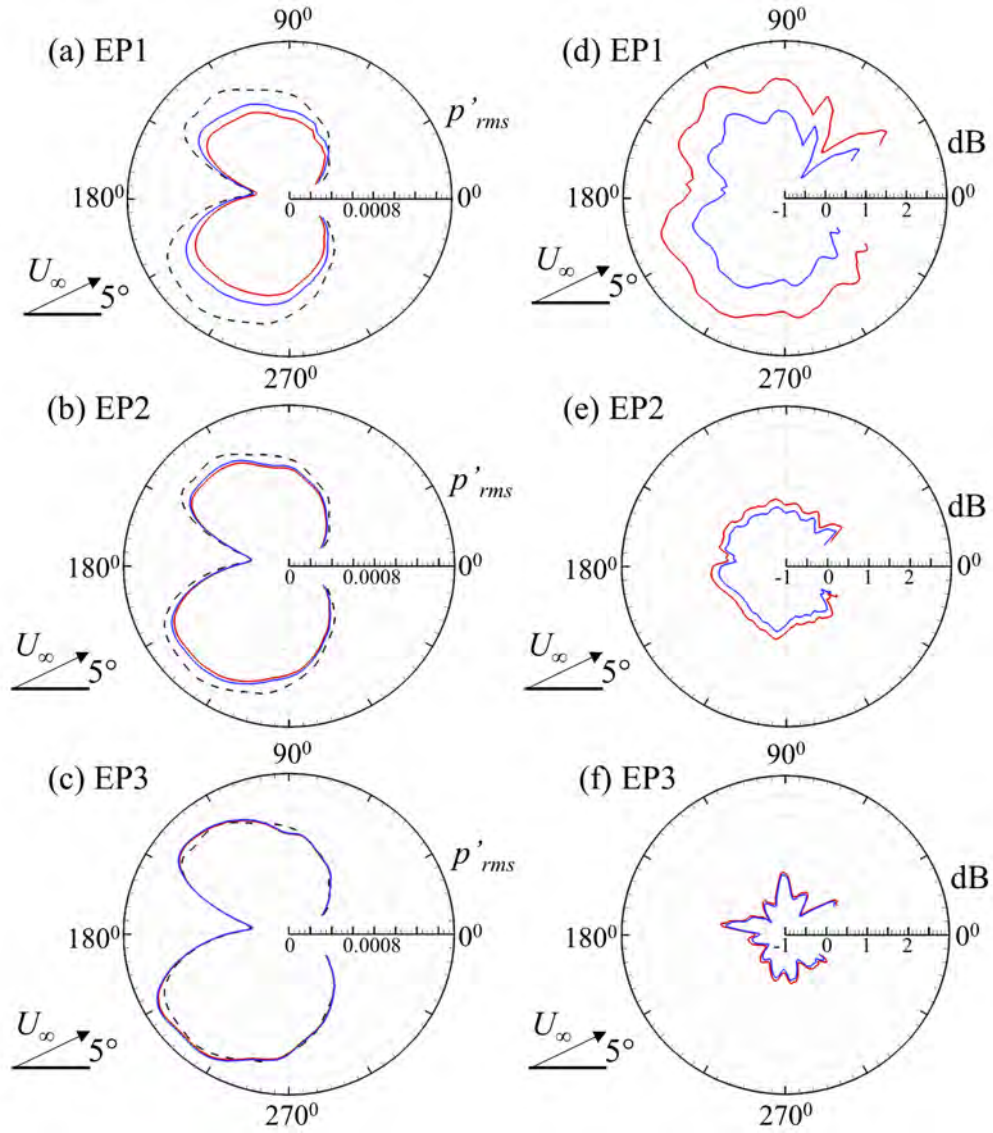


Figure 4.9: Effect of elastic panel on noise generation. (a), (c) and (e) distribution of p'_{rms} ; (b), (d) and (f) $\Delta SPL_{reduction}$. —, with resonant panel; —, with non-resonant panel; - - -, RS cases.

It is evident in Figure 4.10(a) that EP1_R vibrates at its third natural mode with stronger amplitude as compared to the first mode for EP1_{NR}. The fact that EP1_R vibrates in the desired third natural mode validates the panel design methodology to achieve structural resonance in the presence of fluid loading on the panel. Since the panel tension for EP1_R is much lower than EP1_{NR} whose frequency is closest to $(f_{bl})_0$. It implies that the resonant panel is able to effectively absorb more energy from the oncoming flow to sustain its resonance condition. The resulting phenomenon helps in the weakening of T-S waves instabilities within the laminar boundary layer, which ultimately helps in the reduction of noise level due to trailing edge scattering. Similar features can be observed for EP2 in Figure 4.10(b). The elastic panel EP2_R vibrates at its third mode as designed but the noise reduction is much weaker than EP1_R. Although the resonant panel allows the transfer of energy from the incoming flow, its effectiveness is relatively reduced as boundary layer instability is the strongest at this panel location which is already indicated in Figure 4.1. Hence, it poses an opportunity for further investigation in design of panel with better characteristics without inducing other undesired instabilities such as flutter or divergence. Figure 4.10(c) shows a similar pattern for both EP3_R and EP3_{NR}, but there exists a non-uniformity in panel response in terms of amplitude and mode shape for both resonant and non-resonant panels. This non-uniform vibrational response possibly explains the reason for low noise level reduction and even amplification for both resonant and non-resonant panel configurations at different azimuth locations as observed in Figure 4.9(f).

Time histories of panel velocity for elastic panels at center location of each panel are plotted and shown in Figure 4.10 (right column). A time episode of 6-10 time units is chosen for brevity as the panel has sustained sufficient vibrational velocity during this period. It can be observed that EP1_R, EP2_R and EP3_R have

much higher vibrational velocities than their non-resonant counterparts. Furthermore, the magnitude of velocity for EP1_R is much higher than EP2_R and EP3_R. Hence, it is able to absorb much higher energy from the hydrodynamic instabilities to sustain its vibration than EP2_R and EP3_R. Also, the vibrational behavior of all resonant panels is observed to be periodic. Hence, the resonant panels can sustain the dynamical behavior in their designed mode. Therefore, it can be easily ascertained that the resonant panels are much better choice for tonal noise reduction for the present study.

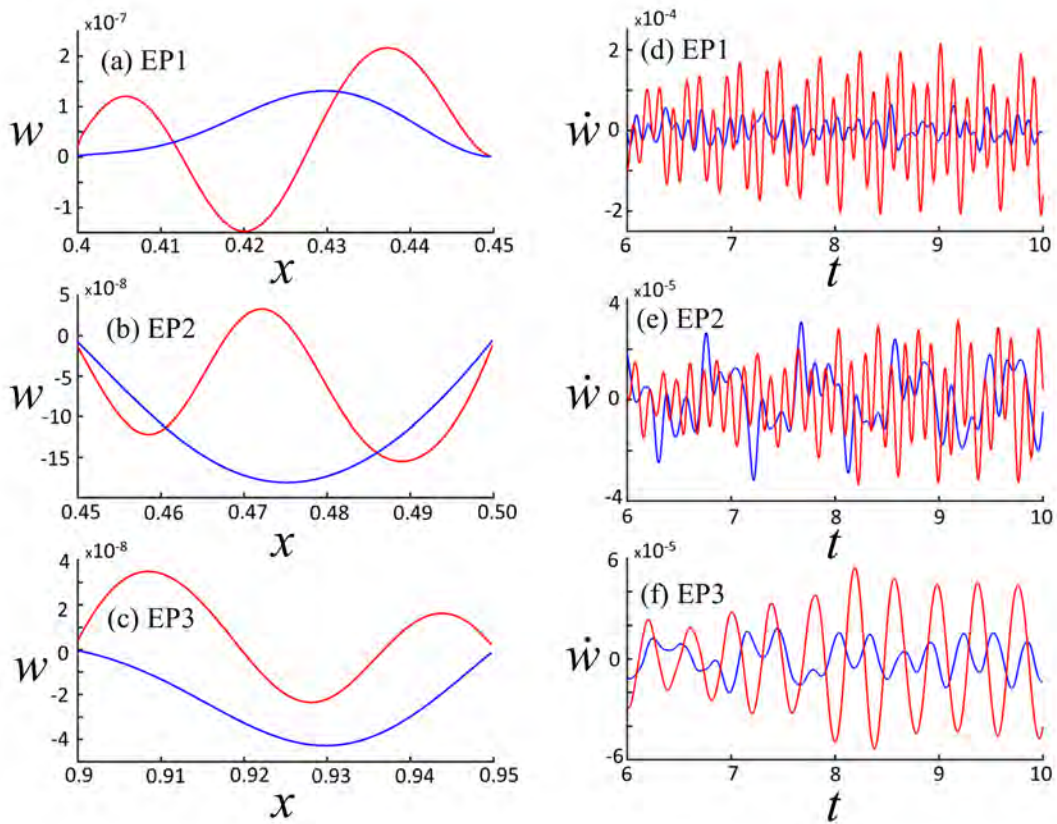


Figure 4.10: Vibratory responses of elastic panels. —, resonant panel;—, non-resonant panel. Left column, snapshots of vibration modes at $t = 6$. Right column, time histories of displacements at panel center.

4.6 Conclusions

In this chapter, a comprehensive panel design methodology is presented which is mainly dependant on panel location, length, and its structural properties. Subsequently, a numerical analysis technique, namely perturbation evolution method (PEM) is designed and adopted due to its lower computational resource requirement than full direct aeroacoustic simulation (DAS). The airfoil takes a NACA 0012 profile at an AoA of 5° with chord-based Re of 5×10^4 and M of 0.4. The panel is expected to absorb the energy of boundary layer instabilities convecting with airfoil flow by means of its own flow-induced vibration. As such the flow fluctuation responsible for scattering at airfoil trailing edge as noise and the subsequent aeroacoustic feedback loop that underlies the sustained tonal noise radiation are weakened. PEM is adopted for the feasibility study of panel design due to its lower computational resource requirement than full DAS. The base flow for PEM is obtained from averaging the time stationary solutions of accompanying DAS of same flow with fully rigid airfoil. In order to allow the elastic panel to set into continuous flow-induced vibration, the analysis is implemented with a broadband excitation instead of a discrete Gaussian perturbation. PEM is applied with various panel structural parameters and panel locations and the resulting potential for reducing airfoil tonal noise is studied. Generally, all elastic panel designs yield varying levels of tonal noise reduction but maintain more or less the same directivity as the rigid airfoil. It implies that the existence of an elastic panel does not alter the nature of the aeroacoustic feedback loop but only modifies its effectiveness at reducing noise. It is found that a panel located just ahead of the sharp growth of natural boundary layer instability within the airfoil separation bubble provides the strongest reduction of instabilities that are responsible for scattering into noise at the airfoil trailing edge and, hence, provides the most noise reduction among all cases studied. A panel located at the

plateau in the boundary layer instability amplitude or in the proximity of the airfoil trailing edge gives a much lower noise reduction. In addition, for a given panel location, higher noise reduction is achieved when the structural parameters of the panel are tuned in such a way that its fluid-loaded natural frequency is coincident with the dominant frequency of the flow fluctuation passing over it. A resonant panel in the best location is able to yield almost uniform azimuthal noise reduction of around 2.1 dB, whereas a non-resonant panel at the worst location gives only 0.5 dB noise reduction. Based on the results of the study, installation of a flush-mounted elastic panel is proven to be a feasible method for airfoil tonal noise reduction. Furthermore, the adopted PEM appears to be a viable tool supporting quick panel design iterations to search for optimal noise reduction as it takes only around 10% computational time of the corresponding DAS calculation. The time saving can then be spent on DAS calculation for the optimal panel design for gaining better understanding of the relevant physics of noise reduction.

Chapter 5

Airfoil Tonal Noise Reduction by Localized Flow-Induced Panel Vibration

5.1 Introduction

In this chapter, direct aeroacoustic simulation (DAS) of airfoil configurations with an elastic panel mounted on the airfoil suction surface is presented to uncover the physical mechanisms responsible for airfoil tonal noise reduction as revealed by PEM analysis in Chapter 4. PEM analysis indicated that a panel located just ahead of the sharp growth of boundary layer instability within airfoil separation bubble provides the strongest reduction of instabilities responsible for noise generation by its scattering at airfoil trailing edge. Hence, resonant elastic panel (EP1_R) and non-resonant elastic panel (EP1_{NR}) cases are selected for full DAS calculation to ascertain the effectiveness of the elastic panel in tonal noise reduction under full realistic flow conditions and its dependence on panel resonance. The numerical settings and computational setup are kept the same as described

in Chapter 2 for consistency and comparative analysis. For all calculations, the solution is initially time-marched to a non-dimensional time of $t = 200$ with a time step size Δt of 1×10^{-5} until the time stationary state is achieved. The solution is then further proceeded for a time episode of $t = 20$ for aerodynamic and acoustic analyses. The calculations are carried out in UBDA of The Hong Kong Polytechnic University (PolyU) which facilitates parallel processing with 494 CPU cores for a total of approximately 90,000 CPU hours for each case. The aerodynamic and aeroacoustic performance of airfoil configurations with elastic panel is presented in this chapter and compared with the corresponding solution of the rigid airfoil (RS).

5.2 Aerodynamic Analysis

The time-averaged coefficients of friction C_f for RS, EP1_R and EP1_{NR} cases are shown in Figure 5.1. Evidently, the presence of an elastic panel does not result in any significant change in aerodynamic characteristics of the airfoil. A minor shift in separation bubble reattachment point is observed in C_f plot for EP1_R and EP1_{NR} cases where the reattachment point for EP1_R is observed at $x = 0.561$ which results in the reduction of length of separation bubble by 3.2% as compared to RS case. For EP1_{NR}, the reattachment point is observed at $x = 0.567$ resulting in a reduction of 2.24%. However, the boundary layer separation point remains identical for both elastic panels and rigid airfoil cases (i.e. $x \sim 0.18$).

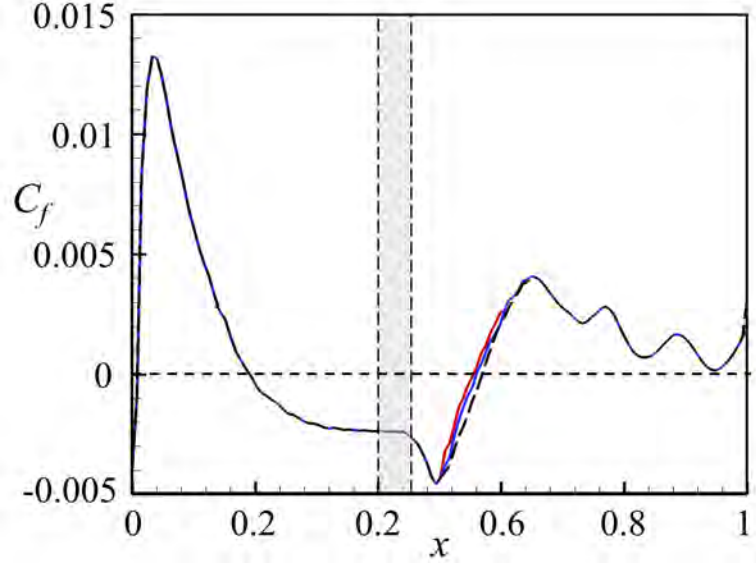


Figure 5.1: Distribution of C_f on airfoil. The highlighted portion indicates the coverage of elastic panel. - - -, RS; —, EP1_{NR}; —, EP1_R.

Figures 5.2(a) to (c) show the streamlines around the airfoil for the time-averaged solutions of RS, EP1_{NR} and EP1_R cases respectively. The flow separation, reattachment, and LSB over the airfoil suction surface can be clearly observed in each case along with recirculation region prior to the flow reattachment point. The recirculation region for RS cases is observed to be 3.25% longer than EP1_{NR} and 4.75% longer than EP1_R due to a shift in flow reattachment locations for the latter cases. This fact is further investigated by closeup view of the airfoil in Figures 5.2(d) to (f) to identify the change in flow separation and reattachment locations indicated by ‘S’ and ‘R’ respectively. The flow separation point is observed to be identical for all three cases whereas the reattachment point shifted towards upstream location is observed for EP1_{NR} and EP1_R resulting in a shorter LSB as identified in Figure 5.1.

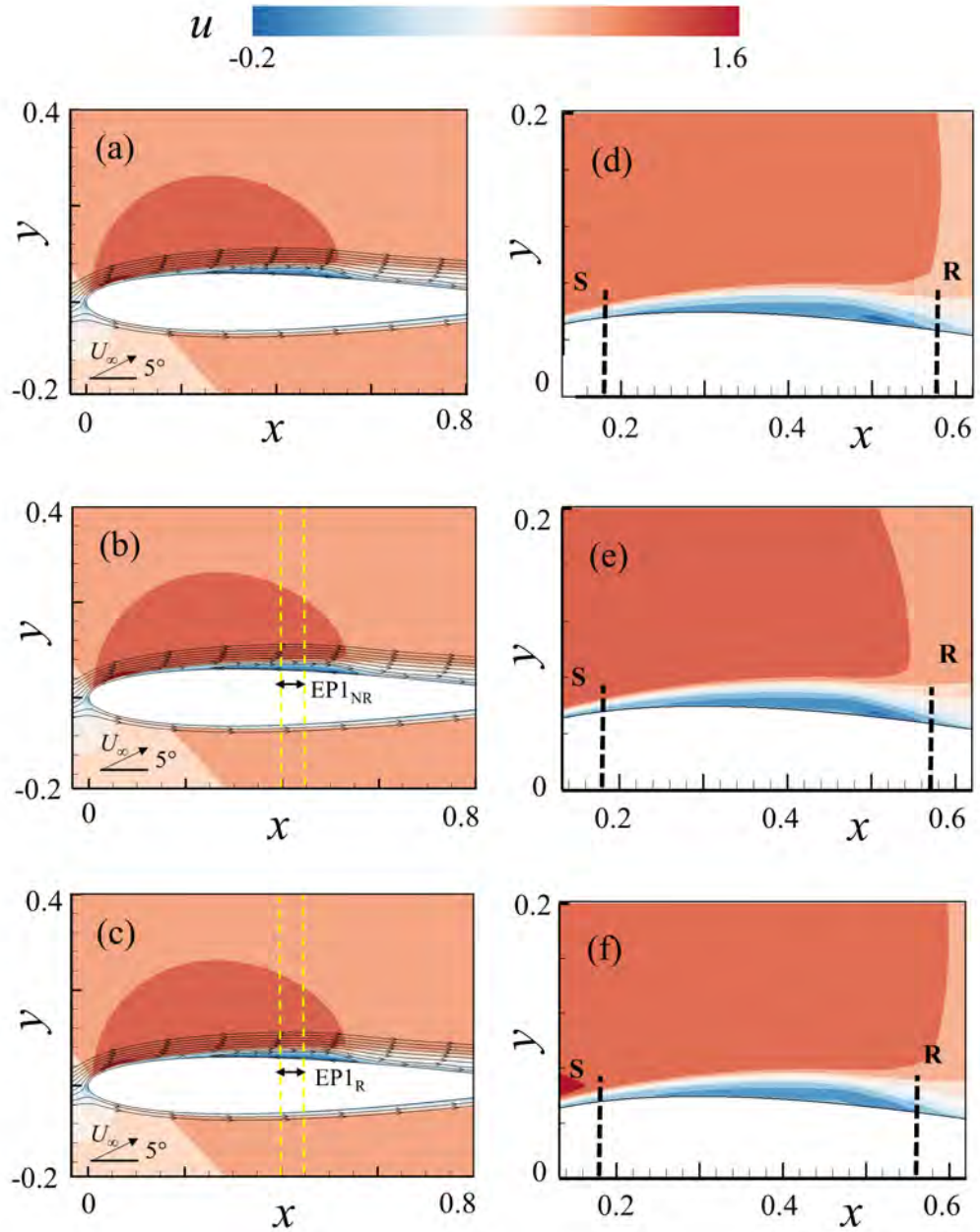


Figure 5.2: Streamlines over the airfoil surface. (a) RS, (b) EP1_{NR}, (c) EP1_R. Closeup view of airfoil suction surface indicating flow separation and reattachment points. (d) RS; (e) EP1_{NR}; (f) EP1_R.

Figures 5.3(a) to (c) present the time-averaged streamwise velocity profiles obtained from the time stationary solutions of RS, EP1_{NR} and EP1_R cases

respectively. The streamwise velocity just after the boundary layer reattachment at $x \sim 0.6$ for the RS case in Figure 5.3(a) shows higher magnitude fluctuations which further move downstream towards the trailing edge and airfoil wake. For EP1_{NR} case in Figure 5.3(b), moderate velocity fluctuations can be observed on the suction surface, whereas, for EP1_R case (Figure 5.3(c)), almost no noticeable fluctuations is observed near the trailing edge or in the wake region. To investigate the flow behavior over the airfoil suction surface, boundary layer profiles for all cases at different chord locations within $0.2 \leq x \leq 0.6$ are plotted in Figure 5.4. A location of $x = 0.58$ is also selected for analysis which is right ahead of boundary layer reattachment over the airfoil suction surface for RS case. Effect of flow separation and adverse pressure gradient due to boundary layer separation at the selected chord locations can be clearly observed near the airfoil surface in the boundary layer profiles. The profiles for all three cases are similar at $x = 0.2, 0.3$ and 0.4 and no significant difference is observed. However, a slight deviation within the boundary layer profiles of RS, EP1_{NR} and EP1_R can be observed at $x = 0.5$ which shows a less intensive back flow for EP1_R as compared to RS and EP1_{NR}. It is important to note that the elastic panel covers $0.4 \leq x \leq 0.45$ and appears to have reduced some instabilities within the boundary layer. At $x = 0.58$, a significant difference between the boundary layer profiles can be observed. The flow appears to be reattached for EP1_R and EP1_{NR} cases with no adverse pressure gradient and backflow, whereas the flow still appears to be separated for RS case. This implies that the elastic panel has effectively reduced the instabilities within the separated flow which results in a slight reduction in the length of the separation bubble. At $x = 0.6$, the flow appears to be reattached for all three cases and no significant deviation is observed.

Time traces of lift and drag coefficients within a time episode of $0 \leq t \leq 3$ for EP1_R, EP1_{NR} and RS are shown in Figure 5.5. A minor deviation is observed

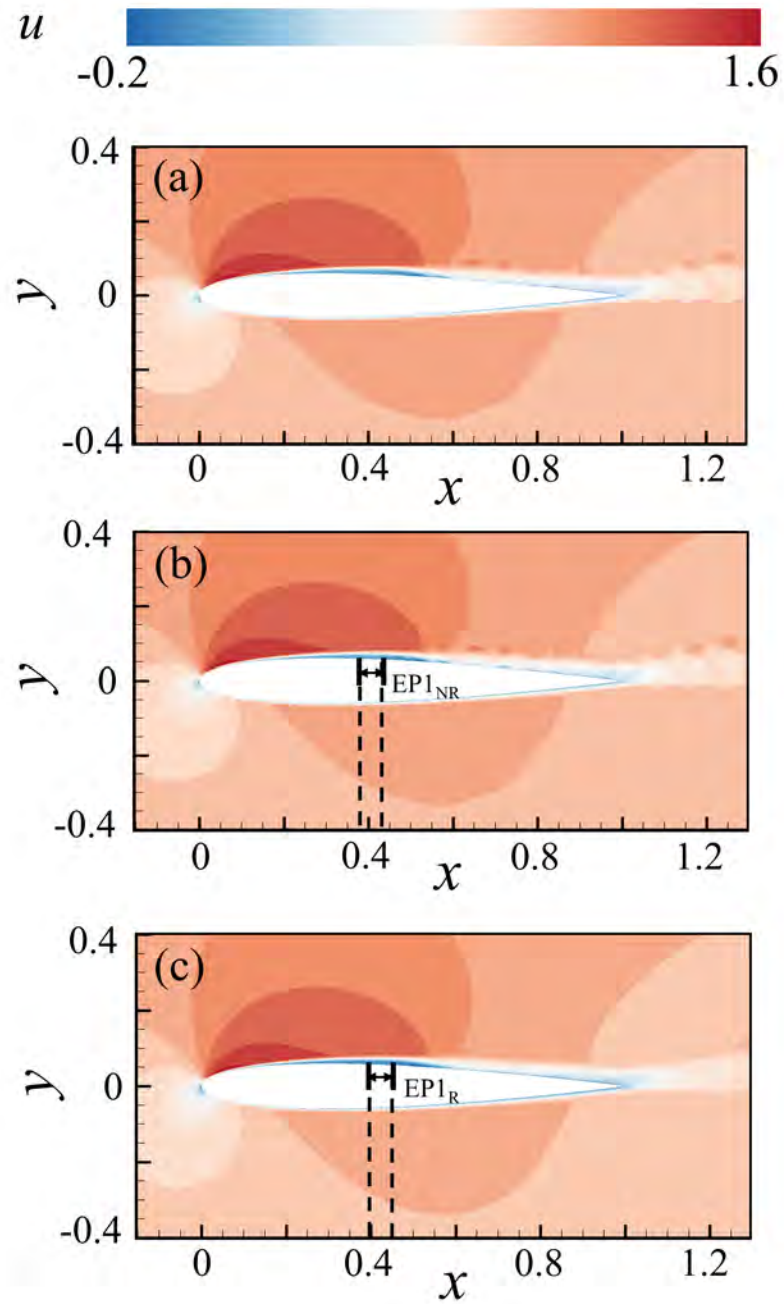


Figure 5.3: Time-averaged streamwise velocity profile. (a) RS, (b) EP1_{NR} and (c) EP1_R.

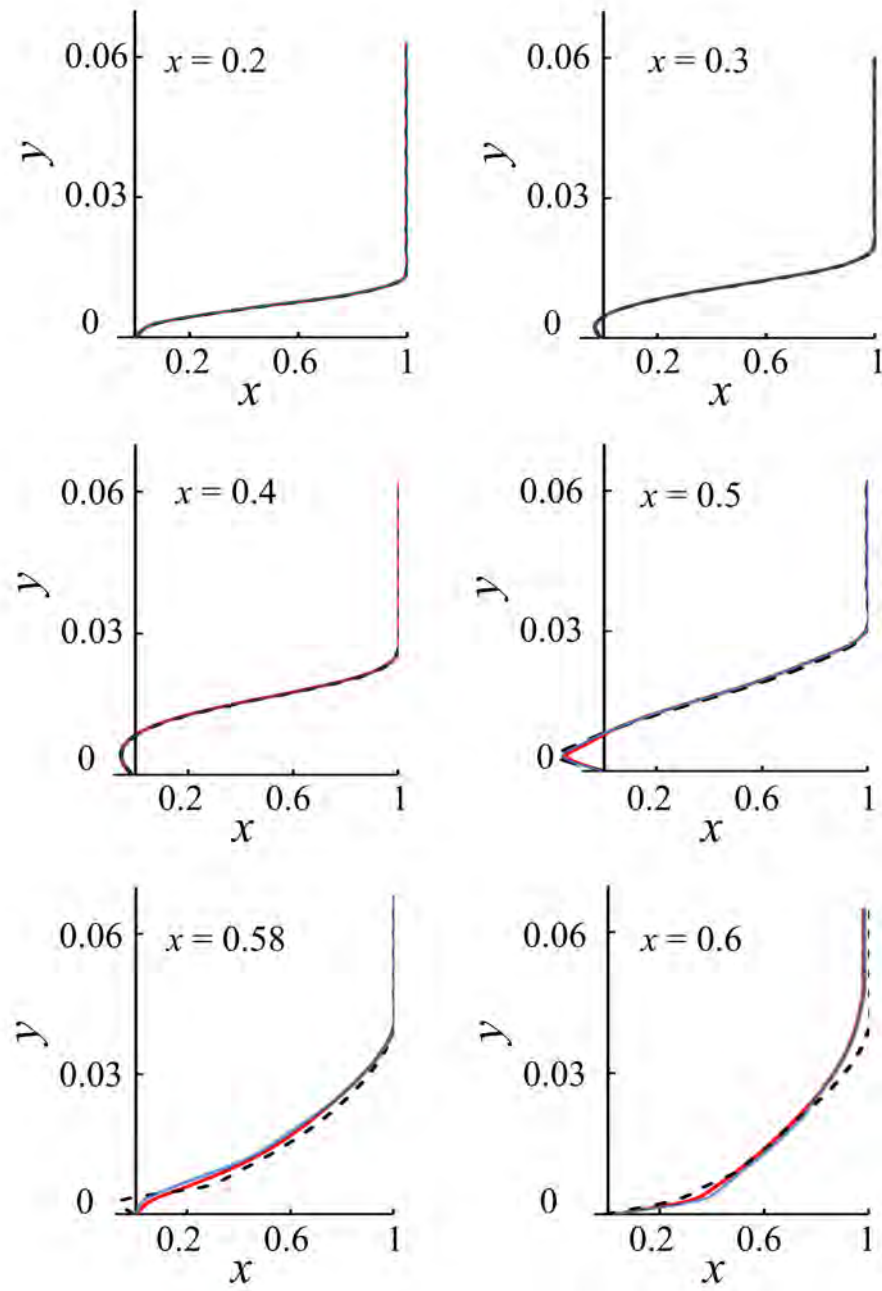


Figure 5.4: Boundary layer profiles at different chord locations. - - -, RS; —, EP1_{NR}; —, EP1_R.

in lift and drag fluctuations due to the presence of elastic panel which signifies the objective of not disrupting airfoil aerodynamic performance while achieving tonal noise reduction. Table 5.1 shows the temporal statistics of aerodynamic coefficients for all cases. The time-averaged $C_{L,mean}$ for EP1_R and EP1_{NR} are found to be 0.4889 and 0.4874 respectively which is slightly higher than that of RS case. A slight variation in $C_{D,mean}$ is also observed. Its values for EP1_R and EP1_{NR} are found to be 0.01875 and 0.01871 respectively as compared to 0.0185 for RS. The dynamic effect of the short elastic panel displacement for airfoil-panel configurations results in a slight increase in overall airfoil drag due to added skin friction drag component (Serrano-Galiano et al. 2018). This aspect is also observed in a number of membrane airfoil studies with much higher increase in overall drag due to large size of flexible structures (Serrano-Galiano et al. 2018, Galvao et al. 2006, Gordnier 2009). A deviation of only 0.64% and 0.72% in overall $C_{L,mean}/C_{D,mean}$ is observed for EP1_R and EP1_{NR} cases respectively with respect to the RS case which implies that the elastic panel configuration has no significant influence on airfoil aerodynamic performance. Furthermore, a slight difference in $C'_{L,rms}$ and $C'_{D,rms}$ of 0.59% and 1.5% is observed for EP1_R respectively, whereas no difference in $C'_{L,rms}$ is observed for EP1_{NR} and a difference of 1.03% is observed in $C'_{D,rms}$ for EP1_{NR}.

Table 5.1: Aerodynamic coefficients for RS, EP1_{NR} and EP1_R cases. Values in brackets show the relative changes from RS case.

Case	$C_{L,mean}$	$C_{D,mean}$	$C_{L,mean}/C_{D,mean}$	$C'_{L,rms}$	$C'_{D,rms}$
RS	0.4855	0.01850	26.24	0.0167	0.00194
EP1 _R	0.4889 (+0.7%)	0.01875 (+1.3%)	26.07 (-0.64%)	0.0168 (+0.59%)	0.00197 (+1.5%)
EP1 _{NR}	0.4874 (+0.39%)	0.01871 (+1.12%)	26.05 (-0.72%)	0.0167 (0%)	0.00196 (+1.03%)

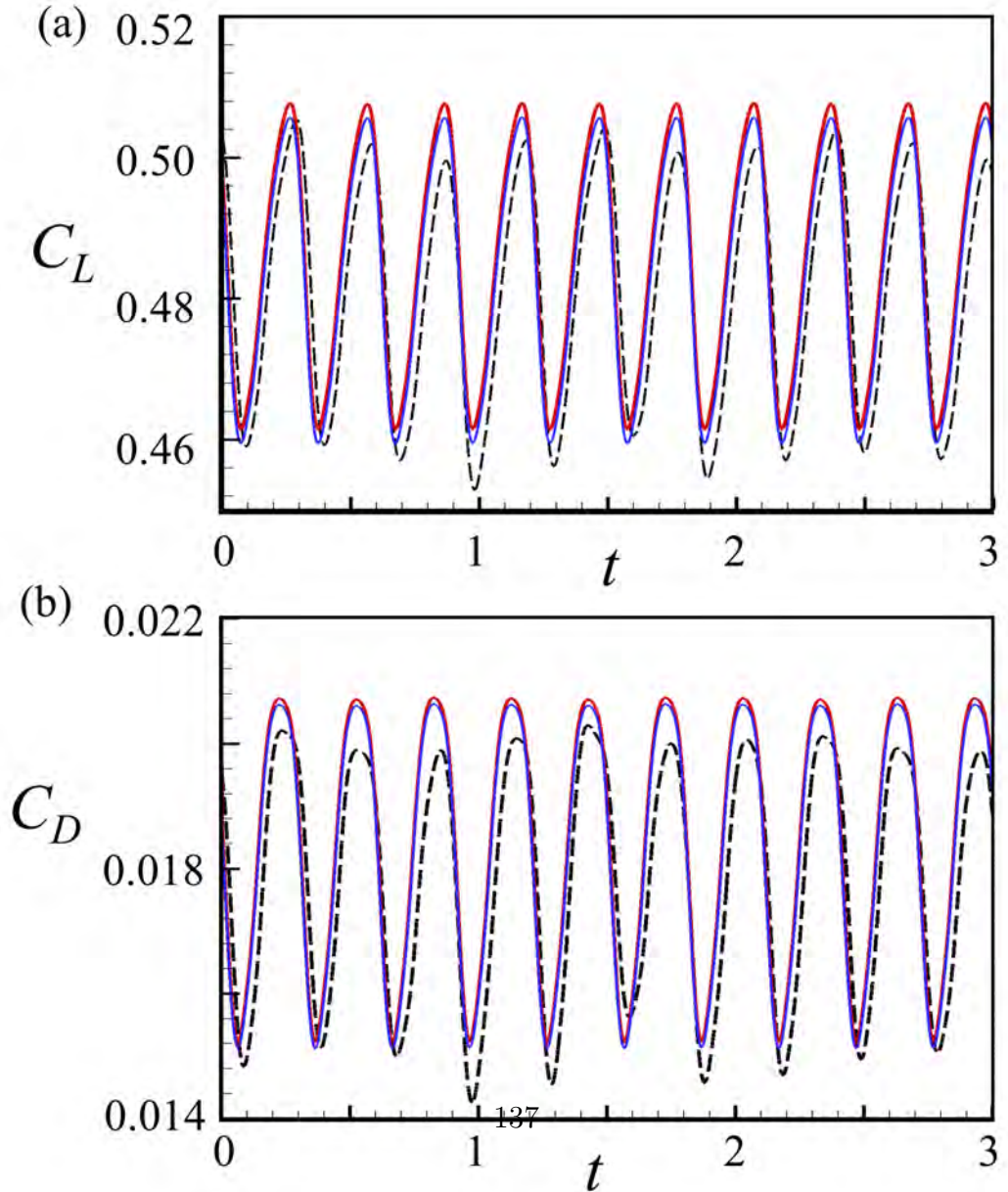


Figure 5.5: Coefficient of (a) lift C_L and (b) drag C_D . - - -, RS; —, EP1_{NR};

—, EP1_R.

Figures 5.6 (a) to 5.6(c) show the distribution of u'_{rms} for RS, EP1_{NR} and EP1_R respectively, whereas Figures 5.6 (d) to 5.6(f) show the distribution of v'_{rms} for RS, EP1_{NR} and EP1_R respectively. Prominent velocity fluctuations for all cases can be observed on the airfoil suction surface within the separation bubble. These instabilities further convect downstream towards airfoil trailing edge and airfoil wake region. It is observed that the magnitude of u'_{rms} and v'_{rms} fluctuations are much stronger for RS and EP1_{NR} as compared to EP1_R. The plot indicates that the resonant panel is able to reduce flow instabilities within the boundary layer over the suction surface. This results in a lower intensity of velocity fluctuations and would possibly cause a lower magnitude of flow scattering at the trailing edge.

To investigate the contribution of flow fluctuations and its subsequent effect on additional momentum fluxes in the flow, Reynolds stress ($|u'v'|/U_\infty^2$) is evaluated for all three cases as shown in Figure 5.7. It is observed that the magnitude of fluctuations for RS case is much higher than EP1_{NR} and EP1_R which indicates the presence of stronger fluctuations within the flow for RS case. For EP1_{NR} and EP1_R cases, the Reynolds stress becomes less intensive and appear earlier (towards upstream) than RS case due to shrinkage of LSB. It indicates that the fluctuations in the flow for EP1_{NR} and EP1_R are reduced due to panel vibrations and enhances the flow stability which conforms with the available literature (Açikel and Genc 2018, Genç et al. 2020).

The velocity profile at $x = 1.05$ and $-0.2 \leq y \leq 0.2$ in airfoil near wake is also investigated for all three cases (Figure 5.8). A significant velocity deficit is observed for all three cases where a minimum velocity (u/U_∞) of 0.34 is observed for RS case. Furthermore, the wake profile is asymmetric about centerline due to flow incidence of $AoA = 5^\circ$. For EP1_R, the wake width is significantly reduced by 22% as compared to RS case due to lower intensity of fluctuations within the

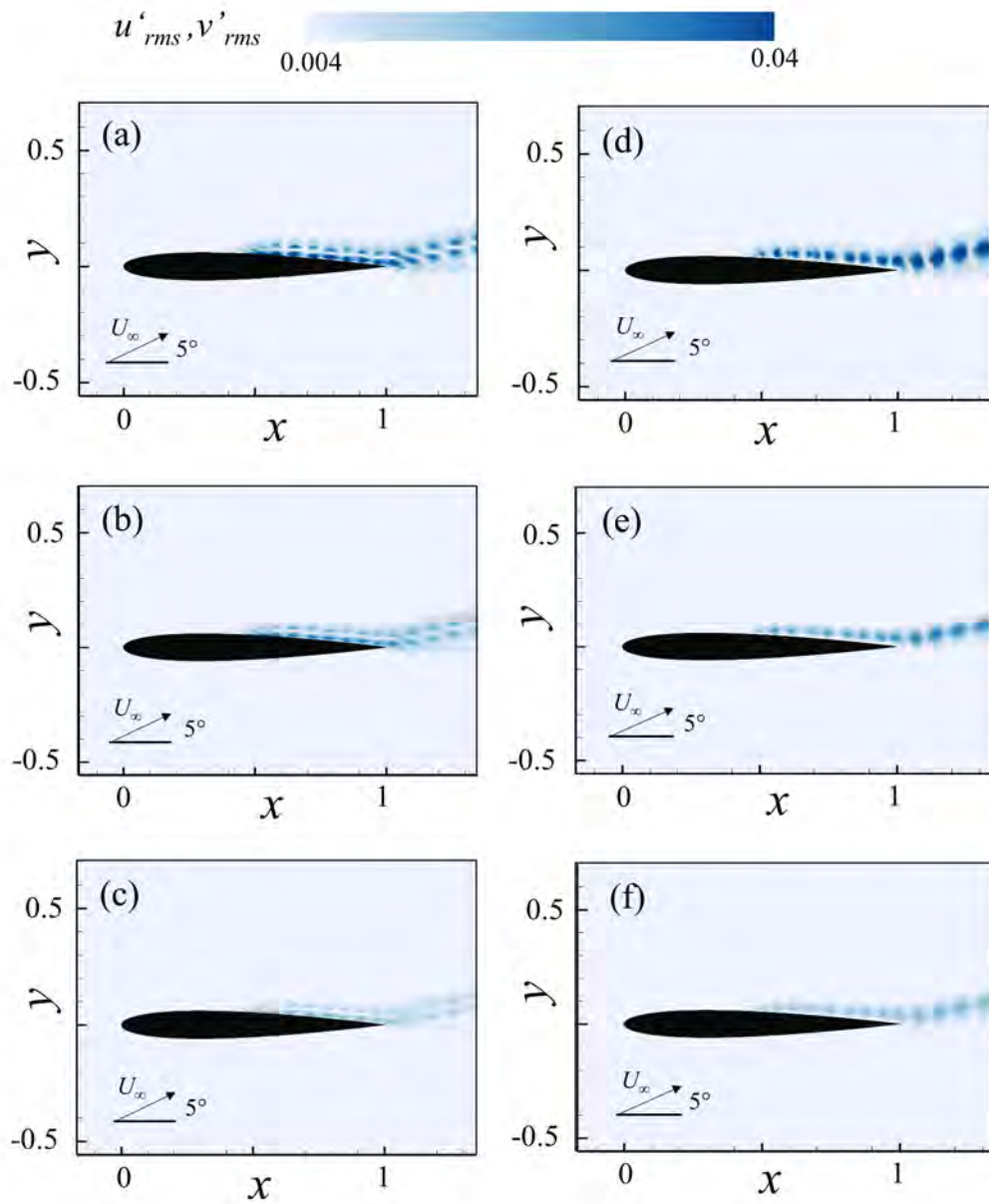


Figure 5.6: Velocity fluctuations u'_{rms} and v'_{rms} . (a) and (d), RS; (b) and (e), EP1NR; (c) and (f), EP1R.

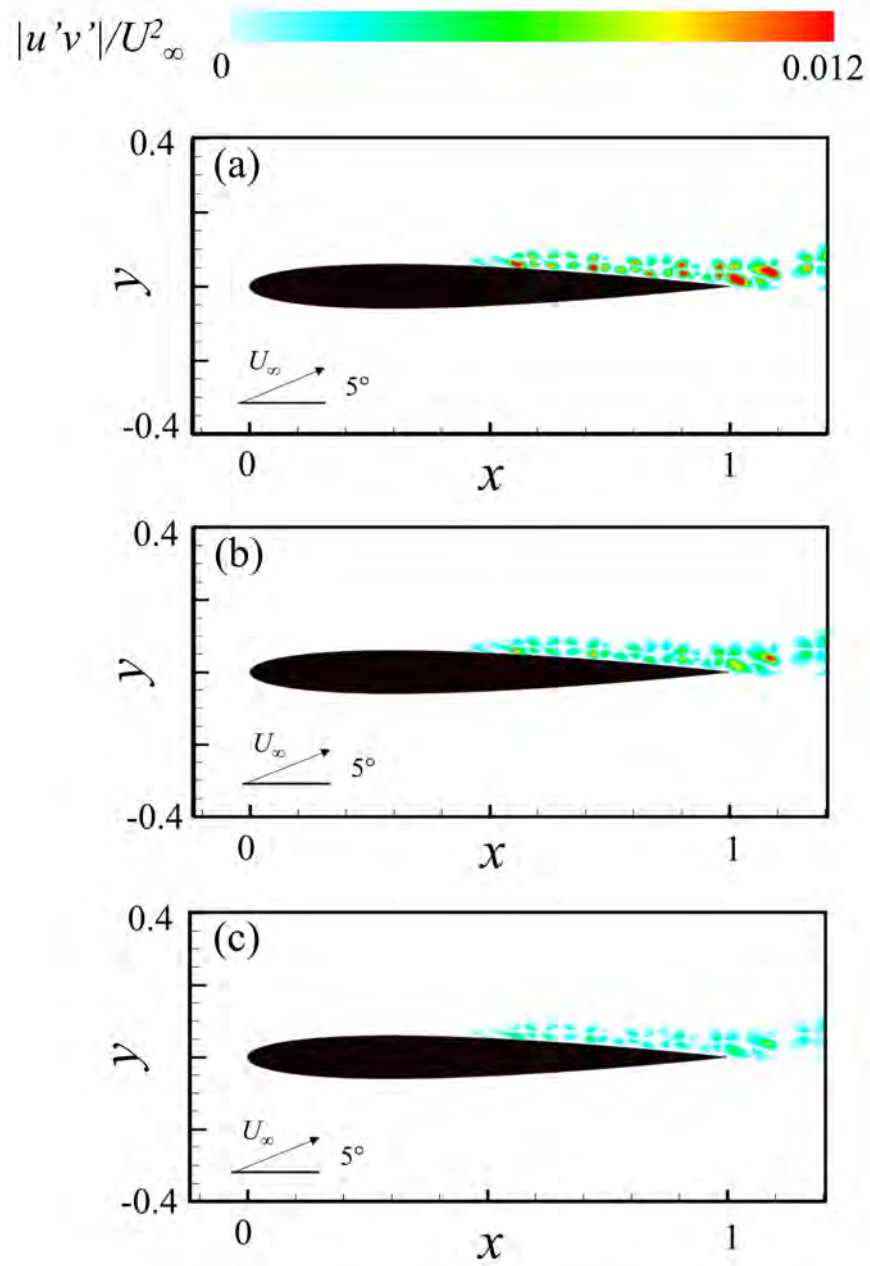


Figure 5.7: Reynolds stress distribution over the airfoil surface. (a) RS, (b) EP1_{NR}, (c) EP1_R.

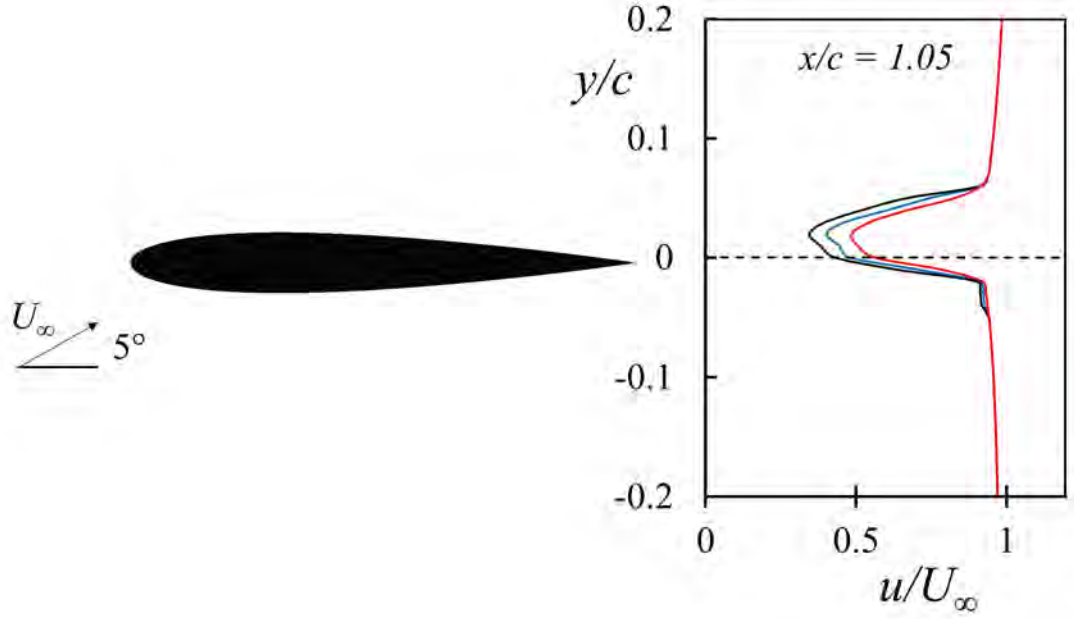


Figure 5.8: Velocity profiles in airfoil near wake region at $x = 1.05$. —, RS; —, EP1_{NR}; —, EP1_R.

boundary layer over the suction surface of the airfoil, whereas for EP1_{NR} the velocity deficit is reduced by only 10% at $y = 0.02$.

5.3 Time-Frequency Analysis

The distributions of the amplitudes of velocity fluctuations v' for both RS and EP1_R at $(f_{bl})_0 = 3.37$ and $(f_{bl})_1 = 6.6$ along airfoil chord are compared in Figure 5.9. For RS case, both amplitudes start to increase at $x \geq 0.27$ and grow within $0.4 \leq x \leq 0.45$. The amplitude of $(f_{bl})_0$ grows remarkably to reach its plateau of 0.043 at $x \sim 0.5$, stays there up till $x \sim 0.58$, then drops rapidly to a dip at $x \sim 0.65$, and eventually grows mildly again. A similar trend is observed for EP1_R and EP1_{NR} where the amplitude at $(f_{bl})_0 = 3.37$ grows significantly from $x \sim 0.4$, however, the magnitude of velocity fluctuations within $0.45 \leq x \leq 0.55$ are much lower and reach its plateau at 0.04 for EP1_R and 0.042 for EP1_{NR}. The amplitude

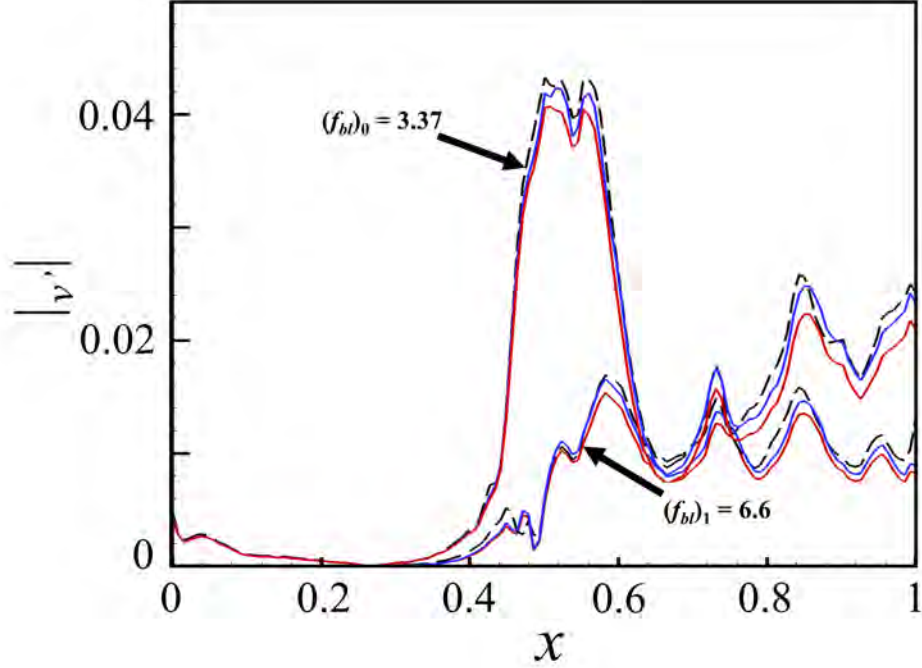


Figure 5.9: Spatial growth of flow instability over airfoil suction surface. - - -, RS; —, EP1_{NR}; —, EP1_R.

of $(f_{bl})_1$ appears to grow in a more gradual fashion and fluctuates mildly around a value of 0.0125 beyond $x \sim 0.57$ for all cases. The difference in the magnitude of EP1_R, EP1_{NR} and RS at $(f_{bl})_1 = 6.6$ is not significant as compared to $(f_{bl})_0 = 3.37$.

To investigate the effect of an elastic panel on the flow fluctuations, the percent deviation in the magnitude of transverse velocity fluctuations $|v'|$ at airfoil suction surface for EP1_R and EP1_{NR} with respect to RS at both $(f_{bl})_0$ and $(f_{bl})_1$ are evaluated and shown in Figures 5.10(a) and (b) respectively. The effect of panel vibration in the reduction of transverse velocity fluctuations within the boundary layer can be observed for both EP1_R and EP1_{NR}. For the resonant panel, a continuous reduction in velocity fluctuations at $(f_{bl})_0$ ranging from 5% to 20% is observed from $x = 0.4$ up till the trailing edge (Figure 5.10(a)). This observation manifests the fact that the panel has weakened the strength of boundary

layer instabilities at their emergence at $x = 0.4$ which results in convection of low magnitude fluctuations towards the trailing edge and subsequently results in less flow scattering at the trailing edge. The observed phenomenon would ultimately result in lower tonal noise generation and would also weaken the strength of the feedback loop. Two sharp peaks at $x = 0.76$ and $x = 0.87$ are also observed possibly due to the roll-up of vortices with significant strength on the airfoil suction surface which intensifies the flow fluctuations to some extent. Nonetheless, still a reduction of $\sim 3\%$ in velocity fluctuations is observed at these locations for the resonant panel. For the non-resonant panel, the overall trend is similar to the resonant panel, however, the reduction in fluctuations is less pronounced which ranges from 5% to 10% from $x = 0.4$ to 0.8 . However, the two sharp peaks at $x = 0.76$ and $x = 0.87$ result in slight amplification of flow instabilities up to 8% as compared to RS case. An average reduction of 14% in velocity fluctuations at $(f_{bl})_0$ is observed for EP1_R but an average of only 4% reduction is observed for EP1_{NR}. It is interesting to note that a slight reduction of 6% is observed from the leading edge of airfoil up till the panel location at $x = 0.4$ for both EP1_R and EP1_{NR} which indicates that the panel is able to weaken the magnitude of propagated acoustic scattering all around the airfoil as a result of reduced strength of feedback loop. The percentage deviation of transverse velocity fluctuations for EP1_R and EP1_{NR} with respect to RS at $(f_{bl})_1$ is shown in Figure 5.10(b). Similar effects of panel on flow instabilities are observed for both EP1_R and EP1_{NR}; however, the magnitude of reduction in fluctuations is less pronounced at $(f_{bl})_1$. An average reduction of 9% in velocity fluctuations is observed for EP1_R whereas an average of only 3% reduction is observed for EP1_{NR}.

The time histories of transverse velocity fluctuations at different chord locations for EP1_R, EP1_{NR} and RS are plotted in Figure 5.11. At $x = 0.3$ (Figure 5.11(a)), the magnitude of fluctuations is one order lower than other downstream

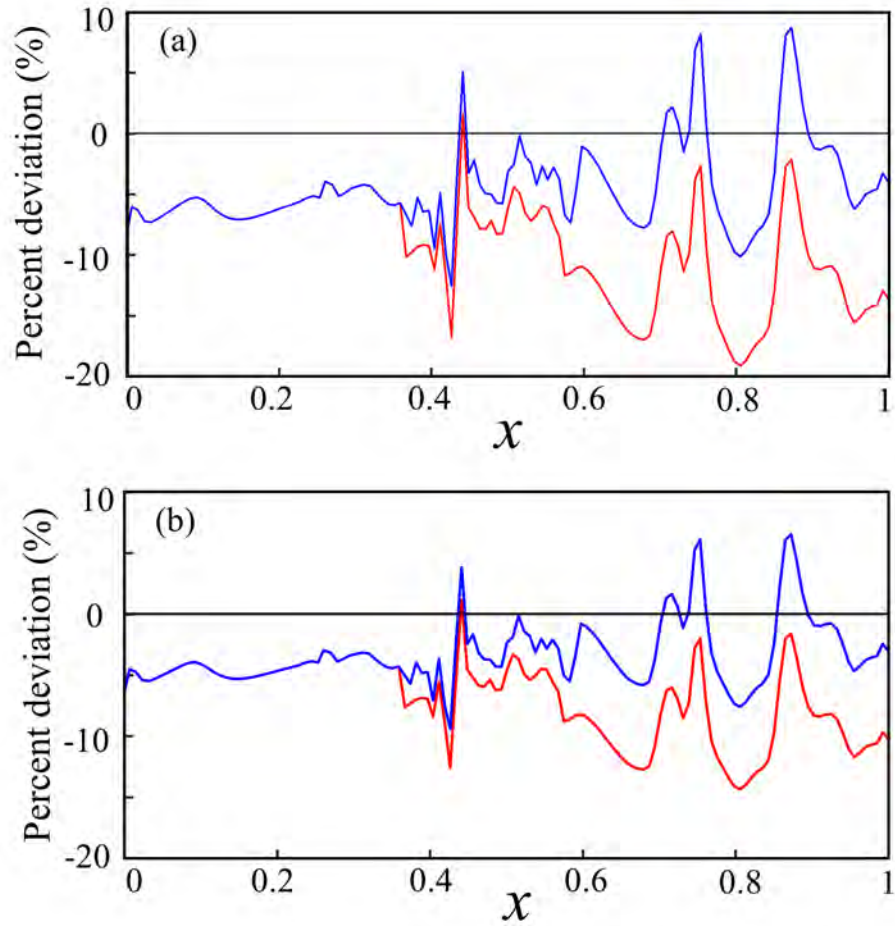


Figure 5.10: Deviation in magnitude of transverse velocity fluctuations $|v'|$ at airfoil suction surface for EP1_R and EP1_{NR} with respect to RS. (a) $(fbl)_0=3.37$, (b) $(fbl)_1=6.6$. —, EP1_{NR}; —, EP1_R.

locations of the airfoil as depicted in Figure 5.9. The overall trend of velocity fluctuations for all cases is periodic and similar with respect to time which indicates that the panel has no significant impact on the nature of hydrodynamic flow. The localized flow-induced vibration of the elastic panel appears to provide continuous suppression of flow instability for instability growth. The extent of instability suppression is stronger in case EP1_R than that in EP1_{NR}. This observation provides good support to the fact that a resonant panel absorbs the flow energy more effectively and leaves less flow distortion for the scattering at airfoil trailing edge as observed at locations near the trailing edge of airfoil in Figures 5.11(c) to 5.11(f). To further investigate the extent of loss of energy for EP1_R and EP1_{NR}, their overall magnitudes of velocity fluctuations are integrated over a time episode of $t = 20$ and their percentage deviations from RS case are evaluated (Figure 5.12). A strong reduction in flow instabilities is evident with resonant EP1_R but only a mild effect comes with non-resonant EP1_{NR}. For EP1_R, the deviation in velocity fluctuations varies along the suction surface and remains much less than RS at all locations except at $x = 0.82$. For EP1_{NR}, both reduction as well as some amplification in velocity fluctuations are observed at different chord locations which undermine the overall effectiveness of non-resonant panel. An average reduction of $\sim 25\%$ is observed for EP1_R whereas an average of $\sim 8\%$ reduction is observed for EP1_{NR}. It is important to note that although the panel is located at $x = 0.4 - 0.45$, reduction in velocity fluctuations is also observed from the leading edge of the airfoil up till the panel location. In this region of the airfoil, the boundary layer is stable and no instability develops. The velocity fluctuations captured are essentially induced by the upstream propagating acoustic waves scattered from the airfoil trailing edge. Substantial reduction of acoustic wave strength by the elastic panel is obvious.

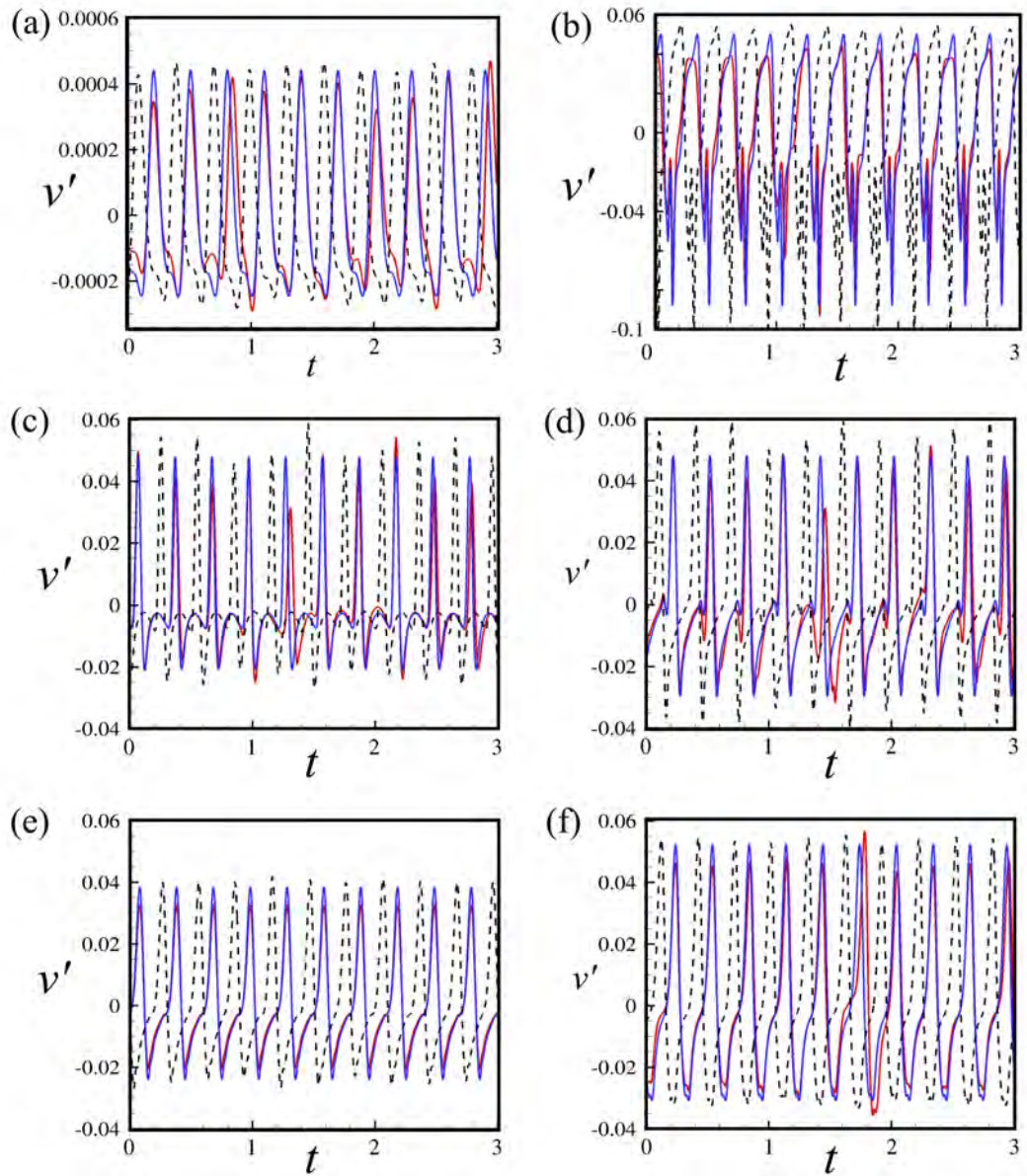


Figure 5.11: Time history of transverse velocity fluctuations v' . (a) $x = 0.3$, (b) $x = 0.5$, (c) $x = 0.7$, (d) $x = 0.8$, (e) $x = 0.9$ and (f) $x = 0.99$, ---, RS; —, EP1_{NR}; —, EP1_R.

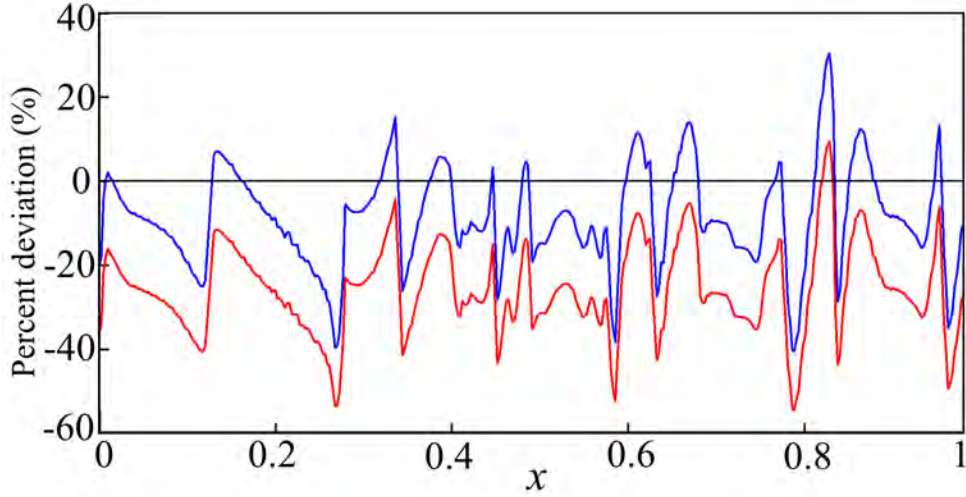


Figure 5.12: Deviation in overall magnitude of transverse velocity fluctuations v' at airfoil suction surface for EP1_R and EP1_{NR} with respect to RS. —, EP1_{NR}; —, EP1_R.

5.4 Airfoil Acoustics

In this section, a detailed analysis on airfoil acoustics for all three cases (RS, EP1_{NR} and EP1_R) is presented. Instantaneous fluctuating pressures p' for RS, EP1_{NR} and EP1_R at the moment corresponding to C_L peak are shown in Figure 5.13. Region of prominent instabilities on the suction surface of airfoil can be observed for all cases. Subsequently, acoustic waves appear to originate from the trailing edge and propagate towards the upstream locations of the airfoil. Although the radiation pattern for all the cases is similar, the magnitude of fluctuating pressure for EP1_R appears to be much less than RS and EP1_{NR}.

Frequency spectra of pressure fluctuations p' all around the airfoil at a radius of three chord lengths are calculated for RS, EP1_{NR} and EP1_R respectively to obtain the acoustic spectral directivity as shown in Figure 5.14. A strong contribution in acoustic wave generation can be observed for all cases at $(f_{bl})_0 = 3.37$ (Figure 5.14). However, the magnitude of pressure fluctuation at the same frequency for EP1_R is much lower than RS case. For EP1_{NR}, a minor deviation

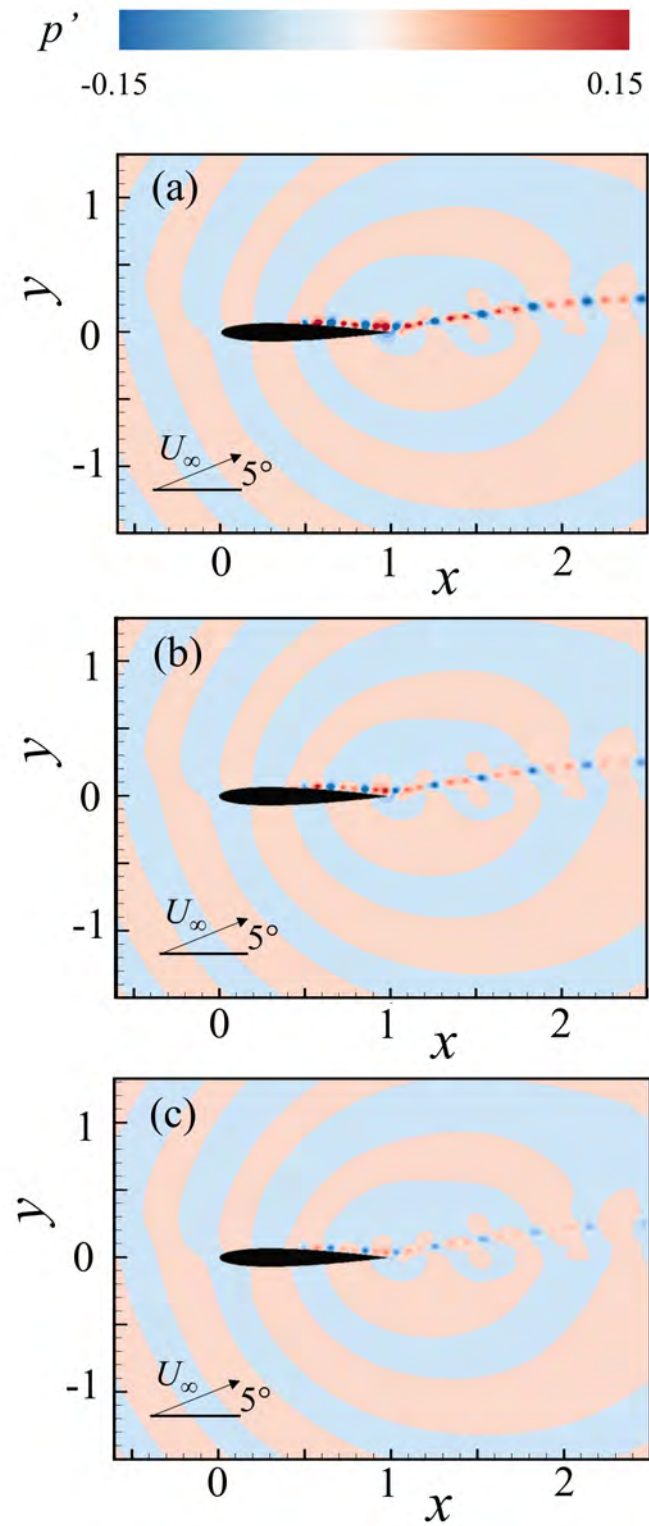


Figure 5.13: Instantaneous acoustic fluctuation p' at the moment of C_L peak.

(a) RS, (b) EP1_{NR} and (c) EP1_R.

in the magnitude can be observed as compared to RS case. The magnitudes of pressure fluctuations for all cases decrease as the frequency further increases up to 6.6 where a mild contribution to acoustics can be observed. The spectral content varies with azimuth location as well. The second and third quadrants contain the strongest and richest spectral content for both fundamental frequency and its first harmonics. The first and fourth quadrants are comparatively quiet with most of the contribution coming from the dominant $(f_{bl})_0$ only. The directivity spectrum indicates that the panel design and its implementation has not altered the overall flow behavior and has resulted in significant reduction in acoustic wave propagation for resonant panel case.

To ascertain the extent of reduction in pressure fluctuations around the airfoil, the overall magnitude of pressure fluctuations around the airfoil is evaluated and integrated at each frequency (Figure 5.15). A reduction of $\sim 24\%$ in the magnitude of pressure fluctuations at $(f_{bl})_0$ for EP1_R is observed, whereas a reduction of 11% is observed for EP1_{NR}. Only a slight reduction of 10% and 6% for EP1_R and EP1_{NR} is observed at the first harmonic $(f_{bl})_1$, whereas a reduction of 4% and 2% is observed for EP1_R and EP1_{NR} at the second $(f_{bl})_2$ respectively. The results indicate that although the panel is designed to resonate with the fundamental frequency of natural boundary layer instability, it is still effective at its higher harmonics to some extent.

To evaluate the extent of reduction in flow instabilities and effectiveness of the panel for the current conditions, azimuth plot of pressure fluctuations at $(f_{bl})_0$ are evaluated and shown in Figure 5.16. The figure renders concrete support to the fact that the suppressed flow instability by EP1_R and EP1_{NR} produces less effective flow scattering at trailing edge and subsequently results in lower noise radiation. The strongest radiation goes along $\theta \sim 145^\circ$ and 240° respectively. Furthermore, the noise reduction toward upstream is observed to

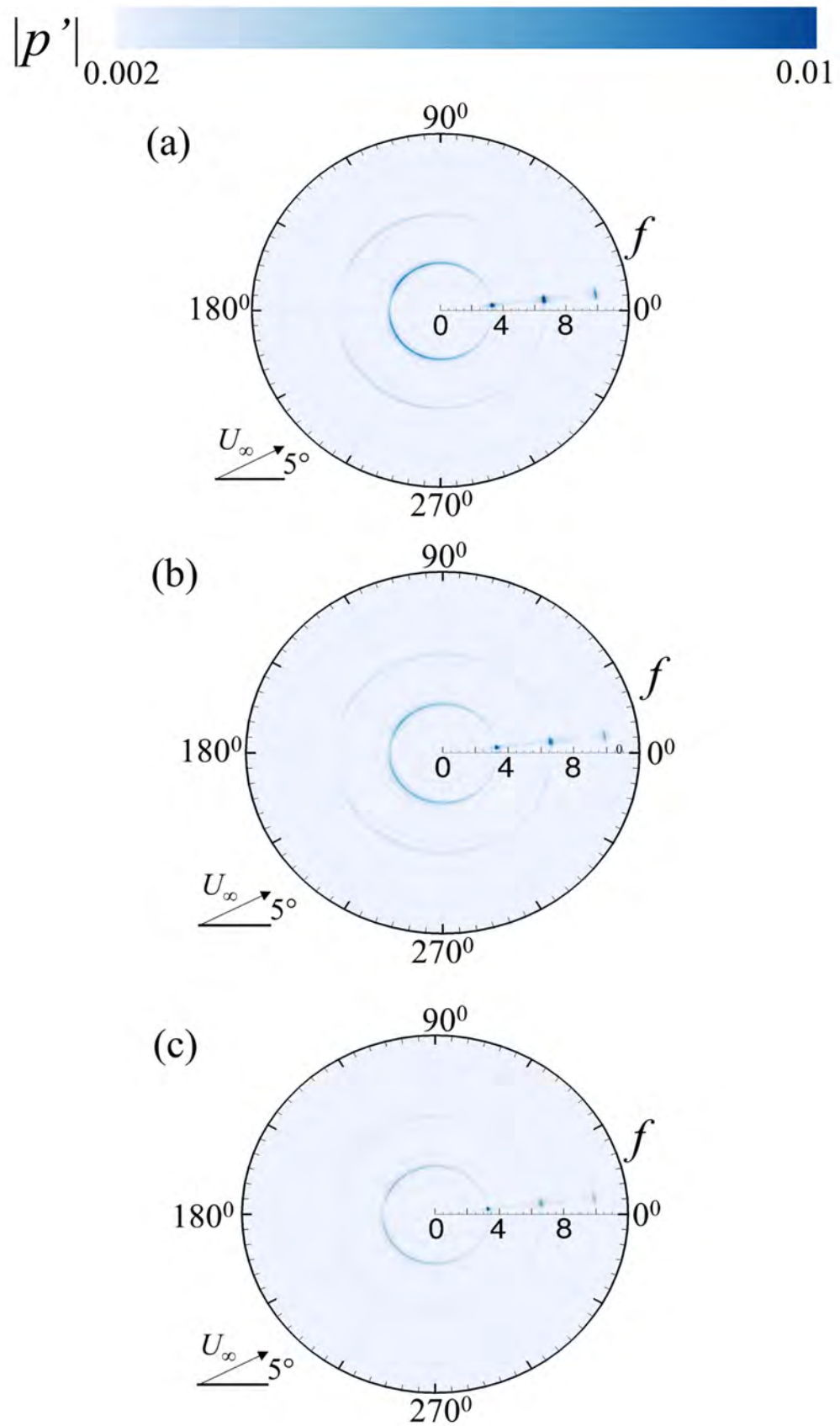


Figure 5.14: Azimuthal distributions of acoustic fluctuations p' spectra at $r = 150$. 3. (a) RS, (b) EP1_{NR} and (c) EP1_R.

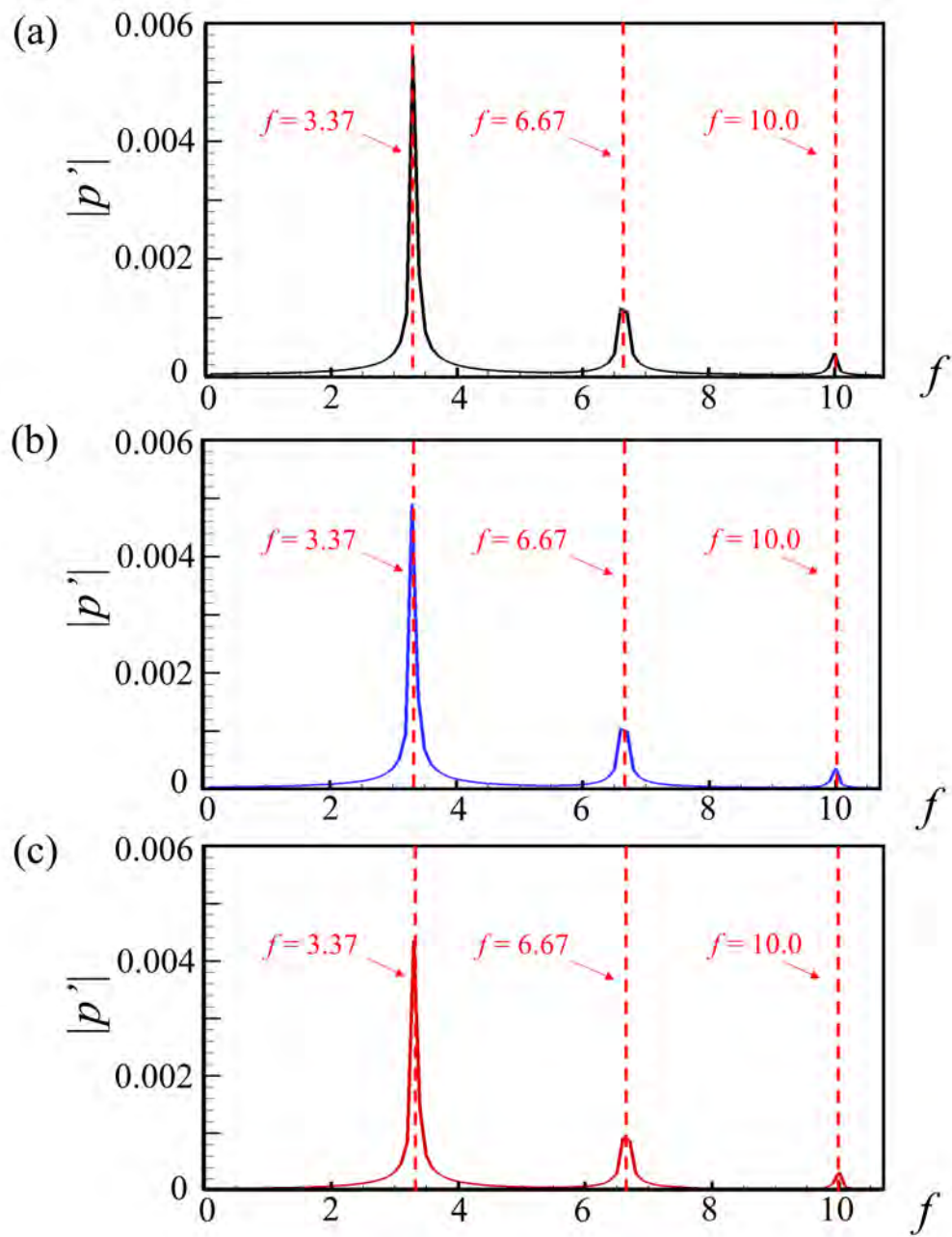


Figure 5.15: Spectra of overall pressure fluctuations around the airfoil at $r = 3$.

(a) —, RS; (b) —, EP1_{NR}; (c) —, EP1_R.

be more significant than downstream. An average SPL reduction of 2.5 dB can be observed for EP1_R whereas for EP1_{NR} an average reduction of 1.1 dB can be observed. For EP1_R, a maximum of 3 dB reduction is observed at $\theta \sim 120^\circ$ whereas a maximum of 1.45 dB reduction is observed for EP1_{NR} along $\theta \sim 120^\circ$.

The noise reduction for the other two panels EP2_R and EP3_R are evaluated at resonance condition only for comparative analysis with EP1_R. The analysis provides a basis to ascertain the effectiveness of the elastic panel located at different chord locations and validate the rationale for designing a resonant elastic panel which is located just ahead of the sharp growth of boundary layer instability within the airfoil separation bubble for tonal noise reduction. Figure 5.17(a) shows the azimuth plot p'_{rms} for EP1_R, EP2_R, EP3_R and RS. The effect of EP1_R in suppressing the flow fluctuations is much more than EP2_R and EP3_R. It can be observed that an elastic panel located near the trailing edge (i.e. EP3_R) is not able to achieve consistent noise reduction and even results in noise amplification towards the forward half-plane in the second and third quadrant. Figure 5.17(b) shows the azimuth plot of $\Delta SPL_{reduction}$ for all three resonant panels at the fundamental frequency of 3.37. An average SPL reduction of 2.5 dB and a maximum of 3 dB reduction is observed for EP1_R, whereas an average SPL reduction of 1.2 dB and a maximum of 1.4 dB is observed for EP2_R. For EP3_R, some noise reduction as well as noise amplification is observed at different azimuth locations. A maximum of only 0.45 dB reduction is observed for EP3_R. It is interesting to note that the extent of noise reduction of EP2_R is much similar to non-resonant panel EP1_{NR} which indicates the strong influence of both panel resonance and its location in determining the reduction of airfoil tonal noise.

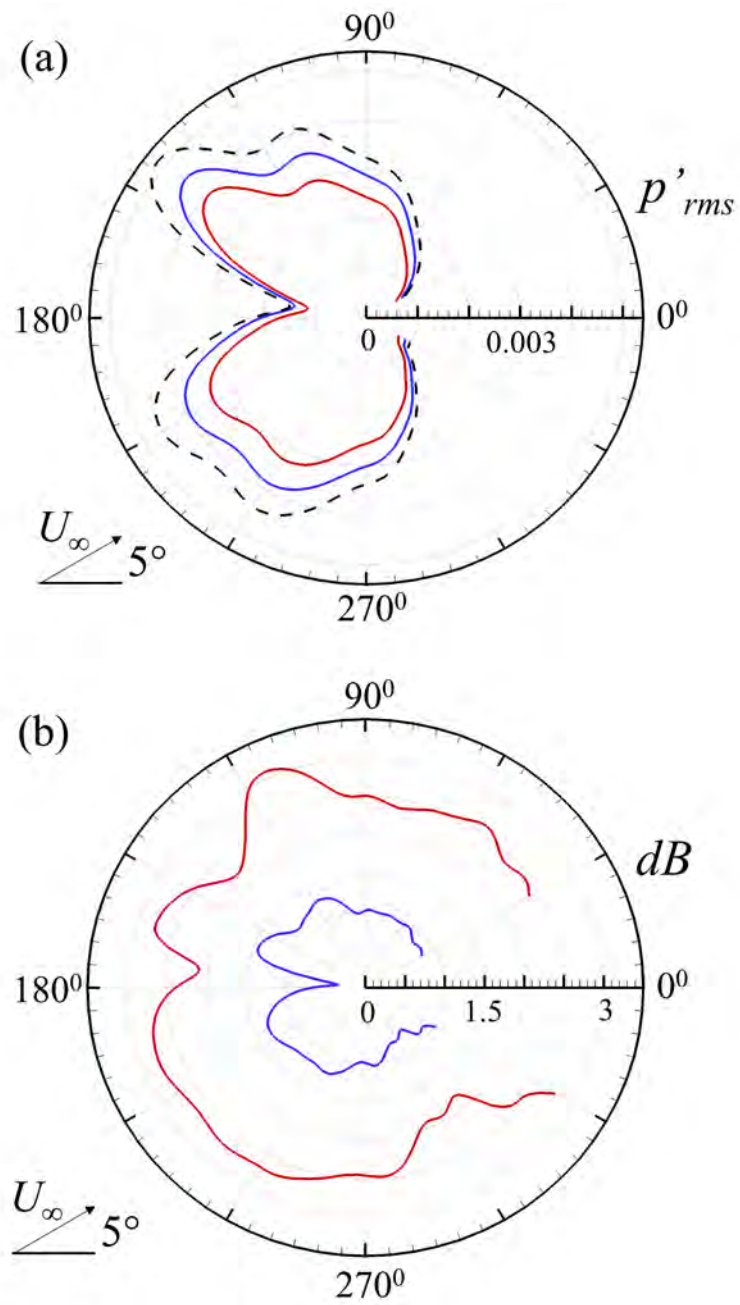


Figure 5.16: Azimuth distribution of (a) p'_{rms} at $r = 3$ and (b) SPL reduction at $r = 3$. - - -, RS; —, EP1_{NR}; —, EP1_R.

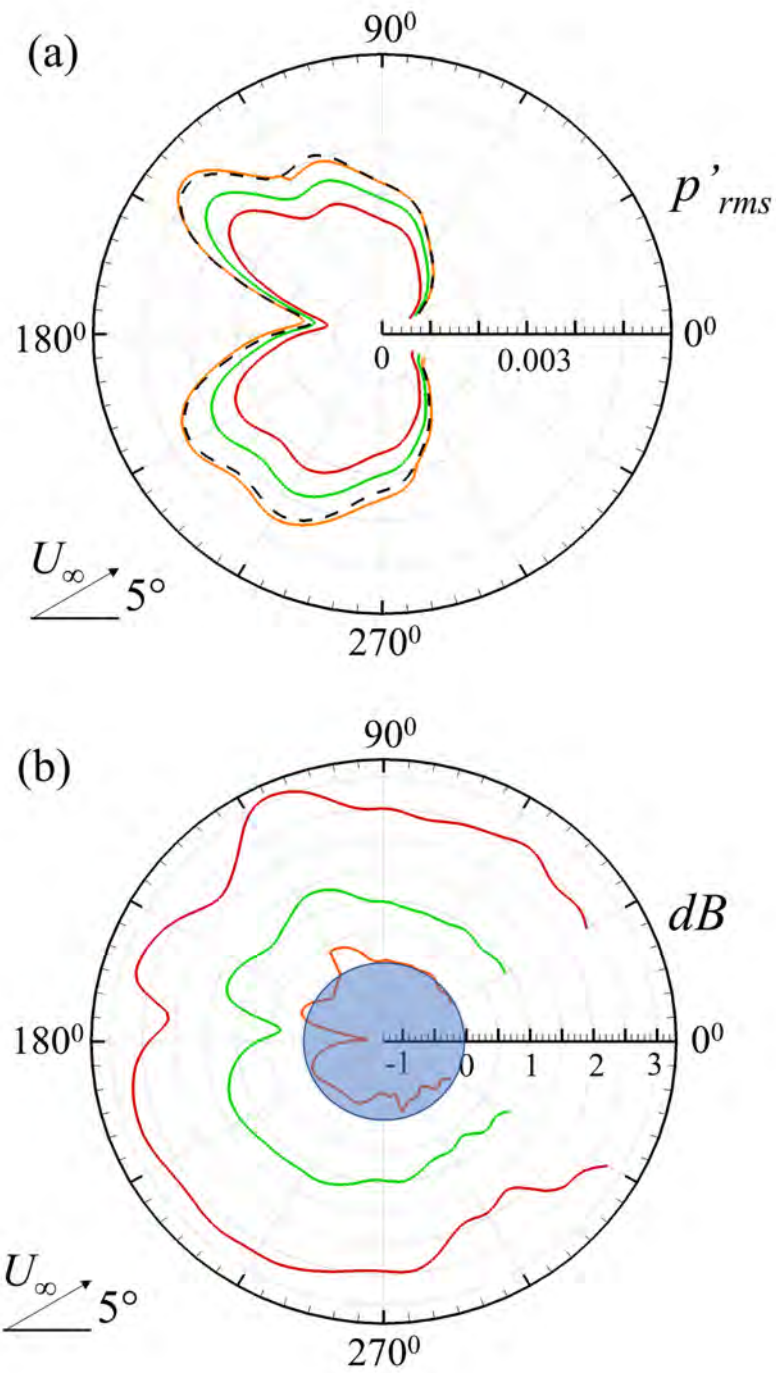


Figure 5.17: (a) Azimuth plot of p'_{rms} at $r = 3$ and (b) SPL reduction plot at $r = 3$. - - -, RS; —, EP1_R; —, EP2_R; —, EP3_R. The blue shaded area indicates noise amplification.

5.5 Panel Dynamics

From the aerodynamic and acoustic analyses, it has been established that the airfoil with a resonant panel is able to achieve much stronger tonal noise reduction than its non-resonant counterpart for the current flow conditions. It is essential to get a better understanding of the dynamics for the resonant panel EP1_R. The time-stationary response of the elastic panel due to boundary layer instabilities and its subsequent localized flow-induced vibration for EP1_R is shown in Figure 5.18. It is evident that EP1_R vibrates at its third natural mode (Table 4.1) at all selected time instances which shows that the panel design correctly captures the intended structural resonance as discussed in Section 4.1.1. In order to evaluate the panel modal response, the panel deflections are recorded for a sufficiently long time and the space-time evolution of panel displacement is presented in Figure 5.19(a). The third panel vibration mode responses are quite discernible and repeatable at all time instances. The fact that the panel vibrates in the desired mode implies that the panel is truly compliant to fluctuating flow-induced loading of oncoming boundary layer instability and is able to absorb its energy effectively to sustain its resonance condition. Figure 5.19(b) illustrates the phase plane plot where the panel displacement and velocity of panel center are plotted for increasing time instances. It clearly indicates that the panel has sustained limit cycle oscillations (Luk et al. 2004). The deflections are observed to be centered around the panel equilibrium position ($w = 0$) which indicates that the panel does not experience any aeroelastic divergence as reported in the literature (Visbal and Gordnier 2004). It is also observed that the trajectory starts from the outside of the cycle and spirals inside where a limit cycle is reached.

The time histories of the ratio of panel displacement to local boundary layer thickness (w/δ) at 20%, 40%, 60% and 80% panel length are evaluated and shown in Figure 5.20. The results confirm that the panel maximum displacement

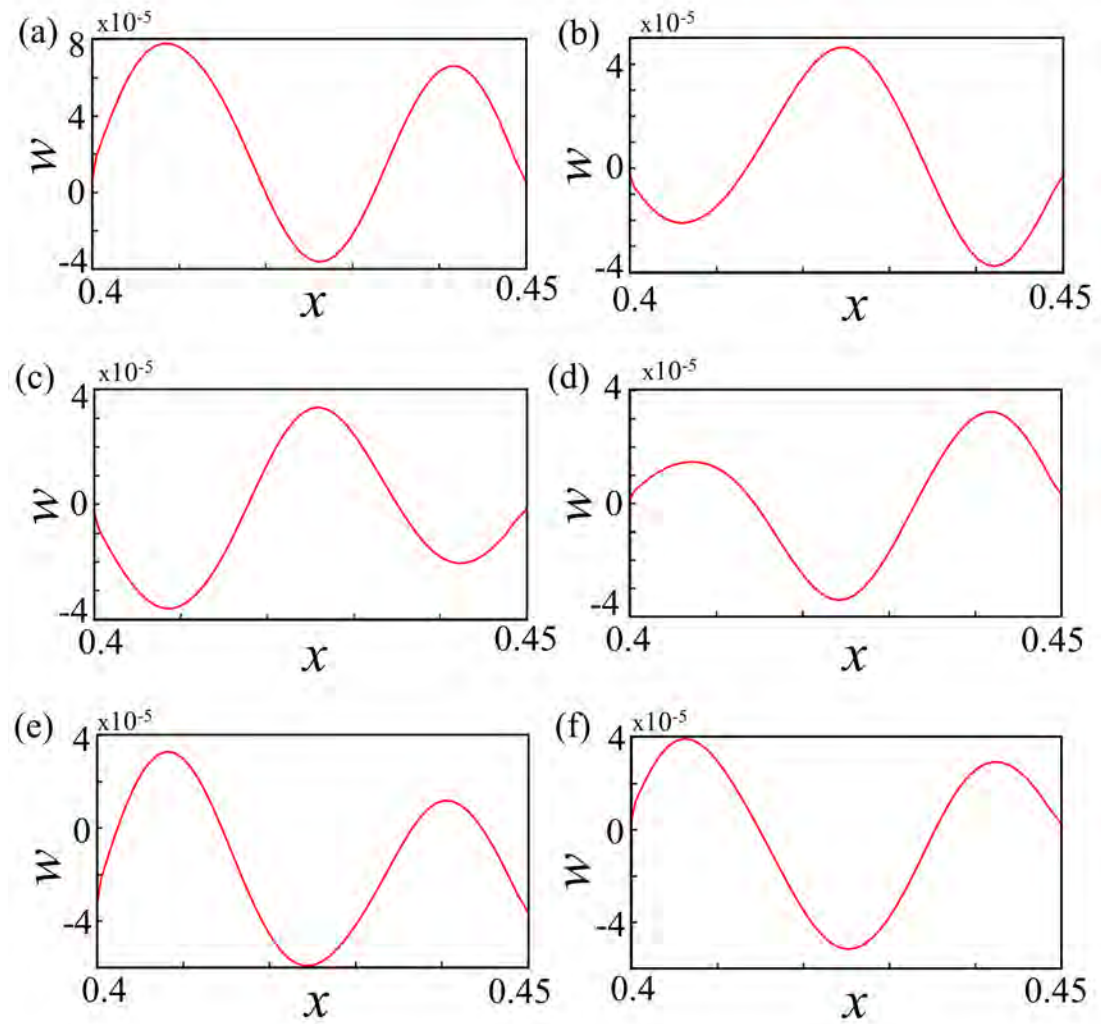


Figure 5.18: Vibration response of EP1_R. (a) $t = 1$, (b) $t = 2$, (c) $t = 3$, (d) $t = 4$, (e) $t = 5$, and (f) $t = 6$.

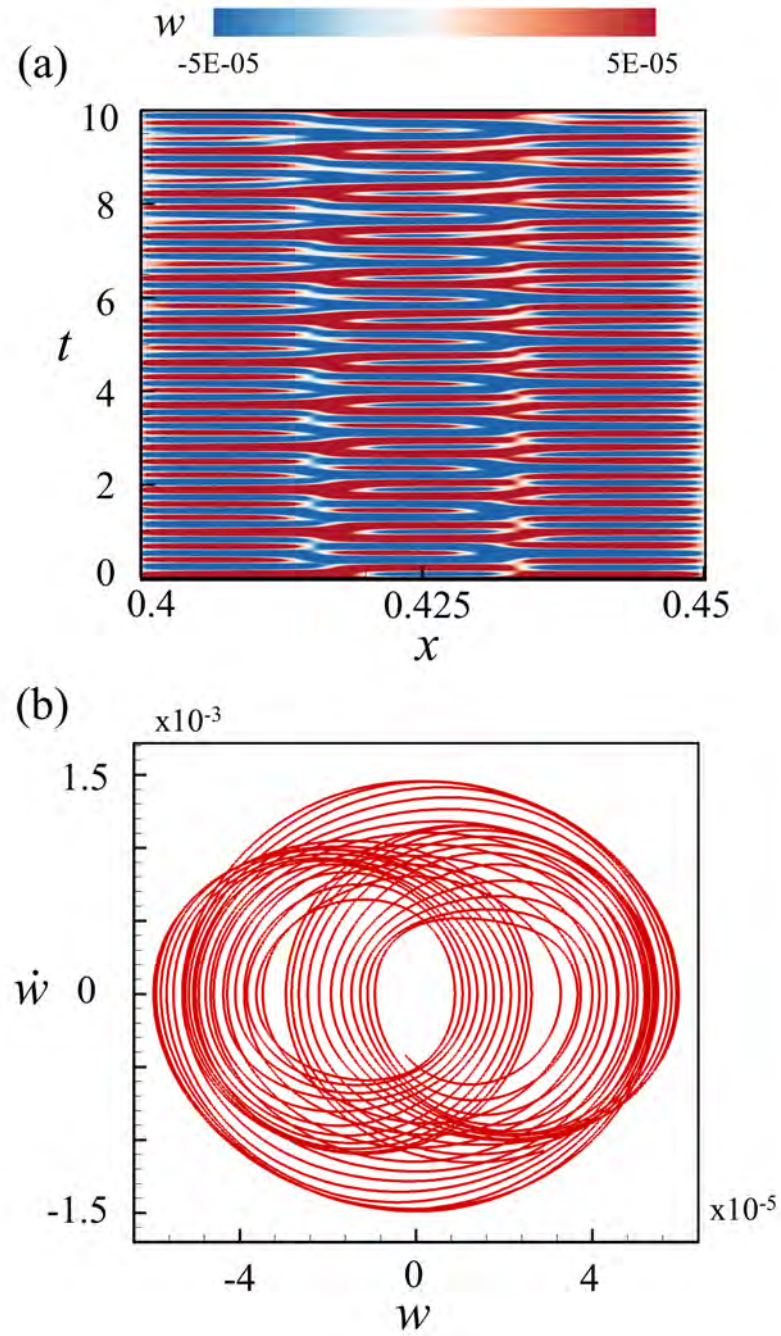


Figure 5.19: (a) Temporal evolution of panel deflection and (b) phase plane plot at center of panel.

is much lower than the maximum boundary layer thickness by a magnitude of three orders which does not distort the mean flow. A regular pattern of displacement at all panel locations can be observed in Figures 5.20(a), (c), (e) and (g) which gives rise to a dominant frequency of 3.37 (third mode) as observed in Figures 5.20(b), (d), (f) and (h). Lower modes of panel natural frequency can also be observed at 1.12 (first mode) and 2.246 (second mode) in frequency plots at much lower amplitudes except at 60% panel length where its magnitude of first mode of panel vibration is comparable to third mode. The uniform periodic vibrational behavior of the panel indicates that the panel is able to absorb the flow energy to maintain its motion. The frequency and displacement plots certainly validate the panel design methodology which is aimed to allow the panel to vibrate in third mode with resonance condition in the presence of fluid loadings.

5.6 Comparison of DAS and PEM Prediction

As PEM is invoked at the beginning of elastic panel design, it is fruitful and informative to assess the correctness and accuracy of PEM prediction with the availability of DAS solution for overall airfoil aeroacoustics with elastic panel. Figure 5.21 shows a comparison of azimuth distributions of p'_{rms} at $(f_{bl})_0$ for EP1R. The p'_{rms} plot obtained from PEM is amplified by a constant factor to make it comparable with DAS result. The plot shows excellent qualitative agreement between the noise radiation pattern observed by DAS and PEM. The levels of noise reduction derived from two types of calculations are found in excellent agreement too (Table 5.2). These results provide confidence in the proposed methodology of using PEM to effectively design elastic panel based on a number of different parameters. The affirmative results also reflect that the PEM can correctly predict the trend of noise reduction by the elastic panel in actual flow by virtue of its capability of capturing the fundamental airfoil tonal noise generation

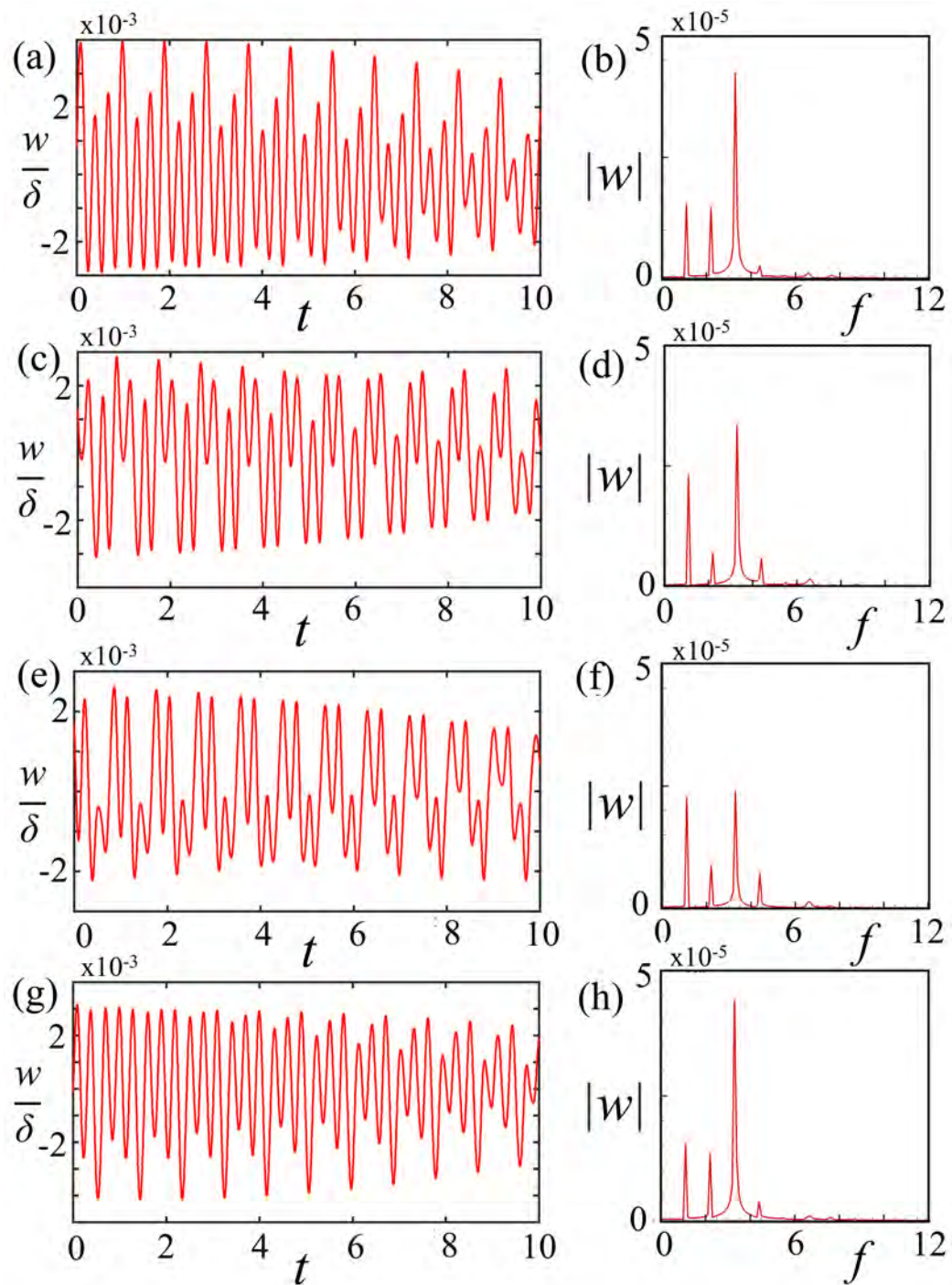


Figure 5.20: Time histories of panel displacements and their frequency spectra.

(a) and (b) 20%, (c) and (d) 40%, (e) and (f) 60%, (g) and (h) 80% panel length.

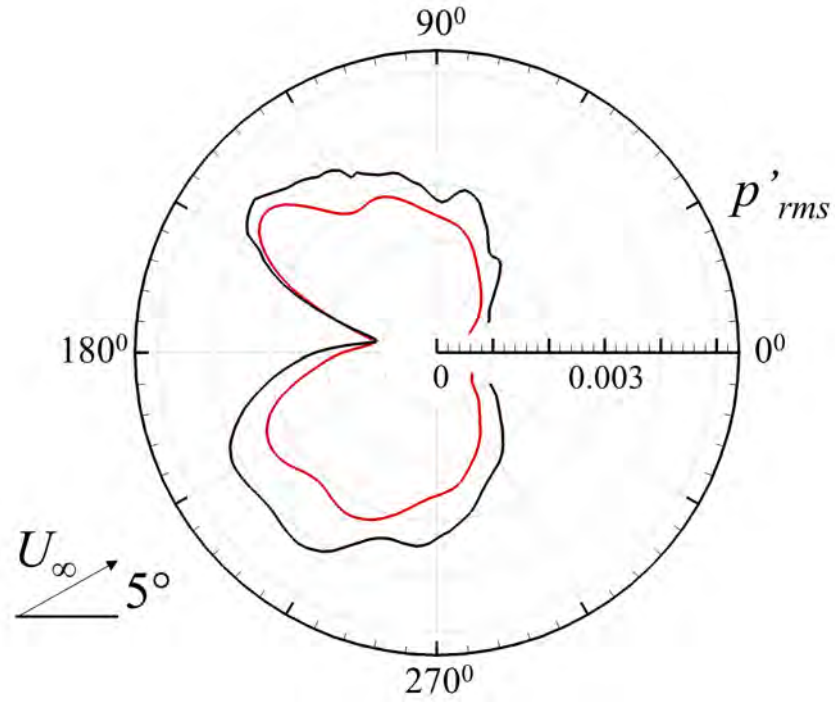


Figure 5.21: Azimuth distribution of p'_{rms} at $r = 3$ for EP1_R case with PEM and DAS.—, PEM solution; —, DAS solution.

processes. It is important to note that the PEM technique takes barely 10% of the computing time of DAS.

Table 5.2: A comparison of level of noise reduction of EP1_R case from PEM and DAS solutions.

	PEM result	DAS result
Average $\Delta SPL_{reduction}$	2.10 dB	2.5 dB
Maximum $\Delta SPL_{reduction} / \theta_{max}$	2.40 dB / 130°	3.0 dB / 120°

5.7 Conclusions

A detailed analysis on the airfoil tonal noise reduction using localized flow-induced vibration of an elastic panel flush-mounted on the suction surface of a NACA 0012 airfoil is presented in this chapter. The idea is fully explored with tonal noise generation by an airfoil flow condition of $M = 0.4$, $AoA = 5^\circ$ and a low $Re = 5 \times 10^4$. The elastic panel is designed in such a way that it weakens the unsteady flow fluctuations within the boundary layer before they scatter as acoustic noise from trailing edge interactions. From PEM results, it is observed that a panel located just ahead of the sharp growth of boundary layer instability within the airfoil separation bubble (EP1) provides the strongest reduction of instabilities responsible for noise generation by its scattering at airfoil trailing edge. Hence, resonant (EP1_R) and non-resonant (EP1_{NR}) panel configurations for this panel are selected for full direct aeroacoustic simulation (DAS) calculations to analyze their effectiveness of the elastic panel in tonal noise reduction.

A comprehensive aerodynamic and acoustic analysis is performed with DAS numerical results to evaluate the panel effectiveness in actual flow conditions. With regard to aerodynamic analysis, boundary layer profiles of the fully rigid airfoil (RS) and EP1 cases indicate that the elastic panels are able to effectively reduce the instabilities within the separated flow which results in a slight reduction in the length of the separation bubble by 3.2% for the resonant panel. The presence of the elastic panel results in a negligibly small change in aerodynamic characteristics of the airfoil which is evident by only a variation of 0.64% and 0.72% in time-averaged C_L/C_D of EP1_R and EP1_{NR} with respect to RS case. The effect of panel vibration in the reduction of transverse velocity fluctuations within the boundary layer is also observed. At the dominant frequency, for the resonant panel, a continuous reduction in velocity fluctuations ranging from 5% to 20% is observed from $x = 0.4$ up till the trailing edge of airfoil. The observed

phenomenon ultimately results in lower tonal noise generation and also weakens the strength of the feedback loop, whereas for the non-resonant panel, the reduction in fluctuations is less pronounced.

Results of acoustic analysis show that the radiation pattern for all the cases appear to be similar; however, the magnitude of fluctuating pressure for $EP1_R$ appears to be much less than RS and $EP1_{NR}$. This fact is further strengthened by the directivity spectrum which indicates that the panel implementation has not altered the overall flow behavior and has resulted in significant reduction in acoustic wave propagation for resonant panel case. The azimuth plot of pressure fluctuations reveals an average *SPL* reduction of 2.5 dB for resonant panel whereas for a non-resonant panel an average reduction of 1.1 dB is observed. A maximum of 3 dB reduction is observed at $\theta = 120^\circ$ for a resonant panel whereas a maximum of 1.45 dB reduction is observed for the non-resonant panel.

Panel dynamic behavior is investigated by phase plots and temporal evolution spectra. The resonant panel vibrates at its third natural mode at all time instances which validates the panel design methodology to achieve structural resonance in the presence of fluid loading on the panel. The fact that the panel vibrates in the desired mode implies that the panel is truly compliant to fluctuating flow-induced loading and is able to effectively absorb energy from the oncoming flow to sustain its resonance condition. Finally, the PEM technique for panel design is compared with DAS results and a strong qualitative agreement is observed in the noise radiation pattern. The fact that the present PEM technique takes barely 10% of the computing time of DAS provides a quick tool for initial panel design. Since the proposed noise reduction method works without any compromise of aerodynamic characteristics, the outcomes of the study evidently suggest that the proposed passive control method with a localized flow-induced vibrating panel is effective in screening out to suppress the fundamental

mechanism for airfoil tonal noise generation. This makes the proposed method a promising technique for modifying the acoustics of any existing aerodynamic or wing profile operating at low Reynolds number.

Chapter 6

Reduction of Airfoil Tonal Noise by Coupled Panel Resonance

6.1 Introduction

The passive method of utilizing a resonant elastic panel has been shown to possess great potential tonal noise reduction up to a maximum of 3 dB at $\theta = 120^\circ$ without any adverse effect on airfoil aerodynamics. Now, the approach for airfoil tonal noise reduction is further enhanced by utilizing structural coupling phenomenon of elastic panels over the airfoil. Details of the panel coupling approach and its implementation on the airfoil are presented in this chapter. The fluid-structure interaction arising from multiple structures in unsteady flow, such as rod-airfoil configuration, cylinders in tandem or multi-cavity system is highly influenced by the hydrodynamic interference among the structures which can result in considerably different acoustic behavior than the individual entities (Lau et al. 2004, Mohany and Ziada 2005, Finnegan et al. 2010, Shaaban and Ziada 2019). In their aeroacoustic study of flow over multiple cavities, Nakiboğlu and Hirschberg (2012) observed constructive and destructive hydrodynamic interference depending on the separation distance between adjacent cavities which is

highly influenced in determining the acoustic behavior of entire flow system. A similar phenomenon of hydrodynamic interference was also observed by Shaaban and Ziada (2019) in their study on multi-cavity pipe arrangement where the effect of constructive interference among the two cavities was found to be much higher than doubling the source of individual cavity. However, the phenomenon of structural coupling of vibrating structures for airfoil noise reduction has not been explored yet. Hence, the possibility of airfoil tonal noise suppression is explored by utilizing the phenomenon of strong and weak structural coupling of two elastic panels mounted on the suction surface of airfoil. The strongly coupled panel configuration (SCC) in the study refers to inter-dynamical structural coupling between the panels whereby their mode shape and vibration pattern remain similar and synchronized at all time instances; and the weakly coupled panel configuration (WCC) refers to the airfoil configuration where the panels vibrate in an asynchronous manner with each other. The condition of strong/weak structural coupling between the panels is highly dependent on the relative fluid loading due to unsteady flow passing over the airfoil surface. Hence, it is imperative to analyze and identify the key airfoil flow characteristics and its interaction with the elastic panels.

In this chapter, the fluid-structure interactions for coupled panel configuration are investigated in detail to identify the key physics (i) of panel structural responses and their mutual influence carried along with the unsteady flow over them, (ii) on the effect of panels coupling on airfoil aerodynamics and acoustics, and (iii) of the governing parameters to achieve coupled structural resonance. It is important to note that the application of multiple panels may result in more complex flow interactions between the flow and panels which may distort the airfoil flow and can even result in noise amplification or aerodynamic performance degradation (Luk et al. 2004, Talboys et al. 2019, Schlanderer and Sandberg

2013). Hence, employing multiple panels on the airfoil surface for noise suppression requires a careful panel configuration design approach. Initially, different airfoil-panel configurations are designed based on the flow characteristics of the rigid airfoil and subsequently analyzed using PEM, to assess their noise suppression potential. The optimal configuration determined from PEM results is then analyzed in detail using DAS and its results are compared with the baseline rigid airfoil and corresponding single panel configurations to uncover the mechanisms responsible for tonal noise suppression arising from fluid-structure interactions and panel inter-dynamics.

6.2 Airfoil-Panel Configurations

The design of airfoil mounted with panels requires certain knowledge of the flow characteristics over the rigid airfoil from which the identification of possible panel placement locations and their required structural properties to achieve resonance condition in the presence of fluid loading can be deduced. Hence, the unsteady flow behavior within the boundary layer over the suction surface of the rigid airfoil is examined first. Subsequently, five different configurations are designed and their effectiveness is assessed with PEM. The adopted design methodology is presented in the following sections.

6.2.1 Panel Length

For the present study, a same short length $L_{EP} = 0.05$ is set for all the configurations because such short length does not provide any significant change in the radius of curvature of airfoil profile as shown in Chapter 4. Furthermore, the effects of such short elastic panel are confined to the flow instability processes with scales comparable to boundary layer thickness to avoid any adverse effect on the

overall airfoil aerodynamics. On the contrary, the dynamic behavior of a long panel driven by flow-induced vibration cannot be easily managed and it may act as an additional acoustic source as the panel/membrane with larger structural wavelength than the acoustic wavelength (or phase speeds $a_{phEP} > a_{phac}$) can create considerable disturbances in the far field and radiate energy into the fluid (Fahy and Gardonio 2007).

6.2.2 Panels Coupling Setup

For the setup of airfoil configuration with coupled panels, the frequency spectrum of transverse velocity fluctuations v' within the boundary layer of rigid airfoil suction surface is initially analyzed (Figure 6.1(a)). A time episode of non-dimensional time $t = 20$ with a sampling frequency of 1×10^5 is taken and a Hamming window with no data overlapping is applied. The spectrum reveals a dominant fundamental frequency $(f_{bl})_0$ of 3.37 within the airfoil boundary layer along with its first and second harmonics at 6.6 and 10 respectively. The magnitude of fluctuations observed at $(f_{bl})_0$ is much higher than its $(f_{bl})_1$ and $(f_{bl})_2$ except at $x = 0.7$ where the fluctuation magnitudes at all dominant frequencies are comparable. The boundary layer natural stability characteristics at $(f_{bl})_0$ for RS are evaluated as shown in Figure 6.1(b). The amplitude of the natural boundary layer growth starts to increase at $x \sim 0.27$ and grow within $0.4 \leq x \leq 0.45$. The amplitude grows remarkably to reach its plateau of 0.043 at $x \sim 0.5$, stays there up till $x \sim 0.58$, then drops rapidly to a dip at $x \sim 0.65$, and eventually grows mildly again up till the trailing edge.

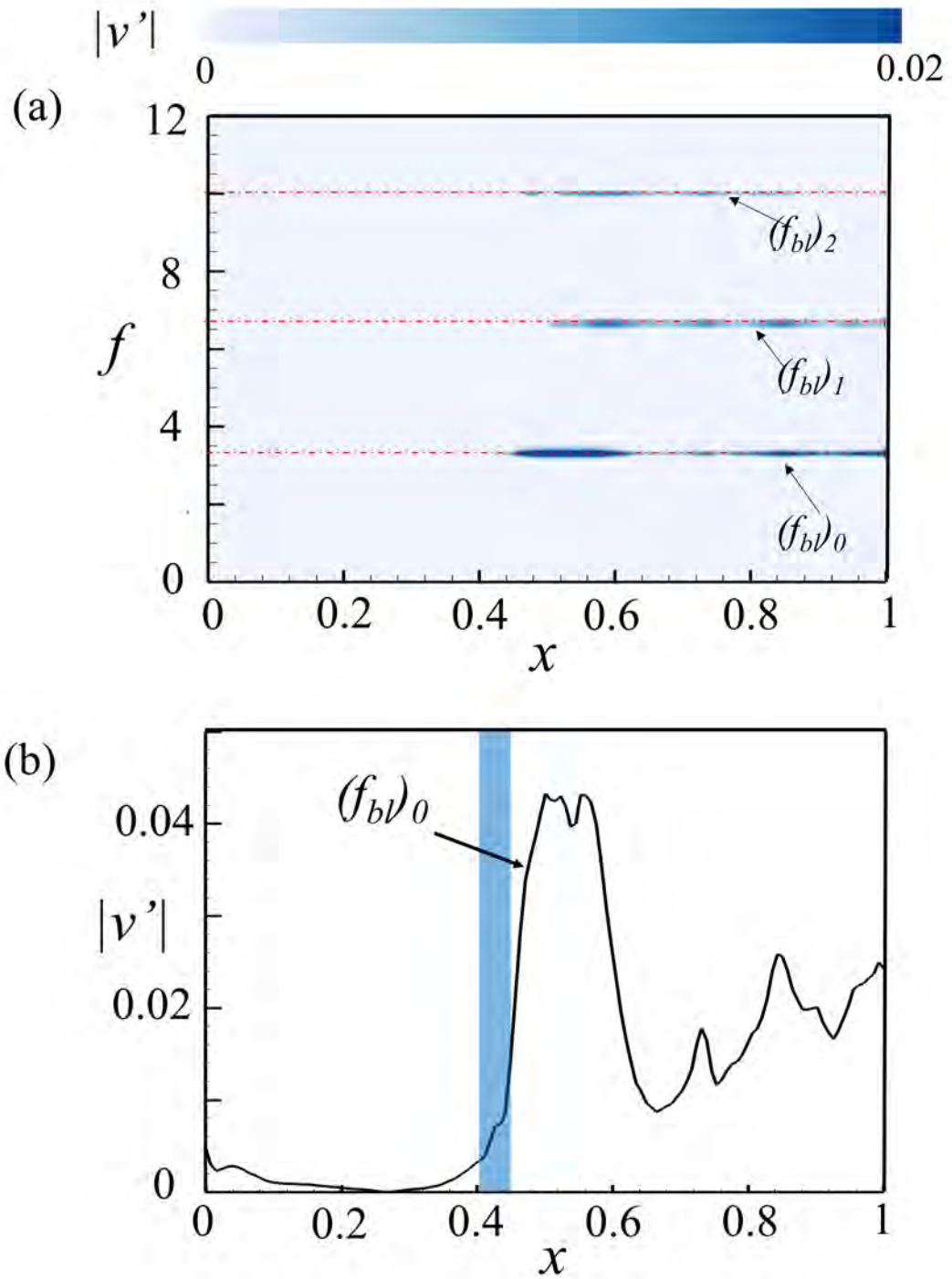


Figure 6.1: (a) Distribution of spectrum of transverse velocity fluctuations along the airfoil, and (b) spatial growth of flow instability over the airfoil suction surface at $(f_{bl})_0$. The blue shaded area in (b) indicates the coverage of panel for SP1 as defined in Section 6.2.2.

The fluid-structure interactions in a coupled structural system are highly influenced by the relative locations between the vibrating structures which may eventually affect the flow and acoustic characteristics of the complete system in a significant manner (Lau et al. 2004, Shaaban and Ziada 2019, Nakiboğlu and Hirschberg 2012). Since the present problem involves complex fluid-panel interactions, it is imperative to carefully ascertain the panel locations in such a way that the panels may be able to sustain strong inter-dynamical coupling in resonance condition. In their study on double cavity system Nakiboğlu and Hirschberg (2012) observed a hydrodynamic interference (constructive/destructive) which directly affects the aeroacoustic characteristics of the system. The nature of hydrodynamic interference was found to be depending on the distance between the cavities and convective wavelength of the hydrodynamic flow. Since the research is also aimed at achieving possible coupling between the panels, it is important to identify the relative location of the panels on the airfoil such that a synchronized structural dynamics is achieved between the panels under the fluid loading. Hence, the apparent convective disturbance wavelength λ_{conv} for the baseline RS case is evaluated to ascertain the relative distance between the panels to achieve coupled structural dynamics. The analysis is performed between the p' signal at a location $(r, \theta) = (-1.12, 135^\circ)$ marked as point A in Figure 6.2 and a series of v' signals along the airfoil surface. The phase difference between a p' and v' signal θ_{12} is evaluated by a transfer-function estimate between the cross power spectral density of both signals (Arcondoulis et al. 2018). The λ_{conv} at $(f_{bl})_0$ is calculated with the phase difference plot for the rigid airfoil (Schumacher et al. 2014, Arcondoulis et al. 2018, Lam and Leung 2018). Figure 6.3(a) shows the wrapped phase plot whereas the unwrapped phase plot is shown in Figure 6.3(b). The region from $x = 0.24$ to 1 sees a regular convective disturbances pattern as the phase change is fairly linear along the airfoil chord whereas the slowly

varying phase in upstream region $x = 0$ to 0.24 shows the acoustic wave pattern (Arcondoulis et al. 2018). A phase difference of 2π indicates a traversal over one disturbance wavelength in Figure 6.3(a). The location corresponding to three full peak-to-peak phase change cycles is chosen in $0.480 \leq x \leq 0.935$ and the apparent wavelength of convective disturbance is found by taking an arithmetic mean (Arcondoulis et al. 2018) which yields $\lambda_{conv} \sim 0.151$. The λ_{conv} can also be evaluated by calculating the inverse of the slope of line obtained by least-square fit as shown in Figure 6.3(b). For example, two different values of $\theta = 2.8\pi$ and 0 are chosen which correspond to $x = 1$ and 0.58 respectively. The λ_{conv} is calculated by inverse of the slope of line by $(1 - 0.58)/(2.8 - 0)$ which yields $\lambda_{conv} \sim 0.15$. The evaluation of λ_{conv} shows that in order to achieve a strong coupling among the panels, the distance between the leading edge of two panels Δd_{le} may be set $n\lambda_{conv}$ wavelength(s) apart, where n is an integer.

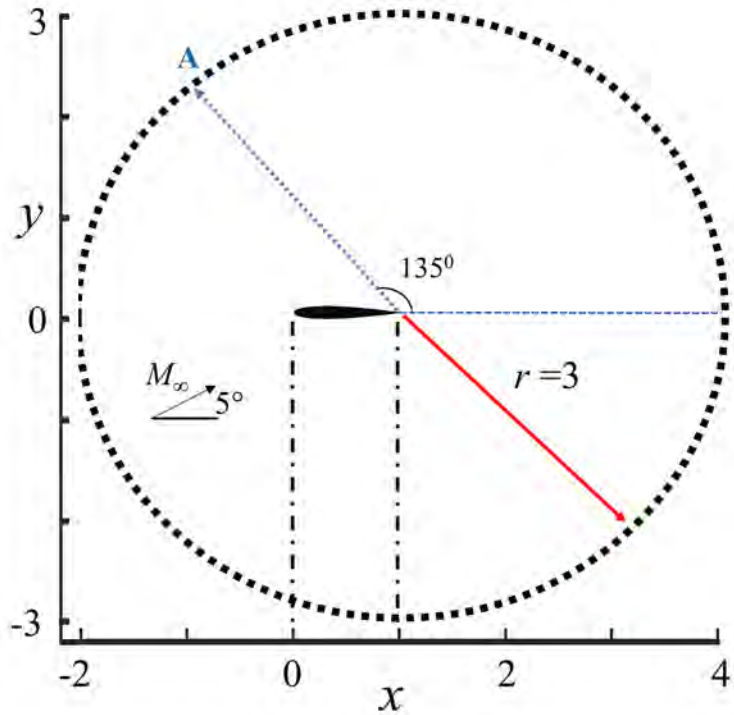


Figure 6.2: Virtual probes location around the airfoil at $r = 3$.

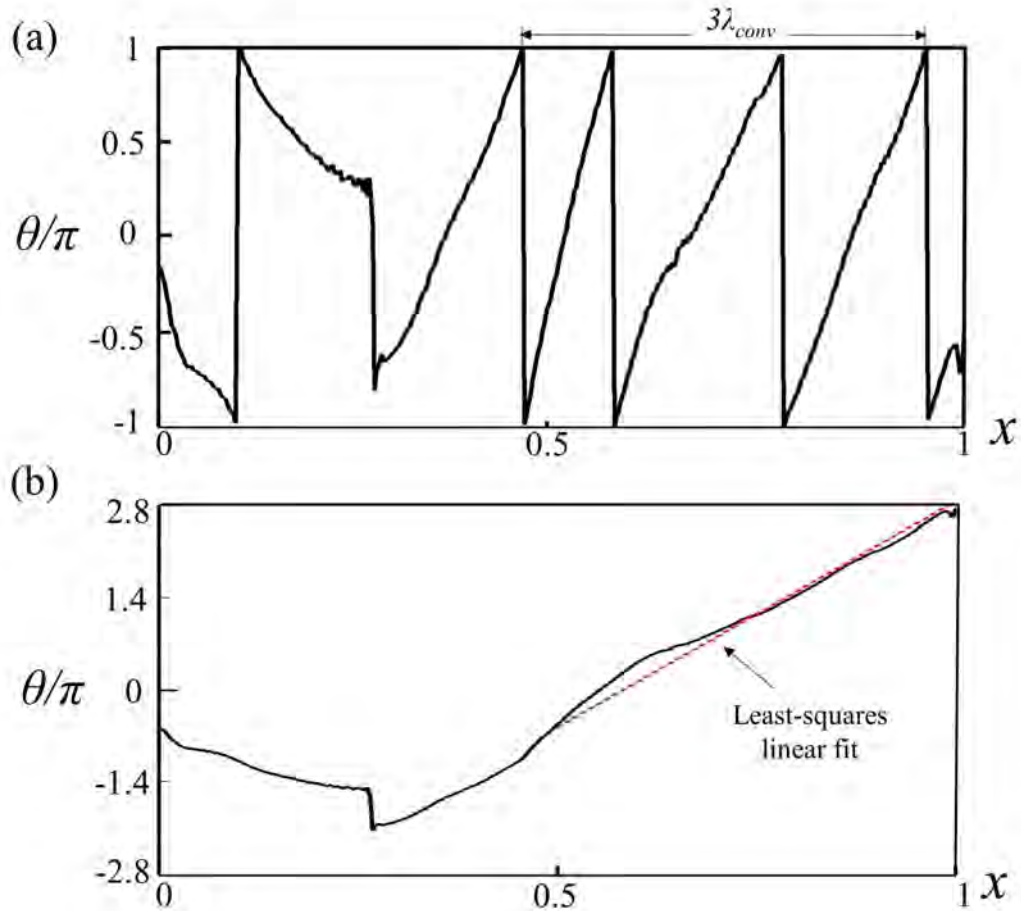


Figure 6.3: Phase difference between the acoustic signals at location $(r, \theta) = (-1.12, 135^\circ)$ and velocity signals along the airfoil chord. (a) wrapped phase plot, and (b) unwrapped phase plot.

Different airfoil-panel configurations are initially designed and their noise suppression potential by PEM is analyzed. To establish a concrete understanding on the configuration setup, it is intended to identify the certain limitations/threshold beyond which the panel configuration may become ineffective or even result in excessive noise generation. For the ease of discussion, the single panel airfoil configurations are designated by “SP”. All strongly coupled panel configurations are designated with “SCC” whereas the weakly coupled panel configurations are designated with “WCC”. Figure 6.4 shows the schematic of airfoil-

panel configuration designs in the present study. As the previous study reveals Arif et al. (2020) that a panel located at an upstream location of sharp boundary layer instability growth within the airfoil separation bubble is found to provide the strongest suppression of flow instabilities and consequently tonal noise, so the location of the first panel is thus fixed with its leading edge at $x_{le} = 0.40$ (designated as SP1 and marked by the blue shaded area in Fig. 6.1(b)) except SCC4. Table 6.1 presents the details of all airfoil-panel configurations considered in this study.

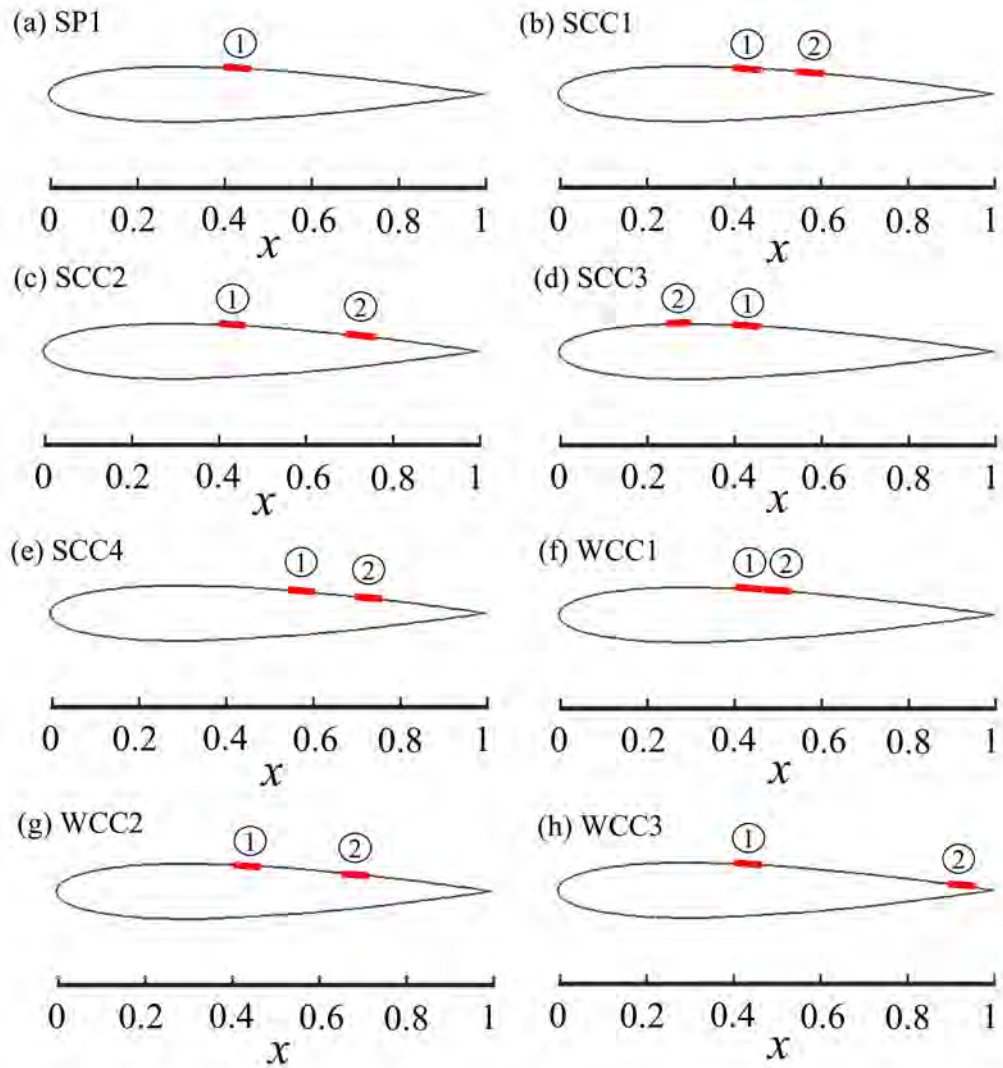


Figure 6.4: Schematic sketch of airfoil-panel configuration designs. ①, first panel; ②, second panel.

6.2.3 Panel Structural Properties

For the panel to effectively absorb the flow energy from the boundary layer instabilities to sustain its vibration in resonance, the panel structural properties are selected such that the panel natural frequency $(f_{EP})_n$ coincides with the $(f_{bl})_n$ as discussed in Chapter 4. All the panels considered in this study are designed to vibrate in structural resonance with their third natural bending mode under

Table 6.1: Details of airfoil-panel configurations design.

Case	First panel	Second panel	Separation of panels (Δd_{te})
SP1	0.40	-	-
SCC1	0.40	0.55	$1\lambda_{conv}$
SCC2	0.40	0.70	$2\lambda_{conv}$
SCC3	0.40	0.25	$-1\lambda_{conv}$
SCC4	0.55	0.70	$1\lambda_{conv}$
WCC1	0.40	0.45	$0.34\lambda_{conv}$
WCC2	0.40	0.625	$1.5\lambda_{conv}$
WCC3	0.40	0.90	$3.4\lambda_{conv}$

the excitation of airfoil boundary instability. Table 6.2 provides the details of the panel structural properties.

Table 6.2: Normalized elastic panel parameters.

Material properties				Panel natural frequency		
L_{EP}	h_{EP}	T_{EP}	ρ_{EP}	$(f_{EP})_1$	$(f_{EP})_2$	$(f_{EP})_3$
0.05	0.009	0.725	6367.35	1.123	2.246	3.369

6.3 Assessment of Noise reduction Potential by PEM

The evolution of flow characteristics in the vicinity of the airfoil through PEM is analyzed. For PEM, the computational domain, grid, and simulation parameters are kept same as those discussed in Chapter 3. The influence of panel location setting on the boundary layer instabilities over the airfoil is analyzed with the

change of the magnitude of v' over the suction surface of the airfoil at the $(f_{bl})_0$ for each airfoil-panel configuration (Fig. 6.5(a)). The analysis reveals that the strongly coupled configurations effectively reduce the boundary layer instabilities to a different extent with respect to the RS case. The extent of reduction in v' varies with the location of the second panel. The case SCC1 provides a much higher reduction as compared to SCC2, SCC3, and SCC4. Furthermore, the reduction in v' for SCC3 is observed to be similar to the SP1 case which implies that the second panel located at an upstream location is ineffective due to weaker instabilities within $0.25 \leq x \leq 0.30$ (Fig. 6.1(b)). The variation of v' for the weakly coupled configurations shows different behavior where both reduction and amplification of boundary layer instabilities are observed. The cases WCC1 and WCC2 result in an increase in v' which indicate that their fluid-structure interaction induces an adverse effect on the flow characteristics. For WCC3, a slight reduction in v' is observed but it is much lower than SP1. Nevertheless, WCC3 still provides some reduction in boundary layer instabilities in contrast to WCC1 and WCC2. To further investigate the extent of reduction/amplification in the flow fluctuations, the percent deviation in the magnitude of v' at airfoil suction surface at $(f_{bl})_0$ for each configuration is evaluated with respect to RS (Fig. 6.5(b)). The weakening effect of panel vibration on v' within the boundary layer is evident for cases SCC1, SCC2, SCC3, SCC4, and WCC3. It is interesting to note that a slight reduction in v' is also observed from airfoil leading edge up till the leading edge of the first panel for these configurations. Such observation is attributed to upstream propagating acoustic wave scattered from airfoil trailing edge and its weakening provides an evidence for reduced strength of aeroacoustic feedback loop in these configurations. Figure 6.5(b) illustrates that the extent of reduction in v' for SCC1 is much higher than the other configurations where an average reduction of $\sim 60\%$ within $0.3 \leq x \leq 1$ is observed with respect to RS. On

the other hand, WCC1 and WCC2 show continuous amplification in the v' along the suction surface. All the results clearly illustrate the effectiveness of SCC1 in leveraging the maximum flow energy absorption for effective suppression of airfoil boundary layer flow unsteadiness before their eventual scattering as noise.

The effectiveness of different airfoil-panel configurations in airfoil noise suppression is ascertained by the azimuthal acoustic pressure fluctuation p'_{rms} evaluated at $r = 3$ from the trailing edge (Fig. 6.6(a)). The noise radiation patterns are observed to form a dipole skewed towards the upstream direction with the strongest radiation at $\theta \sim 135^\circ$ and $\theta \sim 240^\circ$ for all cases. The extent of variation in p'_{rms} varies with configurations where WCC1 and WCC2 show an increase in p'_{rms} at all azimuth locations. All the other configurations show different extents of reduction in p'_{rms} in which SCC1 is able to achieve much higher reduction than other configurations. The extent of noise suppression is further illustrated with the reduction in sound pressure level $\Delta SPL_{reduction} = 20 \times \log_{10} (p'_{rms,EP}/p'_{rms,RS})$ as shown in Fig. 6.6(b). An average noise suppression around the airfoil of 8.8 dB is observed for SCC1. Its maximum suppression of 9.8 dB occurs at $\theta \sim 220^\circ$ which is significantly higher than that (2.4 dB) achieved by the single panel configuration SP1. For SCC2, an average noise suppression of 2.6 dB is observed which is slightly higher than SP1. For SCC3, an average noise suppression of 2.1 dB is observed which is comparable to SP1 noise suppression. Interestingly, an average noise suppression of only 0.9 dB is observed for SCC4 which signifies the importance of the matching of panel placement and coupling characteristics whereas satisfaction of the latter alone does not guarantee high noise suppression. For the weakly coupled configuration WCC3, average noise suppression of 1.1 dB is observed which is much lower than the SP1 case. For WCC1 and WCC2, an increase in noise generation with an average of 0.4 dB and 1.6 dB is observed respectively. The results clearly indicate that the weakly

coupled configurations have adversely affected the noise suppression potential of airfoil-panel configuration.

Table 6.3: Effectiveness of airfoil configurations in tonal noise reduction (PEM prediction).

Configuration	Avg $\Delta SPL_{reduction}$ (dB)	Max $\Delta SPL_{reduction}/\theta_{max}$ (dB)/(°)	Max $\Delta SPL_{amp}/\theta_{max}$ (dB)/(°)
SP1	2.1	2.4 / 130	- / -
SCC1	8.8	9.8 / 220	- / -
SCC2	2.6	3.7 / 124	- / -
SCC3	2.1	2.4 / 130	- / -
SCC4	0.9	1.0 / 240	- / -
WCC1	-0.4	-	0.5 / 150
WCC2	-1.6	-	2.2 / 146
WCC3	1.1	1.8 / 162	-

6.4 DAS Analysis of Airfoil-Panel Configurations

PEM results provided a good qualitative assessment of different configurations based on noise radiation and reduction in flow instabilities. The airfoil-panel configuration with coupled elastic panels SCC1 is found to be most effective in tonal noise reduction among all the configurations studied. However, in order to analyze the physical mechanisms involved in the panel inter-dynamical relationship, their fluid-structure interactions and their effects on airfoil aerodynamics and acoustics, high-fidelity DAS calculation is performed for this case. The airfoil configurations with single panel cases at $x = 0.4$ (SP1) and $x = 0.55$ (SP2) are

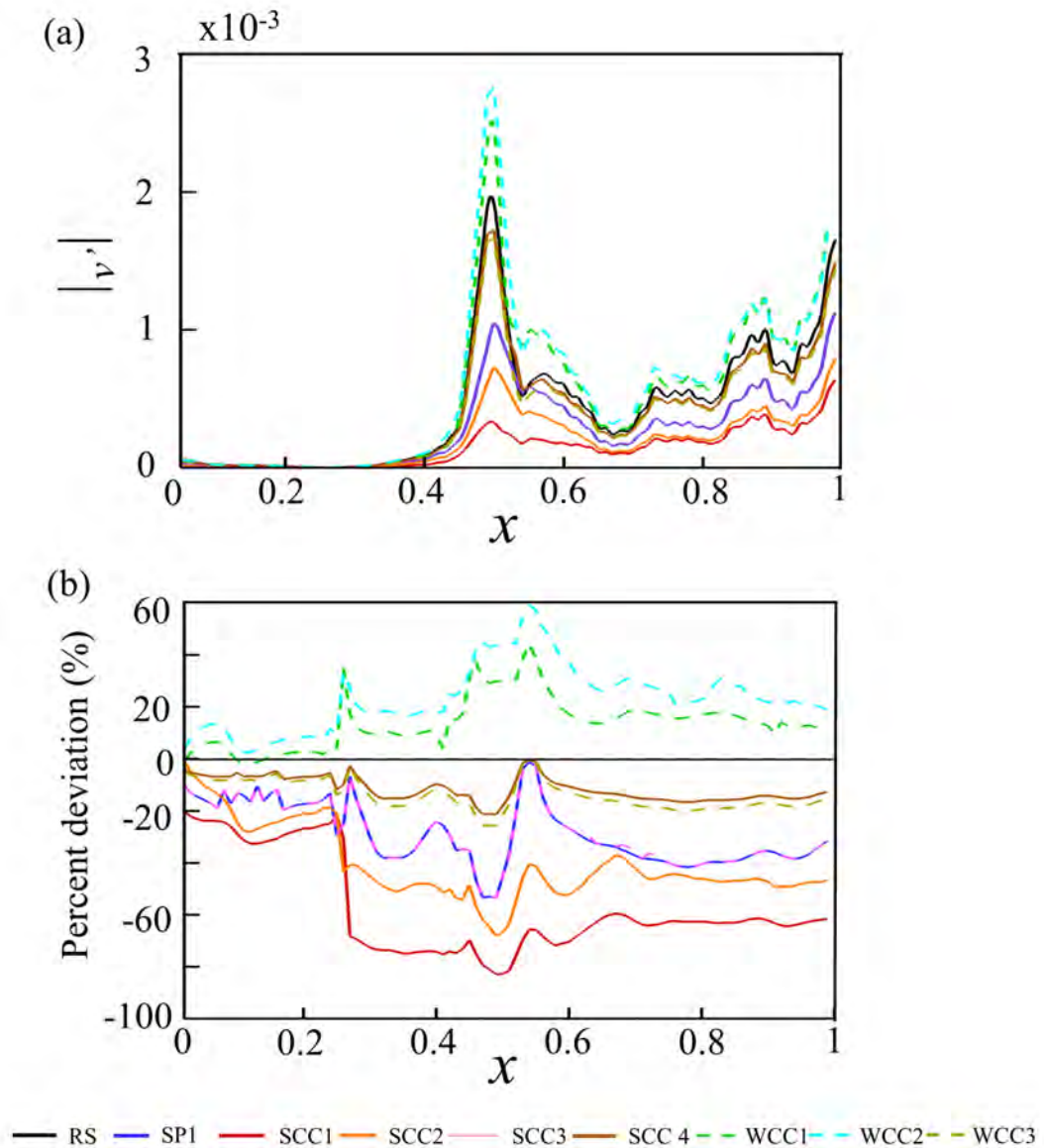


Figure 6.5: (a) PEM prediction of spatial growth of boundary layer instabilities at $(f_{bl})_0$. (b) Deviation in magnitude of transverse velocity fluctuations v' along airfoil suction surface from RS. Note that the results for SCC3 and SP1 almost overlap.

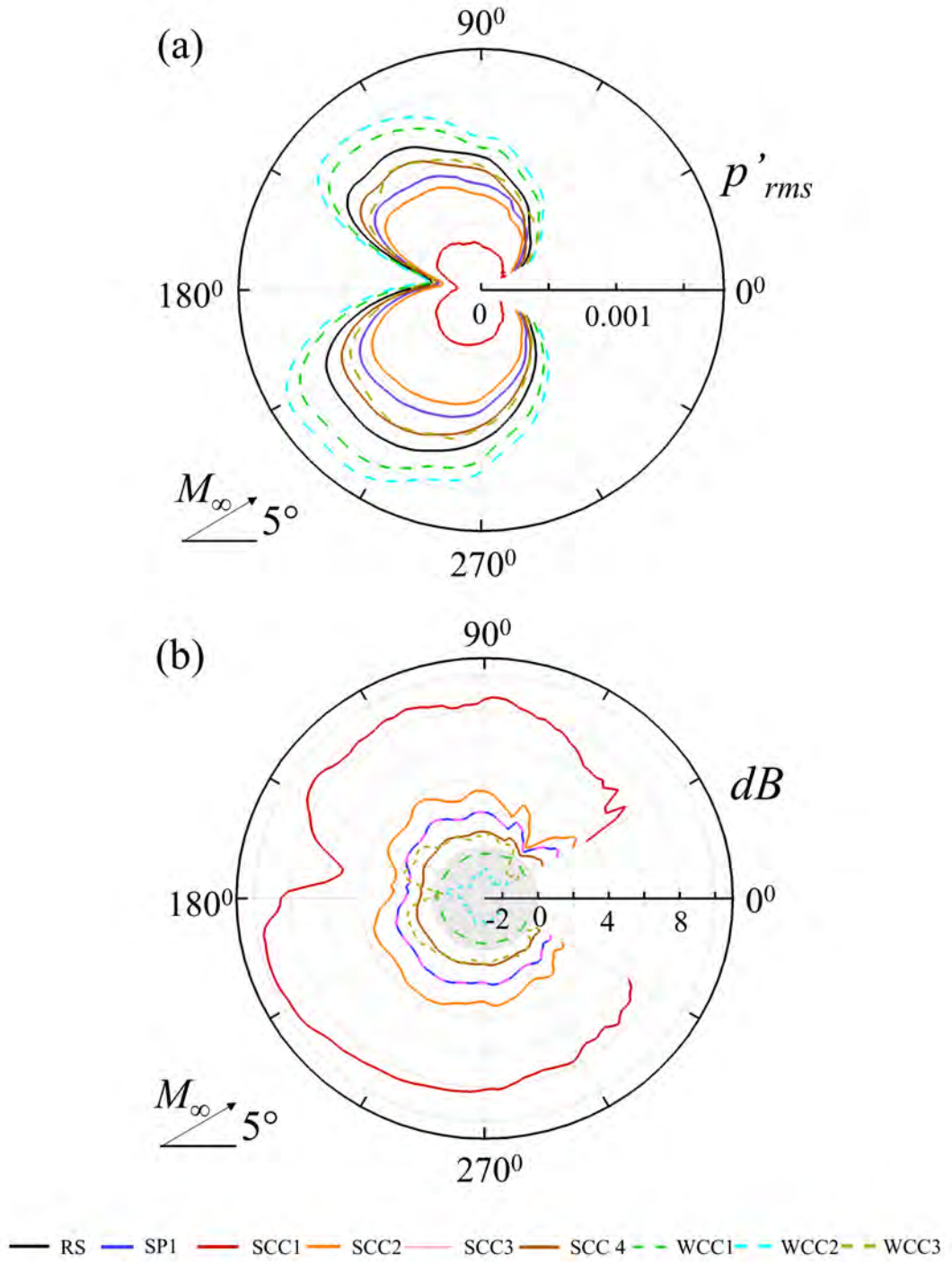


Figure 6.6: Effect of elastic panel(s) on noise generation from PEM analysis. (a) Distribution of p'_{rms} at $r = 3$, and (b) $\Delta SPL_{reduction}$ at $r = 3$. The area shaded in gray indicates SPL amplification. Note that the data for SCC3 and SP1 almost overlaps.

also analyzed individually to identify the effect of coupled structural resonance in comparison with a single resonant panel at the same locations.

6.4.1 Airfoil Aerodynamics

In an attempt to investigate the flow characteristics near the airfoil surface and its wake, the airfoil flow field analysis is carried out for chosen airfoil-panel configurations (RS, SP1, SP2 and SCC1). Figures 6.7(a)-(d) show the time-averaged streamlines around the airfoil for all four configurations. The flow field around the airfoil is observed to be similar for all chosen configurations which confirm that the panel dynamics of such short panel(s) do not produce any observable effects on the overall flow characteristics of the airfoil. The flow separation, reattachment, and LSB over the airfoil suction surface can be clearly observed along with recirculation regions prior to flow reattachment points. The recirculation region for RS case is observed to be much longer than SP1, SP2 and SCC1. The flow separation point is observed to be identical for all chosen configurations whereas the reattachment point shifts upstream for SP1 by 3.2%, SP2 by 2.4% and SCC1 by 4.9% (Table 6.5) resulting in a much shorter LSB for the airfoil-panel configuration with coupled elastic panels. The flow characteristics over the airfoil indicate that the panel vibrations excite the flow in its vicinity so effectively that it presses the detached shear layer closer to panel surface and results in early flow reattachment than RS case.

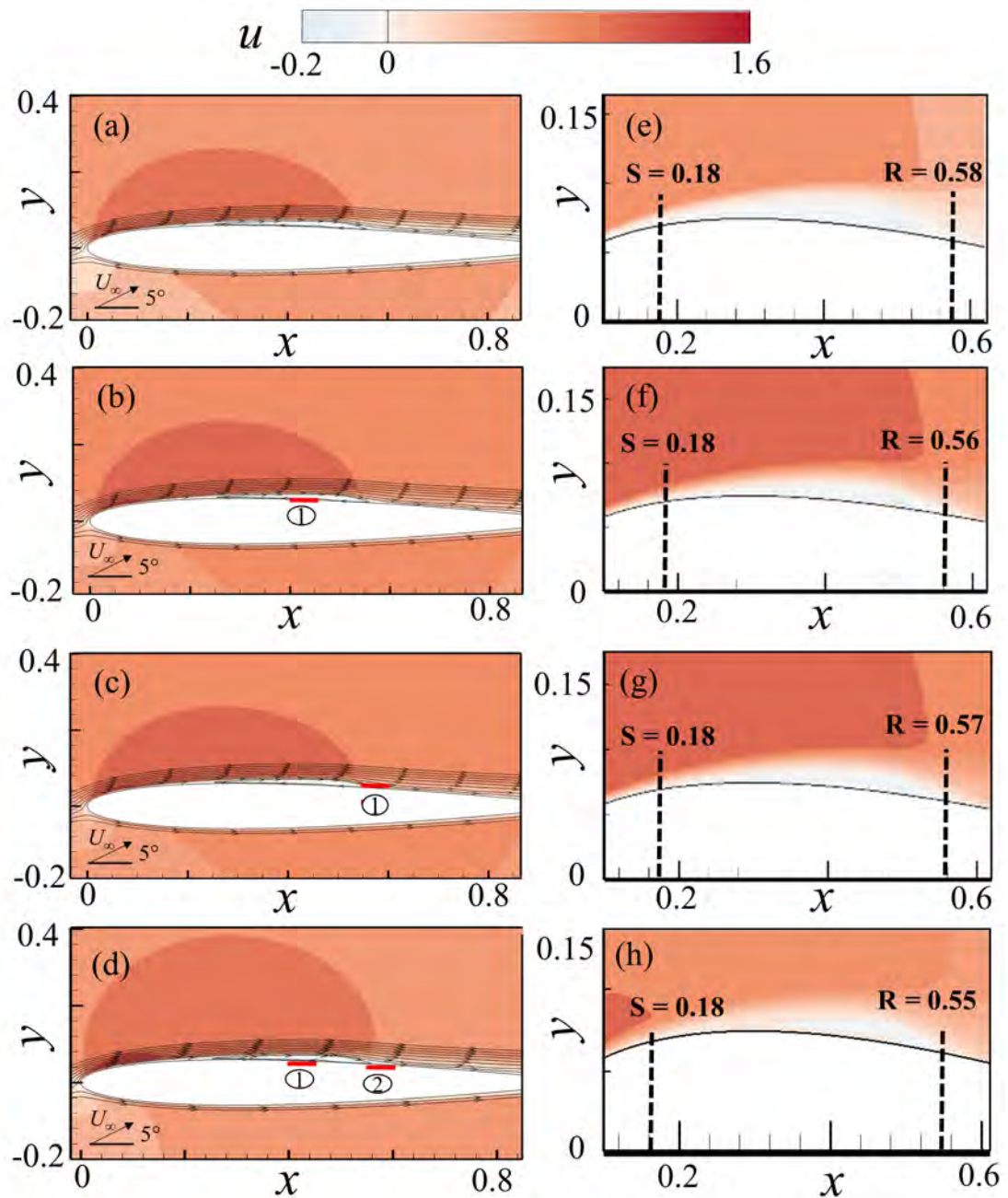


Figure 6.7: Time-averaged streamlines over the airfoil surface; (a) RS, (b) SP1, (c) SP2, and (d) SCC1. Closeup views of airfoil suction surface indicating flow separation and reattachment points; (e) RS, (f) SP1, (g) SP2, and (h) SCC1. ①, first panel; ②, second panel.

The effect of panel vibration on flow instabilities is analyzed by evaluating

the time histories of transverse velocity fluctuations at different chord locations downstream of boundary layer reattachment point over the suction surface of airfoil as shown in Figure 6.8. For brevity, only a time episode of $t = 4$ comprising of ~ 13 periodic cycles is shown. The overall pattern of velocity fluctuations is periodic with respect to time for all cases where the localized flow-induced vibration of elastic panels in SCC1 provides significant reduction of flow instability growth at all chord locations as compared to SP1 and SP2 which indicates that the coupled panel configuration absorbs the flow fluctuation energy more effectively and leaves less flow distortion for the scattering at airfoil trailing edge. To further quantify the extent of loss of energy in the instabilities for all cases, the magnitudes of squared velocity fluctuations $|v'^2|$ are integrated over a consistent time window of $t = 0 - 10$ and listed in Table. 6.4. Terms in brackets indicate the percentage difference with respect to the baseline RS case. A significant reduction in $|v'^2|$ is observed at all chord locations for SCC1 indicating high loss of energy from the flow as compared to other configurations.

In an attempt to investigate the flow characteristics near the airfoil surface and its wake, the airfoil flow field analysis is carried out for all configurations. The airfoil wake characteristics are analyzed by evaluating the velocity profiles downstream of the airfoil at $x = 1.05$ and 1.5 for all cases (Figure 6.9). The wake profile is asymmetric about centerline due to flow incidence of 5° . In the close vicinity of trailing edge ($x = 1.05$), a significant velocity deficit is observed for all chosen cases where a minimum velocity (u/U_∞) of 0.34 is determined for RS case. The wake width is significantly reduced by 32% for SCC1 as compared to RS due to less vigorous flow fluctuations within the boundary layer over the suction surface of the airfoil. For SP1 and SP2 the velocity deficits are respectively reduced by 22% and 17% at $y = 0.02$. At a further downstream location ($x = 1.5$), the wake profile shifts further towards positive y -axis with less intensive velocity

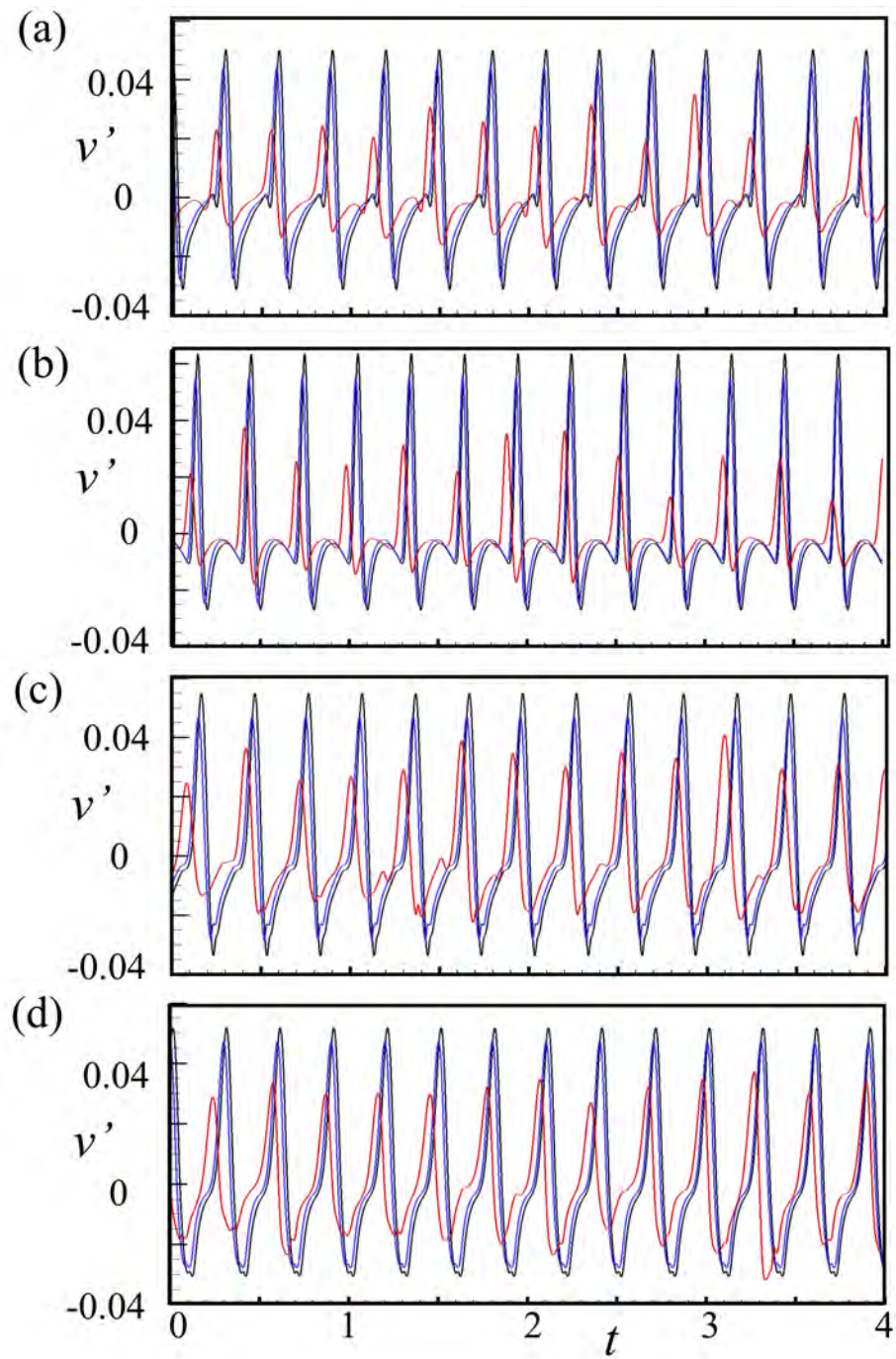


Figure 6.8: Time history of transverse velocity fluctuations v' . (a) $x = 0.7$, (b) $x = 0.8$, (c) $x = 0.9$, and (d) $x = 0.99$. —, RS; —, SP1; —, SCC1.

Table 6.4: Comparison of $|v'^2|$ for different configurations.

Case	Locations			
	$x = 0.7$	$x = 0.8$	$x = 0.9$	$x = 0.99$
RS	4.074×10^{-4}	4.798×10^{-4}	6.006×10^{-4}	6.095×10^{-4}
SP1	3.126×10^{-4} (-23.26%)	3.706×10^{-4} (-22.75%)	4.807×10^{-4} (-20.80%)	5.103×10^{-4} (-16.2%)
SP2	3.298×10^{-4} (-19.04%)	3.951×10^{-4} (-17.67%)	5.061×10^{-4} (-15.73%)	5.221×10^{-4} (-14.33%)
SCC1	0.890×10^{-4} (-78.14%)	1.100×10^{-4} (-77.07%)	1.874×10^{-4} (-68.78%)	2.319×10^{-4} (-61.94%)

deficit. However, the velocity deficit for SCC1 is still lower than SP1, SP2 and RS cases. All in all the results of flow field analysis clearly indicate that the airfoil-panel configuration with coupled elastic panels is able to effectively reduce the strength of boundary layer instabilities and airfoil wake.

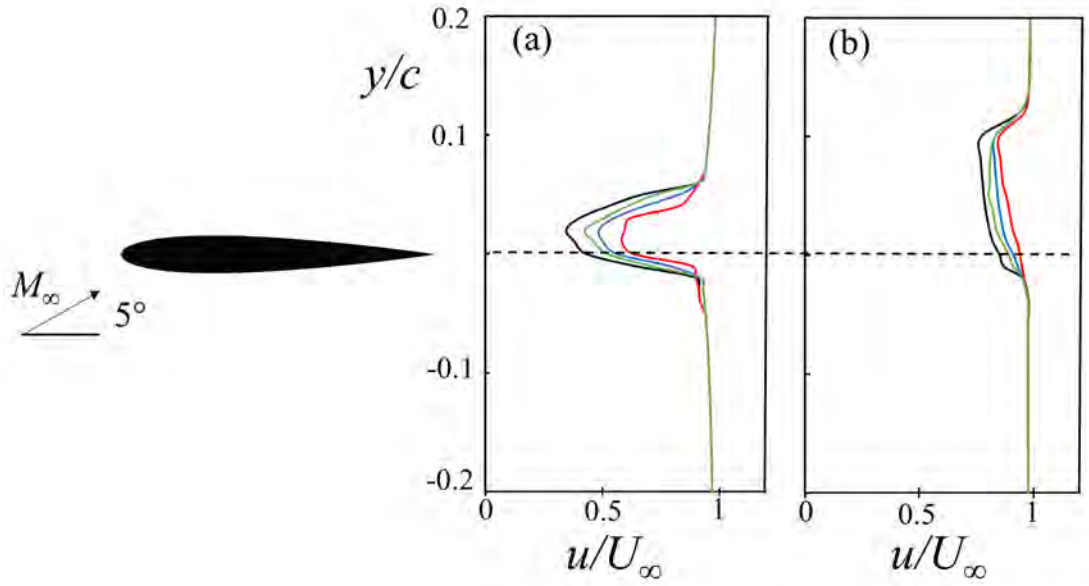


Figure 6.9: Velocity profiles in airfoil near wake region at (a) $x = 1.05$, and (b) $x = 1.5$. —, RS; —, SP1; —, SP2; —, SCC1.

The aerodynamic coefficients for RS, SP1, SP2 and SCC1 configurations are also evaluated and their temporal statistics are compared in Table 6.5. The time-averaged $C_{L,mean}$ for SP1, SP2 and SCC1 are found to be 0.4889, 0.4891 and 0.4861 respectively. All of them are slightly higher than that of RS case due to reduction in the length of LSB and effective mean camber provided by the elastic panel (Galvao et al. 2006). Compared to RS case, the overall lift to drag ratio $C_{L,mean}/C_{D,mean}$ slightly varies for SP1, SP2 and SCC1 by only 0.64%, 0.60% and 1.48% respectively which is much lower than the loss of aerodynamic efficiency with membrane airfoil design ($\sim 21\%$) at lower AoA (Serrano-Galiano et al. 2018). Hence, the overall aerodynamic efficiency of the airfoil is essentially not degraded in the airfoil-panel configuration with coupled elastic panels.

Table 6.5: Aerodynamic coefficients for RS, SP1, SP2 and SCC1 cases. Values in brackets show the percent deviation from RS case.

Case	$C_{L,mean}$	$C_{D,mean}$	$C_{L,mean}/C_{D,mean}$	x_{sep}	x_{reatt}
RS	0.4855	0.01850	26.24	0.180	0.585
SP1	0.4889 (+0.70%)	0.01875 (+1.35%)	26.07 (-0.64%)	0.180 (-)	0.566 (-3.2%)
SP2	0.4891 (+0.74%)	0.01873 (+1.24%)	26.08 (-0.60%)	0.180 (-)	0.571 (-2.4%)
SCC1	0.4861 (+0.12%)	0.01881 (+1.67%)	25.85 (-1.48%)	0.180 (-)	0.556 (-4.9%)

6.4.2 Airfoil Acoustics

The airfoil acoustics is analyzed by plotting the instantaneous fluctuating pressures p' for all configurations at the same time instance of maximum lift fluctuation and shown in Figure 6.10. Region of prominent instabilities on the suction surface of airfoil can be observed for all cases. Subsequently, acoustic waves appear to originate from the trailing edge and propagate towards upstream of the airfoil with much higher magnitude as compared to the acoustic waves in the downstream direction. Although the radiation patterns for all the cases are similar, a significant difference in the magnitude of fluctuating pressures and acoustic radiation can be observed. The strength of acoustic radiation for SCC1 appears to be much less than RS, SP1 and SP2 configurations.

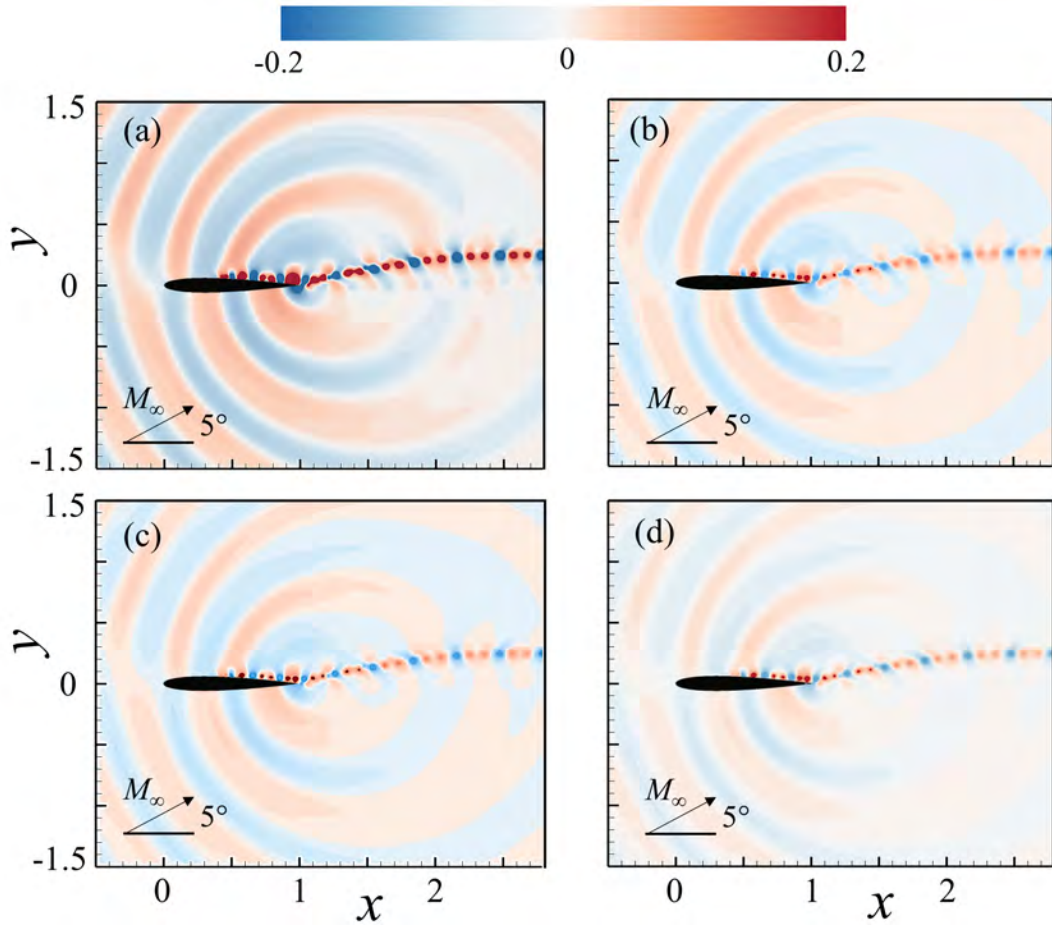


Figure 6.10: Instantaneous pressure fluctuations p' . (a) RS, (b) SP1, (c) SP2, and (d) SCC1.

The azimuth variations of p'_{rms} and $SPL_{reduction}$ at $r = 3$ are evaluated and shown in Figure 6.11. Figure 6.11(a) shows a significant reduction in acoustic radiation by SCC1 at all azimuth locations as compared to RS, SP1 and SP2. The overall reduction is observed to be more significant towards upstream locations. The maximum reduction in p'_{rms} is observed at $\theta = 140^\circ$ and $\theta = 210^\circ$ for SCC1 which correspond to a maximum $SPL_{reduction}$ of ~ 7.9 dB whereas a maximum reduction of ~ 3 dB and ~ 2.3 dB is observed for SP1 and SP2 respectively (Figure 6.11(b)). An average $SPL_{reduction}$ of ~ 7.6 dB is observed all around the airfoil for SCC1 as compared to ~ 2.5 dB and ~ 1.9 dB for SP1 and

SP2 respectively. The acoustic analysis clearly indicate that the overall effect of airfoil-panel configuration with coupled elastic panels in tonal noise reduction is more than the arithmetic sum of the noise reduction achieved by the respective individual single panel configurations (SP1 and SP2). A similar phenomenon of hydrodynamic interference was also observed by Shaaban and Ziada (2019) in their study on multi-cavity pipe arrangement where the effect of constructive interference among the two cavities was found to be much higher than doubling the source of individual cavity. Hence, it signifies the importance of coupling among the panels in noise reduction capabilities for the present study. The physical mechanisms for such high noise reduction capability of this configuration would be further explored in the subsequent sections.

6.4.3 Panel-Structure Coupling

The vibration of elastic panel due to unsteady fluid loading results in a complex structural behavior in both spatial and temporal domain so it is important to analyze the panel dominant structural modes. Fourier mode decomposition (FMD) analysis (Li et al. 2020) is utilized to extract the vibration modes of interest and analyze the panel displacement at these modes. For FMD analysis, the panel displacement data w is arranged in a time-space matrix and FFT is employed to transform it into frequency-space domain. The dominant modes of the elastic panel are extracted by plotting the Fourier amplitude of w along each panel location at $f_{EP} = 1.1, 2.2$ and 3.3 which corresponds to first, second and third mode respectively (Table 4.1). Figures 6.12(a) and (b) show the extracted modal shapes for the selected f_{EP} from SP1 and SP2 configurations. Different mode shapes are easily discernible where the amplitude of third mode is observed to be much higher than other modes. The amplitude of w for the panel in SP2 is slightly higher than that in SP1 which can be attributed to the presence of

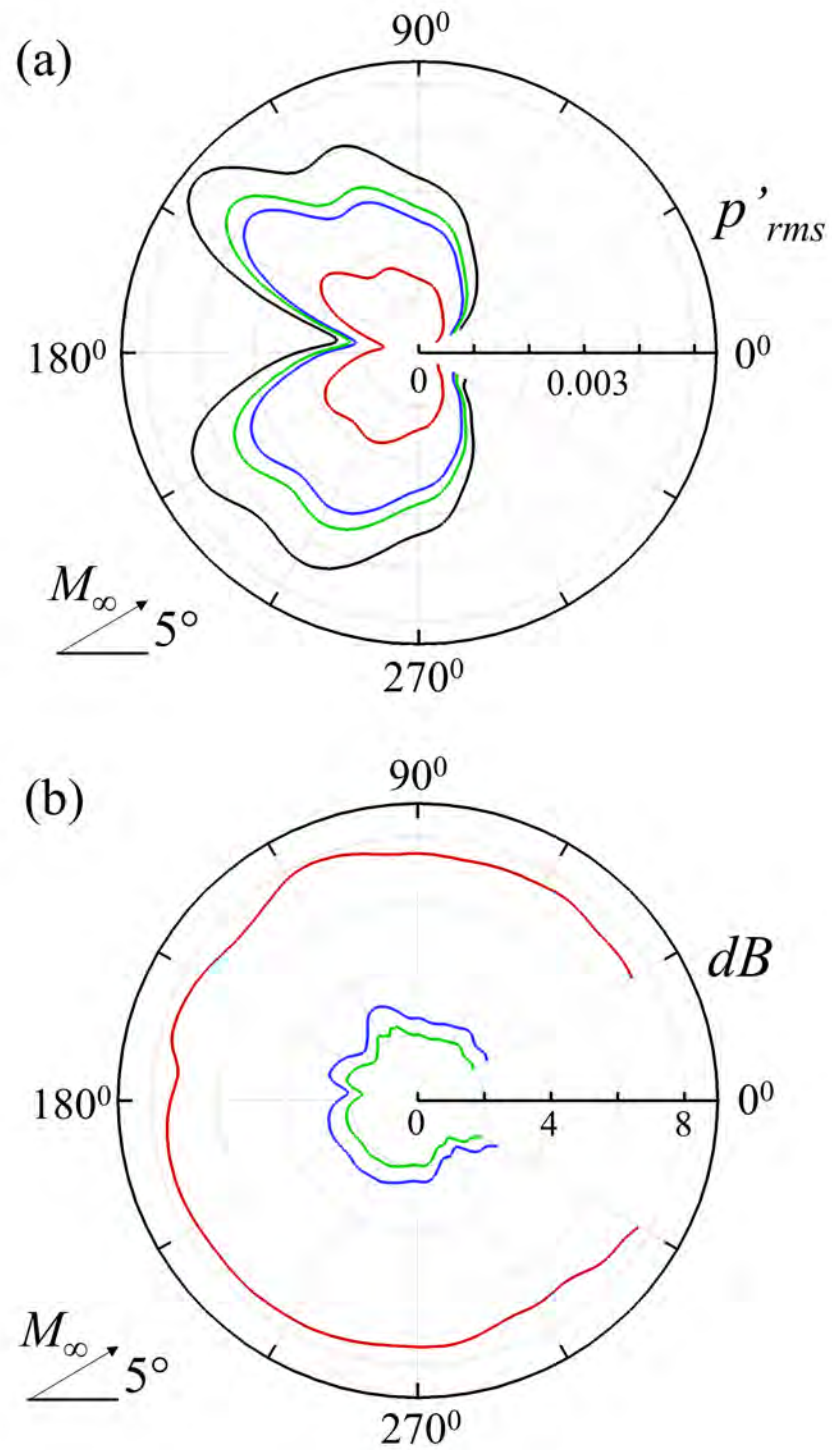


Figure 6.11: Azimuth distributions of (a) p'_{rms} at $r = 3$, and (b) $\Delta SPL_{reduction}$ at $r = 3$. —, RS; —, SP1; —, SP2; —, SCC1.

higher flow instabilities at $x = 0.55$ as compared to $x = 0.4$ (Figure 6.1(b)). The modal shape at selected frequencies for first and second panels of strongly coupled configuration (SCC1) are shown in Figures 6.12(c) and (d). The third structural mode is dominant for both the panels of SCC1 as well. This observation confirms that the designed panels are truly compliant to fluctuating flow-induced loading of oncoming boundary layer instability and are able to vibrate in their desired mode. The amplitude of panels in SCC1 is observed to be much higher than their corresponding individual configurations in SP1 and SP2 which indicates that the effect of coupling resonance among the panels is more pronounced than their behavior in isolation. Higher energy from unsteady flow within the boundary layer is expended to sustain the panel vibrations which leaves less flow distortion proceeding to scattering at airfoil trailing edge and subsequently lower tonal noise generation than other configurations (6.11(b)). It is important to note that the panel maximum displacement w_{max} is observed to be much lower than the local boundary layer thickness δ by two orders (i.e $w_{max}/\delta \leq 10^{-2}$) which ensures that the panel vibration does not alter the airfoil aerodynamics.

Figures 6.13(a) and (b) show the FFT spectrum of w for SP1, SP2 and SCC1 with a sampling frequency of 1×10^5 and a Hamming window with 50% overlapping for fine resolution. A dominant frequency at third structural mode $f = f_{EP} = 3.3$ is observed in all configurations which coincides with f_{bl_0} to achieve the desired structural resonance condition. Although the vibratory response of the elastic panels indicate the desired third mode, however, it is still essential for the panels to maintain their continuous vibrational pattern to effectively absorb the energy consistently from the incident flow to sustain its dynamics. Hence, the panel phase plane plots are analyzed where the panel displacement w and velocity \dot{w} at the center of panel are plotted with increasing time instances (Visbal and Gordnier 2004) as shown in Figures 6.14(a) and (b). The phase plane plots clearly

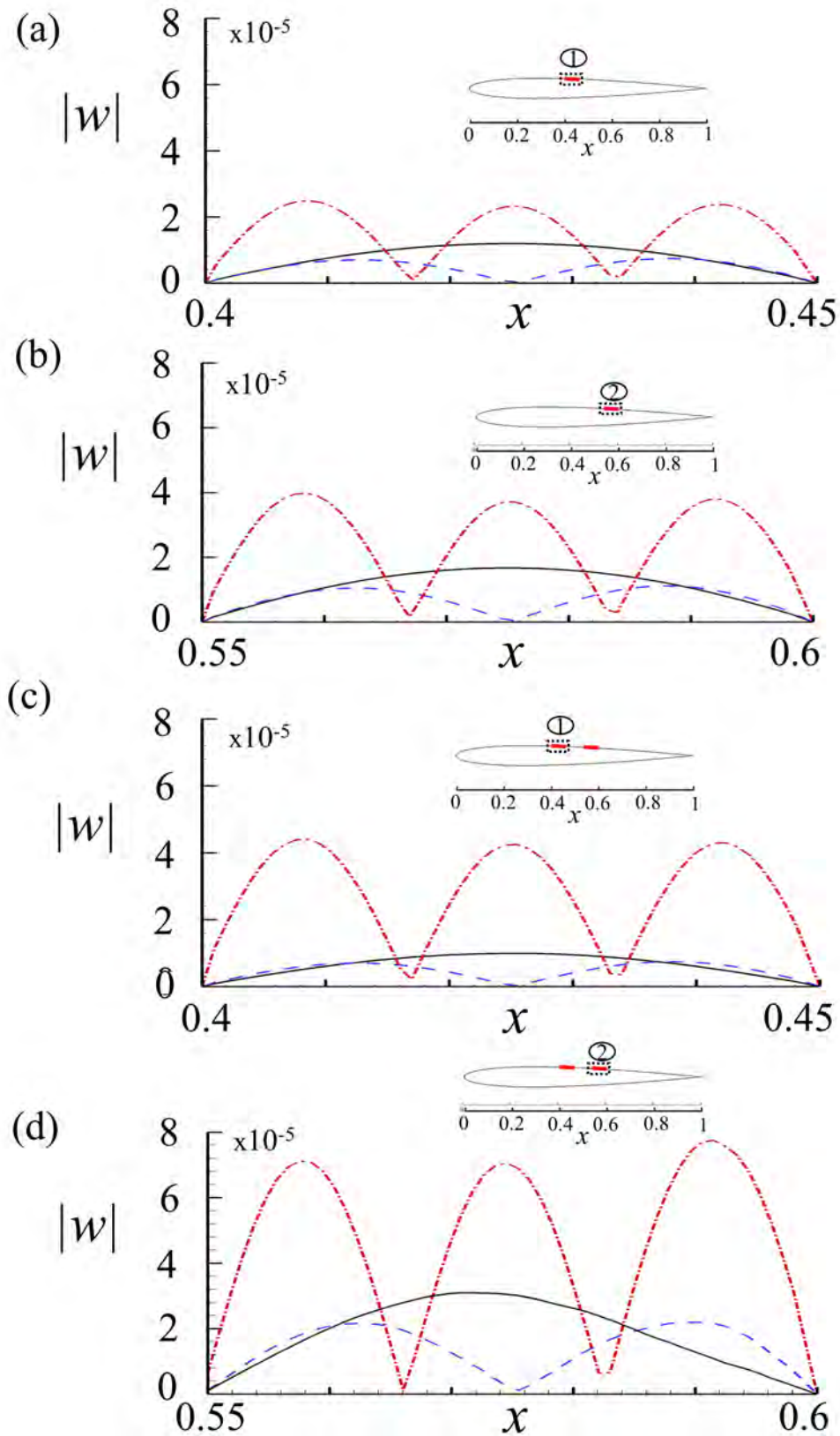


Figure 6.12: Comparison of the amplitude of Fourier transform for first three modes at the selected frequencies $f = 1.1, 2.2$ and 3.3 extracted by FMD. (a) SP1, (b) SP2, (c) first panel of SCC1, and (d) second panel of SCC1. —, first mode; - - -, second mode; ····, third mode.

indicate that for all the configurations, the panels have set into sustained limit cycle oscillations with much higher magnitude for SCC1 as compared to SP1 and SP2. The panel displacements are observed to be centered around the panel equilibrium position ($w = 0$) which indicate that the panels do not experience any aeroelastic divergence. The trajectory starts from the outer cycle and spirals inside where a limit cycle is reached.

The inter-dynamical behavior between both the panels for SCC1 is investigated by the cross wavelet coherence analysis of panel displacement at the center of both panels to obtain further insights. Cross wavelet coherence of the time series of both panels are evaluated by using the Morlet wavelet function (Grinsted et al. 2004):

$$W_{ab} = \frac{|SC_a^*C_b|^2}{S|C_a|^2.S|C_b|^2} \quad (6.1)$$

where S is the smoothing operator in time and scale, C_a and C_b represents the cross wavelet transform of the first and second panel respectively. The superscript * denotes the complex conjugate and W_{ab} represents the cross wavelet coherence among the panels. The panel data for a time episode of $t = 10$ is selected with 50% data overlapping for fine resolution. Appropriate scales are chosen with reference to frequency of interest ranging from 0.01 to 10. The analysis (Figure 6.15(a)) reveals that both the panels maintain a high coherence ($x \geq 0.9$) at $(f_{bl})_0$ for all time instances which indicate that the panels are able to maintain seamless coupling at their third resonant modes and achieve a state of limit cycle oscillation. However, the coherence between the panels decreases significantly at higher frequencies. Figure 6.15(b) illustrates the cross wavelet phase spectrum $W_{\theta_{ab}}$ between the same signals. A constant phase difference of $\sim 12^\circ$ (0.06π) at $(f_{bl})_0$ for all time instances indicates a strong coupling among the panels where they vibrate with similar frequency and mode shapes. However, at higher harmonics, the phase difference among the panels continuously fluctuates

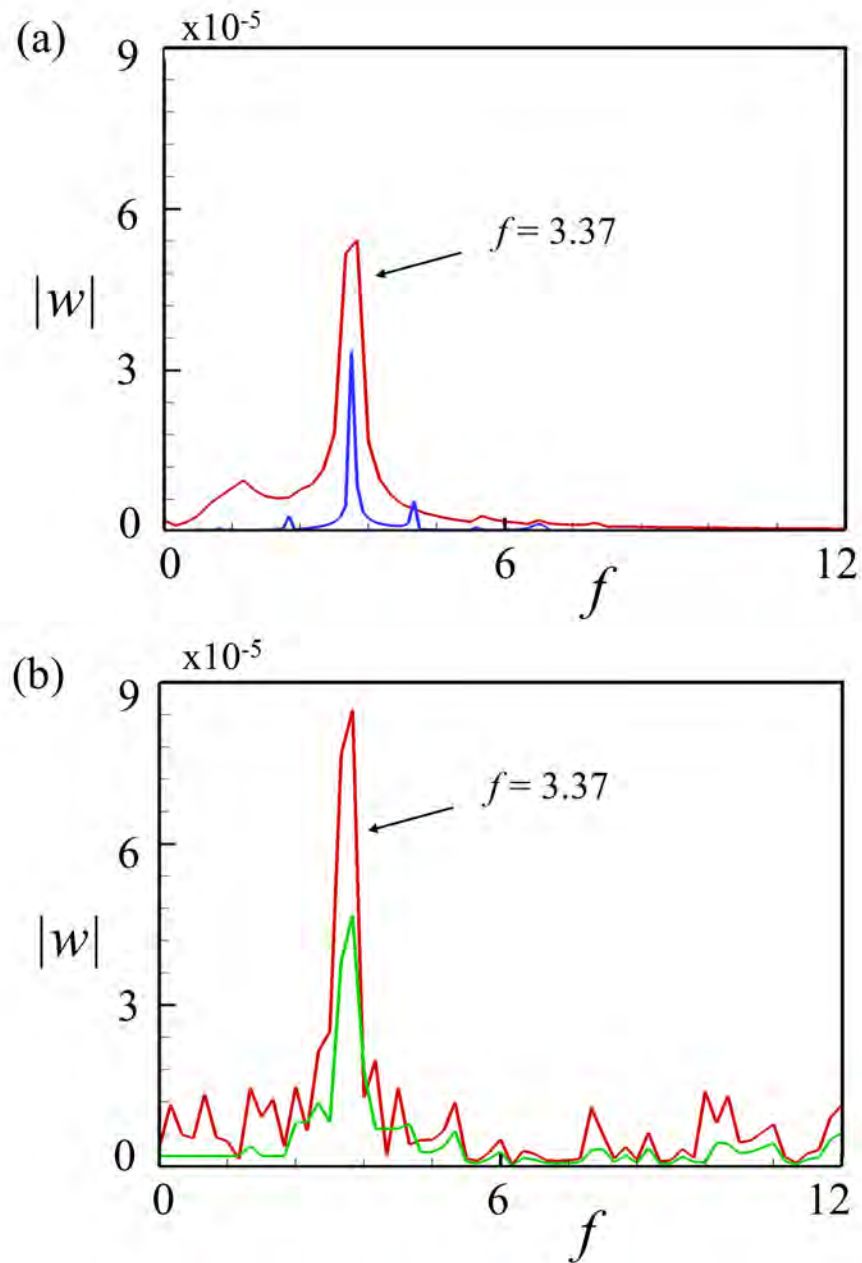


Figure 6.13: Panel dynamics. SP1 and the first panel of SCC1: (a) panel displacement spectra. SP2 and the second panel of SCC1: (b) panel displacement spectra. —, SP1; —, SP2; —, SCC1.

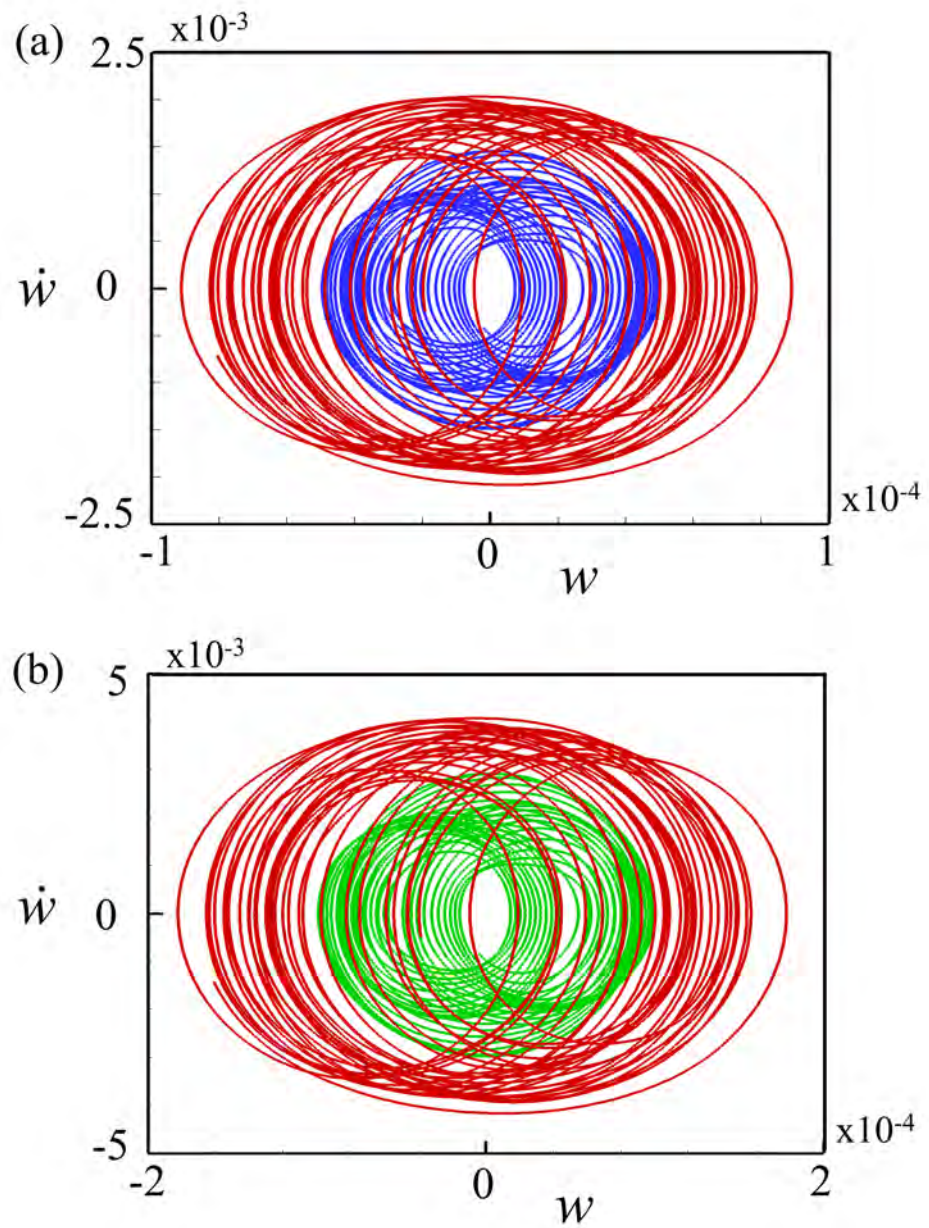


Figure 6.14: Panel dynamics. SP1 and the first panel of SCC1: (a) phase plots of centres of panel. SP2 and the second panel of SCC1: (b) phase plots of centres of panel. —, SP1; —, SP2; —, SCC1.

at $(f_{bl})_1$ and $(f_{bl})_2$.

The extent of mutual coupling between the two panels is analyzed by evaluating the coherence between the vibration responses of two panels over their complete length (Figure 6.16(a)). The magnitude-squared coherence function $\gamma_{12}^2(f)$ between the displacement signals of both the panels is calculated with a frequency resolution of 1×10^{-3} . The coherence function is calculated by (Stoica et al. 2005)

$$\gamma_{12}^2(f) = \frac{|P_{12}(f)|^2}{P_{11}(f)P_{22}(f)} \quad (6.2)$$

where $P_{11}(f)$ and $P_{22}(f)$ are the power spectral densities of w' signals for the first and second panel respectively, and $P_{12}(f)$ is the cross power spectral density of both the signals. The x -axis in the figure gives a panel location l_p measured from its leading edge and is expressed as a percentage of panel length. As an example, a $l_p/L_{EP} = 50\%$ indicates the center location of both the panels, i.e. $x = 0.425$ on the first panel and $x = 0.575$ on the second panel. A strong coherence of $x \sim 0.95$ shows that the panels vibrate with similar modal behavior. Interestingly, a sharp reduction in $\gamma_{12}^2(f)$ is observed at $x = 33\%$ and $x = 66\%$ respectively which corresponds to anti-nodes for third mode of vibration. The observed phenomena indicate some deviation among the panels vibration during the instance when the panel motion crosses its neutral axis. The analysis is further extended to quantify the phase difference θ_{ab} between both corresponding panel locations at $(f_{bl})_0$ as shown in Figure 6.16(b). A constant phase difference ($\theta_{ab} = 10^\circ$) between all corresponding panel locations is observed which indicates that both the panels vibrate in a similar pattern at all instances.

The fluid-structure interactions of the panels and their associated vibration responses are investigated by analyzing the snapshots of instantaneous pressure fluctuations p' for one complete hydrodynamic cycle and plotted along the corre-

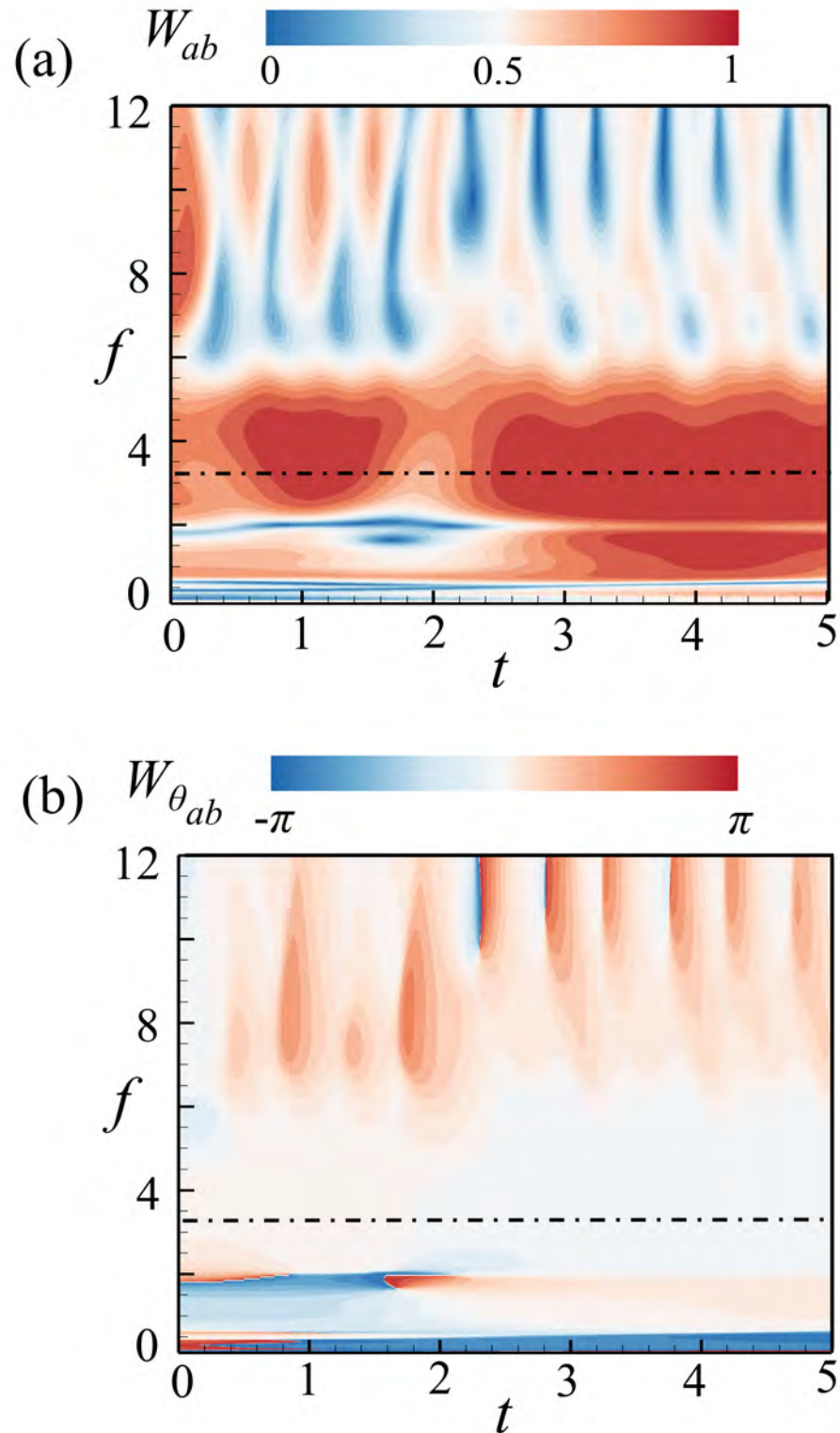


Figure 6.15: (a) Spectrum of cross wavelet coherence among the two panels for SCC1. (b) Spectrum of phase difference among the two panels for SCC1. The horizontal black dot-dashed line indicates the $(f_{bl})_0$.

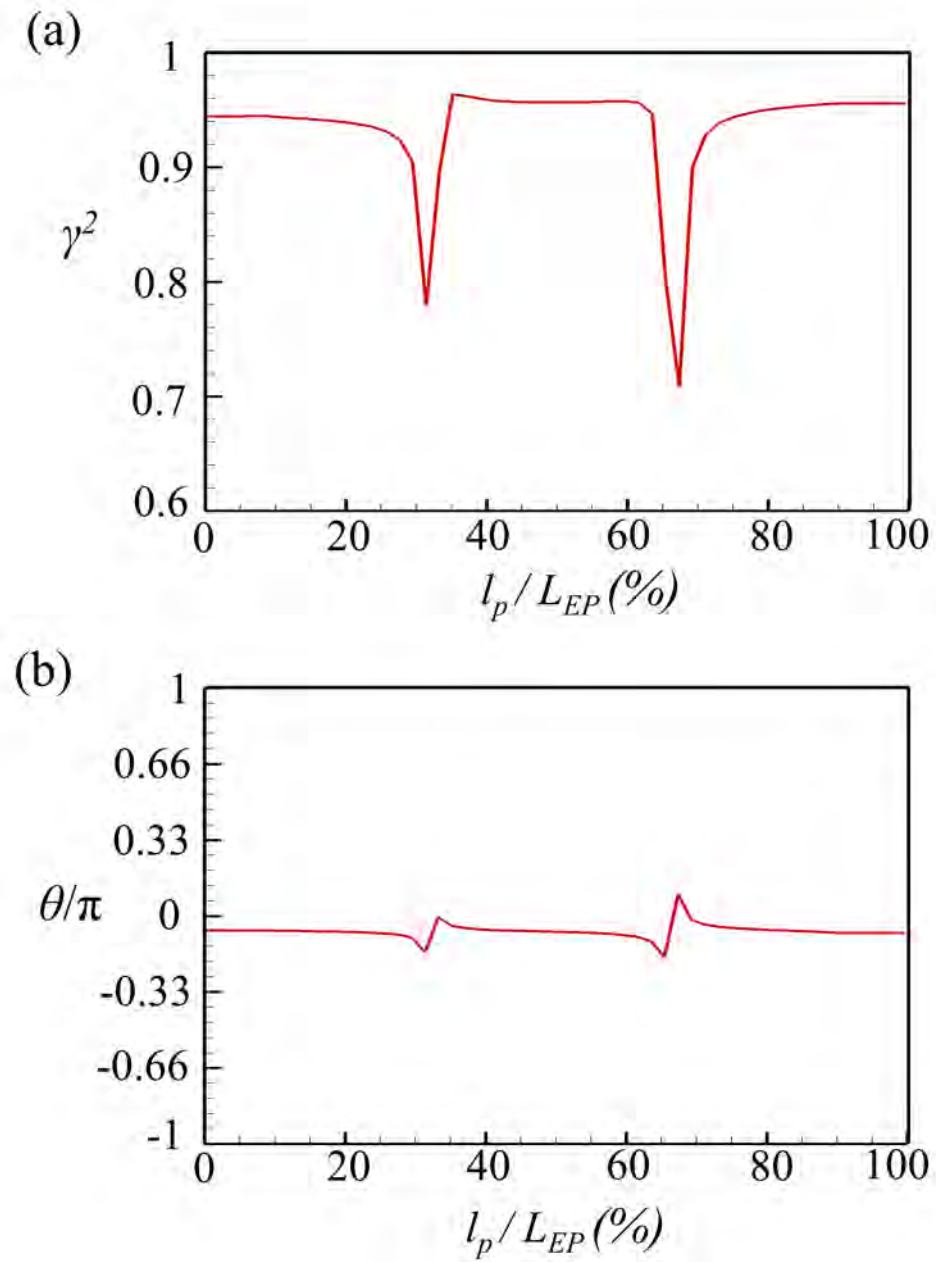


Figure 6.16: Coherence of vibration responses of the two panels for SCC1. (a)

Magnitude-squared coherence γ^2 , (b) phase difference θ_{ab} .

sponding panels displacement in Figure 6.17. Initially at time t_0 , both the panels are subjected to positive pressure fluctuations (indicated by red color patches) where the vibration pattern of both the panels follow the third mode. The amplitude of second panel is observed to be almost twice to that of first panel. After a time increment of $T_d/5$, the fluid loading on the panel changes and affects the panel displacement amplitude to give similar patterns of both panel displacements. At the next time increment $2T_d/5$, the panels are subjected to both positive and negative pressure fluctuations which completely reverse the mode shape of the panels. At later time between $3T_d/5$ and $4T_d/5$, both the panels respond to maintain a high level of coupling between them. The fluctuation cycle repeats at T_d along with the panels displacement. The highly coherent vibration responses observed firmly show that the intended coupled structural resonance of the panels separated by one λ_{conv} is completely achieved.

6.4.3.1 Wavenumber-Frequency Analysis

It is more informative to uncover the coupled fluid-structure interactions between unsteady airfoil flow and the two panels in SCC1; hence, the fluid pressure fluctuations p' right above the panel and panel displacement w signals are transformed from space-time domain $Y(x, t)$ to wavenumber-frequency domain $Y(k, f)$ by performing two-dimensional Fourier transform (2D-FFT) (Desquesnes et al. 2007). The 2D-FFT is evaluated by:

$$Y_{(k,f)} = \frac{1}{2\pi} \int_{-\infty}^{\infty} \int_{-\infty}^{\infty} Y_{(x,t)} e^{-2\pi i(kx+ft)} dx dt. \quad (6.3)$$

For 2-D FFT, the p' and w data over the panel surface is arranged in a space-time matrix. The temporal data is extracted with a length of 1×10^5 samples. The Fourier transform is initially applied to the time signal at each location with a Hamming window without any segmentation or data overlapping. Sub-

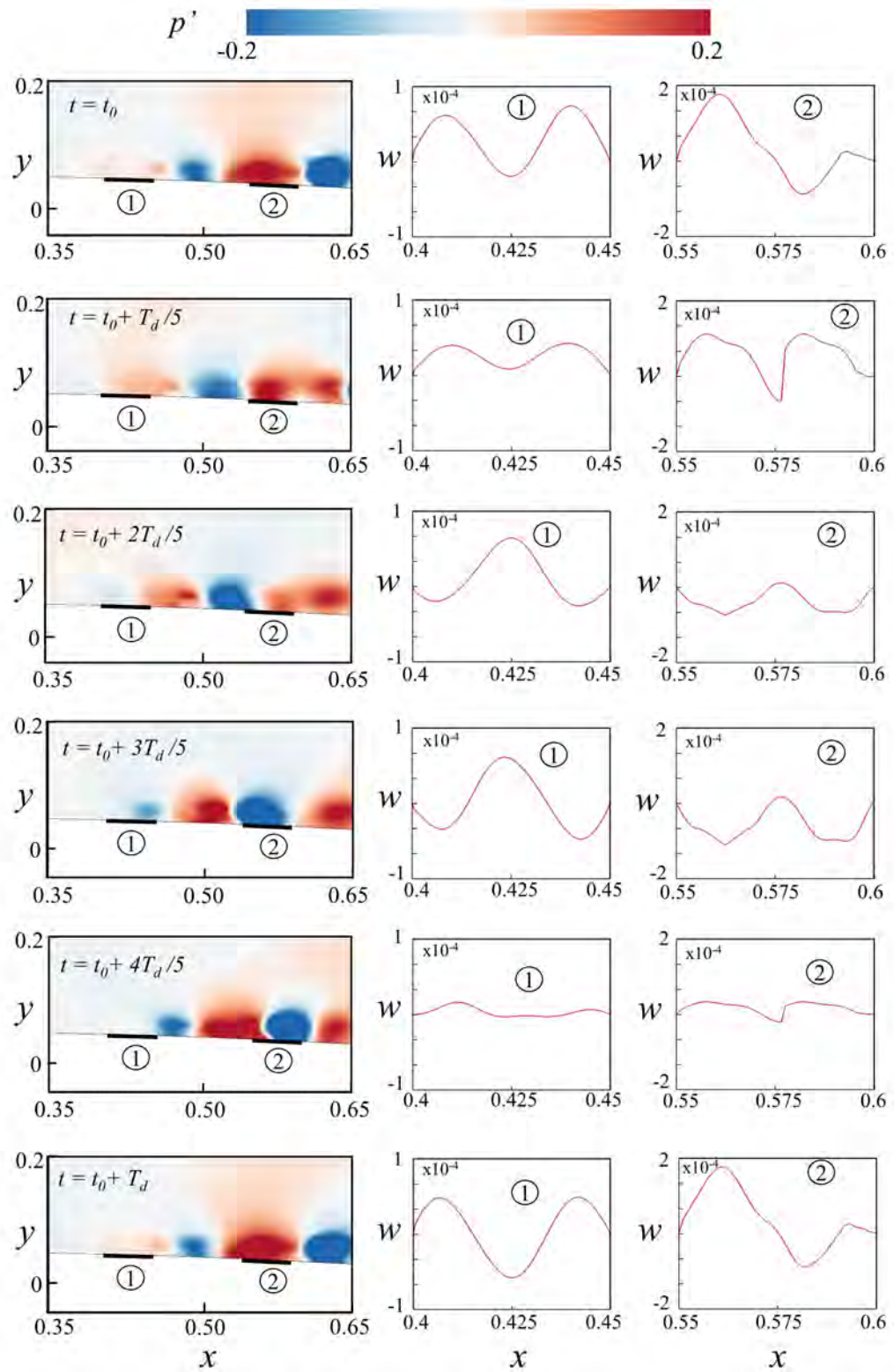


Figure 6.17: Snapshots of the p' over the panels and panel displacements in SCC1 within one period $T_d = 1/(f_{bl})_0$. ①, first panel; ②, second panel.

sequently, for each frequency, the complex-Fourier transform is applied in space domain. The resolution of wavenumber k depends on the spatial length of data in Fourier transform which is not high enough in our case due to short panel length. Hence, zero-padding is applied in spatial direction to increase the length of data by ten times to enhance the resolution of k . It however may increase the aliasing error in the Fourier spectrum. Figure 6.18 shows the resulting spectra of $k - f$ for SCC1. For brevity, only positive axis for frequency is shown which is representative for all physical wave propagation phenomena for the present study. The wave propagating with positive k indicates downstream travelling bending waves on panel whereas the wave propagating with negative k represents upstream travelling waves. The spectrum of w in Figures 6.18(a) and (b) show a symmetric pattern of upstream and downstream bending waves travelling through both the panels due to fluid loading and vice versa. The travelling waves are observed to be convecting with a phase velocity of $\sim 0.65U_\infty$ which is indicated by a line of constant slope (dashed yellow line). The symmetric patterns in the figures show both upstream and downstream waves of same phase velocity prevail on each panel for all frequencies. This observation further confirms the emergence of standing bending waves on panels for structural resonance. The high energy content can be identified at $f_{EP} = 1.1, 2.2$ and 3.3 indicating panel dominant vibration modes. The response at the third mode $f_{EP} = 3.3$ is observed to be much stronger than lower modes which even coincides with the f_{bl_0} as also observed in Figure 6.12. The spectra of p' for both the panels in SCC1 in Figures 6.18(c) and (d) show a similar trend of wave propagation where the downstream waves travel with hydrodynamic convection velocity while the upstream waves propagate with the acoustic phase speed a_{phac} (indicated by red dashed line) with similar frequency content which shows a strong correlation between hydrodynamic fluctuations and acoustic waves (Desquesnes et al. 2007). However, the

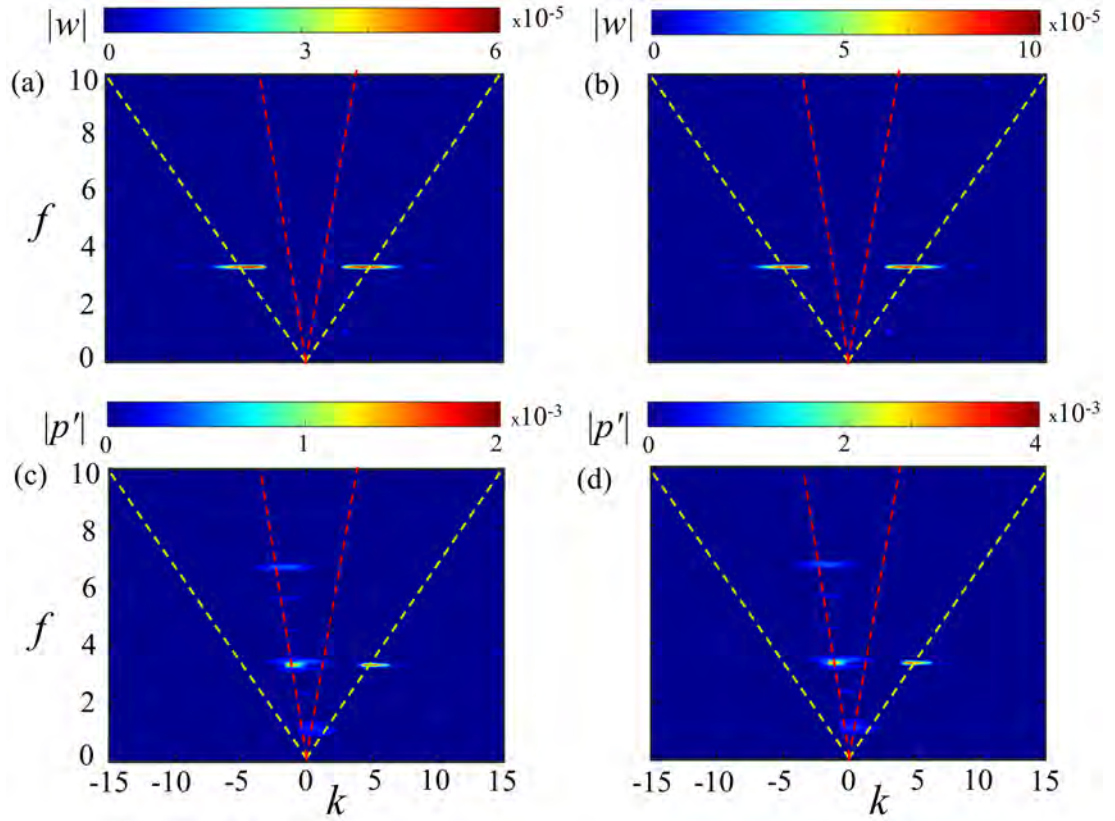


Figure 6.18: Wavenumber-frequency spectra for SCC1. (a) w and (c) p' for the first panel, (b) w and (d) p' for the second panel. Yellow dashed lines correspond to $\pm 0.65U_\infty$; red dashed line corresponds to acoustic velocity.

p' spectra for SCC1 also indicate the presence of very low magnitude energy content at $f = 1.1, 4.4$ and 5.6 respectively. Although the magnitudes of p' at these frequencies are much lower than that at $(f_{bl})_0 = 3.3$, they still indicate that the coupled resonance of the panels has redistributed the frequency content of flow unsteadiness. Same phenomenon is also observed by Serrano-Galiano et al. (2018) for a membrane airfoil with much aggressive re-distribution than the present case. However, due to very weak redistribution observed in the present study, the mean flow for SCC1 remains essentially unaltered and similar to RS configuration as observed in Figure 6.7.

6.4.3.2 Correlation Analysis

The data corresponding to the evolution of p' right above a panel and w for SCC1 has been bifurcated into downstream and upstream propagating waves. This fact allows us to explore the coupling between flow field with panel dynamics and its physical mechanism responsible for the significant airfoil noise reduction for SCC1. The complex process involves filtering of frequency and wavenumber data from 2D FFT domain with respect to each direction of wave propagation. For analysis of downstream propagation, the data related to upstream travelling waves (negative k) are suppressed and the inverse of 2D FFT is performed to transform the remaining data back to space-time domain. Same process is performed for the analysis of upstream travelling waves by filtering the downstream waves (positive k). One must note that the complete process requires careful operation of data filtering as the Fourier inverse operation requires strict conjugate symmetry to yield the time series data in absolute real values rather than complex numbers.

Figure 6.19(a) shows the space-time evolution of w' with respect to time without any data filtering for the first panel of SCC1. The third mode of vibration is easily discernible from the spectrum at all time instances. Despite the complex panel dynamics observed in the spectrum, the standing wave pattern can still be identified. Figure 6.19(b) shows the downstream travelling waves of w' by filtering of upstream waves. The lines with a positive slope indicate the downstream wave propagation in a periodic manner. Figure 6.19(c) shows the upstream travelling waves where the negative slope in the spectrum indicates upstream propagation with a similar magnitude as downstream waves. The magnitude of w' for downstream and upstream travelling waves are observed to be quite similar.

Figure 6.20(a) shows the space-time evolution of p' over the elastic panel without any data filtering for the first panel of SCC1, whereas Figures 6.20(b) and

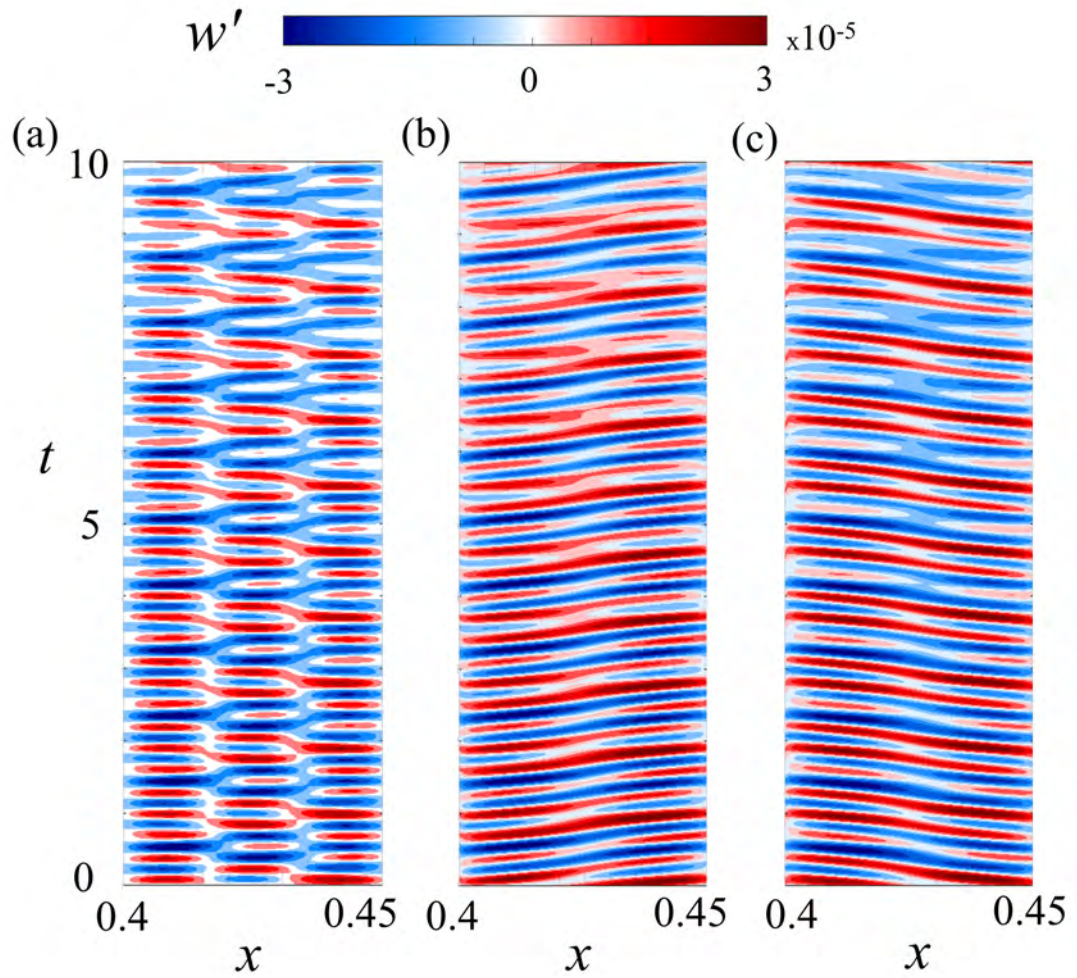


Figure 6.19: Space-time evolution of panel w' for the first panel of SCC1. (a) full w' . (b) Downstream propagating w' waves. (c) Upstream propagating w' waves.

(c) shows the downstream and upstream travelling pressure waves after data filtering respectively. Since the structural wavelength of the panel is much smaller than the hydrodynamic wavelength in the present study, the relative slope of the downstream and upstream waves is almost zero. The observed phenomenon is completely in contrast of typical membrane airfoil wing where the structural wavelength of membrane is usually higher than the hydrodynamic wavelength (Rojratsirikul et al. 2011, Song et al. 2008, Serrano-Galiano et al. 2018). It is interesting to note that the magnitude of the pressure fluctuations for the upstream waves is $\sim 25\%$ lower than downstream travelling waves indicating the influence of elastic panel dynamics on the pressure field. The effects of this phenomenon on airfoil acoustics would be further explored in the following section. A similar trend of w' and p' is observed for the second panel of SCC1 after data filtering and therefore not presented.

A similar trend of w' and p' with different magnitudes is observed for the second panel of SCC1 after data filtering as shown in Figures 6.21 and 6.22 respectively.

With the help of data filtering operation, the correlation analysis is performed between the w' and p' data over the panel which would further uncover the underlying fluid-structure coupling phenomenon and noise reduction mechanism. The cross-correlation \hat{R}_{pw} between the two signals is calculated by (Fillinger et al. 2010):

$$\hat{R}_{pw}(m) = \begin{cases} \sum_{n=0}^{N-1} p_{(n+m)} w_n^*, & m \geq 0, \\ R_{wp}^*(-m), & m < 0. \end{cases} \quad (6.4)$$

where m is the lag coefficient and N is the sample size which is taken as 1×10^5 for the present study for fine resolution. For easy interpretation, Equation 6.4 is usually expressed in normalized form as:

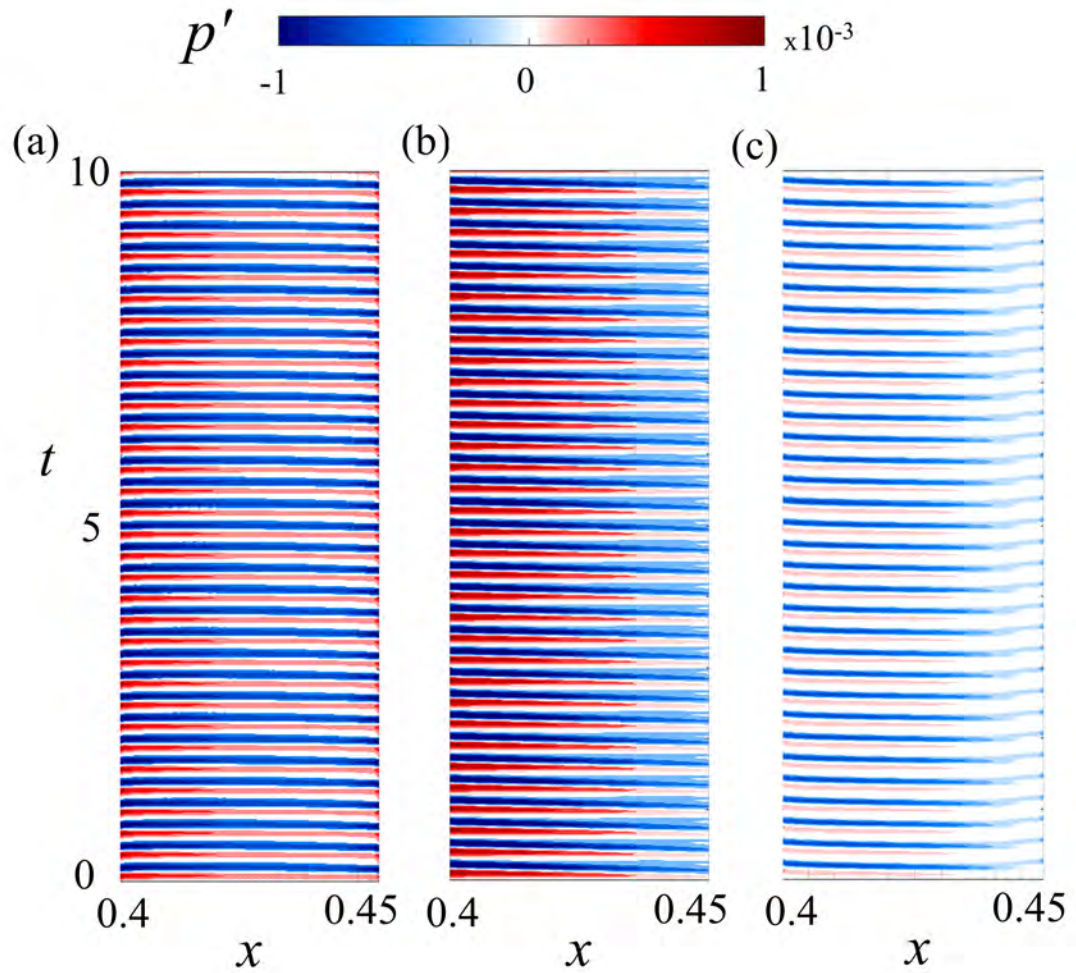


Figure 6.20: Space-time evolution of flow p' for the first panel of SCC1. (a) full p' . (b) Downstream propagating p' waves. (c) Upstream propagating p' waves.

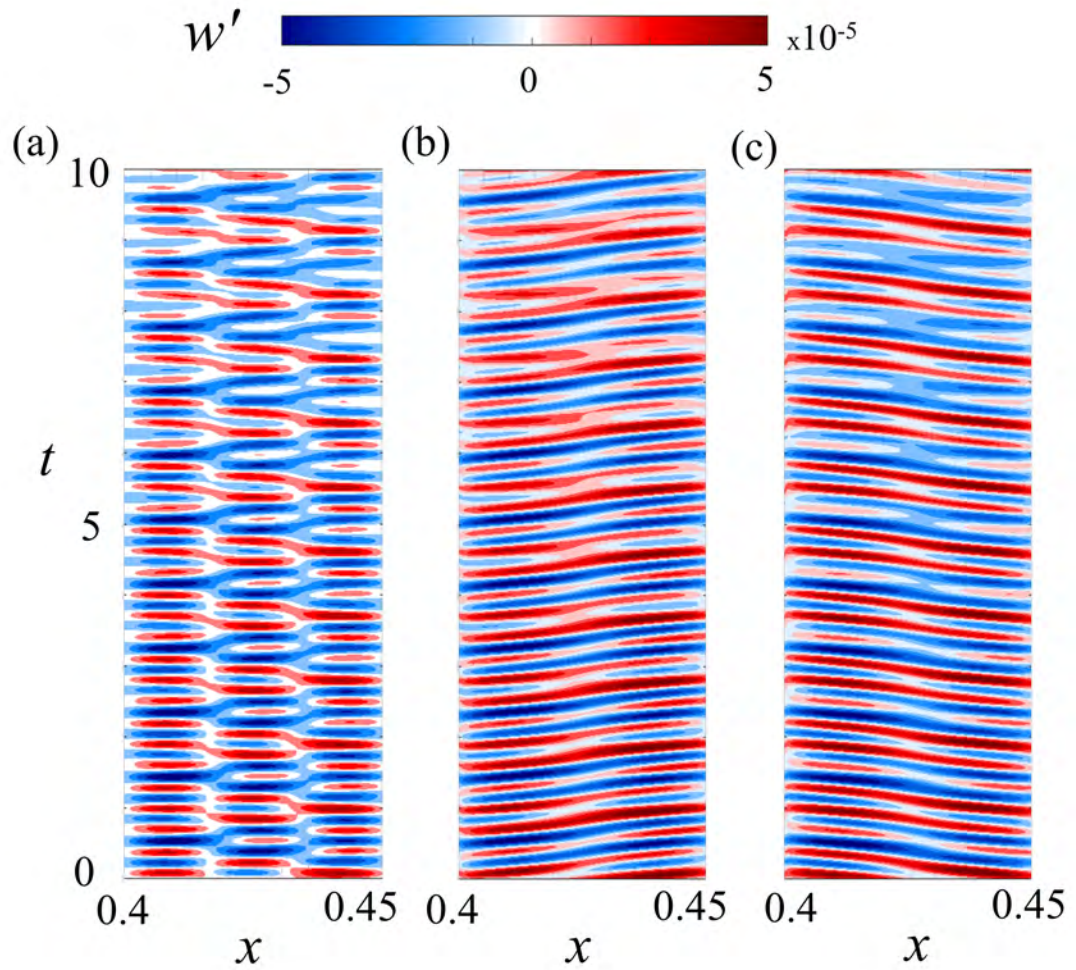


Figure 6.21: Space-time evolution of panel w' for the second panel of SCC1. (a) full w' . (b) Downstream propagating w' waves. (c) Upstream propagating w' waves.

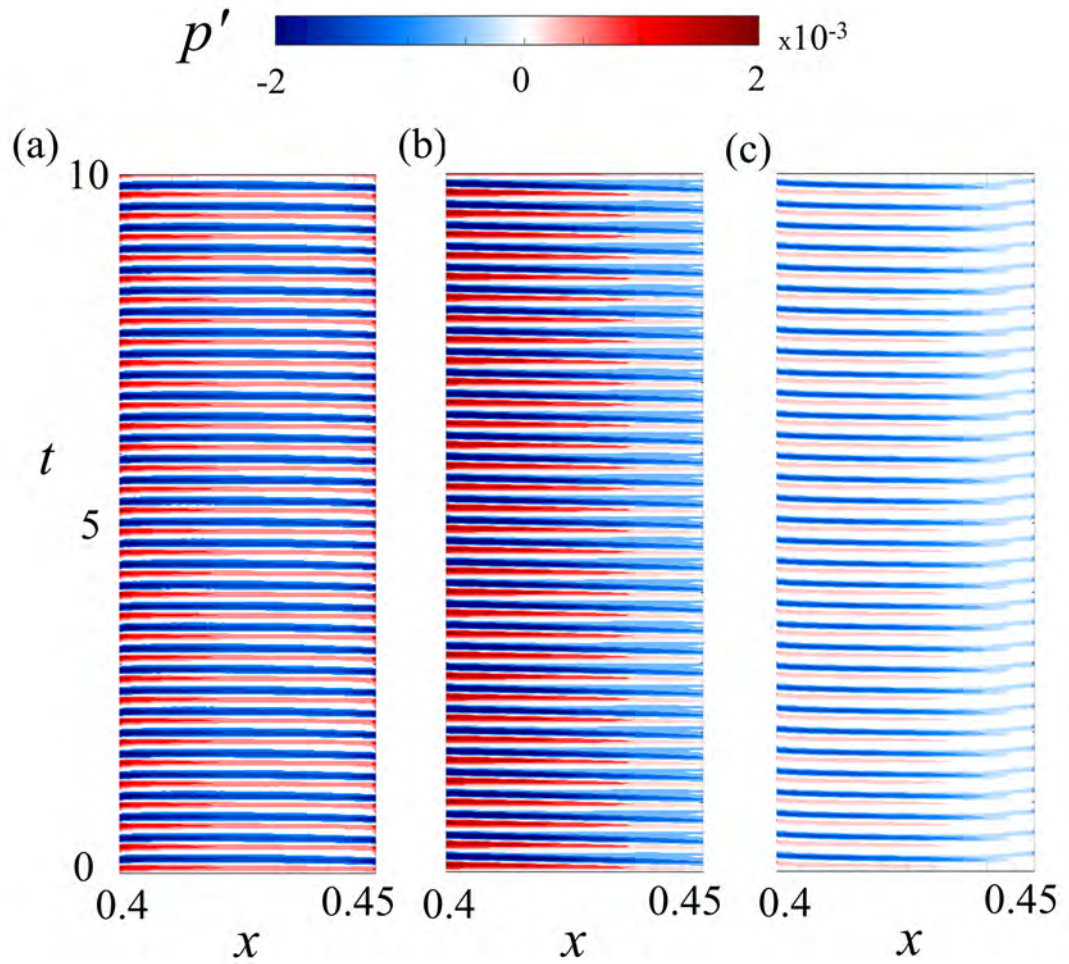


Figure 6.22: Space-time evolution of flow p' for the second panel of SCC1. (a) full p' . (b) Downstream propagating p' waves. (c) Upstream propagating p' waves.

$$R_{pw}(m) = \frac{\hat{R}_{pw}(m)}{\sqrt{\hat{R}_{pp}(0)\hat{R}_{ww}(0)}} \quad (6.5)$$

where $\hat{R}_{pp}(0)$ and $\hat{R}_{ww}(0)$ are the autocorrelation coefficients of p' and w at zero lag respectively. Figures 6.23(a) and (b) show the spectra of R_{pw} between the downstream p' waves and the point of w_{max} (a fixed location of maximum displacement of each panel determined by the time series data) for the first and second panel of SCC1 respectively. A strong correlation can be observed between the downstream propagating p' waves and w_{max} for the second panel. However, the correlation is slightly reduced at the rear half of first panel. Similar phenomenon is observed with membrane airfoil (Serrano-Galiano et al. 2018) which mildly affects the overall aerodynamic characteristics of the airfoil. It explains the slight increase in C_D for SCC1 as compared to other configurations (Table 6.5). Nevertheless, an increase in C_L is still observed for SCC1 as compared to RS as discussed in Section 6.4.1.

The spectra of R_{pw} between the upstream pressure waves and the point of maximum displacement for the first and second panel of SCC1 are shown in Figures 6.23(c) and (d) respectively. For the first panel, the upstream p' waves and w are weakly correlated from panel leading edge up to 30% of the panel length beyond which the correlation between the two signals completely diminishes. On the other hand, for the second panel, the correlation between upstream p' waves and w completely diminishes behind 10% of panel length from the leading edge and slightly recovers again at the rear end of second panel. The observed phenomenon indicates a key fluid-structure coupling feature in the present airfoil-panel configuration SCC1 that the panel displacement is weakly correlated with the upstream propagating acoustic waves generated from the flow scattering at airfoil trailing edge. This weak correlation is attributed to the difference in the phase speeds of upstream acoustic waves and panel displacement as observed in

Figure 6.18. This phenomenon would lead to weakening of aeroacoustic scattering at airfoil trailing edge and results in effective reduction of tonal noise. This aspect is further studied in Section 6.4.4.

6.4.4 Relationship between Near Flow Field and Acoustics

The contributions of coupled panel dynamics to airfoil tonal noise reduction are highlighted by evaluating the distributions of the amplitudes of transverse velocity fluctuations v' for RS, SP1, SP2 and SCC1 at $(f_{bl})_0 = 3.37$ along airfoil chord are compared in Figure 6.24(a). For RS case, the v' amplitude starts to increase at $x \geq 0.27$ and subsequently grows to different extents upon approaching airfoil trailing edge. A similar trend is observed for SP1, SP2 and SCC1 up to $x \geq 0.4$. The magnitude of v' from $x = 0.4$ up till trailing is much lower for SCC1 as compared to SP1 and SP2. The percent deviation in transverse velocity fluctuations v' is evaluated at airfoil suction surface for SP1, SP2 and SCC1 with respect to RS at $(f_{bl})_0$ as shown in Figure 6.24(b). The effect of the vibration of panel(s) on the reduction of v' within the boundary layer can be observed for SP1, SP2 and SCC1. For SP1, a continuous reduction in the magnitude of v' at $(f_{bl})_0$ ranging from 8% to 20% is observed from $x = 0.4$ up till the trailing edge. For SP2, the reduction ranging from 6% to 18% is observed. The reduction in v' for SCC1 is much higher than SP1 and SP2 which ranges from 8% to 34%. This observation manifests the fact that the coupled resonant panels have weakened the strength of boundary layer instabilities at their emergence at $x = 0.4$ and $x = 0.55$ which results in convection of low magnitude velocity fluctuations towards the airfoil trailing edge and subsequently weaker flow scattering there. That leads to lower effectiveness of aeroacoustic feedback loop and weaker tonal noise generation.

The relationship between airfoil flow dynamics and noise generation for

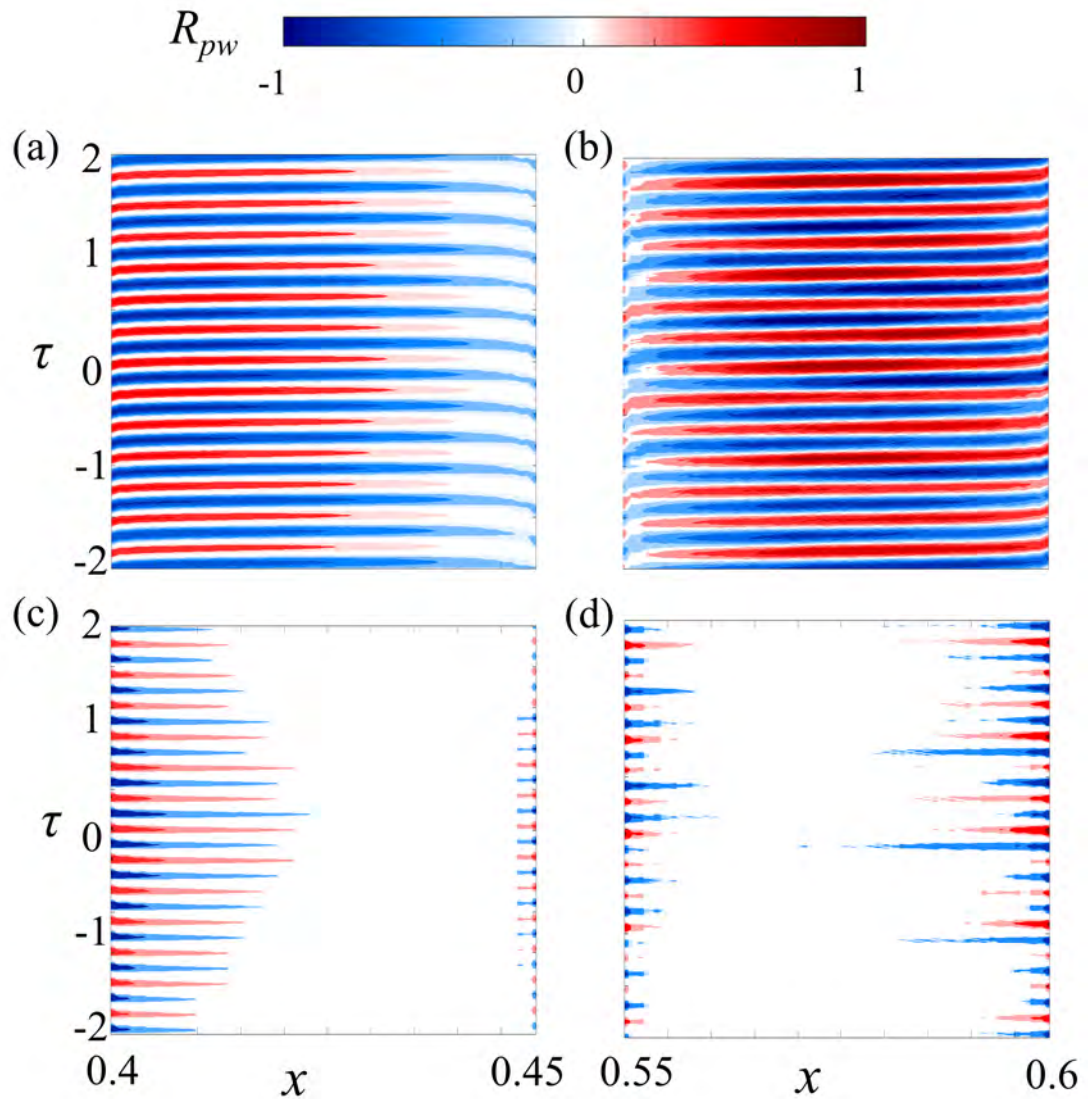


Figure 6.23: Spectra of cross-correlation for SCC1 between time signal of w at location of maximum displacement and (a) downstream propagating p' waves for first panel, (c) upstream propagating p' waves for first panel. Spectrum of cross-correlation for SCC1 between time signal of w at location of maximum displacement and (b) downstream propagating p' waves for second panel, (d) upstream propagating p' waves for second panel.

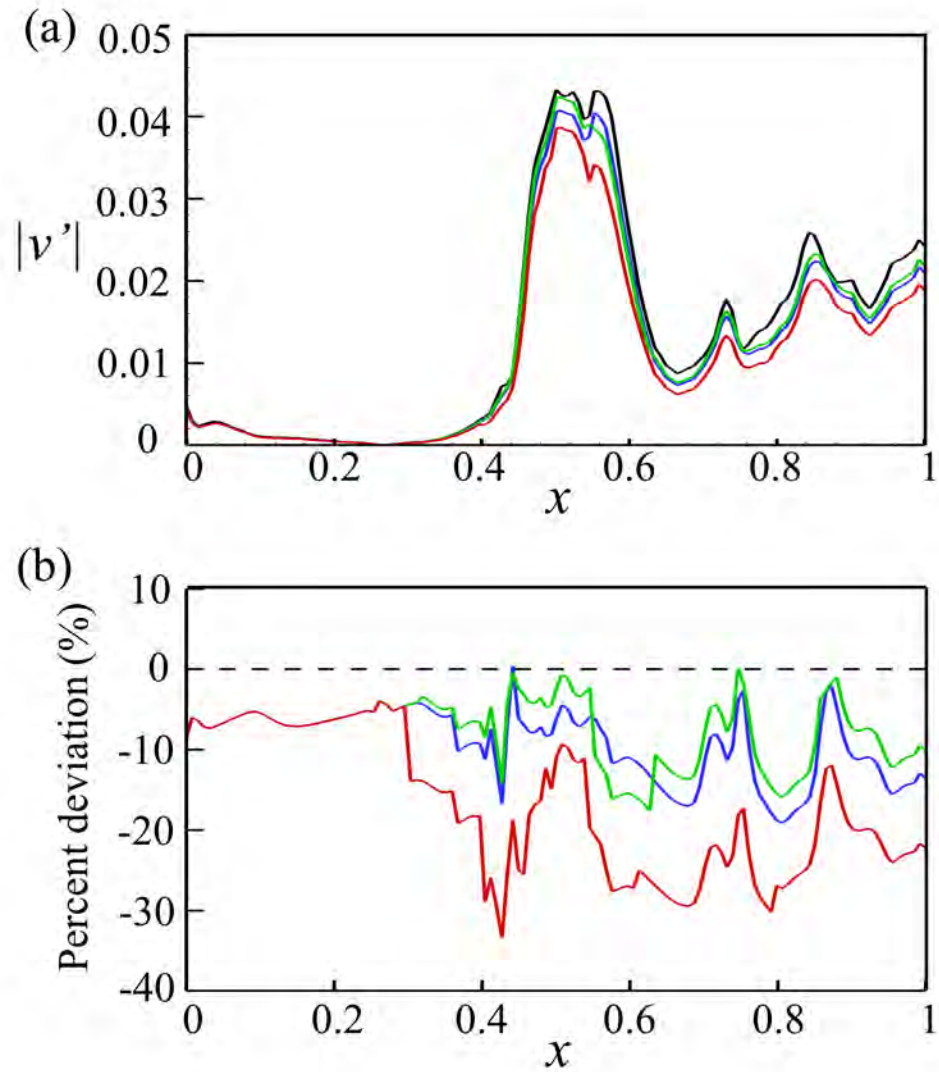


Figure 6.24: (a) Spatial growth of flow instability over the airfoil suction surface at frequency $(f_{bl})_0$. (b) Deviation of spectral amplitude $|v'|$ at airfoil suction surface with respect to RS at $(f_{bl})_0 = 3.3$. —, RS; —, SP1; —, SP2; —, SCC1.

all configurations (RS, SP1, SP2 and SCC1) is analyzed by performing coherence analysis between the p' signal at a location $(r, \theta) = (-1.12, 135^\circ)$ marked as Probe A in Figure 3.4 and v' signal along a streamline at an average offset of $\Delta y = 0.0001$ over the suction surface which is divided into 2000 segments. The γ_{12}^2 between the p' signal and v' signals is calculated using the similar procedure as discussed in Section 6.4.3. Figure 6.25 illustrates the coherence spectrum along the airfoil chord for all configurations. A strong coherence is observed between the acoustic waves and airfoil flow along the chord for RS at $(f_{bl})_0$, $(f_{bl})_1$ and $(f_{bl})_2$. For SP1, a reduction of $\sim 32\%$ is observed at the panel location whereas for SP2, a reduction of $\sim 25\%$ in the magnitude of coherence is observed. However, for SCC1, a significant reduction of $\sim 60\%$ is observed on the first panel and $\sim 50\%$ reduction is observed on the second panel at $(f_{bl})_0$ which exemplifies that the panel vibrations in coupled structural resonance have remarkably influenced the acoustic generation by the airfoil. In contrast to SP1 and SP2, reduction in the coherence at higher harmonics is also observed for SCC1.

Figure 6.26 illustrates the γ_{12}^2 extracted at $(f_{bl})_0$ and its higher harmonics from the coherence analysis. At $(f_{bl})_0$ (Figure 6.26(a)), a high coherence ($\gamma_{12}^2 \geq 0.98$) among the acoustic and velocity signals along the airfoil suction surface is observed for RS case. For SP1, a high coherence is maintained from airfoil leading edge up to the panel leading edge in which the coherence among the signals drops to $\gamma_{12}^2 \sim 0.6$ and jumps back to $\gamma_{12}^2 \geq 0.98$ at the panel trailing edge. For SP2, a reduction in coherence up to $\gamma_{12}^2 \sim 0.75$ is observed at the panel location. For SCC1, the coherence among the signals further reduces to $\gamma_{12}^2 \sim 0.4$ and 0.5 at two panel locations ($x = 0.4$ and 0.55) respectively which endorses the high impact of panel coupling on the coherence between acoustic waves and airfoil flow resulting in the distorted acoustic propagation. At $(f_{bl})_1$, the reduction in coherence for SP1 and SP2 is almost negligible at the panel locations (Figure

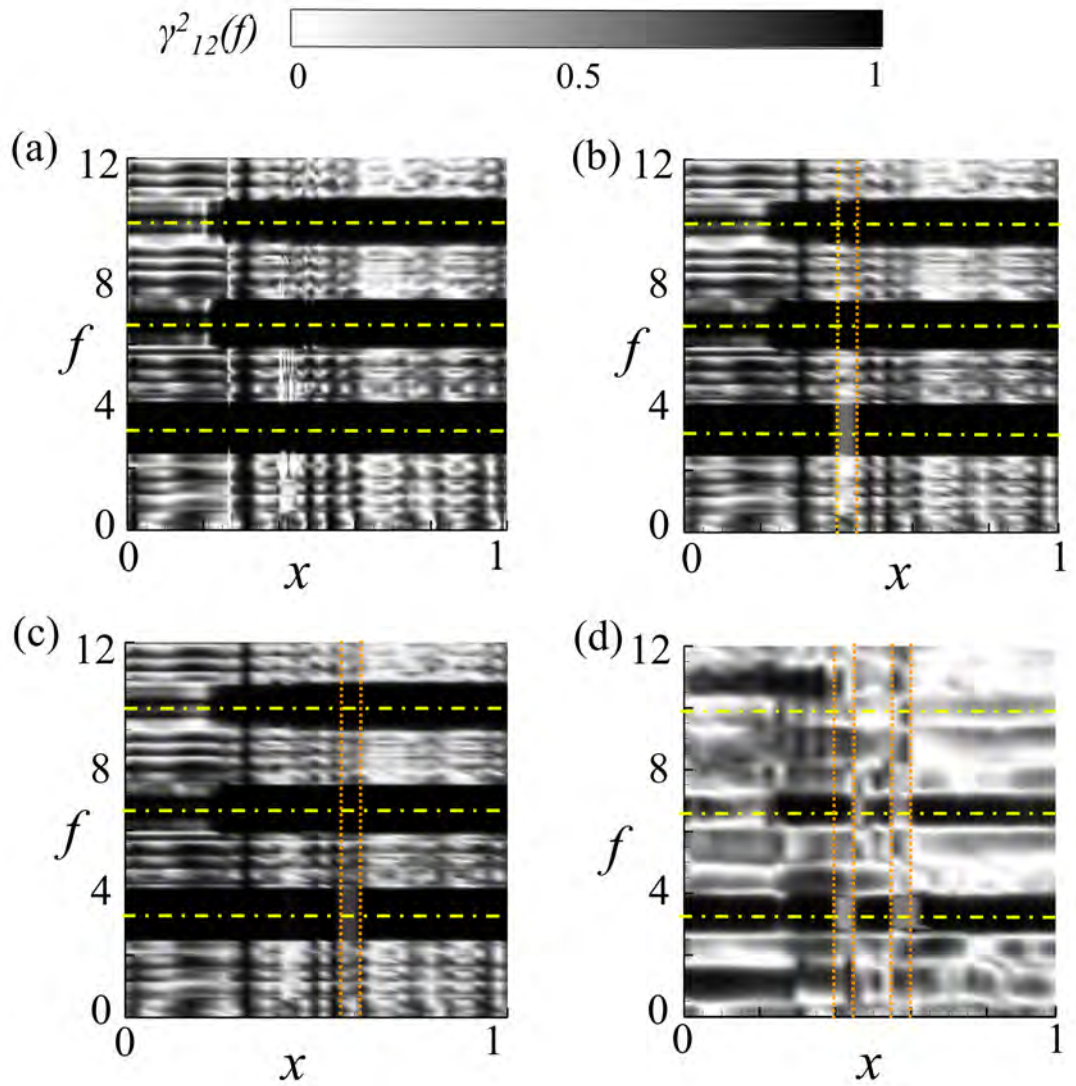


Figure 6.25: Spectra of magnitude-squared coherence γ_{12}^2 between the acoustic signal at $(r, \theta) = (-1.12, 135^\circ)$ and velocity signals along the airfoil chord. (a) RS, (b) SP1, (c) SP2, and (d) SCC1. The horizontal yellow dot-dashed lines indicate the frequencies $(f_{bl})_n$, $n = 0, 1, 2$. The vertical orange dotted lines indicate the panel edges.

6.26(b)); however, the coherence for SCC1 significantly drop at both panels. A similar trend is observed for $(f_{bl})_2$ (Figure 6.26(c)) where the coherence drops at both panels for SCC1 whereas no reduction is observed for SP1 and SP2.

Figures 6.27(a) to 6.27(c) show the spectra of phase difference θ_{12} between pressure and velocity signals for all three cases. A complete phase cycle of 2π is indicated by the combined width of red and blue area in the horizontal direction. For RS, the slow variation of phase from the leading edge of airfoil to $x \sim 0.24$ corresponds to upstream acoustic waves. In the region downstream of this location, the phase shift occurs rapidly which corresponds to combination of convective disturbances within the boundary layer and the acoustic waves. A regular pattern of phase change in convective wave disturbance is observed in the spectrum from $x \sim 0.24$ up to the trailing edge for RS and SCC1 cases. On the other hand, the phase change pattern between the two signals is severely disrupted at the panel locations for SCC1 which supports the phenomenon already observed in Figure 6.25 and Figure 6.11. Furthermore, in contrast to SP1 and SP2, the phase change pattern is also effected at higher harmonics for SCC1. The observed results clearly indicate that the relative phase difference among the airfoil flow and acoustic signals results in mutual cancellation and subsequent noise reduction.

Based on the results of comprehensive aeroacoustics and fluid-structural analyses discussed above, two key characteristics in effective tonal noise reduction are determined for airfoil-panel configuration with coupled elastic panels. Firstly, the panels must vibrate in structural resonance in the presence of fluid loading and sustain standing wave patterns in forms of limit cycle oscillations. Secondly, the dynamics of panels must be strongly coherent and inter-related where the panels vibrating with same phase and modal behavior suppress the boundary layer instabilities very effectively. A complete schematic for the proposed framework

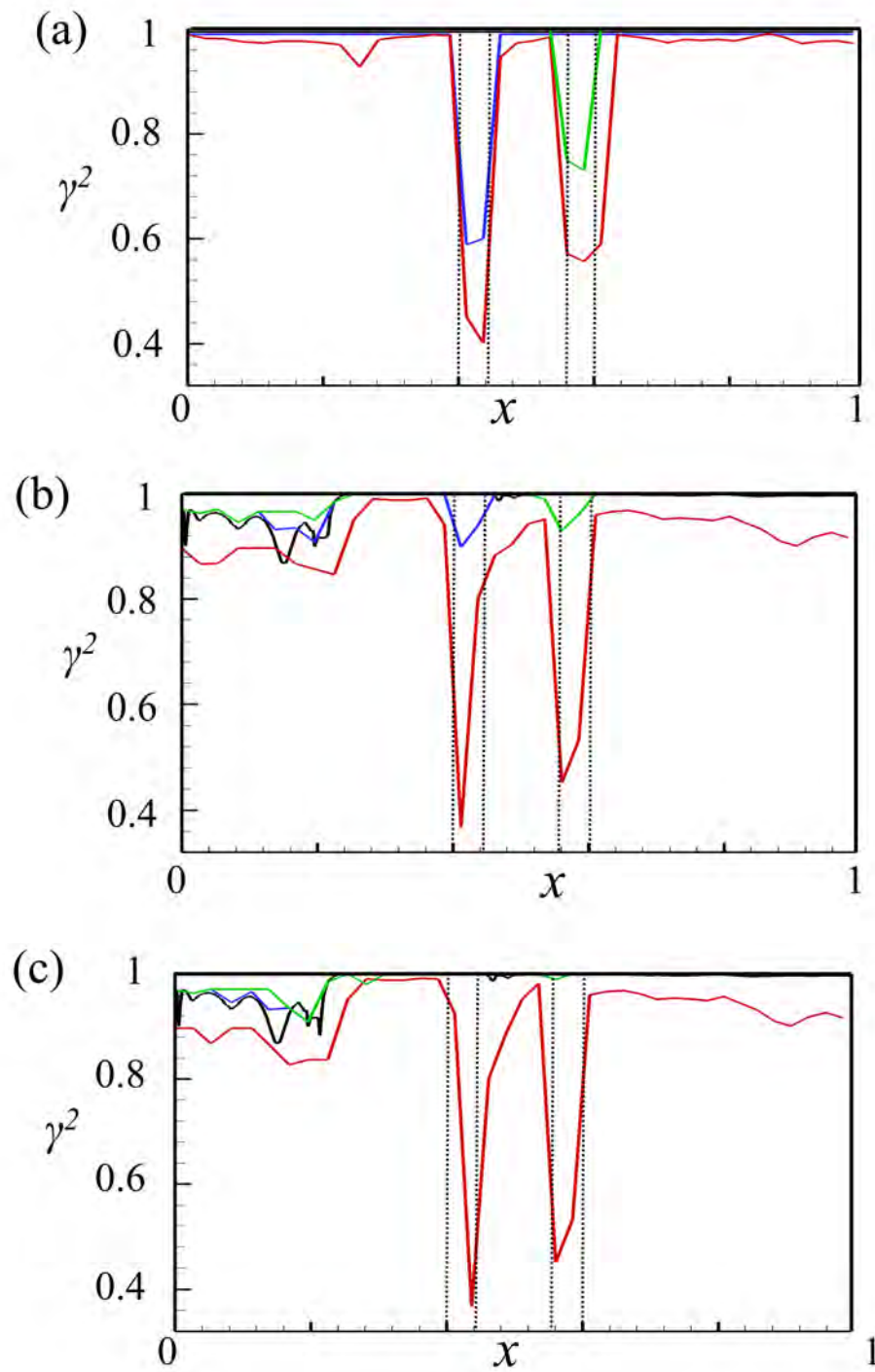


Figure 6.26: Coherence plot at (a) $(f_{bl})_0=3.37$, (b) $(f_{bl})_1=6.6$ and (c) $(f_{bl})_2=10$.
 —, RS; —, SP1; —, SP2; —, SCC1. The vertical black dotted lines indicate the panel edges.

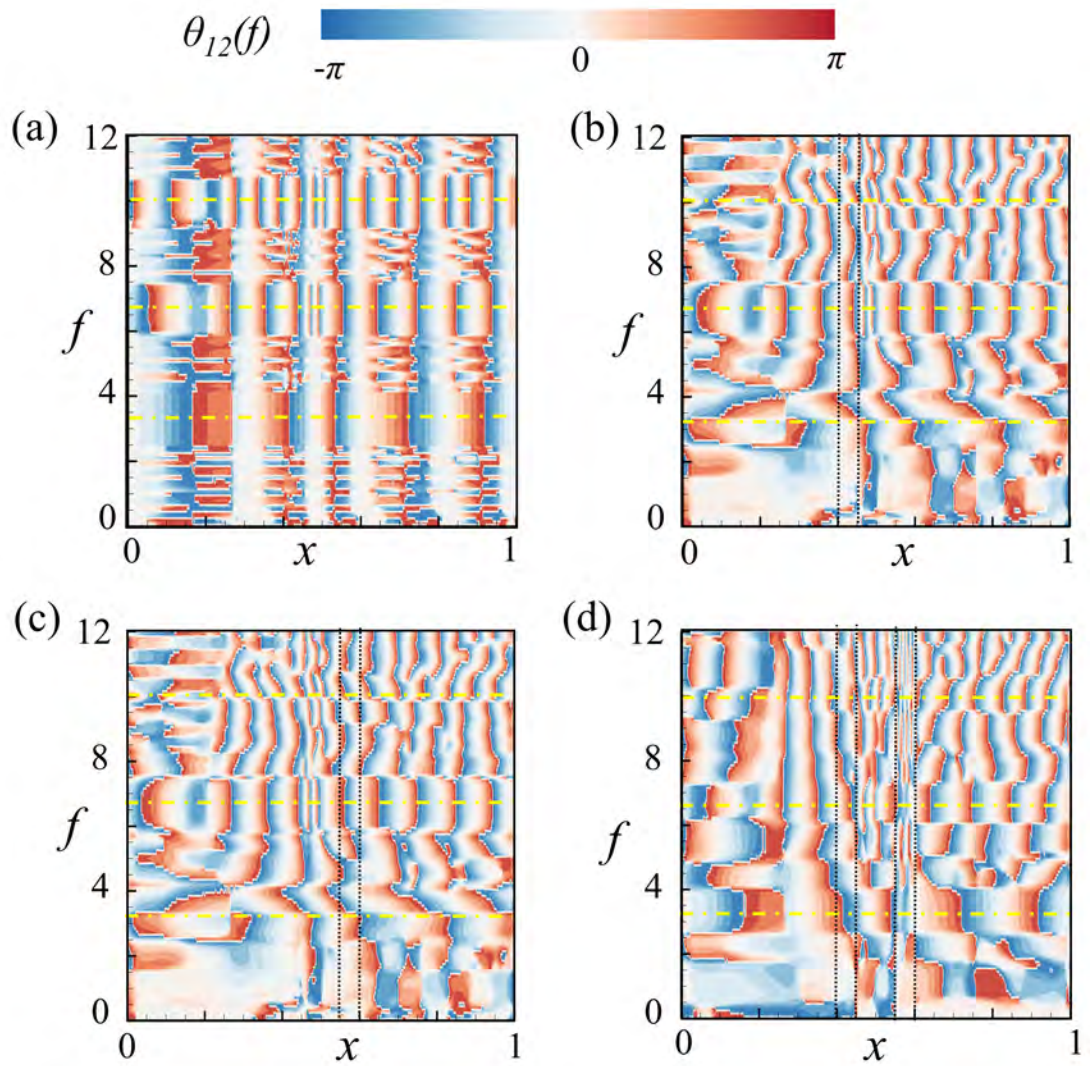


Figure 6.27: Spectra of phase difference θ_{12} between the acoustic signal at a location $(r, \theta) = (-1.12, 135^\circ)$ and velocity signals along the airfoil chord. (a) RS, (b) SP1, (c) SP2, and (d) SCC1. The horizontal yellow dot-dashed lines indicate the $(f_{bl})_n$, $n = 1, 2, 3$, and the vertical black dotted lines indicate the panel edges.

depicting the favorable panel locations based on the panels coupled structural resonance is shown in Fig. 6.28(a) and (b).

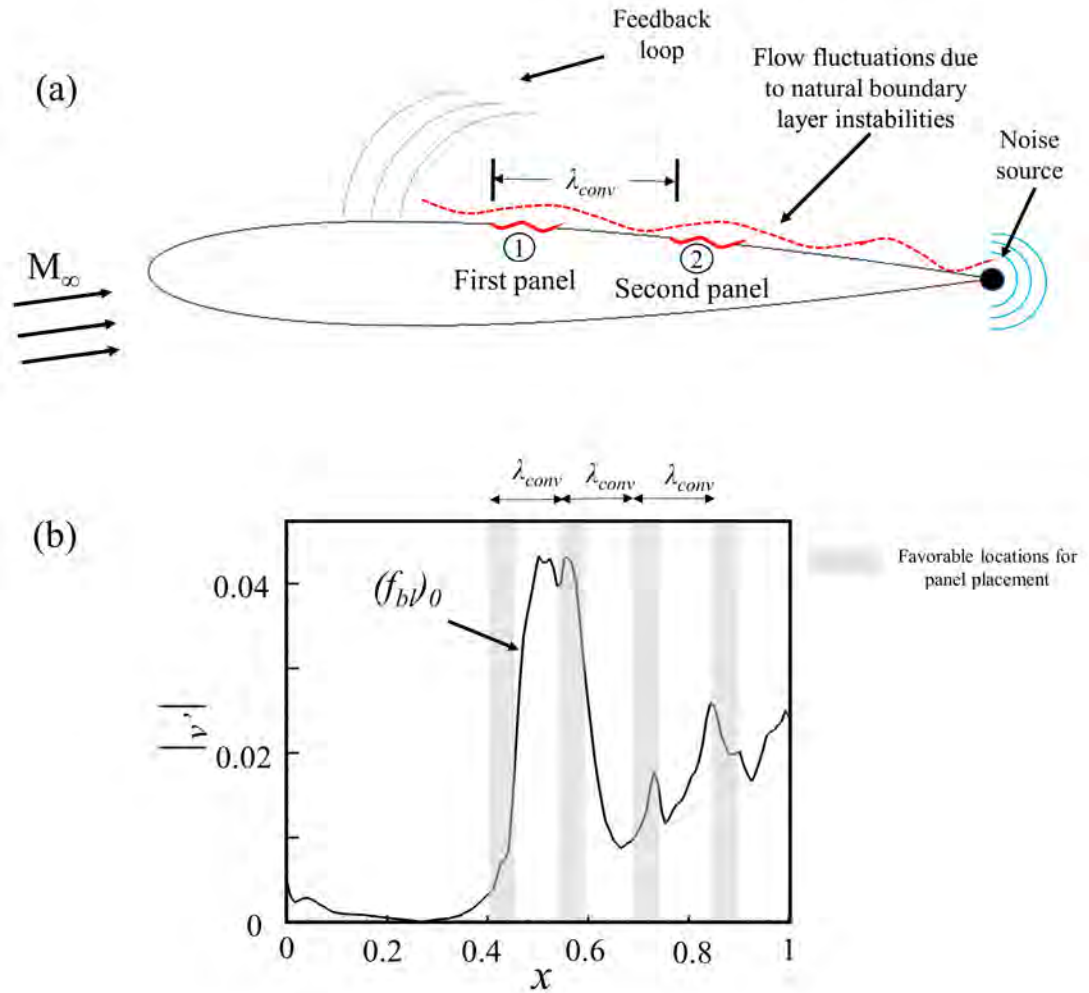


Figure 6.28: (a) Designed framework for panel pair configuration design, and (b) Identification of feasible locations for panel placement.

6.5 Conclusions

The proposed approach to enhance the airfoil tonal noise reduction by utilizing the coupled resonance of elastic panels flush-mounted on the suction surface of

NACA 0012 airfoil is investigated in this chapter. The numerical analysis is conducted at a low Re flow of 5×10^4 at $M = 0.4$ and $AoA = 5^\circ$ for a NACA 0012 airfoil. Initially, different airfoil configurations are designed based on the flow characteristics of rigid airfoil and subsequently analyzed using PEM. The strongly coupled configuration with the panels separated by one convective length λ_{conv} of boundary layer instability (SCC1) is observed to be most effective in tonal noise suppression as compared to other configurations. In order to analyze the underlying physical mechanism of tonal noise suppression for strongly coupled configuration, DAS calculation is performed and a comparative analysis is carried out with baseline rigid airfoil (RS) and single panel configurations (SP1 and SP2).

A comprehensive aeroacoustic and fluid-structure interaction analyses are performed using DAS to explore the insight of panel dynamics with the incoming flow and their inter-dynamical relationship. The acoustic analysis reveals that SCC1 results in a considerable reduction in acoustic wave without altering the overall flow behavior significantly. A significant effect of the coupled resonance on noise suppression is observed where a maximum reduction of 7.9 dB is observed which is even higher than the sum of the contributions of the corresponding single panel configurations. The aerodynamic analysis shows that the SCC1 provides significant suppression of flow instability growth over the suction surface. This is due to the fact that the strongly coupled panel vibration absorb the flow fluctuation energy more effectively and leave a very little flow distortion for scattering at the airfoil trailing edge. Furthermore, no significant deviation in the aerodynamic characteristics of the coupled configuration is observed as compared to the RS case.

Panel dynamic behavior is investigated by phase plots and temporal evolution spectra. Both panels vibrate at the selected third resonant mode at all time instances which implies that the panels are truly compliant to fluctuating

flow-induced loading and are able to effectively absorb energy from the oncoming flow to sustain their resonance condition. Two key characteristics in effective tonal noise suppression are determined for strongly coupled panel configuration. Firstly, the panels must vibrate in structural resonance and sustain standing wave patterns in the forms of limit cycle oscillations. Secondly, the dynamics of panels must be strongly coherent and inter-related where the panels vibrating with the same phase and modal behavior suppress the boundary layer instabilities more effectively.

Chapter 7

Multi-Panel Configuration for Noise Reduction at Various Loaded Conditions

7.1 Introduction

As discussed in Chapter 5 the passive method of utilizing an elastic panel mounted on the suction surface of a NACA 0012 airfoil has been found effective in tonal noise reduction at low Reynolds number Re of 5×10^4 , Mach number $M = 0.4$ and angle of attack $AoA = 5^\circ$. Furthermore, the noise reduction potential of the proposed method has been significantly enhanced by utilizing the coupled structural resonance of two elastic panels separated by a distance of approximately a convective wavelength λ_{conv} between the leading edges of the panels (Chapter 6). The phenomenon of structural coupling among the elastic panels can be effectively achieved for tonal noise reduction for the low Re devices which operate at a fixed freestream AoA such as cooling fans/blades. However, some devices operate at various loading conditions to achieve optimum operational performance

such as MAVs, UAVs etc. It is a well known fact that the changes in flow conditions directly affect the boundary layer characteristics over the airfoil such as flow separation/reattachment points, dominant frequency of the boundary layer instabilities, and the length of LSB (Lowson et al. 1994, Sandberg et al. 2007, Jones 2008, Pröbsting et al. 2015). In the present study, the airfoil is subjected to various loading conditions by means of varying the flow AoA . For the devices operating at variable $AoAs$, the structural coupling among the panels may not be maintained at each AoA and it may affect the tonal noise reduction potential of the airfoil as well. Therefore, an effort is made in this chapter to design and test a multi-panel configuration which could provide tonal noise reduction at various loading conditions. The assessment of the noise reduction potential of such airfoil configuration is carried out using perturbation evolution method (PEM) in this chapter.

7.2 Methodology

In the present chapter, a detailed methodology for the design of an airfoil configuration based on multiple elastic panels is proposed which could provide tonal noise reduction at different $AoAs$. The rationale behind selection of $AoAs$ and the design methodology along with analysis strategy are presented in detail in this section.

7.2.1 Choice of the Range of AoA

The most important aspect for the present analysis is to ascertain the range of AoA over which the effectiveness of airfoil tonal reduction is to be evaluated. As DAS requires very high computational resources it is not practically feasible to test the airfoil configuration for a wide range of AoA . Therefore, a design space is

initially identified based on the variations in the flow characteristics of airfoil at different $AoAs$ along with the physical limitations of employing multiple panels on the airfoil surface.

In the present study, the range of maximum AoA is limited to 7° as the boundary layer tends to be turbulent above this AoA for NACA 0012 airfoil (Pröbsting et al. 2015, Jones et al. 2008, Sandberg et al. 2007) and the generated airfoil noise tends to be broadband in nature. As the developed method aims to suppress the boundary layer instabilities due to formation of LSB on the suction surface of the airfoil. The minimum AoA is set to 1° below which the LSB forms near the trailing edge of the airfoil on both the pressure and suction surface and fails to reattach with the airfoil surface (Desquesnes et al. 2007, Jones 2008).

As discussed in Chapter 6 the structural coupling between two panels is achieved by maintaining a distance of λ_{conv} between the leading edges of the panels, it is essential to ascertain the variation in λ_{conv} with freestream $AoAs$. For the said purpose, DAS analyses of rigid airfoil are carried out for different $AoAs$ ranging from 1° to 7° with an increment of 1° . The average λ_{conv} at each AoA is evaluated using the same methodology as discussed in Chapter 6. The analysis is performed between the p' signal at a location $(r, \theta) = (3, 135^\circ)$ and a series of v' signals along a line slightly offset from the airfoil surface. The phase difference θ_{12} between a p' and v' signal is evaluated by a transfer-function estimate between the cross power spectral density of both signals. Figure 7.1 shows the variation of λ_{conv} with AoA obtained. It is observed that the λ_{conv} tends to reduce with an increase in AoA which is in agreement with the literature (Arcondoulis et al. 2019, Pröbsting and Yarusevych 2015). At lower $AoAs$ ($< 3^\circ$), λ_{conv} is observed to be less sensitive to AoA where λ_{conv} almost remains constant. This observation indicates that the effect of panel structural coupling in this range of AoA can easily be leveraged by maintaining a distance of $\lambda_{conv} \sim 0.17$ between the leading

edges of the panels. Furthermore, at lower $AoAs$ ($< 3^\circ$) the separation bubble forms towards the airfoil trailing edge (Pröbsting et al. 2015, Desquesnes et al. 2007, Jones et al. 2010) which physically limits the placement of multiple panels with a separation of λ_{conv} on the airfoil surface. Hence, the lower limit of AoA for the present study is changed from 1° to 3° while the upper limit is set at 7° .

From Figure 7.1 it is observed that the variation in λ_{conv} between $AoA = 3^\circ$ to 4° and $AoA = 5^\circ$ to 6° is only ~ 0.0073 per degree which accounts for less than 15% of the panel length $L_{EP} = 0.05$. Hence it appears that an increment of up to 1° in freestream AoA does not deviate from the requirement for the panel structural coupling significantly. However, with an increment of 2° in AoA (i.e. between $AoA = 3^\circ$ to 5° and $AoA = 5^\circ$ to 7°), the variation in $\Delta\lambda_{conv}$ is observed to be ~ 0.021 which accounts to $\sim 42\%$ of the panel length and may completely distort the structural coupling phenomenon. Therefore, in the present study, an interval of 2° is selected for the analysis within a range of AoA between 3° to 7° .

7.2.2 Design and Analysis Methodology

The adopted methodology for the design of multi-panel configuration for different $AoAs$ is divided into three major stages as shown in Figure 7.2. In Stage 1, the flow characteristics of the rigid airfoil at selected $AoAs$ are determined individually by DAS. The results of DAS analyses also help in determining the steady base flow at respective $AoAs$ for subsequent PEM analyses. In the next stage (Stage 2), the airfoil configuration with single elastic panel is designed for each AoA . The structural properties and suitable location of the panel on the airfoil surface at each AoA are determined based on the rigid airfoil characteristics evaluated in Stage 1. The rigid airfoil analysis, panel design methodology and PEM analysis at $AoA = 5^\circ$ have already been presented in preceding chapters and their information would be utilized. The effectiveness of the single-panel

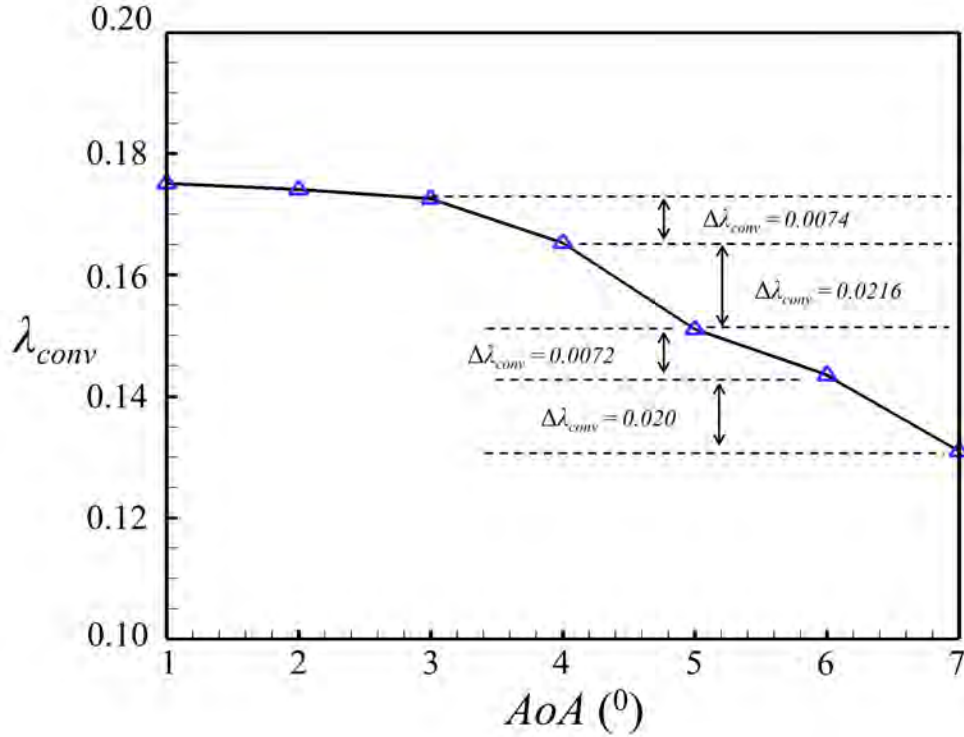


Figure 7.1: Variation of λ_{conv} with AoA .

configurations in tonal noise reduction is determined by PEM at their respective $AoAs$. In the final stage (Stage 3), a conceptual design of a multi-panel configuration is presented which is aimed to possibly achieve tonal noise reduction at different $AoAs$. The structural properties and locations of the elastic panels in this configuration are based on the PEM results obtained in Stage 2 for single-panel configurations at different $AoAs$. Finally, the effectiveness of the designed multi-panel configuration in airfoil tonal noise reduction is evaluated at different $AoAs$ by PEM.

7.3 Rigid Airfoil Analyses

As mentioned in Section 7.2.2, the rigid airfoil analyses at $AoA = 3^\circ$ and 7° are initially carried out in Stage 1 to ascertain the flow characteristics. The results

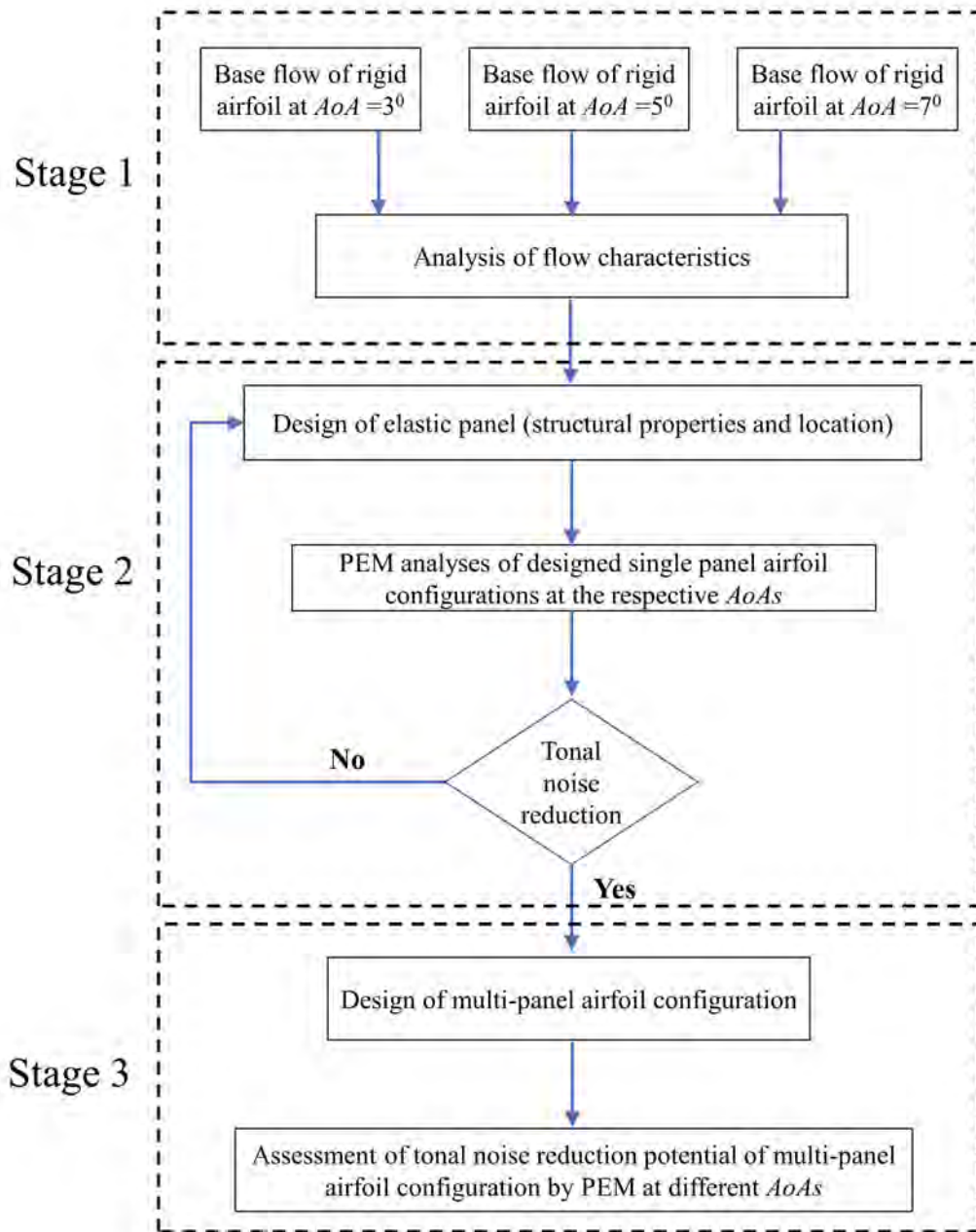


Figure 7.2: Schematic of the proposed methodology.

of rigid airfoil analyses will subsequently be utilized for the design of elastic panel on the airfoil for optimum tonal noise reduction. For DAS calculations, the computational domain, grid size and time step for $AoA = 3^\circ$ are kept same as that for the case of $AoA = 5^\circ$. However, for $AoA = 7^\circ$, the grid size near the airfoil surface is further refined by a factor of 2 so as to capture stronger flow unsteadiness within the boundary layer over the airfoil surface (Sandberg et al. 2007). The time step size is also reduced to 5×10^{-6} for $AoA = 7^\circ$ to maintain the same CFL. For every calculation, the solution is proceeded up till $t \sim 200$ to guarantee a time stationary state is achieved. The solution is then time-marched for an extra non-dimensional time episode of $t = 20$ for further analysis.

7.3.1 Time-Averaged Analysis

Figure 7.3 shows the time-averaged C_p distribution over the suction and pressure surfaces of airfoil. As a reference, the C_p distribution for airfoil at $AoA = 5^\circ$ is also shown in Figure 7.3. For $AoA = 3^\circ$, a sudden increase in C_p near the leading edge due to strong adverse pressure gradient can be observed on the airfoil suction surface. This is followed by a pressure plateau from $0.2 < x < 0.7$ and a rapid transition from $0.7 < x < 0.8$. From $0.8 < x < 0.9$, another pressure plateau is observed which is followed by an increase in C_p up till airfoil trailing edge. The C_p on the pressure surface decreases smoothly from the airfoil leading edge up to $x \sim 0.25$ and remains constant up till $x \sim 0.6$ and then increases slowly up till airfoil trailing edge. A similar pattern of C_p variation is observed for $AoA = 7^\circ$ with much higher magnitude and shorter length of pressure plateau which indicates a reduction in the length of LSB at higher flow incidence.

The time-averaged C_f distributions over the airfoil suction and pressure surfaces are shown in Figures 7.4(a) and (b). On the airfoil suction surface, the boundary layer separation occurs at $x \sim 0.34$ and reattaches at $x \sim 0.85$

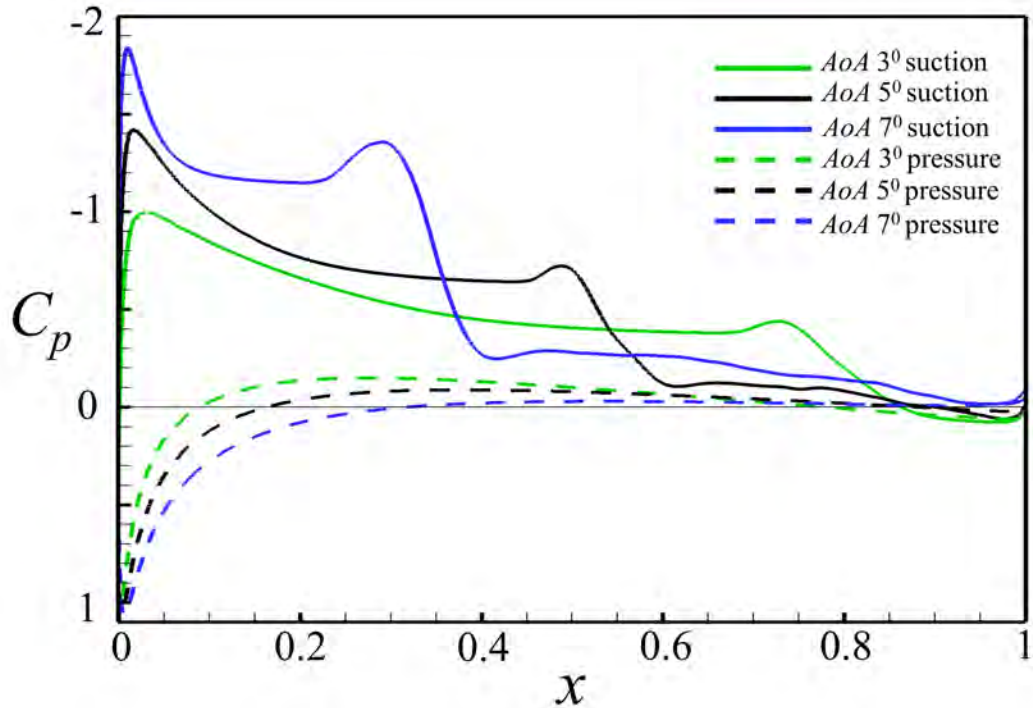


Figure 7.3: Time-averaged C_p distribution over the airfoil.

at $AoA = 3^\circ$, whereas at $AoA = 7^\circ$ the flow separation and reattachment shift further upstream to $x \sim 0.05$ and $x \sim 0.38$ respectively. Overall, a reduction in the length LSB is observed with an increase in AoA . However, no boundary layer separation on the pressure surface is observed at any flow condition. The changes in separation/reattachment points and length of LSB with increasing AoA are shown in Figure 7.5. The length of LSB reduces from 0.51 to 0.33 from $AoA = 3^\circ$ to 7° . Table 7.1 presents a summary of the calculated time-averaged aerodynamic parameters for all three $AoAs$ along with their comparison with the available literature (Jones et al. 2010, Jones 2008). A good agreement is observed in the parameters at all conditions which further validates the numerical methodology adopted for the study.

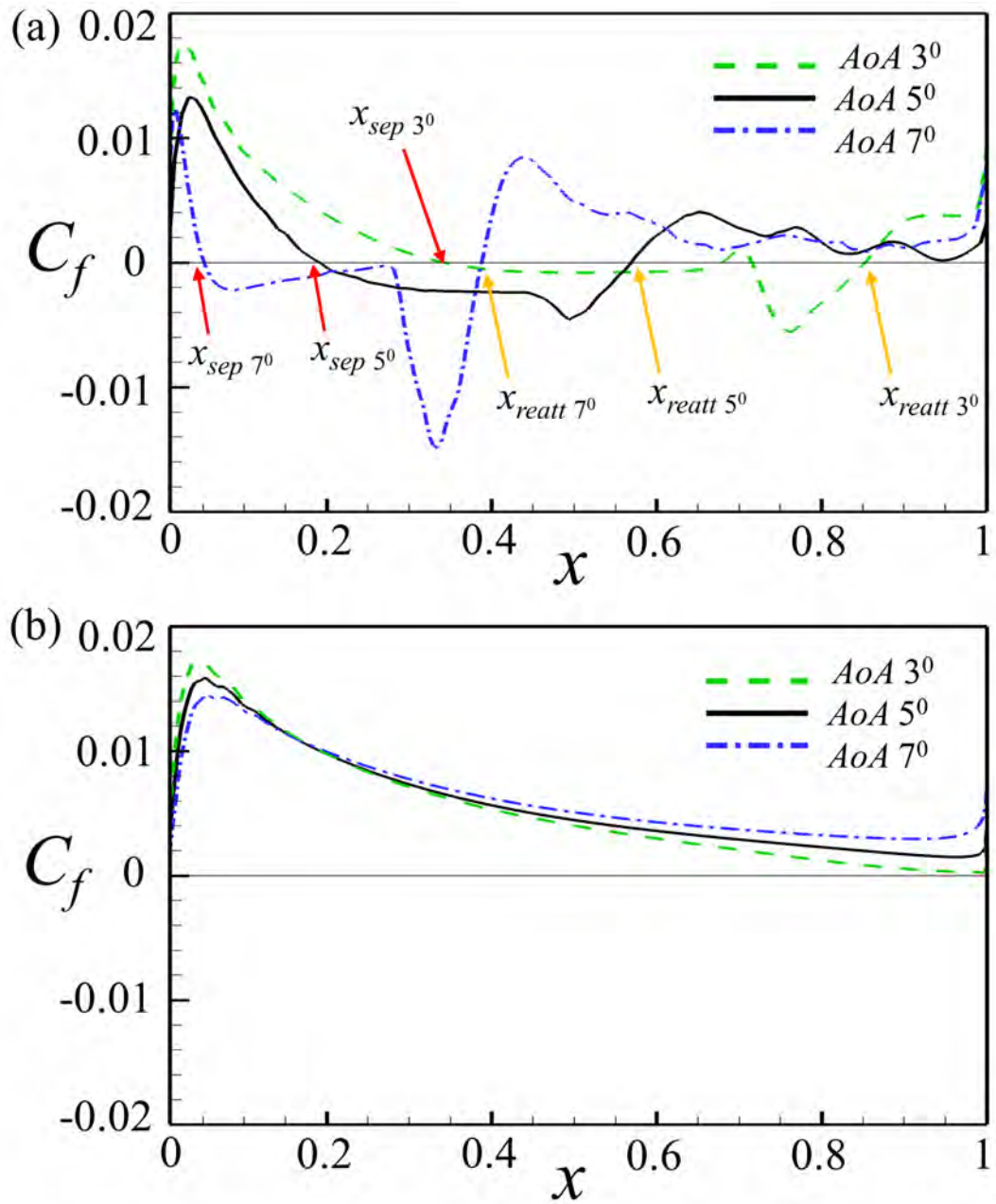


Figure 7.4: Time-averaged C_f distribution over the airfoil. (a) suction surface and (b) pressure surface.

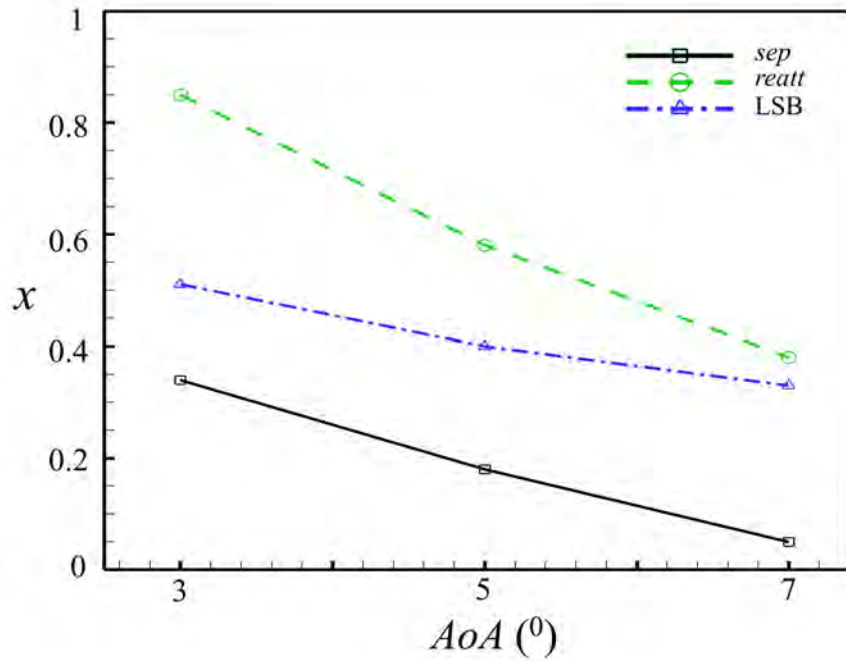


Figure 7.5: Variation of time-averaged separation point, reattachment point and length of separation bubble.

7.3.2 Unsteady Flow Analysis

Figure 7.6 shows the C_L variation with time for all $AoAs$. For brevity, only a time episode of $0 < t < 10$ is shown. The C_L fluctuates essentially in a periodic manner for $AoA = 3^{\circ}$ and 5° , whereas the C_L variation becomes irregular at higher AoA indicating the presence of complex unsteady flow behavior (Sandberg et al. 2007). Figures 7.7(a) to (c) show FFT of C_L for $AoA = 3^{\circ}$, $AoA = 5^{\circ}$ and 7° respectively. The FFT plot for $AoA = 3^{\circ}$ indicates a clear dominant peak frequency of 2.67 with several low amplitude peaks associated with higher-harmonics. At $AoA = 5^{\circ}$, the FFT plot reveals a dominant peak frequency of 3.37. However, at $AoA = 7^{\circ}$, the FFT spectrum exhibits a broadband spectrum with a highest peak at the frequency of 2.40. The analysis indicates that at $AoA > 5^{\circ}$ the vortex shedding behavior transitions from a dominant single frequency

Table 7.1: Comparison of time-averaged aerodynamic parameters.

Parameters	From present DAS / From Jones et al. (2008)		
	$AoA = 3^\circ$	$AoA = 5^\circ$	$AoA = 7^\circ$
$C_{L,mean}$	0.430 / 0.425 (1.17%)	0.485 / 0.490 (1.02%)	0.650 / 0.640 (1.56%)
$C_{D,mean}$	0.017 / 0.018 (5.55%)	0.0185 / 0.0201 (7.96%)	0.040 / 0.041 (2.43%)
x_{sep}	0.34 / 0.33 (3.03%)	0.18 / 0.15 (20%)	0.05 / 0.05 (—)
x_{reatt}	0.85 / 0.85 (—)	0.58 / 0.58 (—)	0.38 / 0.39 (2.56%)
LSB	0.51 / 0.52 (1.92%)	0.40 / 0.43 (6.97%)	0.33 / 0.34 (2.94%)
$f_{dominant}$	2.67 / 2.42 (10.33%)	3.37 / 3.37 (—)	2.40 / 2.40 (—)

Note: The term in brackets indicate the percentage deviation of the present DAS results from Jones et al. (2008).

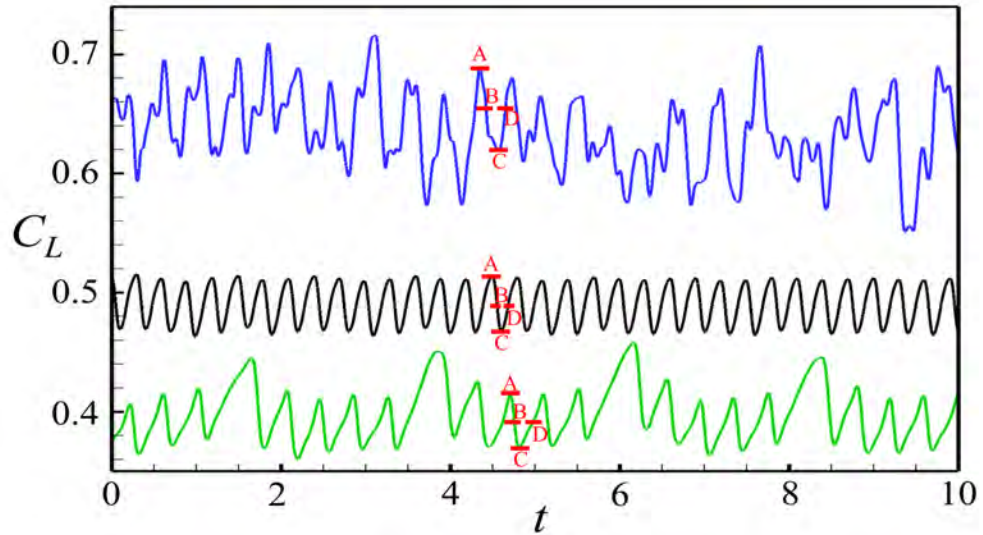


Figure 7.6: Time dependent C_L variation. —, $AoA = 3^\circ$; —, $AoA = 5^\circ$; —, $AoA = 7^\circ$.

to a broadband behavior due to turbulent flow characteristics near the trailing edge at higher $AoAs$ (Hoarau et al. 2003, Jones 2008).

The unsteady flow behavior over the airfoil for $AoA = 3^\circ, 5^\circ$ and 7° is illustrated by plotting the iso-contours of instantaneous vorticity at different time instances as shown in Figures 7.8, 7.9 and 7.10 respectively. The time instances for the vorticity plots are carefully chosen for a single lift cycle for each AoA which are indicated as A, B, C and D in Figure 7.6. The point A represents the instance of maximum lift for each AoA , whereas the time instance of C indicates the point of minimum lift. On the other hand, points B and D indicate the locations of the lift cycle where it crosses the neutral axis. For $AoA = 3^\circ$ as observed in Figure 7.8, the flow unsteadiness over the airfoil suction surface results in the vortex generation from the separated shear layer on airfoil suction surface and its passage over the airfoil trailing edge into the wake. The vortex shedding appears to be periodic with strong coherent structures convecting towards the airfoil trailing edge. For $AoA = 5^\circ$ (Figure 7.9), the formation of the vortices shift upstream

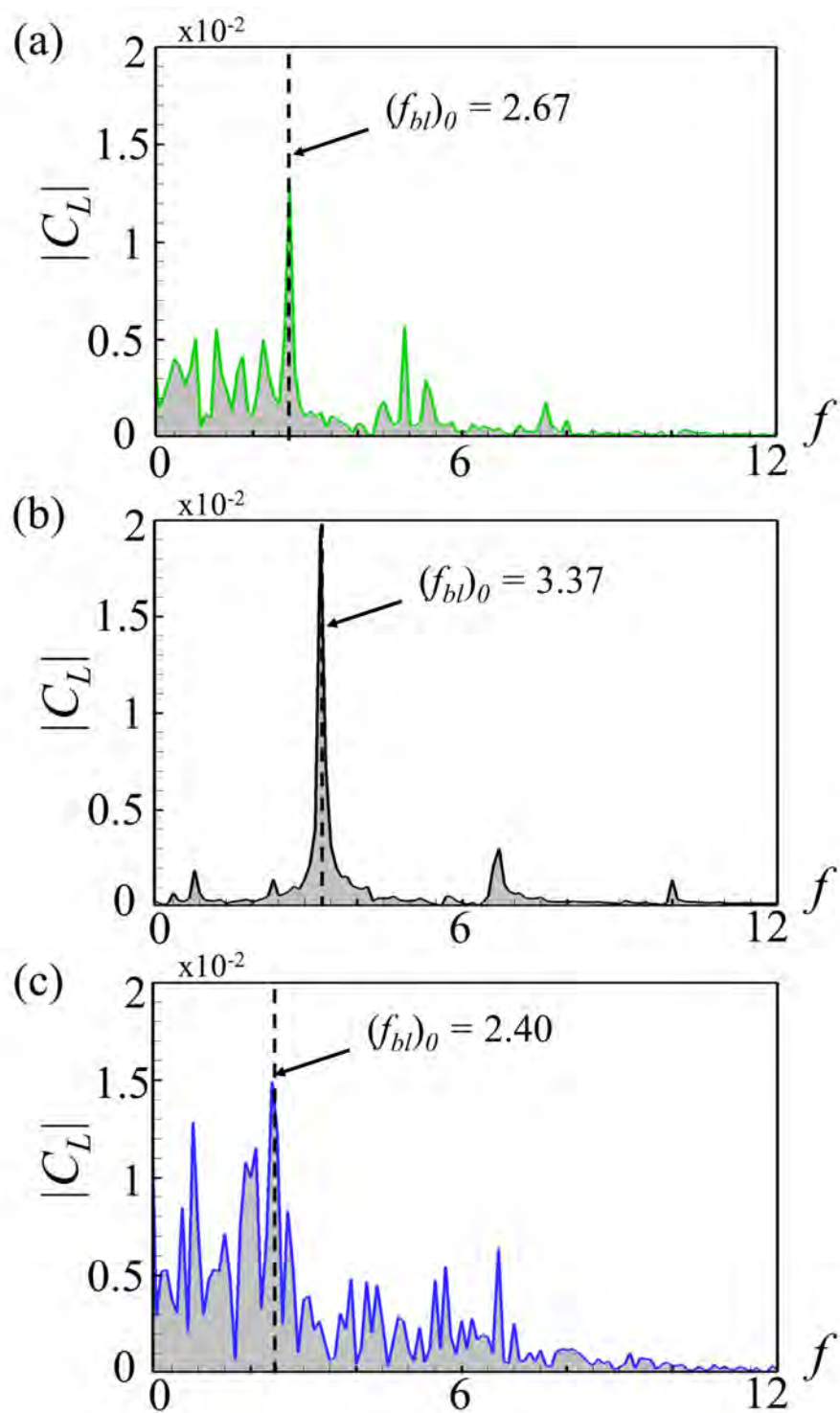


Figure 7.7: FFT spectra of time dependent C_L variation. (a) $AoA = 3^\circ$, (b) $AoA = 5^\circ$ and (c) $AoA = 7^\circ$.

with an increase of AoA due to the variation in the locations of separation and reattachment points as observed in Figure 7.4(a). Again, the vortex shedding appears to be periodic with strong coherent structures shedding into the airfoil wake. For $AoA = 7^\circ$ (Figure 7.10), the vortex shedding appears to be non-periodic due to early occurrence of laminar boundary layer separation and reattachment over the suction surface. Furthermore, vortex merging is also observed at different time instances which promotes high levels of flow instabilities over the later half of airfoil. As a result of non-coherent vortex shedding at $AoA = 7^\circ$, multiple peaks in the FFT spectra are observed in Figure 7.7.

7.4 Elastic Panel Design

In Stage 2, airfoil configuration with single elastic panel is designed for each AoA and the effectiveness of the configuration in tonal noise reduction is determined by PEM. The design of elastic panel is essentially based on three major parameters, namely panel length, structural properties and its location. The length of panel is set as $L_{EP} = 0.05$ for all the cases as such short length does not affect the radius of curvature over the airfoil suction surface as shown in Chapter 4. To determine suitable locations of panels for each AoA , the frequency spectra of transverse velocity fluctuations v' over the airfoil suction surface within the boundary layer are analyzed and shown in Figures 7.11(a) to (c). In these figures, a longer time history of $t = 20$ and a sampling frequency of 1×10^5 are selected for fine spectral resolution. For $AoA = 3^\circ$ (Figure 7.11(a)), its spectrum reveals that the natural airfoil boundary layer growth is dominated by the fundamental frequency $(f_{bl})_0 = 2.67$ along with its harmonics at the $(f_{bl})_1 = 5.20$. The magnitude of v' becomes observable within $0.65 \leq x \leq 0.85$ which indicates the presence of significant boundary layer instabilities within the separation bubble. The magnitude of v' observed at the fundamental frequency $(f_{bl})_0 = 2.67$ is much

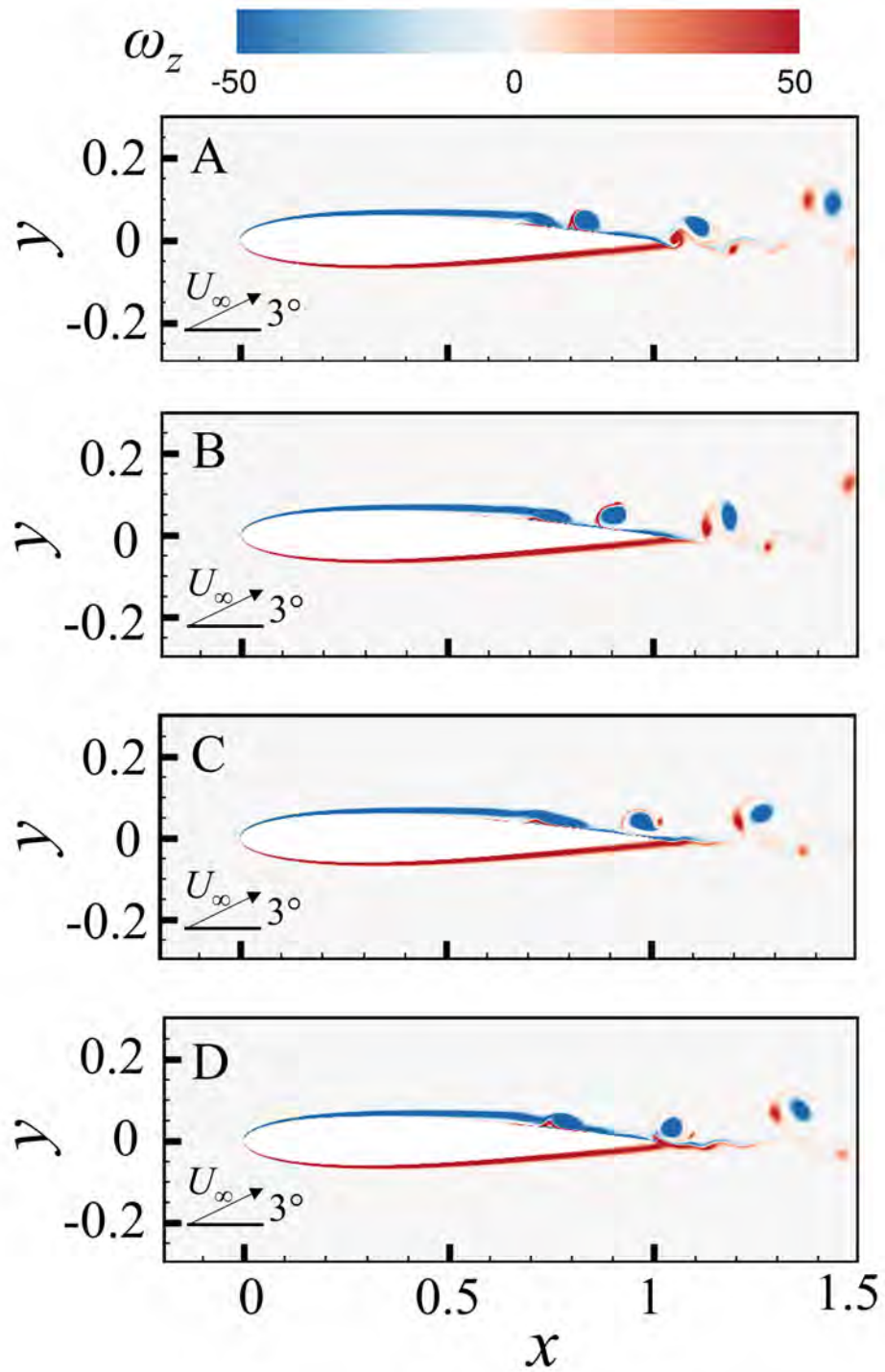


Figure 7.8: Iso-contours of instantaneous vorticity for $AoA = 3^\circ$ at different time instances.

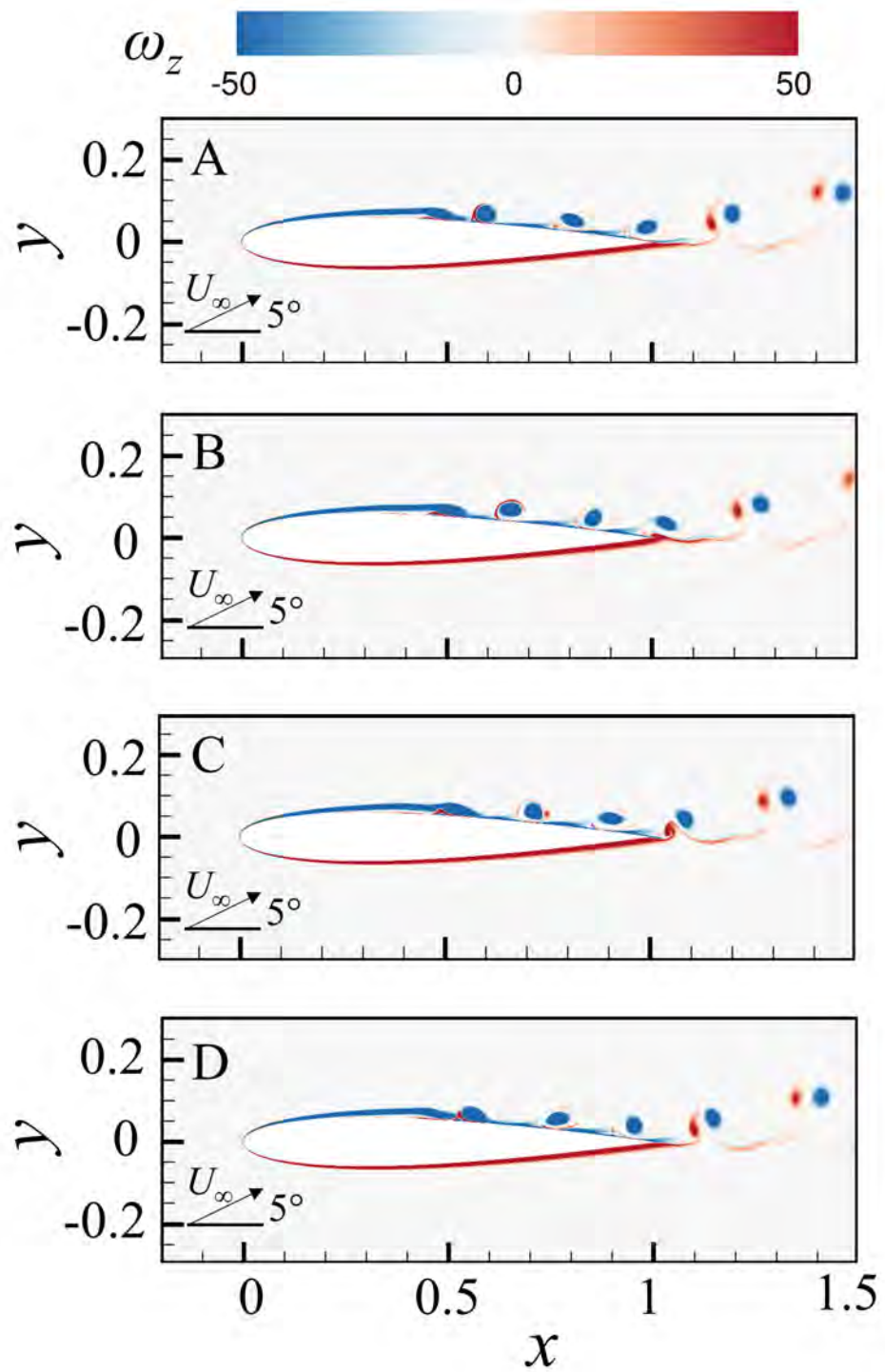


Figure 7.9: Iso-contours of instantaneous vorticity for $AoA = 5^\circ$ at different time instances.

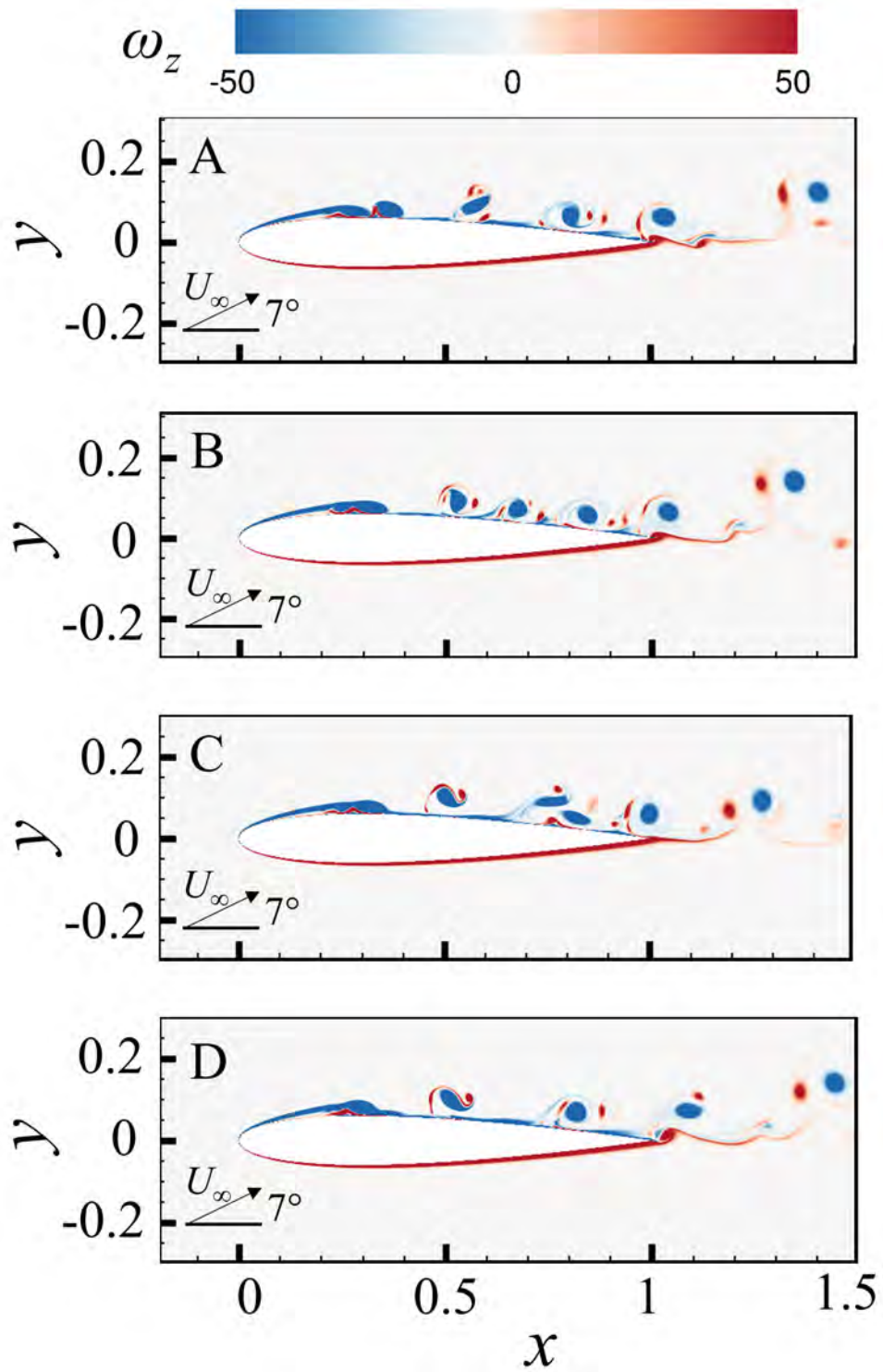


Figure 7.10: Iso-contours of instantaneous vorticity for $AoA = 7^\circ$ at different time instances.

higher than its first harmonics at $(f_{bl})_1 = 5.20$. Lower amplitude flow fluctuations are observed at regular intervals of $\Delta f = 0.05$ which possibly indicate the presence of secondary tones (Desquesnes et al. 2007, Ricciardi et al. 2020). For $AoA = 5^\circ$ (Figure 7.11(b)), the spectrum reveals that the natural airfoil boundary layer growth is dominated by the fundamental frequency $(f_{bl})_0 = 3.37$ along with its higher harmonics. The magnitude of v' becomes observable from $x \sim 0.4$ up to the airfoil trailing edge which indicates the presence of significant boundary layer instabilities. For $AoA = 7^\circ$ (Figure 7.11(c)), the spectrum shows scattered frequency content which is broadband in nature as also observed in Figure 7.7(c). However, a high magnitude of v' is observed at $(f_{bl})_0 = 2.40$. The magnitude becomes observable within $0.2 \leq x \leq 0.38$ within the separation bubble and reduces significantly at the reattachment point. The magnitude slightly increases again at a downstream location near the airfoil trailing edge.

To investigate the unsteady flow behavior within the boundary layer over the suction surface, the natural boundary layer stability characteristics are analyzed at the dominant frequencies for $AoA = 3^\circ$ ($(f_{bl})_0 = 2.67$), $AoA = 5^\circ$ ($(f_{bl})_0 = 3.37$) and $AoA = 7^\circ$ ($(f_{bl})_0 = 2.40$) as shown in Figure 7.12. For $AoA = 3^\circ$, the amplitude of v' starts to increase at $x \geq 0.55$ and grow within $0.65 \leq x \leq 0.7$ whereas the amplitude of v' for $AoA = 5^\circ$ starts to increase at $x \geq 0.27$ and grow within $0.4 \leq x \leq 0.45$. For $AoA = 7^\circ$, the growth of v' moves further upstream where it starts to increase at $x \geq 0.18$ and grow within $0.2 \leq x \leq 0.32$. It is well established that designed elastic panel is able to effectively weaken the boundary layer instabilities when it is located corresponding to the onset of rapid growth of flow instabilities (Chapter 4). Based on the flow instability characteristics over the suction surface of airfoil observed in Figure 7.12, the panel for the case of $AoA = 3^\circ$ is located with its leading edge at $x_{le} = 0.65$ on the airfoil suction surface. For the case of $AoA = 7^\circ$, the panel is located with

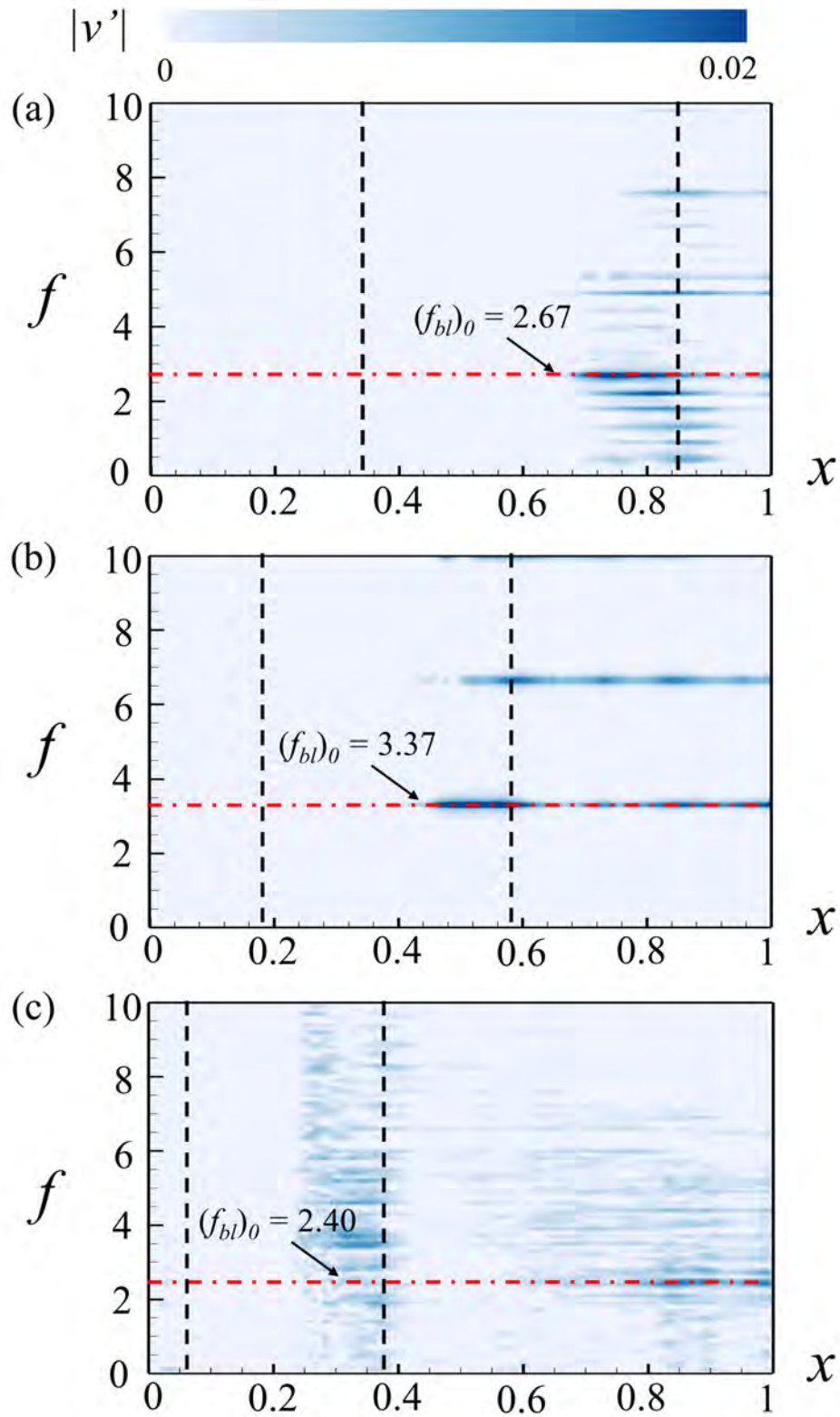


Figure 7.11: Frequency spectra of transverse velocity fluctuations. (a) $AoA = 3^\circ$, (b) $AoA = 5^\circ$ and (c) $AoA = 7^\circ$. The vertical black dashed lines indicate boundary layer separation and reattachment locations. The horizontal red dot-dashed lines indicate the dominant frequencies of the boundary layer instabilities.

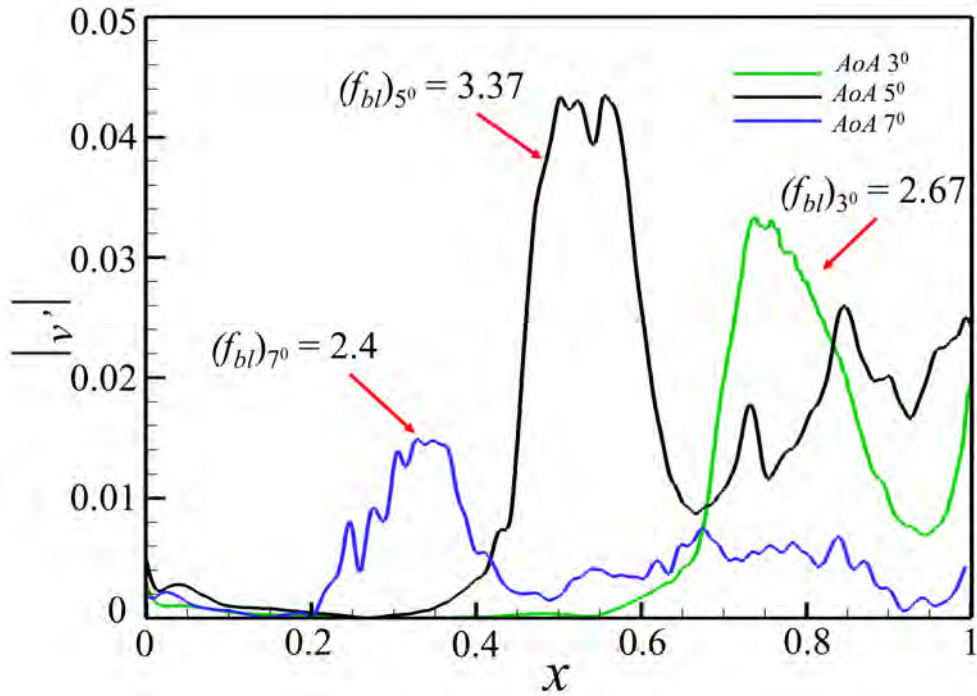


Figure 7.12: Spatial growth of flow instability over the airfoil suction surface.

its leading edge at $x_{le} = 0.20$ on the airfoil suction surface. The location of the panel for the case of $AoA = 5^\circ$ is set with its leading edge at $x_{le} = 0.40$ on the airfoil suction surface as already discussed in detail in Chapter 4. The schematics of the airfoil with elastic panel for all $AoAs$ are shown in Figures 7.13(a) to (c).

For each case, the properties of the panel are selected in a way that its natural frequency (in third natural mode) coincides with the dominant frequency of the flow instabilities within the boundary layer to achieve structural resonance condition under the fluid loading. Details on the mathematical formulation for the calculation of panel natural frequency in the presence of flow have been presented in Chapter 4. The selected parameters for the designed panel in non-dimensional form are tabulated in Table 7.2.

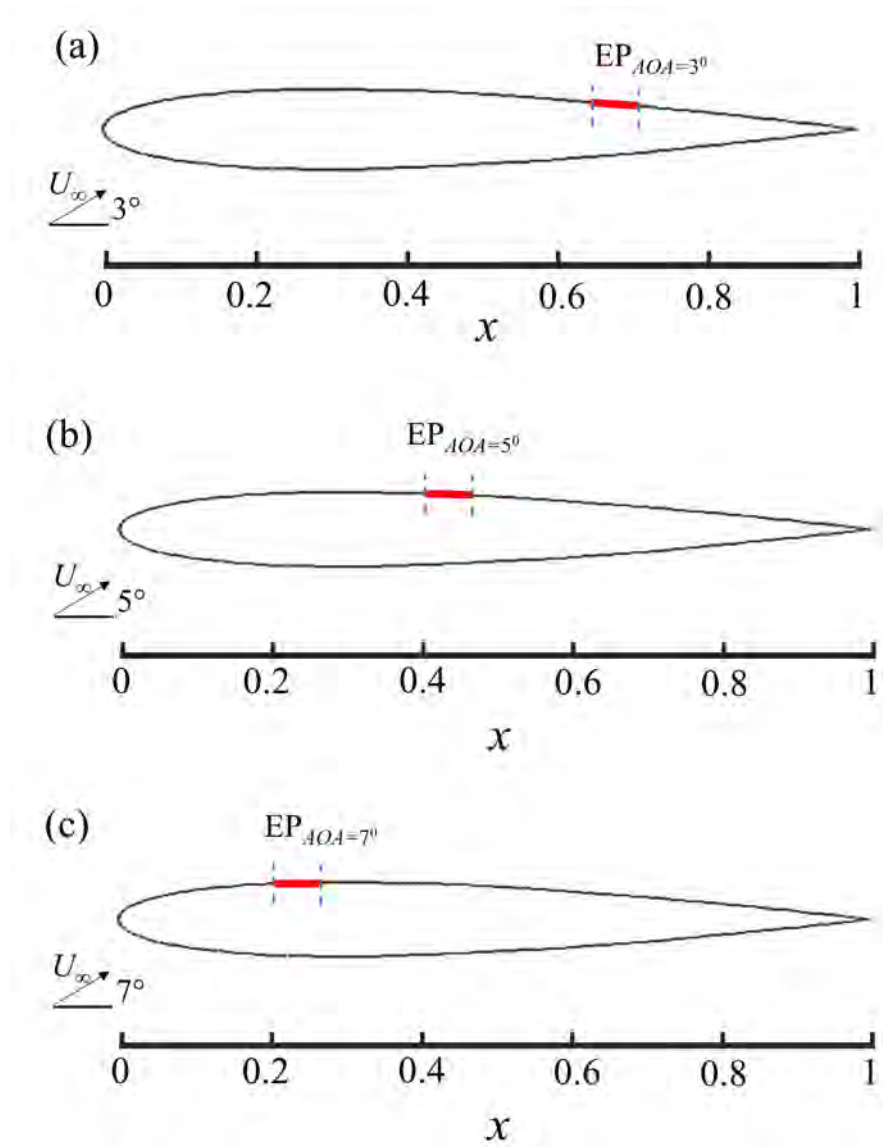


Figure 7.13: Schematic sketch of the airfoil configurations with single elastic panels. (a) $AoA = 3^\circ$. (b) $AoA = 5^\circ$. (c) $AoA = 7^\circ$.

Table 7.2: Normalized elastic panel parameters

Case	x_{le}	L_{EP}	h_{EP}	T_{EP}	ρ_{EP}	$(f_{EP})_1$	$(f_{EP})_2$	$(f_{EP})_3$	$(f_{EP})_4$	$(f_{EP})_5$
EP _{AoA=3°}	0.65	0.05	0.014	0.725	6367.34	0.89	1.78	2.67	3.56	4.45
EP _{AoA=5°}	0.40	0.05	0.009	0.725	6367.34	1.12	2.24	3.37	4.49	5.62
EP _{AoA=7°}	0.20	0.05	0.009	0.366	6367.34	0.81	1.61	2.40	3.20	4.01

7.5 Assessment of Noise Reduction by PEM

A quick assessment of noise reduction potential of the airfoil mounted with single elastic panel for the cases of $AoA = 3^\circ$ and 7° is carried out by PEM. For PEM, same method as described in Chapter 4 is implemented where a broadband excitation with a pressure amplitude $p_A = 10^{-5}$ is introduced near the leading edge of airfoil at a location $(x, y) = (-0.015, -0.01)$ to generate weak artificial perturbations.

The azimuth plots of p'_{rms} at $r = 3$ for $AoA = 3^\circ$ and 7° are shown in Figures 7.14(a) and (b) respectively. For $AoA = 3^\circ$, the strongest radiation goes along $\theta \sim 140^\circ$ and $\sim 300^\circ$ respectively. A significant reduction in p'_{rms} is observed at all azimuth locations for the airfoil configuration with single elastic panel (EP_{AoA=3°}) as compared to RS. For $AoA = 7^\circ$, the strongest radiation goes along $\theta \sim 140^\circ$ and $\sim 220^\circ$ respectively. The reduction in p'_{rms} for EP_{AoA=7°} appears to be much lower than EP_{AoA=3°} and EP_{AoA=5°}. For each AoA , the noise directivity resembles to its corresponding rigid airfoil configuration which confirms that the panel vibration does not affect the mean flow dynamics. To further illustrate the extent of noise reduction, the sound pressure level reduction $\Delta SPL_{reduction}$ is evaluated for all three single-panel configurations as shown in Figure 7.15.

Table 7.3: Panel effectiveness at different flow conditions

Case	Average $\Delta SPL_{reduction}$	Maximum $\Delta SPL_{reduction} / \theta_{max}$
EP _{AoA=3°}	3.5 dB	5.6 dB / 210°
EP _{AoA=5°}	2.1 dB	2.4 dB / 130°
EP _{AoA=7°}	1.1 dB	2.9 dB / 168°

Different extents of noise reduction are observed for each configuration around all azimuth locations. Table 7.3 shows the comparative analysis of noise reduction for all configurations. The noise reduction achieved by EP_{AoA=3°} configuration is observed to be much higher than other configurations. An average $\Delta SPL_{reduction}$ of 3.5 dB is observed for EP_{AoA=3°} with maximum reduction of ~ 5.6 dB along $\theta \sim 210^\circ$. For EP_{AoA=5°} configuration, an average noise reduction of 2.1 dB is observed with a maximum reduction of 2.4 dB along $\theta \sim 130^\circ$. The extent of noise reduction for EP_{AoA=7°} configuration is much lower than other configurations where an average noise reduction of only 1.1 dB is observed. The enhancement in noise reduction performance of the elastic panel at $AoA = 3^\circ$ can be attributed to the presence of longer separation bubble ($x \sim 0.51$) as compared to the separation bubbles observed at $AoA = 5^\circ$ and 7° respectively, which allows the panel to absorb much more energy from the flow insatiabilities within the separated region to sustain its vibration.

PEM analyses of single-panel configurations evidently illustrate significant average tonal noise reduction for all three $AoAs$. Their results are expedient in the design of a multi-panel configuration which could possibly provide some extent of tonal noise reduction at different $AoAs$.

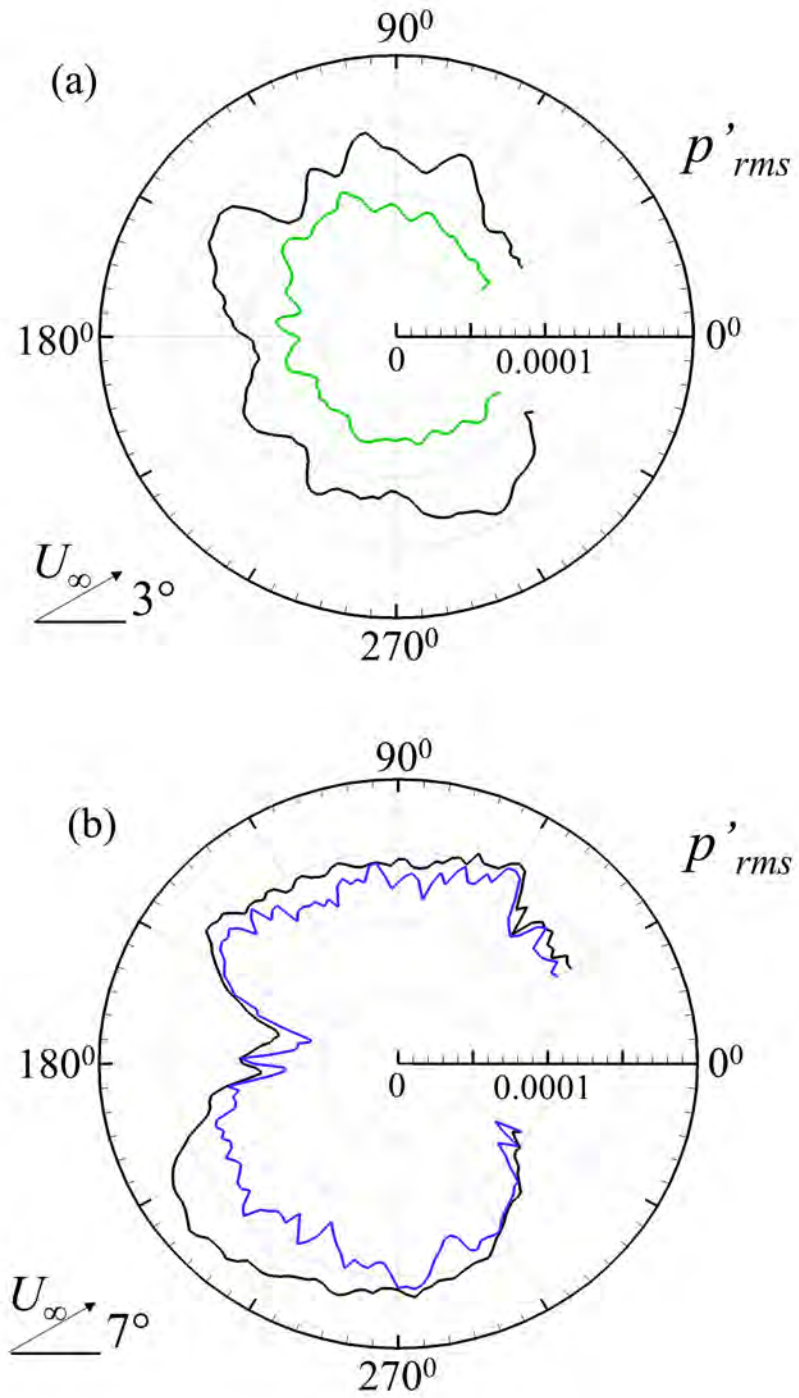


Figure 7.14: Azimuth distribution of p'_{rms} at $r = 3$. (a) $AoA = 3^\circ$. (b) $AoA = 7^\circ$. —, RS; —, $EP_{AoA=3^\circ}$; —, $EP_{AoA=7^\circ}$.

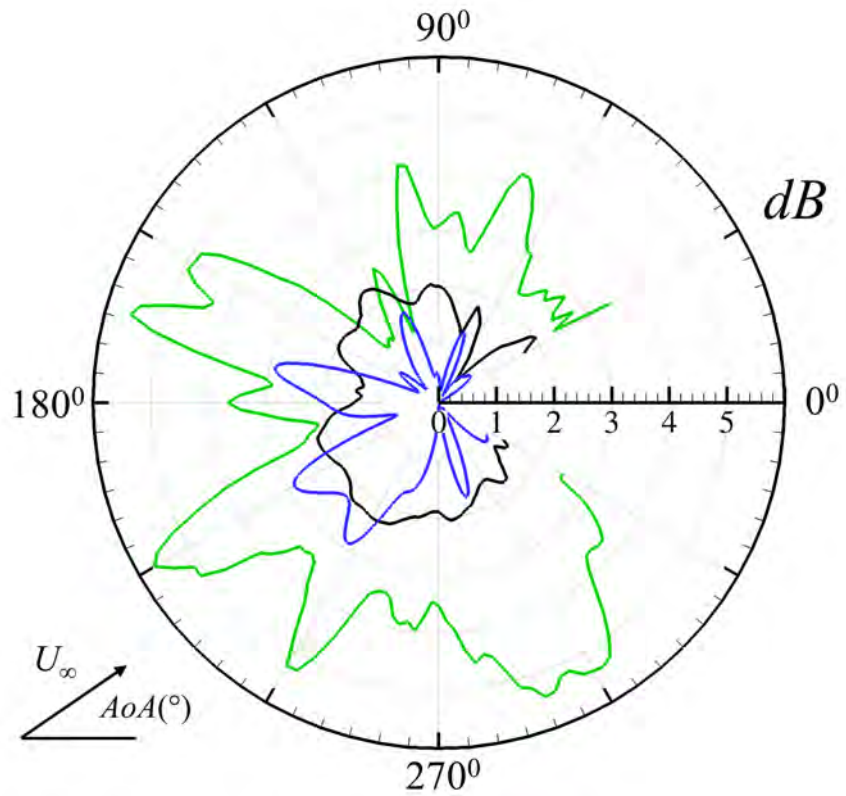


Figure 7.15: Azimuth distribution of $\Delta SPL_{reduction}$ at $r = 3$. —, $EP_{AoA=3^\circ}$;
 —, $EP_{AoA=5^\circ}$; —, $EP_{AoA=7^\circ}$.

7.6 Multi-Panel Configuration

In Stage 3, a conceptual design of a multi-panel configuration is presented which is aimed to achieve tonal noise reduction at different $AoAs$. The structural properties and locations of the elastic panels in this configuration are based on the PEM results obtained in Stage 2 for single-panel configurations at different $AoAs$. Subsequently, the effectiveness of the designed multi-panel configuration in tonal noise reduction is evaluated at different $AoAs$ by PEM.

7.6.1 Panel Design Concept

PEM analyses of single-panel configurations at $AoAs = 3^\circ, 5^\circ$ and 7° indicate different extents of tonal noise reduction. All these configurations have exhibited high potential of noise reduction at a particular AoA . Now, for the design of an airfoil which could provide tonal noise reduction at different $AoAs$ the results of the PEM analyses for single-panel configurations obtained in Stage 2 are utilized and a design scheme is formulated. As discussed in Section 7.2.1, an increment/decrement of freestream AoA by 2° results in a considerable variation in λ_{conv} . Hence, a simple panel design concept is proposed for an airfoil operating within the range of $AoA = 3^\circ$ to 7° by mounting three evaluated elastic panels on the suction surface of the airfoil. This specific airfoil configuration mounted with multiple panels is designated as 'MPC' in the present study (Figure 7.16). For MPC, the first elastic panel (designated as 'EP1') is located with its leading edge at $x_{le} = 0.2$ based on the favorable noise reduction characteristics observed at $AoA = 7^\circ$; the second elastic panel (designated as 'EP2') is located with its leading edge at $x_{le} = 0.4$ based on the favorable noise reduction characteristics at $AoA = 5^\circ$ and the third elastic panel (designated as 'EP3') is located with its leading edge at $x_{le} = 0.65$ due to its high noise reduction potential at $AoA = 3^\circ$. The structural properties and the natural frequencies of the elastic panels EP1,

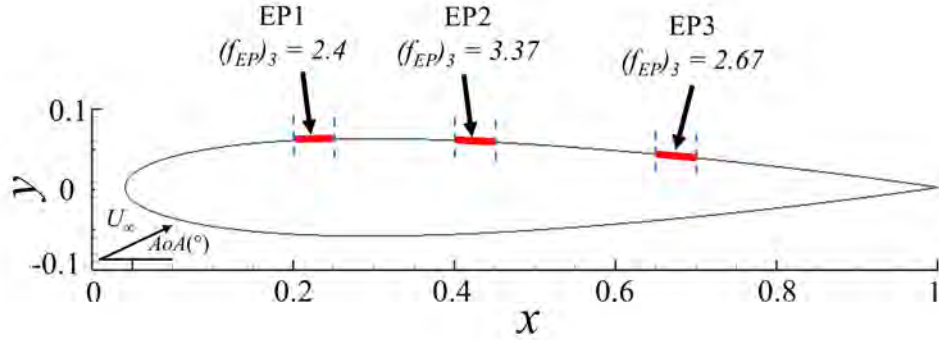


Figure 7.16: Schematic sketch of the MPC design concept.

EP2 and EP3 are same as that of the single-panel configurations for $AoA = 7^\circ$, $AoA = 5^\circ$ and 3° respectively (Table 7.2).

7.6.2 Noise Reduction Potential of MPC

The effectiveness of MPC in tonal noise reduction at different $AoAs$ is evaluated with PEM analysis. Figure 7.17 shows the azimuth plots of p'_{rms} at $r = 3$ for both RS and MPC at each AoA . At $AoA = 5^\circ$ (Figure 7.17(b)), a significant reduction in p'_{rms} is observed at all azimuth locations for MPC as compared to RS. However, the noise directivity for the MPC is observed to be slightly different than the single-panel configuration at $AoA = 5^\circ$ (as illustrated in Chapter 4) which indicates that the complex fluid-structure interactions among the three panels have modified the acoustic radiation pattern of the airfoil. Furthermore, the azimuth plot for MPC appears to be asymmetric around $\theta = 0^\circ$ where the reduction in p'_{rms} appears to be significant in the third quadrant. At $AoA = 3^\circ$ (Figure 7.17(a)), a reduction in p'_{rms} is observed for most azimuth locations; however, a slight amplification is also observed between $120^\circ \leq \theta \leq 140^\circ$. At $AoA = 7^\circ$, the reduction in p'_{rms} in first quadrant is much higher than $AoA = 3^\circ$ and a greater region of amplification in p'_{rms} is also observed between $120^\circ \leq \theta \leq 170^\circ$. The noise directivity patterns for MPC at $AoA = 3^\circ$ and 7° differ from their

respective single-panel configurations as observed in Figures 7.14(a) and (b). It is important to note that the noise directivity pattern for the single-panel airfoil configurations remains similar to that of rigid airfoil (Figure 7.14), however the complex inter-dynamical interaction among the panels for MPC appear to slightly modify the noise directivity pattern as compared to rigid airfoil.

The extent of noise reduction achieved by MPC is evaluated by analyzing the $\Delta SPL_{reduction}$ at different $AoAs$ and shown in Figure 7.18. The noise reduction achieved by MPC at $AoA = 5^\circ$ is much higher than other $AoAs$ where an average reduction of 4.41 dB is observed with a maximum reduction of 7.92 dB at $\theta = 185^\circ$. At $AoA = 3^\circ$, an overall average noise reduction of 2.20 dB is observed with a maximum reduction of 7.73 dB at $\theta = 178^\circ$. However, a maximum noise amplification of 1.46 dB is also observed at $\theta = 126^\circ$. At $AoA = 7^\circ$, an overall average noise reduction of 1.41 dB is observed with a maximum reduction of 6.75 dB at $\theta = 60^\circ$ but a maximum noise amplification of 1.70 dB is also observed at $\theta = 164^\circ$. Table 7.4 shows a comparative analysis of noise reduction at all $AoAs$ along with the noise reduction achieved by the corresponding single-panel configurations. It is interesting to observe that an enhancement in the maximum noise reduction is achieved by MPC as compared to single-panel configuration at each AoA ; however, the average noise reduction is reduced for $AoA = 3^\circ$ and remains almost similar at $AoA = 7^\circ$. The average noise reduction by MPC at $AoA = 5^\circ$ is much lower than the noise reduction achieved by the coupled panel airfoil configuration at the same AoA (Chapter 6). The overall noise reduction for MPC is observed to be highest at $AoA = 5^\circ$ whereas the highest noise reduction for single-panel configuration is observed at $AoA = 3^\circ$. The possible cause of higher noise reduction at $AoA = 5^\circ$ for MPC may be attributed to the fact that all the panels are exposed to region of high boundary layer flow instabilities at this AoA as compared to that for $AoA = 3^\circ$ and 7° (Figure 7.12). Furthermore,

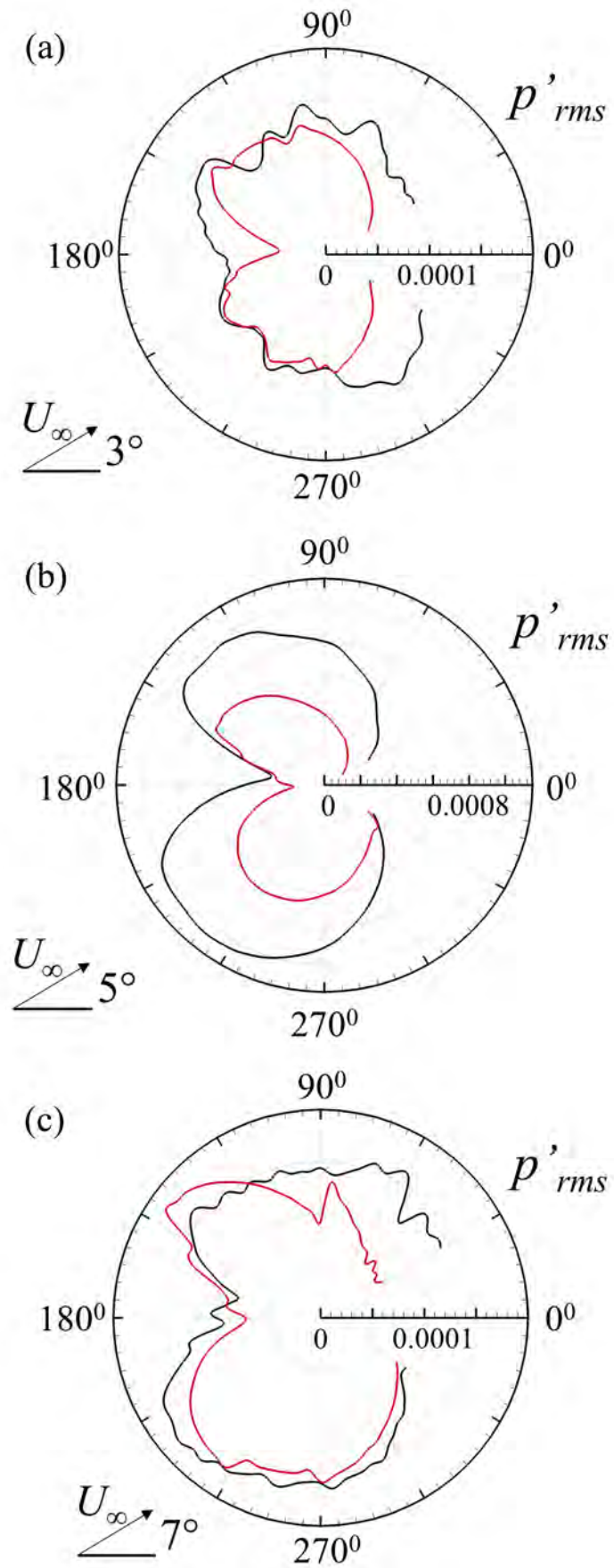


Figure 7.17: Comparison of azimuth distributions of p'_{rms} at $r = 3$ between MPC and RS. (a) $AoA = 3^\circ$, (b) $AoA = 5^\circ$, and (c) $AoA = 7^\circ$. —, RS; —, MPC.

the panels inter-dynamical interactions appear to play a critical role in enhancing/degrading the noise reduction of panel-airfoil configuration as observed in Chapter 6. However, exploration of these effects would require multiple DAS calculations for better in-depth evaluation which is left to future study.

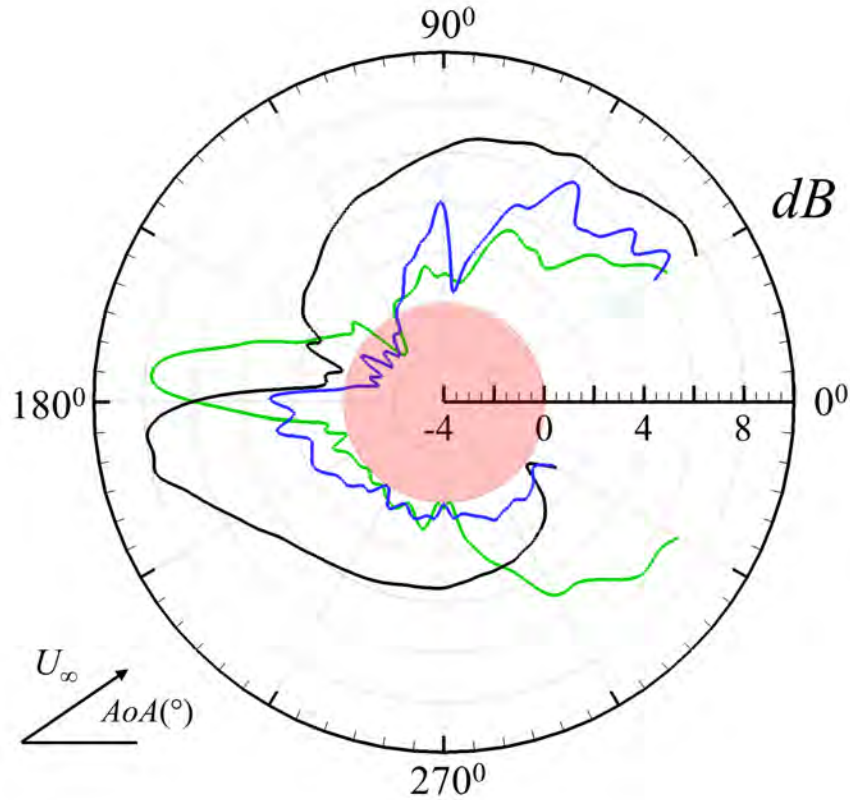


Figure 7.18: Comparison of azimuthal distribution of $\Delta SPL_{reduction}$ at $r = 3$ between MPC and respective RS. —, $AoA = 3^\circ$; —, $AoA = 5^\circ$; —, $AoA = 7^\circ$. The area shaded in red indicates SPL amplification.

From the results of acoustic analysis, a slight variation in the noise directivity pattern for the MPC is observed at different $AoAs$ as compared to their RS configurations. To ascertain the change in flow characteristics due to elastic panels dynamic, FFT spectra of v' for MPC are evaluated at $x = 0.9$ and $x = 0.99$ at different $AoAs$ and compared with their RS configurations as shown

Table 7.4: Effectiveness of multi-panel configuration at different flow conditions

AoA (°)	Multi-panel configuration (MPC) / Single-panel configuration				
	Avg $\Delta SPL_{reduction}$ (dB)	Max $\Delta SPL_{reduction}$ (dB)	θ_{max} (°)	Max ΔSPL_{amp} (dB)	θ_{max} (°)
3	2.20 / 3.53	7.73 / 5.60	178 / 210	1.46 / -	126 / -
5	4.41 / 2.12	7.92 / 2.41	185 / 130	- / -	- / -
7	1.41 / 1.10	6.75 / 2.92	60 / 168	1.70 / -	164 / -

in Figure 7.19. At $AoA = 3^\circ$, the dominant frequency for MPC is observed to be shifted to a higher frequency $(f_{bl})_0 = 3.39$ as compared to $(f_{bl})_0 = 2.67$ for RS. The magnitude of v' at $(f_{bl})_0 = 2.67$ for MPC is observed to be much lower than the magnitude of v' for RS. However, an amplification in the magnitude of v' is observed at $(f_{bl})_0 = 3.39$ for MPC as compared to RS. At $AoA = 5^\circ$, again an increase in the dominant frequency for MPC is observed where the frequency shifts to $(f_{bl})_0 = 3.95$ as compared to $(f_{bl})_0 = 3.37$ for RS. However, the magnitude of v' for MPC at $AoA = 5^\circ$ is much lower than that of RS at all frequencies, which possibly relates to higher noise reduction achieved by MPC at this AoA . At $AoA = 7^\circ$, the dominant frequency for MPC shifts from $(f_{bl})_0 = 2.40$ to $(f_{bl})_0 = 2.78$ where the magnitude of v' at this frequency for MPC is observed to be much lower than the magnitude of v' for RS. However, an increase in the magnitude of v' for MPC is also observed at certain higher frequencies. The shift in dominant frequency reduces with an increase in AoA which possibly affects the noise reduction potential of the MPC. Nevertheless, the designed MPC is still able to achieve an overall noise reduction at varying flow conditions.

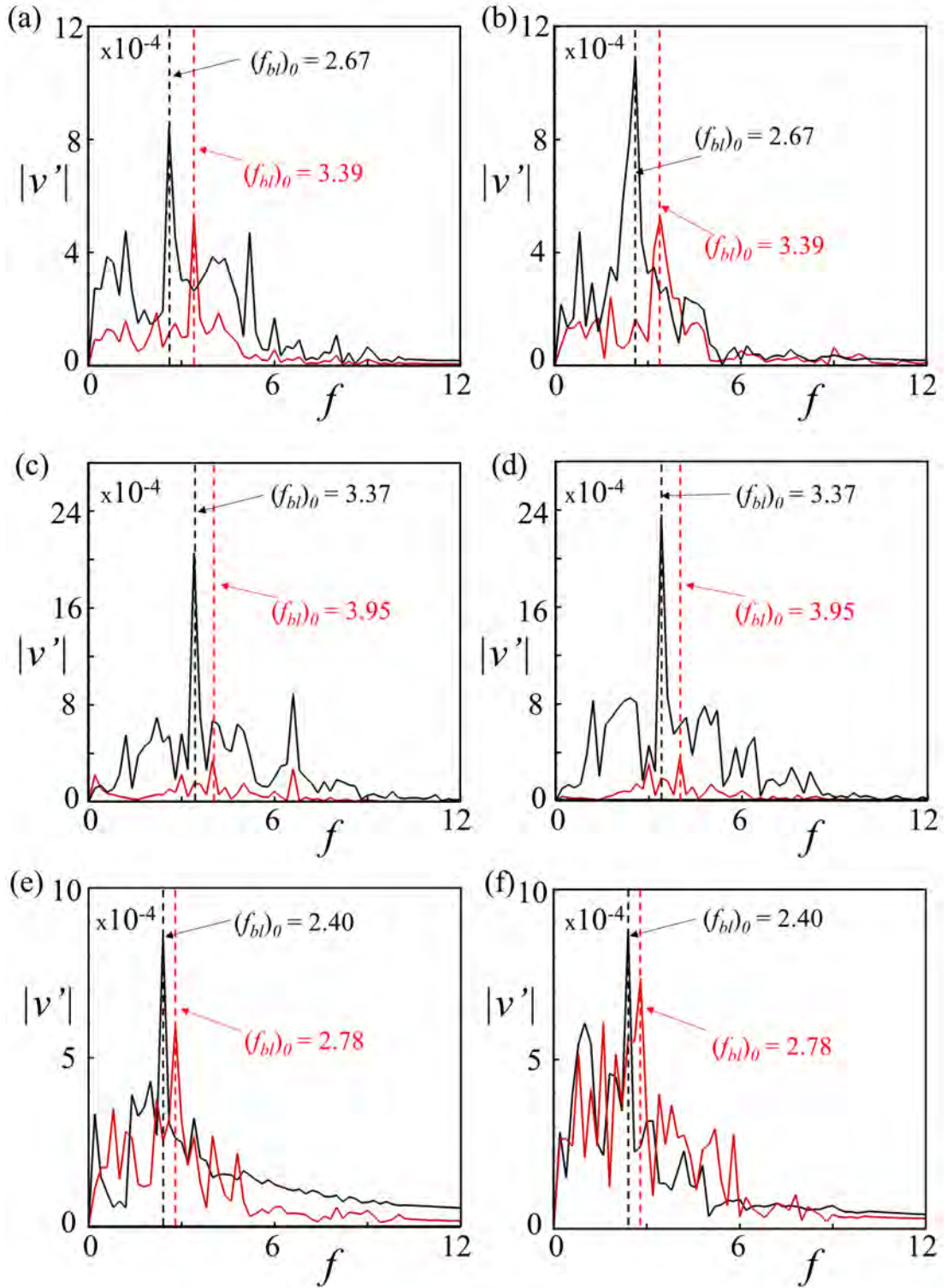


Figure 7.19: FFT spectra at different AoAs. (Left column) $x = 0.9$ and (right column) $x = 0.99$. (a) and (b) $AoA = 3^\circ$, (c) and (d) $AoA = 5^\circ$, (e) and (f) $AoA = 7^\circ$. —, RS; —, MPC.

7.6.3 Structural Responses of Elastic Panels

Structural responses of the elastic panels for MPC airfoil due to boundary layer instabilities and subsequent fluid-structure interactions are evaluated at different time instances of $t = 5, 6$ and 7 where the panels have sustained their vibrations as shown in Figures 7.20, 7.21 and 7.22 respectively. For comparative analysis, the structural response of the elastic panel for the single-panel configuration is also plotted at the respective AoA (indicated by black dashed line). The x -axis in the figure gives a panel location l_p measured from its leading edge and is expressed as a percentage of panel length.

At $AoA = 3^\circ$, for all time instances (Figures 7.20(a), 7.21(a) and 7.22(a)) the panels EP1 and EP2 follow the first mode shape whereas the panel EP3 follows the mode shape which is similar to the second and third modes. It is important to note that the design of the panel EP3 is based on the flow characteristics of the rigid airfoil at $AoA = 3^\circ$; hence, its response appears to be in the desired vibration pattern which is much supportive in inhibiting the boundary layer instabilities than the other panels at this AoA . On the other hand, the response of the elastic panel for single-panel configuration for all time instances at $AoA = 3^\circ$ (indicated by black dashed line) shows the panel vibration at its third natural mode to achieve structural resonance under the fluid loading. A significant phase difference is found among the panels for MPC where EP3 is observed to be completely out of phase with respect to EP1 and EP2 at all time instances which indicate that the panels are not structurally coupled at $AoA = 3^\circ$.

A similar phenomenon is observed at $AoA = 5^\circ$ (Figures 7.20(b), 7.21(b) and 7.22(b)) where the panels EP1 and EP3 vibrate in their first mode. The panel EP2, which is designed in accordance to the flow characteristics of the rigid airfoil at $AoA = 5^\circ$, follows the mode shape somewhat similar to the third mode at all time instances. The response of the elastic panel for single-panel

configuration at $AoA = 5^\circ$ also shows the panel vibration at its third natural mode under the fluid loading. In contrast to the structural dynamics observed at $AoA = 3^\circ$ for MPC, the panels appear to be in phase with each other at $AoA = 5^\circ$. Although, the exact coupling phenomenon cannot be achieved due to variations in the mode shape of panels; nevertheless, still an increase in average noise reduction is observed for MPC at $AoA = 5^\circ$ as compared to single-panel configuration (Table 7.4). However, the observed enhancement in average tonal noise reduction is much lower than the coupled panel configuration (Chapter 6) which signifies the importance of panels coupling in enhancing the noise reduction potential of the proposed approach.

At $AoA = 7^\circ$ (Figures 7.20(c), 7.21(c) and 7.22(c)), the vibration pattern is observed to be different from other $AoAs$ where the panels EP1 and EP3 appears to be in first mode. On the other hand, EP2 appears to vibrate in the different modes and out of phase with other panels at all time instances. It is observed that the panel EP1, which is designed in accordance to the flow characteristics of the rigid airfoil at $AoA = 7^\circ$, does not vibrate in the desired third mode which directly affects the overall performance of MPC in tonal noise reduction. Although a slight increase in average noise reduction potential is observed for MPC at $AoA = 7^\circ$ as compared to single-panel configuration, an amplification in tonal noise is also observed which can be attributed to the non-uniformity among the panels structural response.

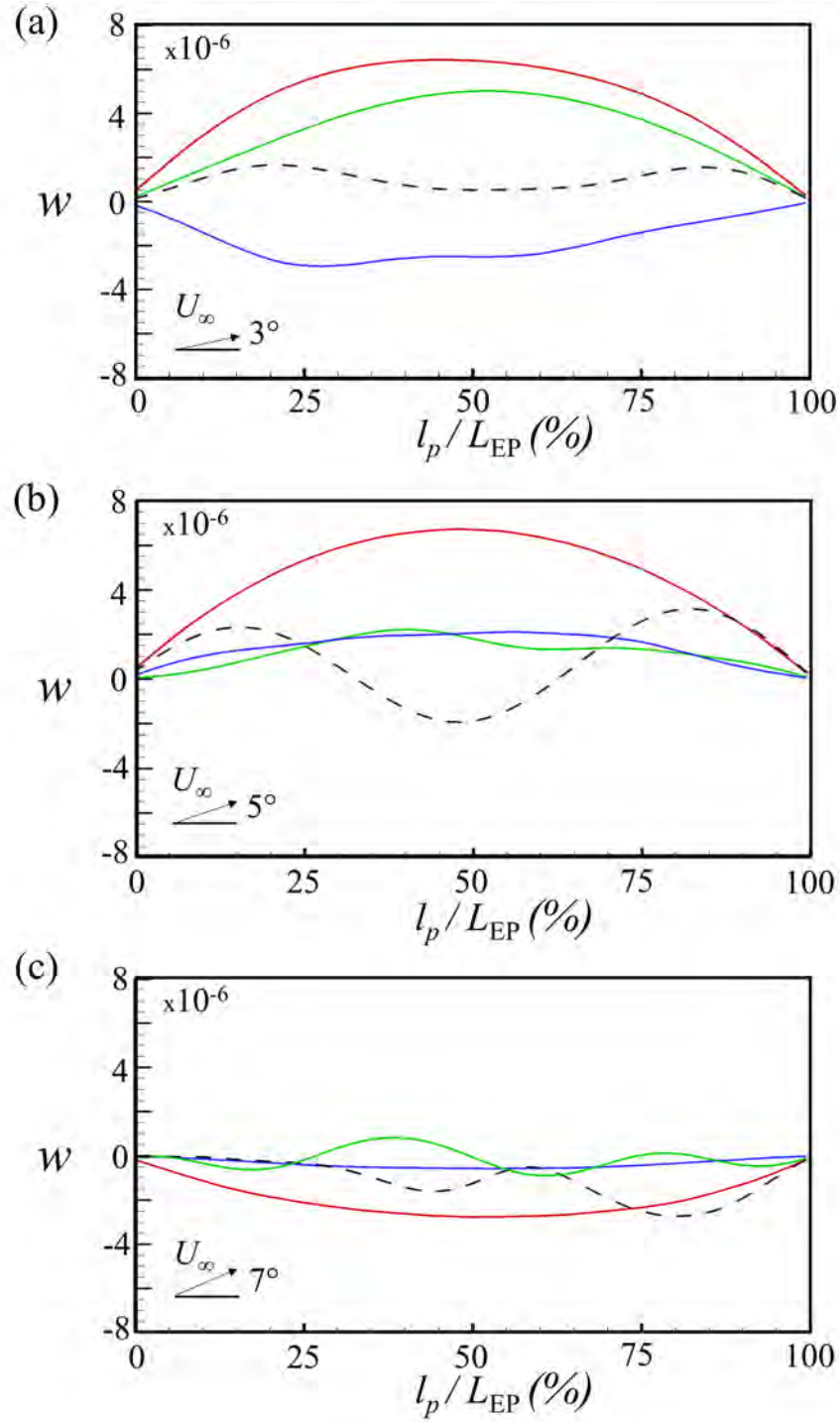


Figure 7.20: Vibratory responses of elastic panels for MPC at $t = 5$. (a) $AoA = 3^\circ$, (b) $AoA = 5^\circ$, and (c) $AoA = 7^\circ$. —, EP1; —, EP2; —, EP3; - - -, single resonant panel for corresponding AoA i.e. $x = 0.65 - 0.70$ for (a), $x = 0.40 - 0.45$ for (b) and $x = 0.20 - 0.25$ for (c).

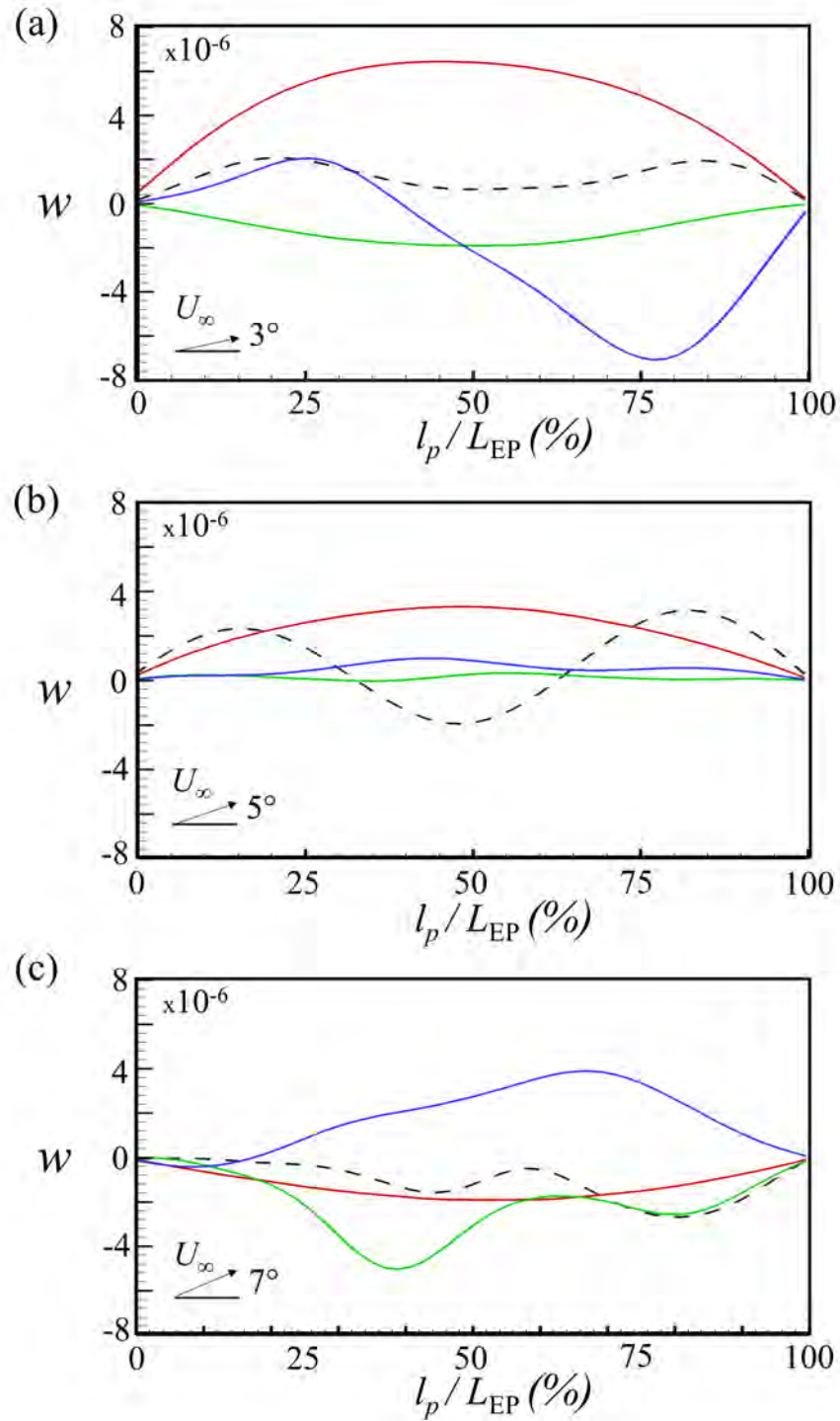


Figure 7.21: Vibratory responses of elastic panels for MPC at $t = 6$. (a) $AoA = 3^\circ$, (b) $AoA = 5^\circ$, and (c) $AoA = 7^\circ$. —, EP1; —, EP2; —, EP3; - - -, single resonant panel for corresponding AoA i.e. $x = 0.65 - 0.70$ for (a), $x = 0.40 - 0.45$ for (b) and $x = 0.20 - 0.25$ for (c).

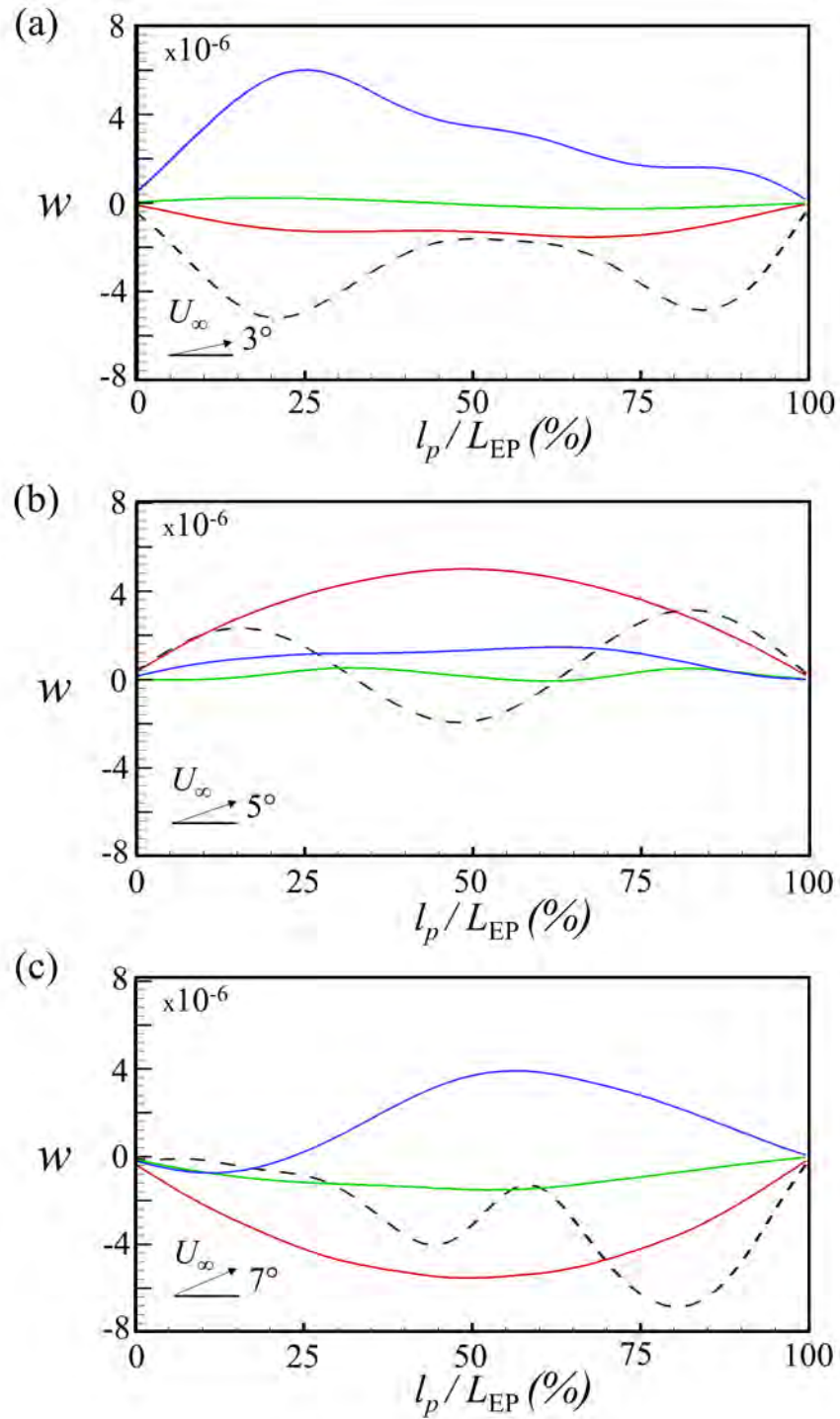


Figure 7.22: Vibratory responses of elastic panels for MPC at $t = 7$. (a) $AoA = 3^\circ$, (b) $AoA = 5^\circ$, and (c) $AoA = 7^\circ$. —, EP1; —, EP2; —, EP3; - - -, single resonant panel for corresponding AoA i.e. $x = 0.65 - 0.70$ for (a), $x = 0.40 - 0.45$ for (b) and $x = 0.20 - 0.25$ for (c).

7.7 Discussion on MPC Noise Reduction Potential

Based on the acoustic and structural analyses by PEM, it is evident that a complex flow-structure interaction occurs with the multi-panel configuration (MPC) operating at different $AoAs$. PEM results show a non-linear response in the noise reduction characteristics for MPC where different extent of average noise reduction is observed with the change in AoA . Nevertheless, an enhancement in the extent of maximum noise reduction is still observed at all $AoAs$. Some of the possible reasons of such non-linearity in the overall response by MPC at different $AoAs$ as identified by PEM analysis are as follows:

1. The panel designed for a specific AoA does not achieve desired mode shape under the fluid loading at different flow conditions due to a change in fundamental boundary instabilities at different AoA . As an example, the panel designed to vibrate in resonance under the fluid loading at $AoA = 5^\circ$ does not achieve structural resonance at $AoA = 3^\circ$ and 7° . As a result, it may affect the overall panel inter-dynamics among the panels.
2. It is established in Chapter 6 that the noise reduction potential of an airfoil mounted with more than one panels is highly dependent on the inter-dynamical structural coupling among the panels. The structural coupling among the panels is achieved only when the panels are located at a distance of $n\lambda_{conv}$ apart. However, as discussed in Section 7.2.1, with the chosen increment of AoA of $\pm 2^\circ$ the apparent λ_{conv} appreciably varies (Figure 7.1). As a result, the structural coupling phenomena among the elastic panels for the MPC is not effectively achieved at different $AoAs$.
3. As discussed in Chapter 5, the magnitude of flow instabilities appears to

play an important role in noise reduction potential of an elastic panel configuration where the panel is deliberately located just ahead of the sharp growth of boundary layer instability within the airfoil separation bubble so as to provide the strongest reduction of flow instabilities and highest noise reduction. With the change in AoA , the overall characteristics of the boundary layer instabilities over the airfoil surface also varies as shown in Figure 7.12. As an example, the panel located at $x = 0.2$ (EP1) for MPC becomes less effective at $AoA = 3^\circ$ due to the presence of low magnitude of fluctuations present at this location.

7.8 Conclusions

A multi-panel configuration (MPC) based on three elastic panels is designed to provide tonal noise reduction over a range of AoA . The panel structural properties and their suitable locations on the airfoil surface at $AoA = 3^\circ$, 5° and 7° are evaluated based on their individual rigid airfoil characteristics. The effectiveness of the airfoil with designed panel is determined by PEM at their respective $AoAs$. PEM analysis of single-panel configurations at different $AoAs$ indicates that a different extent of tonal noise reduction can be achieved at all conditions where the panel is designed to achieve structural resonance. Subsequently, an airfoil configuration based on three panels (MPC) with different structural properties is designed and its noise reduction potential is assessed at varying $AoAs$. A different extent of noise reduction is observed at each AoA . The noise reduction achieved at $AoA = 5^\circ$ is much greater than other $AoAs$ where an average reduction of 4.41 dB is observed with a maximum reduction of 7.92 dB at $\theta = 185^\circ$. At $AoA = 3^\circ$, an overall average noise reduction of 2.20 dB is observed with a maximum reduction of 7.73 dB at $\theta = 178^\circ$. Furthermore, a maximum noise amplification of 1.46 dB is also observed at $\theta = 126^\circ$. At $AoA = 7^\circ$, an overall average noise reduction of 1.41 dB is observed with a maximum reduction of 6.75 dB at $\theta = 60^\circ$; whereas, a

maximum noise amplification of 1.70 dB is also observed at $\theta = 164^\circ$. A shift in the dominant frequency of boundary layer instabilities is also observed for MPC at each AoA . The structural analysis shows a complex vibration pattern for all the panels which clearly indicates the presence of complex structural interaction among the panels for MPC airfoil at varying AoA .

Chapter 8

Conclusions

8.1 Summary and Research Achievements

A novel passive control method for airfoil tonal noise using localized flow-induced vibration is proposed and explored with a short elastic panel(s) flush-mounted on the suction surface of a NACA 0012 airfoil at low Reynolds number (Re). The key idea is to absorb the energy of natural instabilities arising in laminar boundary layer by locally self-sustained flow-induced vibration of the short panel which results in reduced flow instabilities for scattering at airfoil trailing edge and weakened aeroacoustic-feedback loop responsible for tonal noise radiation, without any adverse effect on airfoil aerodynamics.

The present research involves complex interactions between unsteady flow, panel structural vibration, and acoustics. Therefore, direct aeroacoustic simulation (DAS) approach is adopted for its capability to resolve the coupling between the unsteady airfoil aerodynamic and acoustic solutions with high accuracy. To solve the unsteady compressible N-S equations, conservation element and solution element (CE/SE) method is adopted. The nonlinear coupling between flow fluctuation and panel structural dynamics is resolved with a monolithic scheme. Since, the panel design depends on a number of different parameters such as its

material, length and structural properties. Hence, it is too prohibitive in extensive deployment of resources and time to search for optimal panel design with DAS. Therefore, an alternate approach, namely, perturbation evolution method (PEM) is developed to explore the potential of elastic panel configurations in tonal noise reduction requiring much shorter computational time and resources. Details of the numerical methods, their mathematical modeling and implementation are discussed in Chapter 2. The details of the computational setup, grid generation and validation of the numerical scheme are presented in Chapter 3. Furthermore, a comprehensive aeroacoustics analysis of the rigid airfoil is carried out at $Re = 5 \times 10^4$, Mach number $M = 0.4$ and $AoA = 5^\circ$ and presented in Chapter 3. The DAS solution of rigid airfoil serves three major purposes. Firstly, it helps in validation of the CE/SE method in resolving the interaction between flow field dynamics and acoustics effectively. Secondly, it allows to ascertain the important flow field and acoustic features such as boundary layer separation/reattachment, near wake characteristics, tonal noise spectra, and acoustic feedback loop which helps in subsequent design of elastic panel. Lastly, the time-averaged solution of rigid airfoil is later used in setting up the base flow for PEM. In Chapter 4, a complete methodology of elastic panel design is developed and the noise reduction potential of the airfoil configurations with an elastic panel is evaluated using PEM. The base flow for PEM is obtained from time-averaged solution of accompanying DAS solution of same flow with fully rigid airfoil and the analysis is implemented with a broadband excitation near the leading edge of the airfoil. PEM is applied with various panel structural parameters and panel locations and the potential for airfoil tonal noise reduction is analyzed. The results indicate that a panel located just ahead of the sharp growth of natural boundary layer instability within the airfoil separation bubble provides the strongest reduction of instabilities that are responsible for scattering into noise at the airfoil trailing

edge and, hence, provides the highest noise reduction among all cases studied. Subsequently, a comprehensive aerodynamic and acoustic analysis of the optimal airfoil-panel configuration is performed with DAS to evaluate the panel effectiveness in actual flow conditions in Chapter 5. The results show that the airfoil mounted with a resonant elastic panel provides a maximum noise reduction up to 3 dB with no adverse effect on airfoil aerodynamics. Since the proposed noise reduction method works without any compromise of aerodynamic characteristics, the outcomes of the analysis evidently suggest that the proposed passive control method with a localized flow-induced vibrating panel is effective in screening out to suppress the fundamental mechanism for airfoil tonal noise generation. The designed approach for airfoil tonal noise reduction is further enhanced by utilizing the structural coupling of elastic panels over the airfoil. The details of the panel coupling setup and its implementation on the airfoil are presented in Chapter 6. The analysis reveals that an airfoil-panel configuration with two elastic panels separated by approximately one convective wavelength and mounted in a region exposed to high boundary layer flow instabilities yields optimal noise suppression. The aerodynamic and acoustic analyses show that an average and maximum noise suppression up to 7.6 dB and 7.9 dB can be achieved respectively, without any adverse effect on overall airfoil aerodynamics when coupled structural resonance between panels prevails. This noise suppression is higher than twice of that from the configuration with single panel which firmly illustrates the synergy of coupled flow-induced structural resonance of the panels prevailing in noise suppression. Subsequently, a comprehensive framework is also developed for the design of coupled panel configuration for any airfoil operating at any flow condition. Lastly, in Chapter 7, a multi-panel airfoil configuration (MPC) based on three elastic panels is designed to ascertain the effectiveness of the proposed method at different flow conditions such as variable AoA . A different extent of noise reduction

is observed for MPC at each AoA . However, a shift in the dominant frequency of boundary layer instabilities is also observed. The structural analysis shows a complex vibration pattern for all the panels which clearly indicates the presence of complex structural interaction among the panels for MPC airfoil at varying AoA . An in-depth understanding of such interaction can only be studied by full DAS analyses at different flow conditions for MPC. Some of the major research highlights are listed below:

1. Development of a passive noise control method with short elastic panel(s) which is able to achieve a significant noise reduction without affecting the airfoil aerodynamics and easy to implement in real world environment.
2. Exploration of the possibility of employing a noise reduction method at a location other than the conventional methods at airfoil trailing edge or leading edge.
3. Formulation of a comprehensive panel design methodology based on its material, structural properties, length and its location on airfoil which can be utilized for any airfoil or any flow condition.
4. Development of PEM for quick assessment of noise reduction potential of different panel configurations which only requires 10% of the total computational time required for full DAS.
5. Development of a framework for utilization of structural coupling phenomenon of vibrating structures on the airfoil for noise reduction purposes.
6. Feasibility study and assessment of a multi-panel airfoil configuration capable of providing noise reduction at different angles of attack.

8.2 Limitations and Future Works

The research explored the possibility of airfoil tonal noise reduction by using fluid-structure interactions of an elastic panel by DAS. Due to the requirement of very high computational resources and time by DAS, all the calculations are based on two-dimensional analysis. Although, the flow conditions considered for this study are well represented by two-dimensional analysis, for some real world applications the three-dimensional effects may come into play, such as flow condition at high angles of attack or turbulent flows etc. Hence, three-dimensional analysis may provide further details on the effectiveness of the proposed approach at these conditions.

In this research, the nonlinear coupling between flow fluctuation and panel structural dynamics is resolved with a monolithic scheme. The structural solver employed in this research cannot handle large panel deformations. Based on the present approach, the aeroacoustic-structural interaction is directly solved at the solution points on the fluid-panel interface. The effect of panel displacement is based on the distance between a solution point to the interface. If the deformation is larger than the limitation, the fluid solution point would not physically exist at this instance. Its role will become a virtual solution point that applies the effect of the aeroacoustic-structural interaction to the fluid domain through linear projection. Hence, it may result in numerical errors in the calculation of overall panel dynamics. Since this research already utilizes the short elastic panel with very small deformation which are of two order lower than the local boundary layer thickness such that the mean flow dynamics remain unaffected; this limitation does not affect the current analysis. However, in case of large panel deflections, such as membrane airfoils, the current structural solver may provide inaccurate results.

The proposed method of employing flexible structures for noise control has

proved to be quite effective in this research. However, there are some research areas which can be further explored in future studies. Some of the recommendations for future works are listed below:

1. As discussed in Chapter 7, for in-depth understanding of complex interaction among the panels for MPC airfoil, a number of full DAS analyses may be carried out at different *AoAs*. Since, the computational time increases significantly with the increase in number of panels, the analysis would require much large computational power than the existing available resources for full DAS.
2. The proposed method of utilizing elastic panel(s) may be employed for high *Re* turbulent flows to assess its effectiveness at these conditions. It may help in expanding its application for broadband noise control as well.
3. The flow passing over the open cavity also generates sharp tonal noise at certain flow conditions due to shear layer oscillations. Hence, a similar approach of employing elastic panel for noise control may be utilized for this practical problem.
4. The utility of elastic panel may be combined with other noise control methods such trailing edge serrations, sawtooth trailing or porous trailing edge to further enhance the overall airfoil self-noise reduction.

References

- Abbasi, M., Monazzam, M. R., Akbarzadeh, A., Zakerian, S. A., and Ebrahimi, M. H. (2015), “Impact of wind turbine sound on general health, sleep disturbance and annoyance of workers: a pilot-study in Manjil wind farm, Iran,” *Journal of Environmental Health Science and Engineering*, Vol. 13, No. 1, pp. 71.
- Açikel, H. H. and Genc, M. S. (2018), “Control of laminar separation bubble over wind turbine airfoil using partial flexibility on suction surface,” *Energy*, Vol. 165, pp. 176–190.
- Alam, M. and Sandham, N. D. (2000), “Direct numerical simulation of short laminar separation bubbles with turbulent reattachment,” *Journal of Fluid Mechanics*, Vol. 410, pp. 1–28.
- Albertani, R., Stanford, B., Hubner, J. P., and Ifju, P. G. (2007), “Aerodynamic coefficients and deformation measurements on flexible micro air vehicle wings,” *Experimental Mechanics*, Vol. 47, No. 5, pp. 625–635.
- Alejandro, R. C., Roberto, M. M., Francesco, A., Daniele, R., Mirjam, S., and Sybrand, v. d. Z. (2017), “Broadband trailing-edge noise reduction using permeable metal foams,” *INTER-NOISE and NOISE-CON Congress and Conference Proceedings*, Vol. 255, Institute of Noise Control Engineering, pp. 2755–2765.

- Anderson, J. D. and Wendt, J. (1995), *Computational fluid dynamics*, Vol. 206. Springer.
- Anderson Jr, J. (2011), *Fundamentals of aerodynamics*. McGraw-Hill, New York, 5th ed., p. 982.
- Arbey, H. and Bataille, J. (1983), “Noise generated by airfoil profiles placed in a uniform laminar flow,” *Journal of Fluid Mechanics*, Vol. 134, pp. 33–47.
- Arce Leon, C., Avallone, F., Pröbsting, S., and Ragni, D. (2016), “PIV investigation of the flow past solid and slitted sawtooth serrated trailing edges,” *54th AIAA Aerospace Sciences Meeting*, p. 1014.
- Archibald, F. S. (1975), “The laminar boundary layer instability excitation of an acoustic resonance,” *Journal of sound and vibration*, Vol. 38, No. 3, pp. 387–402.
- Arcondoulis, E., Doolan, C. J., Zander, A. C., and Brooks, L. A. (2013), “An experimental investigation of airfoil tonal noise caused by an acoustic feedback loop,” *Proceedings of Acoustics*, pp. 42–49.
- Arcondoulis, E., Doolan, C. J., Zander, A. C., Brooks, L. A., and Liu, Y. (2019), “An investigation of airfoil dual acoustic feedback mechanisms at low-to-moderate Reynolds number,” *Journal of Sound and Vibration*, Vol. 460, pp. 114887.
- Arcondoulis, E., Zander, A., Doolan, C. J., Brooks, L., and Liu, Y. (2018), “Airfoil dual acoustic feedback mechanisms at low-to-moderate Reynolds number,” *2018 AIAA/CEAS Aeroacoustics Conference*, p. 3936.
- Arena, A. V. and Mueller, T. J. (1980), “Laminar separation, transition, and turbulent reattachment near the leading edge of airfoils,” *AIAA Journal*, Vol. 18, No. 7, pp. 747–753.

- Arif, I., Lam, G. C. Y., Wu, D., and Leung, R. C. K. (2020), “Passive Airfoil Tonal Noise Reduction by Localized Flow-Induced Vibration of an Elastic Panel,” *Aerospace Science and Technology*, pp. 106319.
- Avallone, F., Van der Velden, W. C. P., and Ragni, D. (2017), “Benefits of curved serrations on broadband trailing-edge noise reduction,” *Journal of Sound and Vibration*, Vol. 400, pp. 167–177.
- Avallone, F., Van Der Velden, W. C. P., Ragni, D., and Casalino, D. (2018), “Noise reduction mechanisms of sawtooth and combed-sawtooth trailing-edge serrations,” *Journal of Fluid Mechanics*, Vol. 848, pp. 560–591.
- Barkley, D. (2006), “Linear analysis of the cylinder wake mean flow,” *EPL (Europhysics Letters)*, Vol. 75, No. 5, pp. 750.
- Bernicke, P., Akkermans, R. A. D., Ananthan, V. B., Ewert, R., Dierke, J., and Rossian, L. (2019), “A zonal noise prediction method for trailing-edge noise with a porous model,” *International Journal of Heat and Fluid Flow*, Vol. 80, pp. 108469.
- Botelho, A., Arezes, P., Bernardo, C., Dias, H., and Pinto, L. M. C. (2017), “Effect of wind farm noise on local residents’ decision to adopt mitigation measures,” *International Journal of Environmental Research and Public Health*, Vol. 14, No. 7, pp. 753.
- Brooks, T. F., Pope, D. S., and Marcolini, M. A. (1989), “Airfoil self-noise and prediction,” *NASA Reference Publication 1218*.
- Chang, S. and Wang, X. (2002), “Courant number insensitive CE/SE Euler scheme,” *38th AIAA/ASME/SAE/ASEE Joint Propulsion Conference & Exhibit*, p. 3890.

- Chang, S.-C. (1995), “The method of space-time conservation element and solution element a new approach for solving the Navier-Stokes and Euler equations,” *Journal of computational Physics*, Vol. 119, No. 2, pp. 295–324.
- Chang, S.-C., Wang, X.-Y., and Chow, C.-Y. (1999), “The space-time conservation element and solution element method: a new high-resolution and genuinely multidimensional paradigm for solving conservation laws,” *Journal of Computational Physics*, Vol. 156, No. 1, pp. 89–136.
- Chong, T. P. and Dubois, E. (2016), “Optimization of the poro-serrated trailing edges for airfoil broadband noise reduction,” *The Journal of the Acoustical Society of America*, Vol. 140, No. 2, pp. 1361–1373.
- Chong, T. P., Joseph, P. F., and Gruber, M. (2013a), “Airfoil self noise reduction by non-flat plate type trailing edge serrations,” *Applied Acoustics*, Vol. 74, No. 4, pp. 607–613.
- Chong, T. P., Vathylakis, A., Joseph, P. F., and Gruber, M. (2013b), “Self-noise produced by an airfoil with nonflat plate trailing-edge serrations,” *AIAA journal*, Vol. 51, No. 11, pp. 2665–2677.
- Clark, I. A., Alexander, W. N., Devenport, W., Glegg, S., Jaworski, J. W., Daly, C., and Peake, N. (2017), “Bioinspired trailing-edge noise control,” *AIAA Journal*, Vol. 55, No. 3, pp. 740–754.
- Crighton, D. G. (1975), “Scattering and diffraction of sound by moving bodies,” *Journal of Fluid Mechanics*, Vol. 72, No. 2, pp. 209–227.
- Crighton, D. G. (1981), “Acoustics as a branch of fluid mechanics,” *Journal of Fluid Mechanics*, Vol. 106, pp. 261–298.
- Crighton, D. G. and Leppington, F. G. (1971), “On the scattering of aerodynamic noise,” *Journal of Fluid Mechanics*, Vol. 46, No. 3, pp. 577–597.

- Desquesnes, G., Terracol, M., and Sagaut, P. (2007), “Numerical investigation of the tone noise mechanism over laminar airfoils,” *Journal of Fluid Mechanics*, Vol. 591, pp. 155–182.
- Di, G., Wu, Z., and Huang, D. (2017), “The research on active flow control method with vibration diaphragm on a NACA 0012 airfoil at different stalled angles of attack,” *Aerospace Science and Technology*, Vol. 69, pp. 76–86.
- Di Ilio, G., Chiappini, D., Ubertini, S., Bella, G., and Succi, S. (2018), “Fluid flow around NACA 0012 airfoil at low-Reynolds numbers with hybrid lattice Boltzmann method,” *Computers & Fluids*, Vol. 166, pp. 200–208.
- Dong, H., Wang, C., Li, S., and Song, X. Z. (2015), “Numerical research on segmented flexible airfoils considering fluid-structure interaction,” *Procedia Engineering*, Vol. 99, pp. 57–66.
- Dong, H., Xia, T., Chen, L., Liu, S., Cui, Y. D., Khoo, B. C., and Zhao, A. (2019), “Study on flow separation and transition of the airfoil in low Reynolds number,” *Physics of Fluids*, Vol. 31, No. 10, pp. 103601.
- Dowell, E. H. (1975), *Aeroelasticity of plates and shells*. Noordhoff International Publishing, Leyden.
- Drazin, P. G. and Reid, W. H. (2004), *Hydrodynamic stability*. Cambridge University Press, 2nd ed.
- Dugundji, J., Dowell, E. H., and Perkin, B. (1963), “Subsonic flutter of panels on continuous elastic foundations,” *AIAA Journal*, Vol. 1, No. 5, pp. 1146–1154.
- Fahy, F. J. and Gardonio, P. (2007), *Sound and structural vibration: radiation, transmission and response*. Elsevier, 2nd ed.

- Fan, H. K. H. (2018), *Computational aeroacoustic-structural interaction in internal flow with CE/SE method*, Ph.D. thesis, The Hong Kong Polytechnic University.
- Fan, H. K. H., Leung, R. C. K., and Lam, G. C. Y. (2015), “Numerical analysis of aeroacoustic-structural interaction of a flexible panel in uniform duct flow,” *The Journal of the Acoustical Society of America*, Vol. 137, No. 6, pp. 3115–3126.
- Fan, H. K. H., Leung, R. C. K., Lam, G. C. Y., Aurégan, Y., and Dai, X. (2018a), “Numerical coupling strategy for resolving in-duct elastic panel aeroacoustic/structural interaction,” *AIAA Journal*, Vol. 56, No. 12, pp. 5033–5040.
- Fan, T., Weiyang, Q., Weijie, C., Cheng, H., Renke, W., and Xunnian, W. (2018b), “Numerical analysis of broadband noise reduction with wavy leading edge,” *Chinese Journal of Aeronautics*, Vol. 31, No. 7, pp. 1489–1505.
- Ffowcs Williams, J. E. and Hall, L. H. (1970), “Aerodynamic sound generation by turbulent flow in the vicinity of a scattering half plane,” *Journal of Fluid Mechanics*, Vol. 40, pp. 657–670.
- Fillinger, L., Sutin, A., and Sedunov, A. (2010), “Acoustic ship signature measurements by cross-correlation method,” *The Journal of the Acoustical Society of America*, Vol. 129, No. 2, pp. 774–778.
- Finez, A., Jacob, M., Jondeau, E., and Roger, M. (2010), “Broadband noise reduction with trailing edge brushes,” *16th AIAA/CEAS aeroacoustics conference*, p. 3980.
- Fink, M. R. (1975), “Prediction of airfoil tone frequencies,” *Journal of Aircraft*, Vol. 12, No. 2, pp. 118–120.

- Fink, M. R. (1978), “Fine structure of airfoil tone frequency,” *The Journal of the Acoustical Society of America*, Vol. 63, No. S1, pp. S22–S22.
- Finnegan, S. L., Meskell, C., and Ziada, S. (2010), “Experimental investigation of the acoustic power around two tandem cylinders,” *Journal of pressure vessel technology*, Vol. 132, No. 4.
- Fosas de Pando, M., Schmid, P. J., and Sipp, D. (2014), “A global analysis of tonal noise in flows around aerofoils,” *Journal of Fluid Mechanics*, Vol. 754, pp. 5–38.
- Galvao, R., Israeli, E., Song, A., Tian, X., Bishop, K., Swartz, S., and Breuer, K. (2006), “The aerodynamics of compliant membrane wings modeled on mammalian flight mechanics,” *36th AIAA Fluid Dynamics Conference and Exhibit*, p. 2866.
- Genç, M. S., Açikel, H. H., and Koca, K. (2020), “Effect of partial flexibility over both upper and lower surfaces to flow over wind turbine airfoil,” *Energy Conversion and Management*, Vol. 219, pp. 113042.
- Geyer, T. F. and Sarradj, E. (2014), “Trailing edge noise of partially porous airfoils,” *20th AIAA/CEAS aeroacoustics conference*, p. 3039.
- Geyer, T. F., Sarradj, E., and Fritzsche, C. (2010), “Measurement of the noise generation at the trailing edge of porous airfoils,” *Experiments in Fluids*, Vol. 48, No. 2, pp. 291–308.
- Gloerfelt, X., Bailly, C., and Juvé, D. (2003), “Direct computation of the noise radiated by a subsonic cavity flow and application of integral methods,” *Journal of Sound and Vibration*, Vol. 266, No. 1, pp. 119–146.
- Gordnier, R. E. (2009), “High fidelity computational simulation of a membrane wing airfoil,” *Journal of Fluids and Structures*, Vol. 25, No. 5, pp. 897–917.

- Gordnier, R. E. and Attar, P. J. (2014), “Impact of flexibility on the aerodynamics of an aspect ratio two membrane wing,” *Journal of Fluids and Structures*, Vol. 45, pp. 138 – 152.
- Greenshields, C. J. and Weller, H. G. (2005), “A unified formulation for continuum mechanics applied to fluid–structure interaction in flexible tubes,” *International Journal for Numerical Methods in Engineering*, Vol. 64, No. 12, pp. 1575–1593.
- Grinsted, A., Moore, J. C., and Jevrejeva, S. (2004), “Application of the cross wavelet transform and wavelet coherence to geophysical time series,” *Nonlinear Processes in Geophysics*, Vol. 11, No. 5/6, pp. 561–566.
- Gruber, M., Joseph, P. F., and Azarpeyvand, M. (2013), “An experimental investigation of novel trailing edge geometries on airfoil trailing edge noise reduction,” *19th AIAA/CEAS aeroacoustics conference*, p. 2011.
- Gruber, M., Joseph, P. F., and Chong, T. P. (2010), “Experimental investigation of airfoil self noise and turbulent wake reduction by the use of trailing edge serrations,” *16th AIAA/CEAS aeroacoustics conference*, pp. 3803–3825.
- Gruber, M., Joseph, P. F., and Chong, T. P. (2011), “On the mechanisms of serrated airfoil trailing edge noise reduction,” *17th AIAA/CEAS Aeroacoustics Conference (32nd AIAA Aeroacoustics Conference)*, p. 2781.
- Guo, Y., Hsu, A. T., Wu, J., Yang, Z., and Oyediran, A. (2004), “Extension of CE/SE method to 2D viscous flows,” *Computers & fluids*, Vol. 33, No. 10, pp. 1349–1361.
- Hansen, K., Kelso, R., and Doolan, C. J. (2012), “Reduction of flow induced airfoil tonal noise using leading edge sinusoidal modifications,” *Acoust. Australia*, Vol. 40, No. 3, pp. 172–177.

- Hayek, S. I. (2000), *Advanced mathematical methods in science and engineering*. CRC Press, 1st ed.
- He, X. and Wang, J.-J. (2020), “Fluid–structure interaction of a flexible membrane wing at a fixed angle of attack,” *Physics of Fluids*, Vol. 32, No. 12, pp. 127102.
- Herr, M. (2007), “Design criteria for low-noise trailing-edges,” *13th AIAA/CEAS Aeroacoustics Conference (28th AIAA Aeroacoustics Conference)*, p. 3470.
- Herr, M. and Dobrzynski, W. (2005), “Experimental Investigations in Low-Noise Trailing Edge Design.” *AIAA Journal*, Vol. 43, No. 6, pp. 1167–1175.
- Herr, M., Rossignol, K.-S., Delfs, J., Lippitz, N., and Mößner, M. (2014), “Specification of porous materials for low-noise trailing-edge applications,” *20th AIAA/CEAS aeroacoustics conference*, p. 3041.
- Hoarau, Y., Braza, M., Ventikos, Y., Faghani, D., and Tzabiras, G. (2003), “Organized modes and the three-dimensional transition to turbulence in the incompressible flow around a NACA0012 wing,” *Journal of Fluid Mechanics*, Vol. 496, pp. 63–72.
- Howe, M. S. (1991), “Noise produced by a sawtooth trailing edge,” *The Journal of the Acoustical Society of America*, Vol. 90, No. 1, pp. 482–487.
- Hu, H., Tamai, M., and Murphy, J. T. (2008), “Flexible-membrane airfoils at low Reynolds numbers,” *Journal of Aircraft*, Vol. 45, No. 5, pp. 1767–1778.
- Huerre, P. and Monkewitz, P. A. (1990), “Local and global instabilities in spatially developing flows,” *Annual Review of Fluid Mechanics*, Vol. 22, No. 1, pp. 473–537.

- Inasawa, A., Kamijo, T., and Asai, M. (2010), “Generation mechanism of trailing-edge noise of airfoil at low Reynolds numbers,” *Proceedings of the 13th Asian Congress of Fluid Mechanics*, pp. 125–128.
- Jones, L. E. (2008), *Numerical studies of the flow around an airfoil at low Reynolds number*, Ph.D. thesis, University of Southampton.
- Jones, L. E. and Sandberg, R. D. (2011), “Numerical analysis of tonal airfoil self-noise and acoustic feedback-loops,” *Journal of Sound and Vibration*, Vol. 330, No. 25, pp. 6137–6152.
- Jones, L. E., Sandberg, R. D., and Sandham, N. D. (2008), “Direct numerical simulations of forced and unforced separation bubbles on an airfoil at incidence,” *Journal of Fluid Mechanics*, Vol. 602, pp. 175–207.
- Jones, L. E., Sandberg, R. D., and Sandham, N. D. (2010), “Stability and receptivity characteristics of a laminar separation bubble on an aerofoil,” *Journal of Fluid Mechanics*, Vol. 648, pp. 257–296.
- Kamps, L., Brücker, C., Geyer, T. F., and Sarradj, E. (2017), “Airfoil self noise reduction at low Reynolds numbers using a passive flexible trailing edge,” *23rd AIAA/CEAS Aeroacoustics Conference*, p. 3496.
- Kim, D.-H., Chang, J.-W., and Chung, J. (2011), “Low-Reynolds-number effect on aerodynamic characteristics of a NACA 0012 airfoil,” *Journal of aircraft*, Vol. 48, No. 4, pp. 1212–1215.
- Koh, S. R., Meinke, M., and Schröder, W. (2018), “Numerical analysis of the impact of permeability on trailing-edge noise,” *Journal of Sound and Vibration*, Vol. 421, pp. 348–376.
- Lam, G. C. Y. (2012), *Aeroacoustics of merging flows at duct junctions*, Ph.D. thesis, The Hong Kong Polytechnic University.

- Lam, G. C. Y. and Leung, R. C. K. (2018), “Aeroacoustics of NACA 0018 Airfoil with a Cavity,” *AIAA Journal*, Vol. 56, No. 12, pp. 4775–4786.
- Lam, G. C. Y., Leung, R. C. K., Seid, K. H., and Tang, S. K. (2014a), “Validation of CE/SE scheme in low mach number direct aeroacoustic simulation,” *International Journal of Nonlinear Sciences and Numerical Simulation*, Vol. 15, No. 2, pp. 157–169.
- Lam, G. C. Y., Leung, R. C. K., and Tang, S. K. (2014b), “Aeroacoustics of duct junction flows merging at different angles,” *Journal of Sound and Vibration*, Vol. 333, No. 18, pp. 4187–4202.
- Lau, Y. L., So, R. M. C., and Leung, R. C. K. (2004), “Flow-induced vibration of elastic slender structures in a cylinder wake,” *Journal of fluids and structures*, Vol. 19, No. 8, pp. 1061–1083.
- Lei, J., Zhang, J., and Niu, J. (2020), “Effect of active oscillation of local surface on the performance of low Reynolds number airfoil,” *Aerospace Science and Technology*, Vol. 99, pp. 105774.
- León, C. A., Merino-Martínez, R., Pröbsting, S., Ragni, D., and Avallone, F. (2018), “Acoustic emissions of semi-permeable trailing edge serrations,” *Acoustics Australia*, Vol. 46, No. 1, pp. 111–117.
- León, C. A., Merino-Martínez, R., Ragni, D., Avallone, F., and Snellen, M. (2016), “Boundary layer characterization and acoustic measurements of flow-aligned trailing edge serrations,” *Experiments in fluids*, Vol. 57, No. 12, pp. 1–22.
- Leung, R. C. K. and So, R. M. C. (2001), “Noise generation of blade–vortex resonance,” *Journal of sound and vibration*, Vol. 245, No. 2, pp. 217–237.

- Li, G., Khoo, B. C., and Jaiman, R. K. (2020), “Computational aeroelasticity of flexible membrane wings at moderate Reynolds numbers,” *AIAA Scitech 2020 Forum*, p. 2036.
- Lian, Y. and Shyy, W. (2007), “Laminar-turbulent transition of a low Reynolds number rigid or flexible airfoil,” *AIAA Journal*, Vol. 45, No. 7, pp. 1501–1513.
- Lian, Y., Shyy, W., Viieru, D., and Zhang, B. (2003), “Membrane wing aerodynamics for micro air vehicles,” *Progress in Aerospace Sciences*, Vol. 39, No. 6-7, pp. 425–465.
- Lighthill, M. J. (1954), “On sound generated aerodynamically II. Turbulence as a source of sound,” *Proceedings of the Royal Society of London. Series A. Mathematical and Physical Sciences*, Vol. 222, No. 1148, pp. 1–32.
- Lissaman, P. B. S. (1983), “Low-Reynolds-number airfoils,” *Annual Review of Fluid Mechanics*, Vol. 15, No. 1, pp. 223–239.
- Loh, C. Y. (2003), “On a non-reflecting boundary condition for hyperbolic conservation laws,” *16th AIAA Computational Fluid Dynamics Conference*, p. 3975.
- Loh, C. Y. (2005), “Computation of tone noise from supersonic jet impinging on flat plates,” *43rd AIAA Aerospace Sciences Meeting and Exhibit*, p. 418.
- Loh, C. Y., Hultgren, L., and Jorgenson, P. (2001), “Near field screech noise computation for an underexpanded supersonic jet by the conservation element and solution element method,” *7th AIAA/CEAS Aeroacoustics Conference and Exhibit*, pp. 2252–2262.
- Loh, C. Y. and Hultgren, L. S. (2006), “Jet screech noise computation,” *AIAA Journal*, Vol. 44, No. 5, pp. 992–998.

- Lowson, M. V., Fiddes, S. P., and Nash, E. C. (1994), “Laminar boundary layer aeroacoustic instabilities,” *32nd Aerospace Sciences Meeting and Exhibition*.
- Luk, K. F., So, R. M. C., Leung, R. C. K., Lau, Y. L., and Kot, S. C. (2004), “Aerodynamic and structural resonance of an elastic airfoil due to oncoming vortices,” *AIAA Journal*, Vol. 42, No. 5, pp. 899–907.
- Mack, L. M. (1975), “Linear stability theory and the problem of supersonic boundary-layer transition,” *AIAA Journal*, Vol. 13, No. 3, pp. 278–289.
- Mohany, A. and Ziada, S. (2005), “Flow-excited acoustic resonance of two tandem cylinders in cross-flow,” *Journal of Fluids and Structures*, Vol. 21, No. 1, pp. 103–119.
- Moreau, D. J. and Doolan, C. J. (2016), “The generation of tonal noise from sawtooth trailing-edge serrations at low Reynolds numbers,” *The Aeronautical Journal*, Vol. 120, No. 1228, pp. 971.
- Nakano, T., Fujisawa, N., Oguma, Y., Takagi, Y., and Lee, S. (2007), “Experimental study on flow and noise characteristics of NACA0018 airfoil,” *Journal of Wind Engineering and Industrial Aerodynamics*, Vol. 95, No. 7, pp. 511–531.
- Nakiboğlu, G. and Hirschberg, A. (2012), “Aeroacoustic power generated by multiple compact axisymmetric cavities: effect of hydrodynamic interference on the sound production,” *Physics of Fluids*, Vol. 24, No. 6, pp. 067101.
- Nash, E. C., Lowson, M. V., and McAlpine, A. (1999), “Boundary-layer instability noise on aerofoils,” *Journal of Fluid Mechanics*, Vol. 382, pp. 27–61.
- Nguyen, L. D., Hiner, W., Salehian, S., Golubev, V. V., Mankbadi, R. R., Yakhina, G. R., and Roger, M. (2015), “Parametric Investigations of Tonal Trailing-Edge Noise Generation by Low-Reynolds Number Airfoils. Part II-Numerical Studies,” *21st AIAA/CEAS Aeroacoustics Conference*, p. 2528.

- Oerlemans, S., Fisher, M., Maeder, T., and Kögler, K. (2009), “Reduction of wind turbine noise using optimized airfoils and trailing-edge serrations,” *AIAA Journal*, Vol. 47, No. 6, pp. 1470–1481.
- Parchen, R., Hoffmans, W., Gordner, A., and Braun, K. (1999), “Reduction of airfoil self-noise at low Mach number with a serrated trailing edge,” *International Congress on Sound and Vibration, 6 th, Technical Univ. of Denmark, Lyngby, Denmark*, pp. 3433–3440.
- Paterson, R. W., Vogt, P. G., Fink, M. R., and Munch, C. L. (1973), “Vortex noise of isolated airfoils,” *Journal of Aircraft*, Vol. 10, No. 5, pp. 296–302.
- Patil, M. J., Hodges, D. H., and Cesnik, C. E. S. (2001), “Nonlinear aeroelasticity and flight dynamics of high-altitude long-endurance aircraft,” *Journal of Aircraft*, Vol. 38, No. 1, pp. 88–94.
- Pedersen, E. and Persson Waye, K. (2004), “Perception and annoyance due to wind turbine noise—a dose–response relationship,” *The Journal of the Acoustical Society of America*, Vol. 116, No. 6, pp. 3460–3470.
- Plogmann, B., Herrig, A., and Würz, W. (2013), “Experimental investigations of a trailing edge noise feedback mechanism on a NACA 0012 airfoil,” *Experiments in fluids*, Vol. 54, No. 5, pp. 1480.
- Pröbsting, S., Scarano, F., and Morris, S. C. (2015), “Regimes of tonal noise on an airfoil at moderate Reynolds number,” *Journal of Fluid Mechanics*, Vol. 780, pp. 407–438.
- Pröbsting, S., Serpieri, J., and Scarano, F. (2014), “Experimental investigation of aerofoil tonal noise generation,” *Journal of Fluid Mechanics*, Vol. 747, pp. 656–687.

- Pröbsting, S. and Yarusevych, S. (2015), “Laminar separation bubble development on an airfoil emitting tonal noise,” *Journal of Fluid Mechanics*, Vol. 780, pp. 167–191.
- Reed, H. L., Saric, W. S., and Arnal, D. (1996), “Linear stability theory applied to boundary layers,” *Annual review of fluid mechanics*, Vol. 28, No. 1, pp. 389–428.
- Ricciardi, T. R., Arias-Ramirez, W., and Wolf, W. R. (2020), “On secondary tones arising in trailing-edge noise at moderate Reynolds numbers,” *European Journal of Mechanics-B/Fluids*, Vol. 79, pp. 54–66.
- Roberts, W. B. (1980), “Calculation of laminar separation bubbles and their effect on airfoil performance,” *AIAA journal*, Vol. 18, No. 1, pp. 25–31.
- Rojratsirikul, P., Genc, M. S., Wang, Z., and Gursul, I. (2011), “Flow-induced vibrations of low aspect ratio rectangular membrane wings,” *Journal of Fluids and Structures*, Vol. 27, No. 8, pp. 1296–1309.
- Rojratsirikul, P., Wang, Z., and Gursul, I. (2010a), “Effect of pre-strain and excess length on unsteady fluid–structure interactions of membrane airfoils,” *Journal of Fluids and Structures*, Vol. 26, No. 3, pp. 359–376.
- Rojratsirikul, P., Wang, Z., and Gursul, I. (2010b), “Unsteady fluid-structure interactions of membrane airfoils at low Reynolds numbers,” *Animal Locomotion*, Springer, pp. 297–310.
- Ruban, A. I. (1984), “On the generation of Tollmien-Schlichting waves by sound,” *Fluid Dynamics*, Vol. 19, No. 5, pp. 709–717.
- Rubio Carpio, A., Avallone, F., and Ragni, D. (2018), “On the role of the flow permeability of metal foams on trailing edge noise reduction,” *2018 AIAA/CEAS Aeroacoustics Conference*, p. 2964.

- Rubio Carpio, A., Avallone, F., Ragni, D., Snellen, M., and van der Zwaag, S. (2019), “Mechanisms of broadband noise generation on metal foam edges,” *Physics of Fluids*, Vol. 31, No. 10, pp. 105110.
- Rugonyi, S. and Bathe, K.-J. (2001), “On finite element analysis of fluid flows fully coupled with structural interactions,” *CMES- Computer Modeling in Engineering and Sciences*, Vol. 2, No. 2, pp. 195–212.
- Sandberg, R. D., Jones, L. E., Sandham, N. D., and Joseph, P. F. (2007), “Direct numerical simulations of noise generated by airfoil trailing edges,” *13th AIAA/CEAS Aeroacoustics Conference (28th AIAA Aeroacoustics Conference)*, p. 3469.
- Sanjose, M., Towne, A., Jaiswal, P., Moreau, S., Lele, S., and Mann, A. (2019), “Modal analysis of the laminar boundary layer instability and tonal noise of an airfoil at Reynolds number 150,000,” *International Journal of Aeroacoustics*, Vol. 18, No. 2-3, pp. 317–350.
- Sarradj, E. and Geyer, T. F. (2007), “Noise generation by porous airfoils,” *13th AIAA/CEAS Aeroacoustics Conference (28th AIAA Aeroacoustics Conference)*, p. 3719.
- Schlanderer, S. C. and Sandberg, R. D. (2013), “DNS of a Compliant Trailing-Edge Flow,” *19th AIAA/CEAS Aeroacoustics Conference*, p. 2013.
- Schumacher, K. L., Doolan, C. J., and Kelso, R. M. (2014), “The effect of a cavity on airfoil tones,” *Journal of Sound and Vibration*, Vol. 333, No. 7, pp. 1913–1931.
- Selig, M. (2016), “UIUC airfoil coordinates database,” *UIUC Applied Aerodynamics Group, Urbana, IL*, Vol. 18.

- Serrano-Galiano, S., Sandham, N. D., and Sandberg, R. D. (2018), “Fluid–structure coupling mechanism and its aerodynamic effect on membrane aerofoils,” *Journal of Fluid Mechanics*, Vol. 848, pp. 1127–1156.
- Shaaban, A. A. and Ziada, S. (2019), “Effect of the separation distance on the aeroacoustic source of multiple shallow cavities,” *Journal of Fluids Engineering*, Vol. 141, No. 1.
- Shyy, W., Berg, M., and Ljungqvist, D. (1999), “Flapping and flexible wings for biological and micro air vehicles,” *Progress in Aerospace Sciences*, Vol. 35, No. 5, pp. 455–505.
- Shyy, W., Lian, Y., Tang, J., Viieru, D., and Liu, H. (2008), *Aerodynamics of low Reynolds number flyers*, Vol. 10. Cambridge university press New York.
- Singer, B. A., Brentner, K. S., Lockard, D. P., and Lilley, G. M. (2000), “Simulation of acoustic scattering from a trailing edge,” *Journal of Sound and Vibration*, Vol. 230, No. 3, pp. 541–560.
- Smith, R. and Shyy, W. (1995), “Computation of unsteady laminar flow over a flexible two-dimensional membrane wing,” *Physics of Fluids*, Vol. 7, No. 9, pp. 2175–2184.
- So, R. M. C., Liu, Y., and Lai, Y. G. (2003), “Mesh shape preservation for flow-induced vibration problems,” *Journal of fluids and structures*, Vol. 18, No. 3-4, pp. 287–304.
- Song, A., Tian, X., Israeli, E., Galvao, R., Bishop, K., Swartz, S., and Breuer, K. (2008), “Aeromechanics of membrane wings with implications for animal flight,” *AIAA Journal*, Vol. 46, No. 8, pp. 2096–2106.
- Stanford, B., Ifju, P., Albertani, R., and Shyy, W. (2008), “Fixed membrane wings

- for micro air vehicles: Experimental characterization, numerical modeling, and tailoring,” *Progress in Aerospace Sciences*, Vol. 44, No. 4, pp. 258–294.
- Stanford, B., Sytsma, M., Albertani, R., Viieru, D., Shyy, W., and Ifju, P. (2007), “Static aeroelastic model validation of membrane micro air vehicle wings,” *AIAA Journal*, Vol. 45, No. 12, pp. 2828–2837.
- Stoica, P., Moses, and L, R. (2005), *Spectral analysis of signals*. Pearson Prentice Hall Upper Saddle River, NJ, 1st ed.
- Takagi, S. and Konishi, Y. (2010), “Frequency selection mechanism of airfoil trailing-edge noise,” *Journal of Aircraft*, Vol. 47, No. 4, pp. 1111–1116.
- Talboys, E. and Brücker, C. (2018), “Upstream shear-layer stabilisation via self-oscillating trailing edge flaplets,” *Experiments in Fluids*, Vol. 59, No. 10, pp. 145.
- Talboys, E., Geyer, T. F., and Brücker, C. (2019), “An aeroacoustic investigation into the effect of self-oscillating trailing edge flaplets,” *Journal of Fluids and Structures*, pp. 2–11.
- Tam, C. K. W. (1974), “Discrete tones of isolated airfoils,” *The Journal of the Acoustical Society of America*, Vol. 55, No. 6, pp. 1173–1177.
- Tam, C. K. W. and Ju, H. (2012), “Aerofoil tones at moderate Reynolds number,” *Journal of Fluid Mechanics*, Vol. 690, pp. 536–570.
- Tamai, M., Murphy, J., and Hu, H. (2008), “An experimental study of flexible membrane airfoils at low Reynolds numbers,” *46th AIAA Aerospace Sciences Meeting and Exhibit*, p. 580.
- Teruna, C., Manegar, F., Avallone, F., Ragni, D., Casalino, D., and Carolus, T.

- (2020), “Noise reduction mechanisms of an open-cell metal-foam trailing edge,” *Journal of Fluid Mechanics*, Vol. 898.
- Theofilis, V. (2003), “Advances in global linear instability analysis of nonparallel and three-dimensional flows,” *Progress in Aerospace Sciences*, Vol. 39, No. 4, pp. 249–315.
- Unnikrishnan, S. and Gaitonde, D. V. (2016), “A high-fidelity method to analyze perturbation evolution in turbulent flows,” *Journal of Computational Physics*, Vol. 310, pp. 45–62.
- van der Velden, W. C. and Oerlemans, S. (2017), “Numerical analysis of noise reduction mechanisms on improved trailing edge serrations using the Lattice Boltzmann method,” *35th Wind Energy Symposium*, p. 1379.
- van der Velden, W. C., van Zuijlen, A., and Ragni, D. (2016), “Flow topology and noise emission around straight, serrated and slitted trailing edges using the Lattice Boltzmann methodology,” *22nd AIAA/CEAS Aeroacoustics Conference*, p. 3021.
- van Kamp, I. and van den Berg, F. (2018), “Health effects related to wind turbine sound, including low-frequency sound and infrasound,” *Acoustics Australia*, Vol. 46, No. 1, pp. 31–57.
- Vathylakis, A., Chong, T. P., and Joseph, P. F. (2015), “Poro-serrated trailing-edge devices for airfoil self-noise reduction,” *AIAA Journal*, Vol. 53, No. 11, pp. 3379–3394.
- Venkatachari, B. S., Cheng, G. C., Soni, B. K., and Chang, S. C. (2008), “Validation and verification of Courant number insensitive conservation element and solution element method for transient viscous flow simulations,” *Mathematics and Computers in Simulation*, Vol. 78, No. 5-6, pp. 653–670.

- Visbal, M. R. and Gordnier, R. E. (2004), “Numerical simulation of the interaction of a transitional boundary layer with a 2-D flexible panel in the subsonic regime,” *Journal of fluids and structures*, Vol. 19, No. 7, pp. 881–903.
- Vitturi, M. d., Ongaro, T. E., Neri, A., Salvetti, M. V., and Beux, F. (2007), “An immersed boundary method for compressible multiphase flows: application to the dynamics of pyroclastic density currents,” *Computational Geosciences*, Vol. 11, No. 3, pp. 183–198.
- Wang, C. (2018), “Trailing Edge Perforation for Interaction Tonal Noise Reduction of a Contra-Rotating Fan,” *Journal of Vibration and Acoustics*, Vol. 140, No. 2.
- Wang, J., Zhang, C., Wu, Z., Wharton, J., and Ren, L. (2017a), “Numerical study on reduction of aerodynamic noise around an airfoil with biomimetic structures,” *Journal of Sound and Vibration*, Vol. 394, pp. 46–58.
- Wang, J., Zhang, C., Wu, Z., Wharton, J., and Ren, L. (2017b), “Numerical study on reduction of aerodynamic noise around an airfoil with biomimetic structures,” *Journal of Sound and Vibration*, Vol. 394, pp. 46–58.
- Waye, K. P. and Öhrström, E. (2002), “Psycho-acoustic characters of relevance for annoyance of wind turbine noise,” *Journal of sound and vibration*, Vol. 250, No. 1, pp. 65–73.
- Wright, S. E. (1976), “The acoustic spectrum of axial flow machines,” *Journal of Sound and Vibration*, Vol. 45, No. 2, pp. 165–223.
- Wu, D., Lam, G. C. Y., and Leung, R. C. K. (2018), “An Attempt to Reduce Airfoil Tonal Noise Using Fluid-Structure Interaction,” *2018 AIAA/CEAS Aeroacoustics Conference*, pp. 3790–3816.

- Yen, J. and Wagner, D. (2005), “Computational aeroacoustics using a simplified Courant number insensitive CE/SE method,” *11th AIAA/CEAS Aeroacoustics Conference*, p. 2820.
- Yu, S. T. and Chang, S. C. (1997), “Applications of the space-time conservation element/solution element method to unsteady chemically reacting flows,” *13th Computational Fluid Dynamics Conference*, p. 2099.
- Zhou, P., Liu, Q., Zhong, S., Fang, Y., and Zhang, X. (2020), “A study of the effect of serration shape and flexibility on trailing edge noise,” *Physics of Fluids*, Vol. 32, No. 12, pp. 127114.